MICROWAVE RESONATORS FOR HIGHLY SENSITIVE COMPOSITIONAL ANALYSIS OF SOLVENTS IN MICROCAPILLARY SYSTEMS

A thesis submitted to Cardiff University
In candidature for the degree of

Doctor of Philosophy

By

Adnan Masood, MSEE

Division of Electrical and Electronic Engineering
School of Engineering
Cardiff University
United Kingdom

June 2009

DECLARATION

This work has not previously been accepted in substance for any degree and is not concurrently submitted in candidature for any degree.

Signed …….. (Candidate)

Date ……

STATEMENT 1

This thesis is being submitted in partial fulfilment of the requirements for the degree of PhD.

Signed …….. (Candidate)

Date ……

STATEMENT 2

This thesis is the result of my own independent work/investigation, except where otherwise stated. Other sources are acknowledged by explicit references.

Signed …….. (Candidate)

Date ……

STATEMENT 3

I hereby give consent for my thesis, if accepted, to be available for photocopying and for inter-library loan, and for the title and summary to be made available to outside organisations.

Signed …….. (Candidate)

Date ……

STATEMENT 4

I hereby give consent for my thesis, if accepted, to be available for photocopying and for inter-library loans after expiry of a bar on access approved by the Graduate Development Committee.

Signed …….. (Candidate)

Date ……

ABSTRACT

The ability to precisely analyse the composition of liquid mixtures by non-contact techniques in both static and flow situations is extremely desirable for a diversity of industrial, analytical and quality control procedures. Microwave resonators allow very accurate and sensitive characterisation of the dielectric properties of polar liquids due to the strong interaction of the latter with microwave electric fields. They have the useful dual role of both exact characterisation of the complex permittivity of a dielectric sample when it is inserted within a region of high electric field of the resonator, and effective volumetric heating of the same sample if its dielectric loss is large enough to permit heating. They offer tremendous potential for investigation of very small amounts of polar solvents in non-polar hosts. In this regard they are superior to other traditional composition analysis techniques such as liquid chromatography, gas chromatography and mass spectrometry in the speed of analysis (≈ 1 s), non destructive nature and scope for miniaturisation of the resonator size to suit the system under test.

For minute sample volumes, the resonator perturbation technique is extensively used for dielectric measurements on polar liquids. In this project, it has been employed for highly sensitive compositional analysis of two-component dielectric mixtures contained in microcapillary segments. The first evaluation system used here was mixtures of acetonitrile and toluene, chosen because of the large difference in their molecular electric dipole moments. The results obtained from this first system provided the inspiration to assess mixtures made of acetonitrile and water, which are much more closely matched in terms of their electric dipole moments. Three different types of resonators namely hairpin resonator, split ring resonator and sapphire dielectric resonator were used to analyse both the aforementioned solution systems. The results show very sensitive characterisation and are in close agreement with the theoretical predictions governing perturbation of resonators by dielectric samples. In the last phase of this research, a miniaturised sapphire dielectric resonator was designed and fabricated that provided added enhancement in measured sensitivity of both evaluation mixtures.

ACKNOWLEDGEMENT

I would like to thank my supervisors Prof. David Barrow and Prof. Adrian Porch for giving me the opportunity to study for this degree. I am enormously grateful to them both for their unwavering support, direction and mentoring during the last three years. I have benefited deeply from Prof. Barrow's expertise in the area of microfluidics while Prof. Porch has ably guided me through the intricate aspects of the theory and design of microwave resonators. I am also thankful to Oliver Castell and Neil Sykes for their useful advice and practical assistance in helping me achieve the ultimate target of my project i.e. a miniaturised resonator based microfluidic device for enabling extremely sensitive compositional analysis.

I acknowledge the support extended by Dr. Jonathan Less with regards to making available to me Agilent N5242A PNA-X Network Analyser for undertaking characterisation experiments in the miniaturised microfluidic device. I also appreciate the cooperation of my fellow PhD students namely Chris Roff, Simon Woodington and Nilaped Russamee for helping me out with development of the IGOR Pro software code used for carrying out resonator measurements. I must also mention here Aslam Sulaimalebbe and Mohammad Shabi Hashmi, who besides becoming my closest friends during my time at Cardiff University provided me with valuable help in different facets of my research and thesis writing.

I owe a debt of gratitude to my parents and extended family in Pakistan, whose prayers and encouragement have been the biggest source of motivation for me during the course of my PhD. My dear wife Shazia deserves a special word of appreciation for her persistent moral support and patience in the past three years. I have the utmost regard for her in the way she has coped with the responsibilities of running our household and caring for our three children singlehandedly, especially for the duration of last year or so.

LIST OF PUBLICATIONS

1. A. Masood, O. Castell, D. A. Barrow, C. Allender and A. Porch, "Split Ring Resonator Technique for Compositional Analysis of Solvents in Microcapillary Systems", *The Proceedings of MicroTAS 2008 Conference*, San Diego, pp.1636-1638, October 2008.
2. R. Göritz, A. Masood, O. Castell, D. A. Barrow, C. Allender and A. Porch "Microwave Compositional Analysis of Solvent Matrices in Microcapillary Manifold Systems", *The Proceedings of MicroTAS 2007 Conference*, Paris, pp.1689-1691, October 2007.
3. O. Castell, A. Masood, R. Göritz, D. A. Barrow, C. Allender and A. Porch, "Microwave Technique for Monitoring Separation of a Multiphase-Flow Regime Utilised for Continuous Molecular Enrichment", *The Proceedings of MicroTAS 2008 Conference*, San Diego, pp.137-139, October 2008.

LIST OF ACRONYMS

DR – Dielectric Resonator

TL – Transmission Line

RF – Radio Frequency

GC– Gas Chromatography

LC – Liquid Chromatography

HPLC – High Performance Liquid Chromatography

TLC – Thin Layer Chromatography

VNA – Vector Network Analyzer

GPIB – General Purpose Instrument Bus

SDR – Sapphire Dielectric Resonator

SPDR – Split Post Dielectric Resonator

MeCN – Methyl Cyanide (Acetonitrile)

PEEK – Polyetheretherketone

PTFE – Polytetrafluoroethylene

IL – Insertion Loss

IEEE – Institute of Electrical and Electronics Engineers

HEM – Hybrid Electro Magnetic

TE – Transverse Electric

TM – Transverse Magnetic

TEM – Transverse Electro Magnetic

NMR – Nuclear Magnetic Resonance

MS – Mass Spectrometry

TBP – True Boiling Point

UV – Ultra Violet

CE – Capillary Electrophoresis

CL – Chemiluminescence

TABLE OF CONTENTS

CHAPTER 1

INTRODUCTION AND THESIS SUMMARY

On-chip, non-invasive and fast compositional analysis of liquid mixtures is desirable in a variety of industrial, analytical and quality control applications, but is generally unavailable. Microwave resonators allow extremely precise and sensitive characterisation of the dielectric properties of polar liquids due to their strong interaction with microwave electric fields. Any or all of the three main material properties i.e. relative permittivity (ε), relative permeability (μ) and electrical conductivity (σ) can be measured in a contactless manner by microwave techniques. With specific regards to polar liquids, microwave resonators have the useful dual role of both sensitive characterisation of ε_1 (i.e. dielectric constant) and ε_2 (i.e. dielectric loss) when a sample is inserted within a region of high electric field of a host microwave resonator, and effective volumetric heating of the same sample if ε_2 is large enough to permit heating. In the context of this thesis, the focus will be solely on the dielectric characterisation of polar liquids using novel host resonators.

For very small sample volumes, the resonator perturbation technique is widely used for dielectric measurements on polar liquids. In this project, it has been employed for highly sensitive compositional analysis of two-component dielectric mixtures contained in microcapillary segments. The initial evaluation system used was mixtures of acetonitrile and toluene, selected due to the large difference in their molecular electric dipole moments. The results obtained from this first system provided the motivation to evaluate mixtures made of acetonitrile and water, which are much more closely matched in terms of their electric dipole moments. Both distributed and lumped element type resonators were used for compositional analysis and their results show agreement with the theoretical predictions. There are multiple benefits of using a resonant microwave technique over other methods. Firstly, it is fast, with data accumulation on a timescale of about 0.1 s, thereby enabling compositional analysis in situations where fluid flow and/or chemical reaction are occurring. Secondly, it is non-destructive and applicable to arbitrarily-shaped sample volumes. Thirdly, the resonator size can be miniaturised to suit the system under test, providing for even higher measurement sensitivity. The specific structure of this thesis is as follows:

- **Dielectric Characterisation of Liquids by Microwaves (Chapter 2)**

  The properties of polar liquids and their interaction with microwave electric field are discussed and an overview of the main microwave techniques for dielectric measurements on polar liquids is provided. The theory of resonator perturbation is covered in detail and its applicability to compositional analysis of liquids is described.

- **Microwave Resonator Theory (Chapter 3)**

  The fundamental concepts of microwave resonators emanating from resonant transmission lines are explained. The principles of microwave network analysis, scattering parameters and transmission mode measurements with microwave resonators are detailed.

- **Description of Resonators (Chapter 4)**

  The various microwave resonator devices used in this project namely the hairpin resonator, the split ring resonator and sapphire dielectric resonator are described. The design and construction of all resonators is covered along with derivation of expressions for their resonant frequency and unloaded quality factor.

- **Compositional Analysis of Solvents in Microcapillary Systems (Chapter 5)**

  An essential part of this research was to corroborate the validity of the theoretical predictions by experimental methods. In this regard, in-situ compositional analysis of acetonitrile:toluene and acetonitrile:water mixtures in microcapillary manifold systems was carried out in each of the aforementioned three resonators. This chapter discusses the relevant experimental details and obtained results.

- **The Miniaturised Sapphire Dielectric Resonator (Chapter 6)**

  This chapter provides a full account of the design, simulation and fabrication of a miniaturised dielectric resonator device that enabled extremely sensitive

compositional analysis of solvent matrices. This in fact proved to be the most challenging task encountered in this project and took almost a year to complete.

- **Conclusions and Recommendations (Chapter 7)**

  A brief summary of the work carried out so far and suggestions for future course of action are discussed.

Key Contributions Made

- Extremely sensitive characterisation of acetonitrile:toluene and acetonitrile:water solution systems in hairpin, split ring and sapphire dielectric resonator. Use of these resonators enables detection of less than 0.1% by volume of acetonitrile in toluene. The results of these experiments show good agreement with theory.
- Development of an automated data acquisition and analysis system (using IGOR Pro software) for gathering characterisation data from vector network analyser and processing it to extract microwave parameters of interest.
- Design, simulation and fabrication of a microfluidic characterisation device based on a miniaturised version of the sapphire dielectric resonator, which provided extra enhancement in measurement sensitivity. This apparatus is also novel in the sense that no microcapillary is needed for solution flow; instead a micro channel is laser ablated on resonator surface for carrying the samples being characterised.

CHAPTER 2

DIELECTRIC CHARACTERISATION OF LIQUIDS BY MICROWAVES

2.1 Introduction

The central dielectric parameter of interest pertaining to their characterisation by microwave radiation is the complex relative permittivity $\varepsilon_r = \varepsilon_1 - j\varepsilon_2$, where ε_1 is the real part (generally known as permittivity or dielectric constant) and ε_2 is the imaginary part (or the loss factor) [1]. Polar liquids are those whose molecules have permanent dipole moments [2]. Conversely, non-polar liquids are those whose molecules only develop a net electrical polarisation upon application of an external electric field. The dielectric constant of polar liquids is much higher than non-polar liquids, lying in the approximate range of 10 to 100. Similarly, the microwave dielectric loss of polar liquids is also comparatively high, with loss tangents (i.e. $\varepsilon_2/\varepsilon_1$) typically around 0.1 – 1 [1]. Some examples of commonly found polar liquids are water, acetonitrile, acetone and ethanol. The characterisation of dielectric liquids is finding increased interest because of a number of reasons. Firstly, the dielectric relaxation behaviour of polar liquids provides hints to their molecular structure. Secondly, biomedical applications of polar liquids have gained prominence because of the fairly good match of their complex permittivity to those of biological tissues over the frequency range of 300 MHz – 6 GHz. This region of the electromagnetic spectrum is extensively used for mobile and local area telecommunications [1]. Thirdly, dielectric measurements are required for numerous applications in industry, medicine and pharmaceuticals [2]. A review of existing microwave techniques for dielectric measurements on polar liquids will be provided in this chapter followed by the theoretical facets of the mechanism of dielectric polarisation and relevant resonator perturbation theory.

2.2 Main Microwave Methods for Dielectric Characterisation

Microwave methods have great potential for very sensitive characterisation of the dielectric properties of polar liquids due to their strong interaction with microwave electric fields. They enable precise, non-invasive and fast compositional analysis of liquid mixtures for a variety

of industrial, analytical and quality control applications. The microwave methods used for dielectric measurements on polar liquids can be divided into three major categories: reflection methods, transmission methods and resonance methods. The first and second techniques are non-resonance, based on measurements of broadband scattering parameters (*S* parameters)[1] while the third method is founded on spot frequency *S* parameters measurements yielding quality factor (*Q*) and resonant frequency (f_0) [1]. As the name suggests, the reflection technique makes use of the complex reflection coefficient for calculation of complex permittivity. It is the most widespread method currently in use because of the popularity of the coaxial sensor, also called as a coaxial probe, a coaxial-line probe, a coaxial reflectance probe or an open-ended probe. The coaxial sensor is used in combination with a vector network analyser (VNA), which measures the complex reflection coefficient [1,3]. The second non-resonant method, i.e. transmission method employs measurement of the *S* parameters of two-port liquid-filled cells constructed in waveguide or coaxial line, such as that described in [4]. From the standpoint of this project, however, the most relevant methods are those based on resonance i.e. using resonators and cavities. VNAs are usually employed in all modern resonance techniques for measuring the resonator *Q* and f_0. For measurement of very small volumes (i.e. << resonator volume) as is the case for this research, the term cavity (or resonator) perturbation technique is frequently used because the effect of introducing the sample into a resonator on *Q* and f_0 was traditionally dealt with by first order perturbation theory [1]. Nonetheless, the perturbation technique is widely used in many current practical applications when resonators are modified by making small changes in their shape or by introduction of small dielectric or metallic samples [5]. The underlying assumption in the perturbation technique is that $\Delta f_0 \propto \varepsilon_1$ and $\Delta(1/Q) \propto \varepsilon_2$, where Δf_0 and $\Delta(1/Q)$ are changes in f_0 and $1/Q$, respectively, on sample insertion [1,6,7]. It is pertinent to mention here that the changes in both parameters have to be small for the perturbation theory to be valid.

[1] For a detailed description of *S* parameters, see section 3.3.2 of this thesis.

2.3 Literature Review of Cavity Perturbation Technique

The cavity perturbation technique has been in use to make material property measurements for the past at least sixty years. Birnbaum and Franeau [8] reported measurement of the dielectric constant and loss of solids and liquids by a cavity perturbation method, as early as 1949. Since then it has been consistently employed in cavity as well as resonator based systems with most researchers preferring metal cavities operating in the low order TE_{011} or TM_{011} modes. For example, Kumar and Smith [9] have used an X-band (i.e. 8-12GHz) TE_{011} mode cylindrical cavity for accurate complex permittivity measurements on methyl alcohol, ethylene glycol and *n*-propyl alcohol. Similarly, Martinelli *et al*. made dielectric loss measurements on solutions of n.butyl acrylate in benzene solvent with a TE_{011} mode cylindrical cavity. Han *et al*. [11] have reported a cavity perturbation system for measurement of microwave magnetic properties of superconducting $YBa_2Cu_3O_{7-\delta}$ thin films in a TE_{011} mode cavity at 13 GHz. Regarding use of TM mode cavities, Mansingh and Parkash [12] measured conductivity and permittivity of semiconductor (n-type silicon and germanium) spheres using a cylindrical TM_{011} mode cavity resonating at about 3.7 GHz. They reported good agreement of their results with literature values. Another instance of use of TM_{011} mode cylindrical cavity is by Mansingh *et al*. [13], where they measured complex permittivities of pure liquids and solutions in benzene of ortho and meta isomers of difluoro-, dichloro-, dibromo- and diiodo-benzene at 2.4 GHz. A very recent employment of cylindrical cavity operating in TM_{011} mode is by Ikeda *et al*. [7], who have used cavity perturbation method for investigation of the influence of coupling on the measured value of complex permittivity of a ceramic material. In addition to the low order mode cavities, cavity perturbation technique has been used for accurate permittivity measurement of extremely low-loss dielectric materials in TE_{112} mode (9 GHz) cylindrical cavity [14]. Another pertinent and a very interesting paper is by Ye et al.[15], wherein they have measured the complex permittivity of apple juice to validate the accuracy of their method. They have used a TE_{315} mode rectangular cavity that is resonant at centre frequency of 5.8 GHz. Apart from the large scale employment of perturbation technique in metal cavities, other types of resonant structures have also been reported. In this connection, Raveendranath *et al*. [16,17] have used two coaxial cavity resonator (i.e. section of a coaxial line with one end open) for complex permittivity measurement of liquids in the range 0.6 – 7 GHz and 5 – 14 GHz. They reported accurate measurement of both ε_1 and ε_2 of water and nitrobenzene over the aforementioned frequency range. Anderson *et al*. [18] employed a cavity perturbation technique for

determination of the conductivity of potassium loaded zeolite powder samples with a 3 GHz copper hairpin resonator. Moreover, a sapphire dielectric resonator operating in the TE_{011} mode at f_0 = 14.4 GHz has been reported by Lee *et al*. [19] for obtaining the microwave surface impedance of a $Bi_2Sr_2CaCu_2O_8$ single crystal from resonator perturbation. Last but not the least, Saeed *et al*. [20] have used a novel adaptation of the resonator perturbation technique via microstrip resonators to measure the complex permittivity of solvents and characterise glucose-water solutions of different concentrations at 1 GHz. To the best of the author's knowledge, this is the only reported utilization of resonator perturbation technique for solution sensing i.e. similar to the compositional analysis application of this research. The remaining all publications have employed it for measuring the dielectric constant and/or loss factor.

2.4 **Alternative Approaches for Compositional Analysis**

Given the infrequent employment of microwave methods for analysing compositions, it is prudent to make mention of other pertinent methods. A survey of literature (that is by no means exhaustive) has divulged the following major non-microwave compositional analysis techniques:

- Gas chromatography (GC)
- Liquid chromatography (LC)
- High performance liquid chromatography (HPLC)
- Thin layer chromatography (TLC)
- Prolysis–gas chromatography (Py–GC)
- Nuclear magnetic resonance (NMR)
- Mass spectrometry (MS)
- Use of true boiling point (TBP) distillation data
- Use of physical properties (refractive index, density, sound transmission speed and isentropic compressibility)
- Capillary electrophoresis (CE)
- Chemiluminescence (CL) detection

Whereas a detailed description of each of the above mentioned methods is beyond the scope of this thesis, it is instructive to mention the main areas where they are mostly used for compositional analysis, as shown in Table 2.1.

Major Area(s) of Use	**Method(s)**	**Reference Publication(s)**
Petroleum science and technology	GC, GC-use of TBP distillation data*	[21,22]
Pharmaceutical and biomedical analysis	TLC, GC-MS, LC-MS, NMR	[23]
Microchemistry	CE-CL detection	[24]
Analytical and applied Prolysis	Py–GC	[25]
Spectroscopy (leaf oils of trees)	GC-NMR	[26]
Chromatography	HPLC-MS	[27]
Solution Chemistry	Use of Physical Properties	[28]

* - indicates that a combination of techniques is used.

Table 2.1. Summary of alternative compositional analysis techniques along with the main areas of their respective applications.

Each of the above mentioned techniques have their relative strengths and weaknesses in their application area. A glance through [21-28] reveals that the main limitation of these methods is their relative insensitivity as compared to the resonator perturbation technique, thereby implying need for larger sample volumes for use with the former. Other comparative benefits of microwave analysis are its fast speed (≈ 0.1 s), hence enabling compositional analysis in situations where fluid flow and/or chemical reaction are occurring and possibility for miniaturisation of resonator size to suit the system under test. On the other hand, the major limitation of the microwave technique in the context of compositional analysis is requirement of polar samples for sensitive characterisation.

2.5 Dielectric Polarisation Mechanism

A dielectric is an insulator i.e. it contains no conduction electrons. If a dielectric mass is placed in a uniform electric field ($\underline{E}$) its electrons stay bound to its atoms but the electron cloud of each distorts. There is a change of the centre of symmetry of the electron cloud with

respect to the nucleus in each atom. Resultantly, the dielectric becomes polarised (i.e. an electric dipole is induced on each atom) as shown in Figure 2.1 [6, 29].

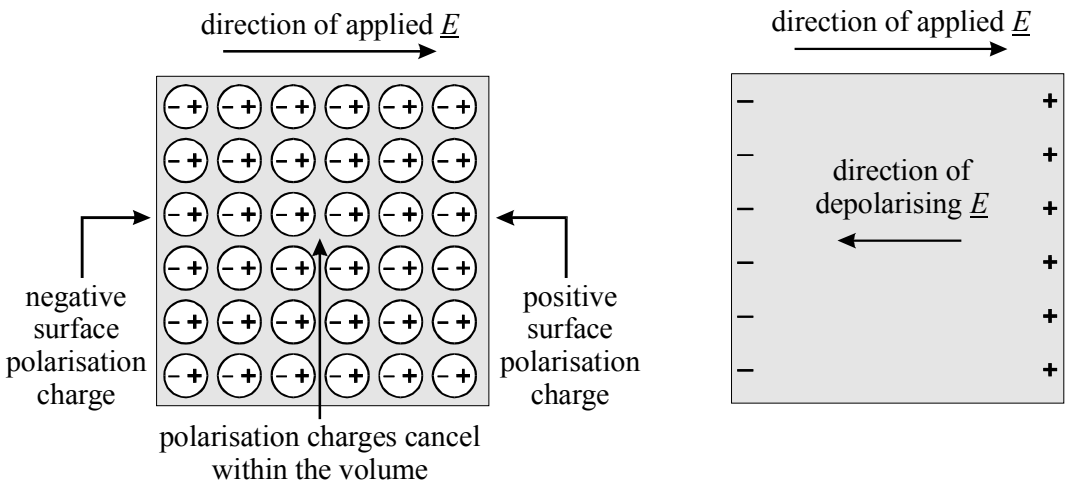

Figure 2.1. The polarisation of a dielectric; the direction of depolarising electric field is opposite to that of the applied field [6].

The surfaces perpendicular to $\underline{E}$ develop polarisation charges and $\underline{E}$ inside the dielectric is reduced due to the depolarising field. This phenomenon is similar to a metal; however, unlike metals $\underline{E}$ isn't reduced to zero in dielectrics. If the applied electric field is denoted by $\underline{E}_A$ and the depolarising field by $\underline{E}_P$, the net electric field inside the dielectric is

$$\underline{E} = \underline{E}_A - \underline{E}_P , \tag{1}$$

i.e. in general $E < E_A$. If there are n atoms per unit volume, each of dipole moment $\underline{p}$, the polarisation (i.e. dipole moment per unit volume) is $\underline{P} = n\underline{p}$ [6].

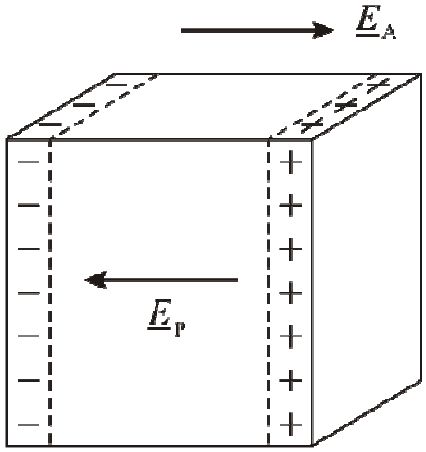

Figure 2.2. The applied electric field and the depolarising field inside a dielectric block [6].

Consider the dielectric cube shown in Figure 2.2. Its end surfaces develop surface polarisation charges $Q_{pol} = PS$, where S is the surface areas of the ends of cube. Generally, an area element $\underline{dS}$ acquires a surface polarisation charge $dQ_{pol} = \underline{P}.\underline{dS}$. The effect of the surface polarisation charges is to modify $\underline{E}$ inside the dielectric. For $\underline{P}$ parallel to a dielectric surface there is no surface polarisation charge. However, if $\underline{P}$ is perpendicular to a surface, there is maximum surface polarisation charge [6].

2.5.1 **Linear and Isotropic Dielectric Materials**

The polarisation produced by the electric field in a dielectric is a function of its material properties. If the response of the dielectric is the same for all directions of the $\underline{E}$ vector, it is called isotropic (i.e. $\underline{P}$ is independent of the direction of $\underline{E}$). A dielectric is linear if the ratio of $\underline{P}$ to $\underline{E}$ is independent of amplitude (i.e. $\underline{P} \propto \underline{E}$). For isotropic, linear dielectric materials the polarisation is proportional to the electric field intensity, which can be expressed as

$$\underline{P} = (\varepsilon_r - 1)\varepsilon_0 \underline{E} \equiv \chi_e \varepsilon_0 \underline{E}. \qquad (2)$$

In (2), ε_0 is the permittivity of free space $\approx 8.854 \times 10^{-12}$ F/m, ε_r is the relative permittivity of the dielectric and $\chi_e = \varepsilon_r - 1$ is a dimensionless quantity called the electric susceptibility of the dielectric. χ_e quantifies how strongly a dielectric will polarise when placed in an applied $\underline{E}$ field [6, 29].

2.5.2 **Polarisation Dependence on Sample Geometry**

Consider a randomly shaped object to which an electric field $\underline{E}_0$ is applied, as shown in Figure 2.3.

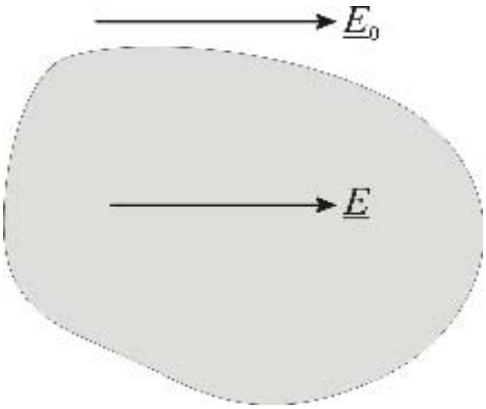

Figure 2.3. The applied electric field $\underline{E}_0$ and internal field $\underline{E}$ in an arbitrarily shaped dielectric object

The magnitude of the internal electric field $\underline{E}$ can be written as [6]

$$E = \frac{E_0}{1 + N\chi_e} = \frac{E_0}{1 + N(\varepsilon_r - 1)}, \tag{3}$$

where N is a dimensionless quantity called the depolarisation factor. It depends on the shape of the object and the direction of the applied field with respect to it. Typically, the depolarisation for various dielectric shapes are calculated by assuming a uniform internal field, and an external field consisting of the applied filed in addition to a dipole term [6]. The fluids characterised in this research were contained in microcapillary columns that can be taken as long cylinders. The applied field can either be parallel or perpendicular to the microcapillary, as shown in Figure 2.4.

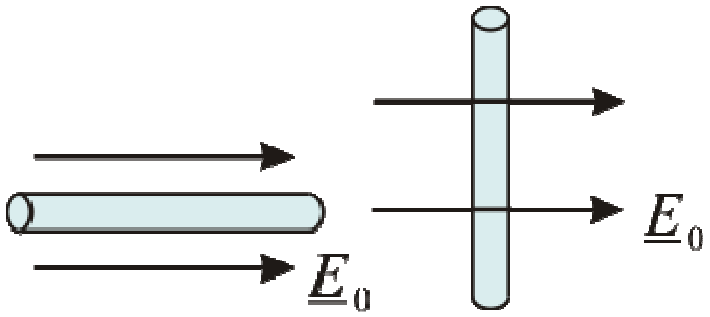

Figure 2.4. The applied electric field $\underline{E}_0$ is parallel to the microcapillary (i.e. cylinder) on left while perpendicular to it on right [6].

The depolarisation factor for field parallel to the microcapillary is approximately zero; hence, from (3)

$$E \approx E_0 . \tag{4}$$

For field perpendicular to capillary geometry, $N \approx 1/2$, so the internal field magnitude can be written as [6]

$$E = \frac{2E_0}{1+\varepsilon_r} . \tag{5}$$

2.6 **Resonator Perturbation Analysis**

The placement of a sample in the high electric field region in a microwave resonator will reduce both the resonant frequency f_0 and quality factor Q owing to polarisation. The expressions for resulting change Δf_0 and $\Delta(1/Q)$ have been derived in various standard texts (e.g. [5]) but mostly using Maxwell's equations that involve complicated mathematics. Here, a simplified resonator perturbation analysis based on [6] is presented. Consider the placement of a dielectric sample in uniform $\underline{E}$ field (i.e. fixed applied voltage $v(t) = V_0 e^{j\omega t}$) in a resonator, the equivalent circuit for which is shown in Figure 2.5.

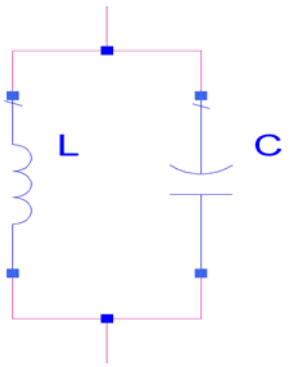

Figure 2.5. The equivalent resonant circuit for a dielectric sample placed in uniform $\underline{E}$ field.

The change in energy ΔU over time averaged stored energy in the resonator is given as

$$\frac{\Delta U}{U_{tot}} = \frac{\frac{1}{2}\Delta C \mathrm{v}^2}{\frac{1}{2}C\mathrm{v}^2} = \frac{\Delta C}{C}, \tag{6}$$

where C is the capacitance of resonator equivalent circuit. The resonant frequency for the circuit of Figure 2.5 is $f_0 = \frac{1}{2\pi\sqrt{LC}}$ that can be used to arrive at the following expression [6]:

$$\frac{\Delta f_0}{f_0} = -\frac{1}{2}\frac{\Delta U}{U_{tot}} \tag{7}$$

If a dielectric sample is placed in largest electric field magnitude (i.e. E_0) and gains a dipole moment p, then

$$\Delta U = \frac{1}{2}\mathrm{Re}(pE_0), \tag{8}$$

where Re represents the real part. Combining (7) and (8) yields the under mentioned expression for change in frequency over the resonant frequency:

$$\frac{\Delta f_0}{f_0} \approx -\frac{\mathrm{Re}(pE_0)}{4U_{tot}} \equiv -\frac{\mathrm{Re}(\alpha)}{2V_{\mathrm{eff}}}. \tag{9}$$

In (9), $U_{tot} = \frac{1}{2}\varepsilon_0 \int_{res} E^2 dV$ is the time averaged stored electromagnetic energy in the resonator, α is the sample's polarisability (defined by $p = \alpha\varepsilon_0 E_0$) and V_{eff} is the effective

volume of the resonator in terms of the distribution of electrical energy [6]. Now, consider the resonator quality factor that is defined as [5]

$$Q = \omega_0 \frac{\text{(time-averaged stored energy)}}{\text{(time-averaged power dissipated)}} = \frac{\omega_0 U_{tot}}{\langle P \rangle} \tag{10}$$

From (10), it can be written that

$$\Delta\left(\frac{1}{Q}\right) = \frac{1}{\omega_0 U_{tot}} \Delta\langle P \rangle, \tag{11}$$

which can be combined with the relation for power dissipated i.e. $\langle P \rangle = -\frac{1}{2}\omega_0 \operatorname{Im}(pE_0)$ to give

$$\Delta\left(\frac{1}{Q}\right) \approx -\frac{\operatorname{Im}(pE_0)}{2U_{tot}} \equiv -\frac{\operatorname{Im}(\alpha)}{V_{\text{eff}}}. \tag{12}$$

(9) and (12) are the standard resonator perturbation results for electric field, which will be used to establish the variation of resonant frequency and quality factor for dielectric sample carrying microcapillary segments in the next section.

2.7 Applications of Resonator Perturbation

In this project, three different resonators namely hairpin, split ring and sapphire dialectic resonator have been used for compositional analysis of acetonitrile:toluene and acetonitrile:water mixtures. In the first two resonators, the microcapillary segments carrying the fluids were placed such that the microwave electric field was perpendicular to them. This was necessitated by the particular geometries of the resonator structures. However, the configuration of the sapphire dielectric resonator allowed placement of the microcapillary parallel to the electric field. Resonator perturbation theory will now be applied to both these cases to determine the expected results for $\Delta f_0 / f_0$ and $\Delta(1/Q)$, as follows:

2.7.1 Perpendicular Electric Field

The starting point is sample's induced electric dipole moment *p*, the magnitude of which from (2) can be written as

$$p = V\left(\varepsilon_r - 1\right)\varepsilon_0 E\,, \tag{13}$$

where V is the sample volume. Substituting the internal field magnitude for the perpendicular direction from (5) in (13) gives

$$p = V\left(\varepsilon_r - 1\right)\varepsilon_0\left(\frac{2E_0}{1+\varepsilon_r}\right) = 2V\varepsilon_0\left(\frac{\varepsilon_r - 1}{\varepsilon_r + 1}\right)E_0\,. \tag{14}$$

For polar samples, which is where microwave resonators are usually employed, the relative permittivity is complex i.e. $\varepsilon_r = \varepsilon_1 - j\varepsilon_2$. Thus, (14) becomes

$$p = 2V\varepsilon_0\frac{\left(\varepsilon_1 - 1\right) - j\varepsilon_2}{\left(\varepsilon_1 - 1\right) + j\varepsilon_2}E_0 \tag{15}$$

and accordingly

$$pE_0 = 2V\varepsilon_0\frac{\left(\varepsilon_1 - 1\right) - j\varepsilon_2}{\left(\varepsilon_1 + 1\right) - j\varepsilon_2}{E_0}^2 \tag{16}$$

To separate the real and imaginary parts of (16), it has to be divided and multiplied by the complex conjugate of the denominator term i.e. $\left(\varepsilon_1 + 1\right) + j\varepsilon_2$. This results in

$$\mathrm{Re}\left(pE_0\right) = 2V\varepsilon_0{E_0}^2\left(\frac{\left(\varepsilon_1 - 1\right)\left(\varepsilon_1 + 1\right) - {\varepsilon_2}^2}{\left(\varepsilon_1 + 1\right)^2 + {\varepsilon_2}^2}\right) \tag{17}$$

and

$$\mathrm{Im}\left(pE_0\right) = 2V\varepsilon_0{E_0}^2\left(\frac{-2\varepsilon_2}{\left(\varepsilon_1 + 1\right)^2 + {\varepsilon_2}^2}\right). \tag{18}$$

Combining (17) with (9) produces

$$\frac{\Delta f_0}{f_0} \approx \frac{-V\varepsilon_0{E_0}^2}{2U}\left(\frac{\left(\varepsilon_1 - 1\right)\left(\varepsilon_1 + 1\right) - {\varepsilon_2}^2}{\left(\varepsilon_1 + 1\right)^2 + {\varepsilon_2}^2}\right), \tag{19}$$

while substitution of (18) in (12) gives

$$\Delta\left(\frac{1}{Q}\right) = 2V\varepsilon_0{E_0}^2\left(\frac{\varepsilon_2}{\left(\varepsilon_1 + 1\right)^2 + {\varepsilon_2}^2}\right). \tag{20}$$

Using Mathcad, the variations in resonant frequency and quality factor have been plotted against increasing loss factor (i.e. ε_2) with constant ε_1, for arbitrary values of U, E_0 and V, as shown in Figures 2.6 and 2.7, respectively.

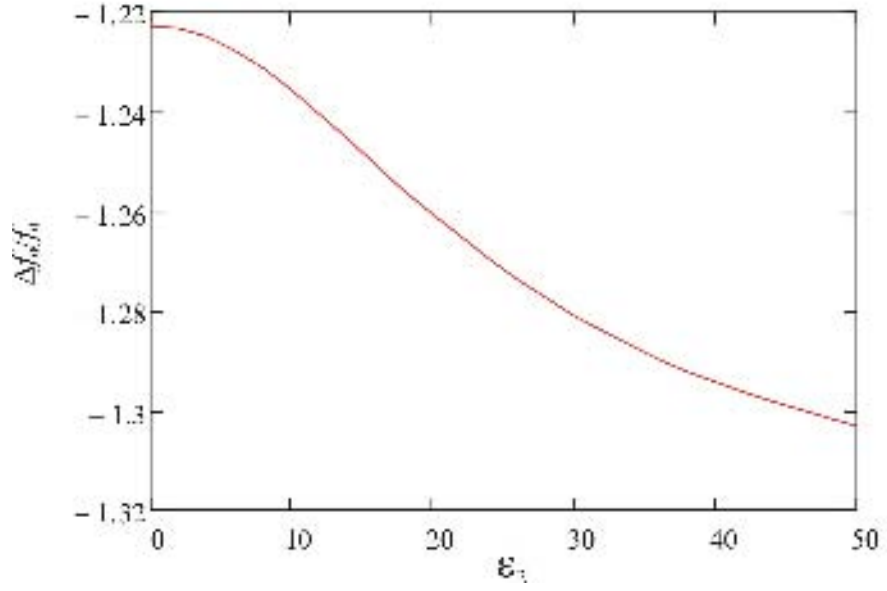

Figure 2.6. The variation of $\Delta f_0 / f_0$ with increasing loss factor of a polar solvent in a resonator where the electric field is perpendicular to the sample.

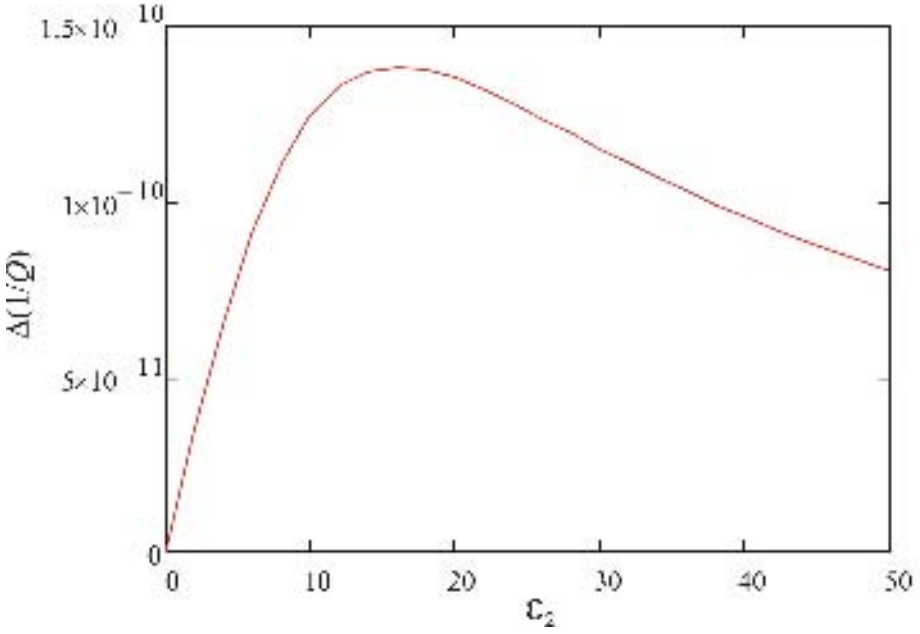

Figure 2.7. The variation of $1/Q$ with increasing loss factor of a polar solvent in a resonator where the electric field is perpendicular to the sample.

Figure 2.6 shows that the resonant frequency monotonically decreases for electric field perpendicular to a cylindrical sample, with increasing dielectric loss. This is because the frequency shift is determined by external E distribution and is thus not affected by depolarisation. The plot of $\Delta(1/Q)$ in Figure 2.7 appears as unusual because it reaches a peak and then starts decreasing. In other words, the Q is minimised for a certain value of ε_2, after which it again increases. The theoretical explanation behind this phenomenon is that as ε_2 increases, E decreases due to depolarisation; therefore, microwave losses exhibit a maximum. It is to be noted here that the graphs of Figures 2.6 and 2.7 for the simple case of cylindrical fluid samples without consideration of any microcapillary. However, for the practical case of samples contained in microcapillary segments, the internal field assumes the complicated form [6]

$$E = \frac{4\varepsilon_t E_0}{(\varepsilon_t + 1)(\varepsilon_t + \varepsilon_r) + (\varepsilon_t - 1)(\varepsilon_r + \varepsilon_t)a^2/b^2}, \tag{21}$$

where ε_t is the permittivity of the microcapillary material and ε_r that of the filler, which is a mixture in compositional analysis experiments. a and b are the inner and outer radii of the microcapillary, respectively. The dipole moment induced in a sample for the field of (21) is given by the equation

$$p \approx 2\pi\varepsilon_0 b^2 \ell \left(\frac{(\varepsilon + \varepsilon_t)(\varepsilon_t - 1) + (\varepsilon - \varepsilon_t)(\varepsilon_t + 1)q^2}{(\varepsilon + \varepsilon_t)(\varepsilon_t + 1) + (\varepsilon - \varepsilon_t)(\varepsilon_t - 1)q^2} \right) E_0, \tag{22}$$

where $q^2 = a^2 / b^2$.

2.7.2 **Parallel Electric Field**

For the case of electric field parallel to the microcapillary, there is no depolarisation as no reduction of internal field occurs (i.e. $E \approx E_0$). Thus, there will be monotonic decrease in both resonant frequency as well as quality factor with increase in the dielectric loss (i.e. increasing proportion of a polar solvent in a mixture) of the sample being characterised.

References

[1] A. P. Gregory and R. N. Clarke, "A Review of RF and Microwave Techniques for Dielectric Measurements on Polar Liquids", *IEEE Transactions on Dielectrics and Electrical Insulation*, Vol. 13, No. 4, pp. 727-743, August 2006.

[2] L. Perreux and A. Loupy, "A tentative realization of microwave effects in organic synthesis according to the reaction medium, and mechanistic considerations", *Tetrahedron*, Vol. 57, pp. 9199-9223, 2001.

[3] J.P. Grant, R N. Clarke, G. T. Symm and N. M. Spyrou, "A Critical Study of The Open-Ended Coaxial Line Sensor Technique for RF and Microwave Complex Permittivity Measurements", *Journal of Physics E – Scientific Instruments*, Vol. 22, No. 9, pp. 757-770, 1989.

[4] S. Jenkins, T. E. Hodgetts, R. N. Clarke and A. W. Preece, "Dielectric Measurements on Reference Liquids Using Automatic Network Analysers and Calculable Geometries", *Measurement Science and Technology*, Vol. 1, pp. 691-702, 1990.

[5] D. M. Pozar, *Microwave Engineering*, Third Edition, John Wiley & Sons, N.Y., 2005, ISBN 0-471-44878-8.

[6] A. Porch, *Private Communications*, 2007-8.

[7] M. Ikeda, K. Nishida, H. Shimasaki and M. Akiyama, "Influence of the Coupling between a Cavity and a Transmission Line on the Measurement of Complex Permittivity by the Resonant Cavity Perturbation Method", *Asia-Pacific Microwave Conference 2008*, December 2008.

[8] G. Birnbaum and J. Franeau, "Measurement of the Dielectric Constant and Loss of Solids and Liquids by a Cavity Perturbation Method", *Journal of Applied Physics*, Vol. 20, Issue 8, pp. 817-818, August 1949.

[9] A. Kumar and D. G. Smith, "Microwave Properties of Liquids Using a Modified Cavity Perturbation Technique", *IEE Proceedings – H, Microwaves, Optics and Antennas*, Vol. 127, No. 1, pp. 1-3, February 1980.

[10] M. Martinelli, P. A. Rolla and E. Tombari, "A Method for Dielectric Loss Measurements by a Microwave Cavity in Fixed Resonance Condition", *IEEE Transactions on Microwave Theory and Techniques*, Vol. MTT-33, No. 9, pp. 779-783, June 1985.

[11] S. K. Han, J. Kim and K. Kang, "Measurement of Microwave Magnetic Properties of Superconducting $YBa_2Cu_3O_{7-\delta}$ Thin Films", *IEEE Transactions on Applied Superconductivity*, Vol. 7, No. 2, pp. 1873-1876, June 1997.

[12] A. Mansingh and A. Parkash, "Microwave Measurement of Conductivity and Permittivity of Semiconductor Spheres by Cavity Perturbation Technique", *IEEE Transactions on Microwave Theory and Techniques*, Vol. MTT-29 No. 1, pp. 62-65, January 1981.

[13] A. Mansingh, D. B. McLay and K. O. Lim, "A Cavity Perturbation Technique for Measuring Complex Dielectric Permittivities of Liquids at Microwave Frequencies", *Canadian Journal of Physics*, Vol. 52, No. 23, pp. 2365-2369, 1974.

[14] L .Chen, C. K. Ong and B. T. G. Tan, "Amendment of Cavity Perturbation Method for Permittivity Measurement of Extremely Low-Loss Dielectrics", *IEEE Transactions on Instrumentation and Measurement* , Vol. 48, No. 6, pp. 1031-1037, December 1999.

[15] Y. Ye, T. Liu, X. Zeng, J. He and C. Akyel, "Accurate Permittivity Measurement Using the Cavity Perturbation Technique at ISM 5.8GHz Radio Band", *International Conference on Microwave and Millimeter Wave Technology*, pp. 1-4, April 2007.

[16] U. Raveendranath, S. Bijukumar and K. T. Mathew, "Broadband Coaxial Cavity Resonator for Comples Permittivity Measurements of Liquids", *IEEE Transactions on Instrumentation and Measurement*, Vol. 49, No. 6, pp. 1305-1312, December 2000.

[17 U. Raveendranath, J. Jacob and K. T. Mathew, "Complex Permittivity Measurement of Liquids with Coaxial Cavity Resonators Using a Perturbation Technique", *Electronics Letters*, Vol. 32, No. 11, pp. 988-990, May 1996.

[18] P. A. Anderson, A. R. Armstrong, A. Porch, P. P. Edwards and L. J. Woodall, "Structure and Electronic Properties of Potassium-Loaded Zeolite L", *Journal of Physical Chemistry B*, Vol. 101, No. 48, pp. 9892-9900, 1997.

[19] S. Lee, D. C. Morgan, R. J. Ormeno, D. M. Broun, R. A. Doyle and J. R. Waldram, "*a-b* Plane Microwave Surface Impedance of a High-Quality $Bi_2Sr_2CaCu_2O_8$ Single Crystal", *Physical Review Letters*, Vol. 77, No. 4, pp. 735-738, July 1996.

[20] K. Saeed, A. C. Guyette, I. C. Hunter and R. D. Pollard, "Microstrip Resonator Technique for Measuring Dielectric Permittivity of Liquid Solvents and for Solution Sensing", *IEEE/MTT-S International Microwave Symposium 2007*, pp. 1185-1188, June 2007.

[21] H. Behbehani and M. K. Andari, "Comparison of Kuwaiti Crude Oils, Compositional Analysis Using Gas Chromatography Techniques", *Petroleum Science and Technology*, Vol. 17, No. 1&2, pp. 115-124, 1999.

[22] A. Y. Dandekar, S. I. Andersen and E. H. Stenby, "Compositional Analysis of North Sea Oils", *Petroleum Science and Technology*, Vol. 18, No. 7&8, pp. 975-988, 2000.

[23] A. Lommen, R. Schilt, J. Weseman, A. H. Roos, J. W. van Velde and M. W. F. Nielen, "Application of 1D ^{1}H NMR for Fast Non-Targeted Screening and Compositional Analysis of Steroid Cocktails and Veterinary Drug Formulations Administered to Livestock", *Journal of Pharmaceutical and Biomedical Analysis*, Vol. 28, pp. 87-96, 2002.

[24] H. P. Hendrickson, P. Anderson, X. Wang, Z. Pittman and D. R. Bobbitt, "Compositional Analysis of Small Peptides Using Capillary Electrophoresis and $Ru(bpy_3^3)$ -based Chemiluminescence Detection", *Microchemical Journal*, Vol. 65, pp. 189-195, 2000.

[25] H. Matsubara, A. Yoshida, H. Ohtani and S. Tsuge, "Compositional Analysis of UV-Cured Acrylic Ester Resins by Pyrolysis–Gas Chromatography in the Presence of Organic Alkali", *Journal of Analytical and Applied Pyrolysis*, Vol. 64, pp. 159-175, 2002.

[26] M. H. P. van Genderen, P. A. Leclercq, H. S. Delgado, P. B. Kanjilal and R. S. Singh, "Compositional Analysis of the Leaf Oils of *Piper Collosum* Ruiz & Pav. rom Peru and *Michelia mntana* Blume from India", *Spectroscopy*, Vol. 14, pp. 51-59, 1999.

[27] S. van der Wal, Y. Mengerink, J. C. Brackman, E. M. M. de Brabander, C. M. Jeronimus-Stratingh , A. P. Bruins, "Compositional Analysis of Nitrile Terminated Poly (Propylene Imine) Dendrimers by High-Performance Liquid Chromatography Combined with Electrospray Mass Spectrometry," *Journal of Chromatography A*, Vol. 825, pp. 135-147, 1998.

[28] A. Arce, M. Blanco, E. Rodil, A. Soto and J. A.Vieitez, " Use of Physical Properties for ositional Analysis of Ternary Mixtures. Application to Mixtures of 2-Methoxy-2-methylbutane, Methanol, and 2,2,4-Trimethylpentane or Methylcyclohexane", *Journal of Solution Chemistry*, Vol. 27, No. 7, 1998.

[29] Ramo, J. R. Whinnery, and T. V. Duzer, *Fields and Waves in Communication Electronics*, Third Edition, John Wiley & Sons, N.Y., 1994, ISBN 978-81-265-1525-7.

CHAPTER 3

MICROWAVE RESONATOR THEORY

3.1 Introduction

Resonators at low frequencies (i.e. up to a few MHz) are commonly made of lumped element parallel *LC* circuits, such as the one shown in Figure 3.1.

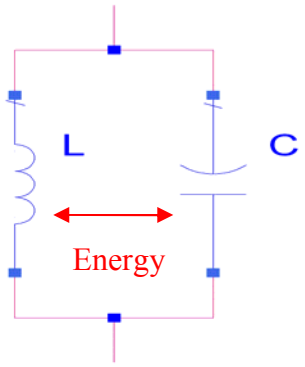

Figure 3.1. *LC* Resonator.

In such a circuit, at resonance the stored energy oscillates between the electric field of capacitor and the magnetic field inductor at a frequency given by the expression

$$f_0 = \frac{1}{2\pi\sqrt{LC}} \tag{1}$$

However, at microwave frequencies (i.e. between 300 MHz and 300 GHz) the dimensions of lumped elements become comparable to the operating wavelength thereby causing loss of energy by radiation. Consequently distributed circuits such as sections of transmission lines (TLs) often (but not always) replace the lumped element capacitors and inductors in microwave resonant circuits [1,2]. Thus a basic understanding of the way in which microwave frequency signals propagate along a TL is imperative in order to comprehend the theory behind microwave resonators. A variety of transverse electromagnetic (TEM) TL structures are available for high frequency operation, with coaxial cable, microstrip, stripline, coplanar waveguide, and coplanar slotline being the more common. In strictness, though, only coaxial cable can support pure TEM waves with the others being quasi-TEM; i.e. they

can be considered to carry TEM waves to quite a good approximation [2]. Practically all of the aforementioned TLs can be used for microwave signal propagation. This chapter will discuss the fundamental concepts pertaining to resonant transmission lines, microwave network analysis and transmission mode measurements with microwave resonators.

3.2 TEM TL Resonators

The need behind description of TL resonators in this thesis is that one of their configurations (i.e. hairpin resonator) was the starting point for compositional analysis experiments carried out herein. The hairpin resonator is equivalent to a quarter wavelength long resonant TEM TL section terminated in a short circuit. However, it is deemed more apt to start with the analysis of an open-circuited line – to gain a full insight into the way TEM TL resonators operate – before venturing onto the short-circuited case.

3.2.1 Open-circuited Line

3.2.1.1 Line Voltage

Consider a length l of a low loss TEM TL in the z axis, which is open at both source and load ends as depicted in Figure 3.2.

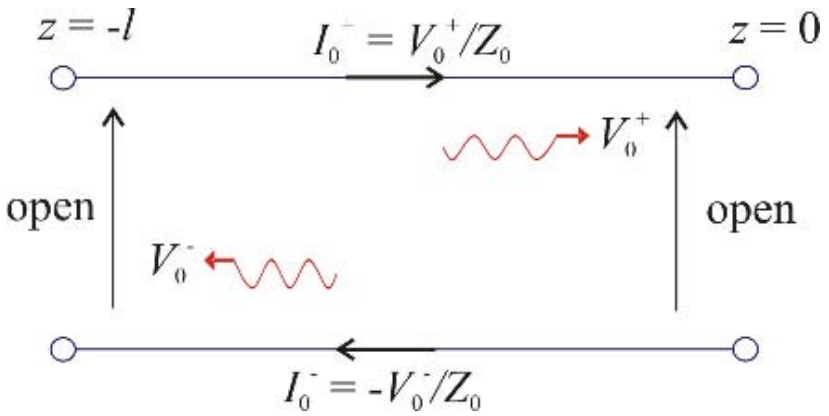

Figure 3.2. Open-circuited TL.

Assume that a wave of voltage amplitude V_0^+ is incident from the negative z direction. Due to the open circuit at the other end (i.e. z = 0), a reflected wave travelling in the negative z

direction would be excited having an amplitude V_0^- [1-3]. The amplitudes of the two travelling waves are related by the voltage reflection coefficient, ρ as follows:

$$\rho = \frac{V_0^-}{V_0^+} = \frac{Z_L - Z_0}{Z_L + Z_0}, \tag{2}$$

where Z_0 is the characteristic impedance of TL, defined as the ratio of voltage to current for one of the travelling waves at any given point and given time [3]. Since Z_L (i.e. load impedance) is infinite for the given open line, the value of ρ is unity, leading to $V_0^+ = V_0^- = V_0$. The total line voltage is the sum of incident and reflected waves [1,2]

$$\begin{aligned} v(z,t) &= V_0^+ e^{j(\omega t - \beta z)} + V_0^- e^{j(\omega t + \beta z)} \\ &= V_0 e^{j\omega t}\left[e^{-j\beta z} + e^{j\beta z}\right], \end{aligned} \tag{3}$$

where t represents time, ω is the angular frequency, and $\beta = \omega\sqrt{LC}$ is the wavenumber or phase constant of the TL (L and C are the inductance and capacitance per unit length l of the TL respectively) [1]. The first term in (3) shows the incident wave propagating in the positive z direction while the second term represents the reflected wave travelling in the negative z direction [1,4]. Since $e^{-j\beta z} = \cos\beta z - j\sin\beta z$ and $e^{j\beta z} = \cos\beta z - j\sin\beta z$, the term within the square brackets of (3) reduces to $2\cos\beta z$, which can then be rewritten as

$$v(z,t) = 2V_0 \cos\beta z e^{j\omega t}. \tag{4}$$

The phase velocity, v_p, of the microwave signals is given by the relation [2]

$$v_p = \frac{1}{\sqrt{LC}} = \frac{c}{\sqrt{\varepsilon_{\text{eff}}}} = \frac{\omega}{\beta}, \tag{5}$$

where $c = 2.998 \times 10^8 \text{m/sec}$ is the velocity of light in free-space and ε_{eff} is the effective dielectric constant of the TL. For a line filled entirely with dielectric, such as coaxial cable or stripline, $\varepsilon_{\text{eff}} = \varepsilon_1$ i.e. the dielectric constant of the filling material. In all other TLs, part of the electric field persists in the air outside of the dielectric that is accounted by the fact that $\varepsilon_{\text{eff}} < \varepsilon_1$ [2]. Phase velocity is so called because it is the velocity with which a wave front of fixed phase travels [1]. It is convenient here to state the relationship between wavelength, λ,

and β, as it would be used later on in this chapter. Since λ is the distance between two consecutive maxima or minima (or any other reference points) on the wave, at a fixed point in time, [1]

$$[\omega t - \beta z] - [\omega t - \beta(z + \lambda)] = 2\pi .$$

So,
$$\lambda = \frac{2\pi}{\beta} = \frac{2\pi v_p}{\omega} = \frac{v_p}{f} . \tag{6}$$

(4) describes a standing wave (i.e. resonance), which is the sum of forward and backward travelling waves. Since both ends of the line are open, the voltage there must attain either positive or negative peak value (i.e. voltage anti nodes) thus meaning that cosβz can only be ±1 at the ends. At z = 0 end, βz = 0 leading to cos0 = 1; for the other end at z = -l, βz = -βl and cos(-βl) = cos(βl) must be either 1 or -1. Since cos$n\pi$ = ±1 (for all integers n), we have for resonance to occur

$$\beta l = n\pi \;\Rightarrow \frac{2\pi}{\lambda} l = n\pi \Rightarrow l = n\frac{\lambda}{2} \;(n = 1,2,3 \text{ etc}), \tag{7}$$

where use has been made of $\beta = 2\pi/\lambda$ from (6). Therefore the condition for resonances to be produced on the open-ended line is that l equals an integral number of half wavelengths. (6) and (7) give us the condition for resonance in terms of β and the resonant frequencies as

$$\beta = \frac{n\pi}{l} , \tag{8}$$

$$f_0 = \frac{\omega_0}{2\pi} = \frac{v_p}{\lambda} = \frac{nc}{2l\sqrt{\varepsilon_{\text{eff}}}} . \tag{9}$$

If the line is filled with air, then $\varepsilon_{\text{eff}} = \varepsilon_1 = 1$ and (9) becomes

$$f_0 = \frac{nc}{2l} . \tag{10}$$

Hence an air-spaced, open-ended TL would resonate at frequencies equal to $\frac{c}{2l}, \frac{c}{l}, \frac{3c}{2l}$ etc.

3.2.1.2 **Line Current**

Consider again the open-circuited TL shown in Figure 3.2. The total line current is

$$i(z,t) = I_0^+ e^{j(\omega t - \beta z)} + I_0^- e^{j(\omega t + \beta z)} \tag{11}$$

where I_0^+ and I_0^- are the incident and reflected current amplitudes respectively. The voltage and current on the line are related by the characteristic impedance as [1]

$$\frac{V_0^+}{I_0^+} = Z_0 = \frac{-V_0^-}{I_0^-}. \tag{12}$$

Thus (11) can be rewritten as

$$i(z,t) = \frac{V_0^+}{Z_0} e^{j(\omega t - \beta z)} - \frac{V_0^-}{Z_0} e^{j(\omega t + \beta z)}. \tag{13}$$

Since $\rho = 1$, $V_0^+ = V_0^- = V_0$ and (13) becomes

$$i(z,t) = \frac{V_0}{Z_0} e^{j(\omega t - \beta z)} - \frac{V_0}{Z_0} e^{j(\omega t + \beta z)}$$

$$= \frac{V_0}{Z_0} e^{j\omega t} \left[e^{-j\beta z} - e^{j\beta z} \right] \tag{14}$$

The term within the square brackets of (14) reduces to $-2j\sin\beta z$, so we have

$$i(z,t) = -2j \frac{V_0}{Z_0} e^{j\omega t} \sin\beta z, \tag{15}$$

which shows that the current is zero at the load, as expected for the open circuit there. Letting $I_0 = \frac{V_0}{Z_0}$ [1], we could rewrite (15) as

$$i(z,t) = -2jI_0 e^{j\omega t} \sin\beta z. \tag{16}$$

Since $-j = e^{-j\pi/2}$, (16) becomes

$$i(z,t) = 2I_0 e^{-j\pi/2} e^{j\omega t} \sin\beta z = 2I_0 e^{j\left(\omega t - \pi/2\right)} \sin\beta z, \tag{17}$$

which on comparison with (4) points to the fact that the line voltage leads the current (i.e. electric field $\underline{E}$ leads magnetic field $\underline{H}$) by 90°.

3.2.2 **Short-circuited Line**

3.2.2.1 **Line Voltage**

Consider now the TL shown in Figure 3.3, which is terminated in a short circuit, $Z_L = 0$ [1,2].

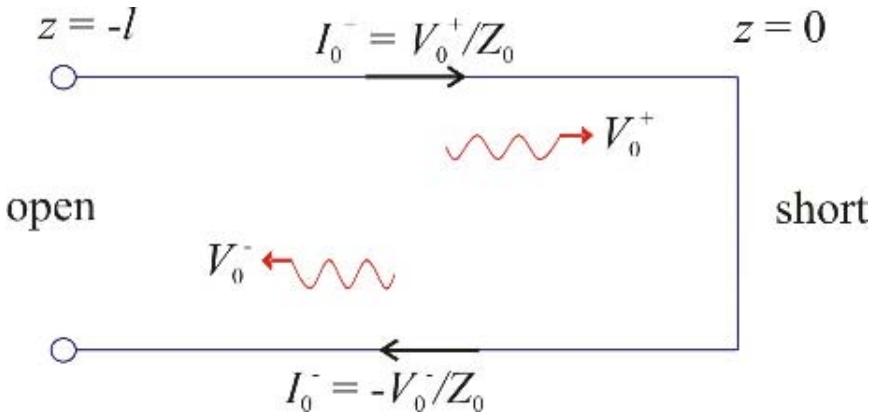

Figure 3.3. Short-circuited TL.

The amplitude of incident voltage wave is again V_0^+ while that of the reflected wave is V_0^-. From (2), the reflection coefficient for this line is ρ= -1 implying that $V_0^+ = -V_0^-$. The total line voltage is then

$$v(z,t) = V_0^+ e^{j(\omega t - \beta z)} + V_0^- e^{j(\omega t + \beta z)}$$

$$= V_0^+ e^{j(\omega t - \beta z)} - V_0^+ e^{j(\omega t + \beta z)}$$

or

$$v(z,t) = V_0 e^{j\omega t}\left[e^{-j\beta z} - e^{j\beta z}\right]$$

$$= -2jV_0 \sin\beta z e^{j\omega t} = 2V_0 e^{j(\omega t - \pi/2)} \sin\beta z \qquad (18)$$

(18) shows that the voltage at load is zero (i.e. voltage node) as we would expect because of the short circuit there. At the open end at (i.e. z = -l), however, there must be a voltage anti

node thereby meaning that sin(β*l*) = -sin(β*l*) can only be ±1. Given that $\sin\frac{n\pi}{2} = \pm 1$ (for odd integers *n*), the resonance condition for this case is

$$\beta l = \frac{n\pi}{2} \Rightarrow \frac{2\pi}{\lambda} l = \frac{n\pi}{2}$$

$$\Rightarrow l = n\frac{\lambda}{4} \ \left(n \ = \ 1,3,5 \text{ etc}\right). \tag{19}$$

The resonant frequencies for air-spaced short-circuited TL would therefore be

$$f_0 = \frac{\omega_0}{2\pi} = \frac{v_p}{\lambda} = \frac{nc}{4l} \ \left(n \ = \ 1,3,5 \text{ etc}\right). \tag{20}$$

Thus an air-paced, short-circuited TL would resonate at frequencies equal to $\frac{c}{4l}, \frac{3c}{4l}, \frac{5c}{4l}$ etc.

It is evident from (10) and (20) that the resonant frequencies for both open-circuited and short-circuited cases only depend on length *l* of the line - a fact which is a distinct property of the TEM line.

3.2.2.2 **Line Current**

We again start from (13), which for *ρ*= -1 (i.e. $V_0^+ = -V_0^-$) can be rewritten as

$$i(z,t) = \frac{V_0^+}{Z_0} e^{j(\omega t - \beta z)} + \frac{V_0^+}{Z_0} e^{j(\omega t + \beta z)}.$$

$$= \frac{V_0}{Z_0} e^{j\omega t} \left[e^{-j\beta z} + e^{j\beta z} \right]$$

$$= 2\frac{V_0}{Z_0} e^{j\omega t} \cos\beta z = 2I_0 e^{j\omega t} \cos\beta z\,, \tag{21}$$

which shows that the current is a maximum at the load and leads the voltage (i.e. <u>*H*</u> leads <u>*E*</u>) by 90˚.

3.2.3 **The Quarter-wavelength Resonant TL**

The short-circuited TL is widely used in electrical engineering applications as in addition to exhibiting resonance, it has the added advantage of providing mechanical support between the line conductors, which is not the case for the open-circuited line [5]. One such implementation is the hairpin resonator, illustrated in Figure 3.4.

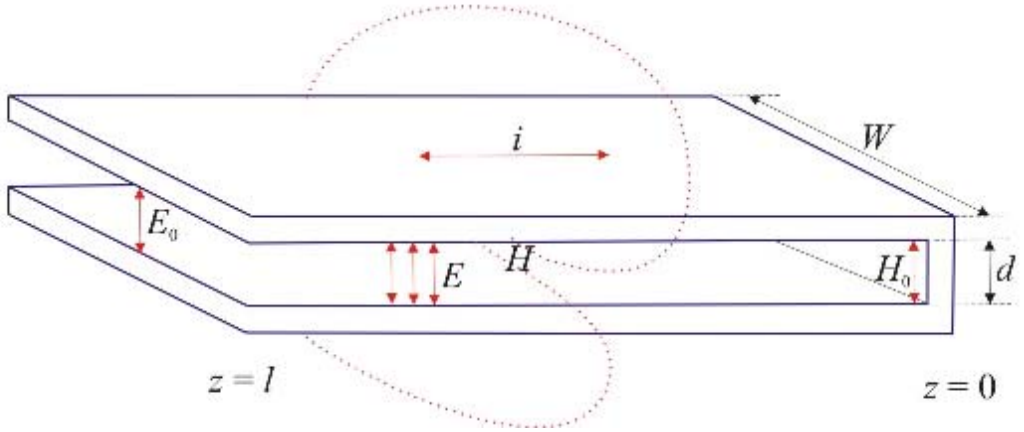

Figure 3.4. The hairpin resonator (*W*, plate width; *l*, plate length; *d*, plate separation; *i*, current; *H*, magnetic field strength; *E*, electric field strength; H_0, maximum amplitude of *H*; E_0, maximum amplitude of *E*).

The hairpin resonator* is a variant of the wide microstrip line, hence supporting TEM travelling waves along its length. It is made out of a copper strip bent at one end to form the short-circuited termination while the other end is left open, thereby forming the two-plated hairpin structure. It is known from (19) that such a segment of TL would resonate when its length equals odd integer multiples of a quarter wavelength, with fundamental resonance mode (*n*=1) occurring at $l = \frac{\lambda}{4}$ and the corresponding resonant frequency being $f_0 = \frac{c}{4l}$. The electric field strength *E* is supported vertically between the two plates of the hairpin and at resonance its amplitude is largest at the open-circuited end, denoted by E_0. *H* is the magnetic field strength generated by the current *i* flowing in the plates and is shown by dotted lines in Figure 4. It forms concentric circles around the plate and attains peak amplitude of H_0 at the

* The detailed construction of the hairpin used in this research along with expressions for resonant frequency and quality factor will be discussed in chapter 4.

short-circuited end at resonance. Now expressions for E and H for the hairpin resonator will be derived; taking E first, it is related to voltage v by the relation:

$$E(z,t) = |\underline{E}| = \frac{\mathrm{v}(z,t)}{d}. \tag{22}$$

For the case in question, $\mathrm{v}(z,t) = 2V_0 e^{j(\omega t - \pi/2)} \sin\beta z$, as given by (18); therefore

$$E(z,t) = \frac{2V_0}{d} e^{j(\omega t - \pi/2)} \sin\beta z$$

$$= |E| e^{j(\omega t - \pi/2)}. \tag{23}$$

In (23), $|E| = \frac{2V_0}{d} \sin\beta z$ is the magnitude of $E(z,t)$ while the phase is represented by the exponential term. Letting $E_0 = \frac{2V_0}{d}$ gives

$$|E| = E_0 \sin\beta z, \tag{24}$$

where $\beta = \frac{\pi}{2l}$ for the fundamental resonance mode. Thus (24) becomes

$$|E| = E_0 \sin\left(\frac{\pi z}{2l}\right), \tag{25}$$

which shows that $|E| = E_0$ at the open ($z = l$) end and $|E| = 0$ at the short ($z = 0$) end. Turning now to the magnetic field strength H, it is related to current i by the following relation:

$$H(z,t) = |\underline{H}| = \frac{i(z,t)}{W}, \tag{26}$$

where $i(z,t) = 2I_0 e^{j\omega t} \cos\beta z$ for the hairpin. Consequently

$$H(z,t) = \frac{2I_0}{W} e^{j\omega t} \cos\beta z$$

$$= |H| e^{j\omega t}. \tag{27}$$

In (27), $|H| = \frac{2I_0}{W}\cos\beta z$ is the magnitude of $H(z,t)$ while the phase is given by the exponential term. Letting $H_0 = \frac{2I_0}{W}$ gives

$$|H| = H_0\cos\beta z = H_0\cos\left(\frac{\pi z}{2L}\right), \tag{28}$$

which shows that at resonance $|H| = H_0$ at the short-circuited end and $|H| = 0$ at the open end.

3.3 Microwave Network Analysis

Although network analysis techniques used for low-frequency electric circuits are equally applicable to microwave resonators, other methods are required for the full coverage of the latter because of the following reason: The often distributed nature of the voltages and currents in microwave structures means that their values vary with their position making it difficult to measure them in the same manner as in low-frequency networks. A convenient way of describing voltages and currents in microwave devices is the scattering matrix (*S* parameters), which describes them in terms of their incident and reflected waves [1,6]. Since thorough understanding of *S* parameters requires familiarity with the concept of network ports, the latter will be considered first in the discussion below:

3.3.1 Network Ports

Consider an arbitrary network made up entirely of passive elements, which is assigned the symbol of a rectangle (or a box) so as to indicate its general nature. If a conductor is tied to any node in the network and brought out of the box for access, the end of this conductor is assigned as a terminal. Terminals are needed for connecting driving forces to the network, for connecting some other network (such as a load), or for making measurements. The minimum number of terminals so as to be useful is two. Moreover, the terminals are linked in pairs, one pair for a driving force, another pair for the load, etc. Two associated terminals are given the name terminal pair, or more commonly port, signifying a port of entry into the network [7].

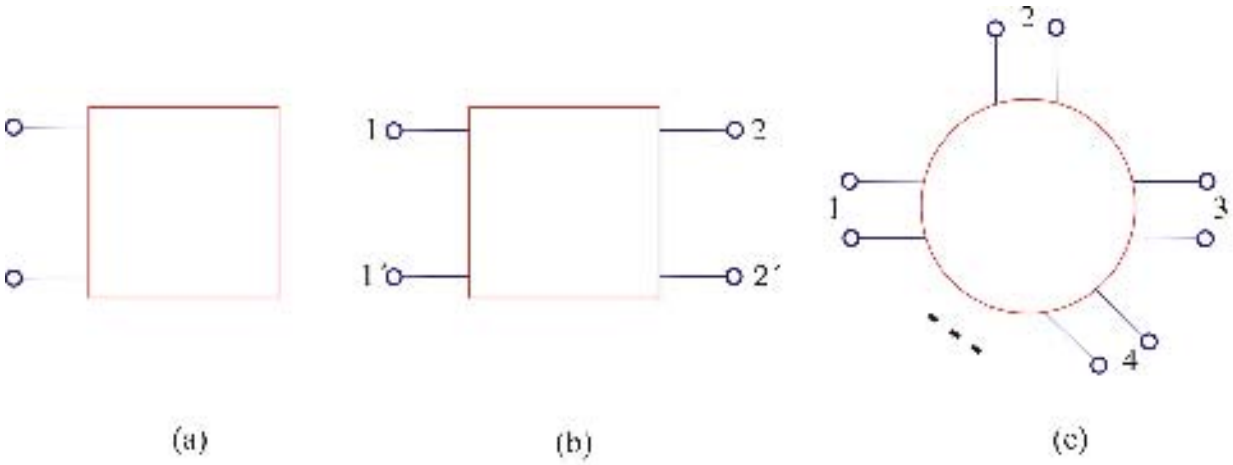

Figure 3.5. (a) One-port network (b) two-port network and (c) a representation of the n-port network [7].

Figure 3.5 shows a one-port, a two-port, and an n-port network for the general case. Since all microwave resonator measurements carried out in this project are transmission (i.e. two-port) measurements, the same would now be considered in further detail. A two-port measurement involving a microwave resonator is depicted in Figure 3.6 below.

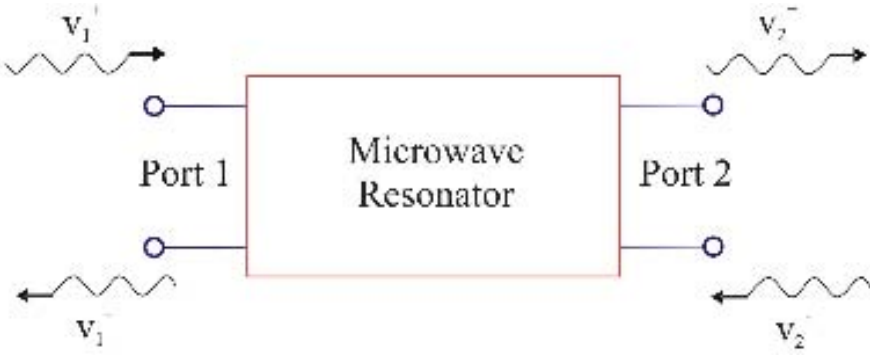

Figure 3.6. Two-port microwave network.

The ports above may be any type of transmission line or transmission line equivalent of a single propagating waveguide mode. The convention used here is that a voltage wave travelling from left to right (i.e. port 1 to 2) is considered as moving in the positive direction; hence the symbols v_1^+ and v_2^+ for the corresponding waves [2]. Conversely, voltage waves going the opposite way (i.e. right to left) are taken as moving in the negative direction and are

therefore expressed as v_1^- and v_2^-. In terms of incident and reflected voltage waves, v_1^+ is the wave incident on port 1 whereas v_1^- represents the voltage wave reflected back from port 1. Similarly v_2^- signifies the wave incident on port 2 while v_2^+ is the wave reflected back from port 2.

3.3.2 ***S* Parameters (The Scattering Matrix)**

S parameters are voltage ratios; hence in the context of microwave measurements, they are dimensionless, complex numbers expressed in terms of magnitude and phase [2]. For the two-port microwave network of Figure 3.6, the four voltage waves are interrelated by the following two equations, where S_{11}, S_{12}, S_{21}, and S_{22} are the 'scattering' or *S* parameters of the network [6]:

$$v_1^- = S_{11}v_1^+ + S_{12}v_2^- \tag{29}$$

and

$$v_2^+ = S_{21}v_1^+ + S_{22}v_2^-. \tag{30}$$

(29) and (30) can also be written in matrix form, called the scattering matrix, or [*S*] matrix as [1-3]

$$\begin{pmatrix} v_1^- \\ v_2^+ \end{pmatrix} = \begin{pmatrix} S_{11} & S_{12} \\ S_{21} & S_{22} \end{pmatrix} \begin{pmatrix} v_1^+ \\ v_2^- \end{pmatrix}. \tag{31}$$

The individual elements of the [*S*] matrix are the *S* parameters, which can be determined as

$$S_{11} = \frac{v_1^-}{v_1^+} = |S_{11}|\, e^{j\phi_{11}}, \tag{32}$$

$$S_{12} = \frac{v_1^-}{v_2^-} = |S_{12}|\, e^{j\phi_{12}}, \tag{33}$$

$$S_{21} = \frac{v_2^+}{v_1^+} = |S_{21}|\, e^{j\phi_{21}}, \tag{34}$$

and

$$S_{22} = \frac{V_2^+}{V_2^-} = |S_{22}| \, e^{j\phi_{22}} . \quad (35)$$

In (32) – (35), the phases of the *S* parameters are represented by the angles ϕ_{ij} in the exponential terms. Hence, the *S* parameters can be defined in words briefly as follows:

$S_{11} \equiv$ Input reflection coefficient

$S_{12} \equiv$ Reverse transmission coefficient (isolation)

$S_{21} \equiv$ Forward transmission coefficient (gain)

$S_{22} \equiv$ Output reflection coefficient

An important point to make here is that since microwave resonators are passive devices, the magnitude of any *S* parameter can never exceed unity i.e.$0 \leq | S_{ij} | \leq 1$. Also, for a microwave resonator $S_{12} = S_{21}$; this property is termed as the reciprocity of *S* parameters, which holds good for all passive networks. On the other hand S_{11} is generally equal in magnitude to S_{22}, but differs in phase [2].

3.4 Transmission Mode Measurements with Resonators

When resonators are measured in transmission mode, there are four parameters of interest related to the resonance: the resonant frequency, f_0, the half-power (or 3 dB) bandwidth, f_B, the insertion loss at resonance, *IL*, and the quality factor, *Q*. Each of these will be described in the succeeding paragraphs.

3.4.1 Resonator Spectral Response in Transmission

In transmission mode, a VNA is used to measure the magnitude of the voltage transmission coefficient S_{21} (i.e. $|S_{21}|$) of a resonator as a function of frequency. If $|S_{21}|$ is unity, it would imply perfect transmission through the resonator thereby meaning that it is completely lossless and doesn't absorb or reflect any power. On the other hand zero value of $|S_{21}|$ leads to total absorption or reflection of power by the resonator with no transmission at all.

However, it is much more convenient to define the above mentioned resonator parameters if $|S_{21}|$ is expressed in logarithmic unit (i.e. dB) rather than linear magnitude. The characteristic spectral response of a resonator would then be as shown in Figure 3.7 [2].

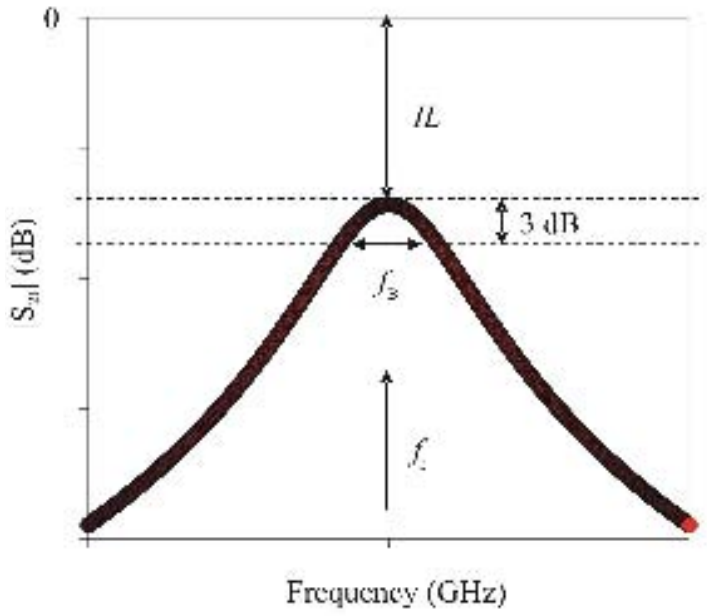

Figure 3.7. Idealised spectral response of a resonator in transmission mode [2].

In Figure 3.7, f_0 is the resonant frequency, f_B is the half-power (or 3 dB) bandwidth, and *IL* is the insertion loss at resonance, which is expressed in dB relative to the input power – typically 0 dBm (i.e. 1 mW rms) for the Agilent (HP) 8753E VNA used mostly in this project [2]. The *Q*, although not obvious from the spectral response of Figure 7, can be evaluated from f_0 and f_B as described later in this chapter.

3.4.2 **The Quality Factor**

The *Q* of a resonator determines its frequency selectivity and is defined as [1,2]

$$Q = \omega_0 \frac{\text{(time-averaged stored energy)}}{\text{(time-averaged power dissipated)}} = \frac{\omega_0 \langle U \rangle}{\langle P \rangle}. \tag{36}$$

Hence *Q* is a measure of the loss of a resonant circuit – lower loss means a higher *Q*. It is more appropriate to call the *Q* of (36) as the unloaded *Q* (denoted as Q_U) as it is an attribute

of the resonator device itself, in the absence of any loading effects caused by the external circuitry. Practically, though, a resonant circuit is customarily coupled to other circuitry, which would always lower the overall or loaded Q of the circuit [1], represented by Q_L. Quite obviously the quality factor measured in resonator experiments carried out in this project is the loaded Q. This needs to be corrected to form Q_U, which reflects the properties of the material occupying the resonator [2].

3.4.3 Coupling of Resonators

Resonators can be excited by either capacitive (*E* field) or inductive (*H* field) coupling, depending on the application. Capacitive coupling is normally used for excitation of open-ended planar TL resonators by coupling to the *E* field anti node at the resonator end. On the other hand, inductive coupling is usually used to excite non-planar (i.e. 3D) resonators such as coupling to the *H* field anti node at the centre of an open-ended coaxial resonator [2]. Since all resonators used in this project are of the non-planar type, inductive coupling through loop-terminated coaxial feedlines has been used for their excitation. Details of the coupling arrangement used for each resonator will be provided in their respective sections; nonetheless it is pertinent to mention here that for all cases the coupling loops were made nearly identical to ensure symmetrical input/output couplings. The *IL*, which is determined by the input and output coupling strength to the resonator, was kept in the range -40 to -10 dB. The reason for this is that a very weakly coupled resonator (i.e. $IL < -40$ dB) would suffer from a low signal to noise ratio (SNR) in transmission, whilst a strongly coupled resonator (i.e. $0 \text{ dB} > IL > -10$ dB) has a reduced Q because of the loading effects of the coupling circuitry [2].

3.4.4 Two-Port Resonator Analysis with Symmetrical Coupling

An ideal microwave resonator can be modelled as a series *RLC* circuit as depicted in Figure 3.8 [2,8].

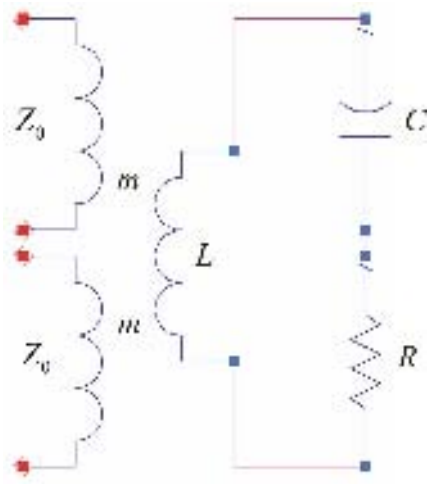

Figure 3.8. Series *RLC* circuit representation of a resonator [8].

It is assumed that the resonator is symmetrically coupled to transmission lines of impedance Z_0 by mutual inductances *m*. The resonator impedance is [1]

$$Z_r = R + j\omega L - j\frac{1}{\omega C}. \tag{37}$$

At resonance, the inductive and capacitive reactance cancel each other out and Z_r is purely real (i.e. $Z_r = R$); hence the equivalent circuit with applied voltage and current is as shown in Figure 3.9.

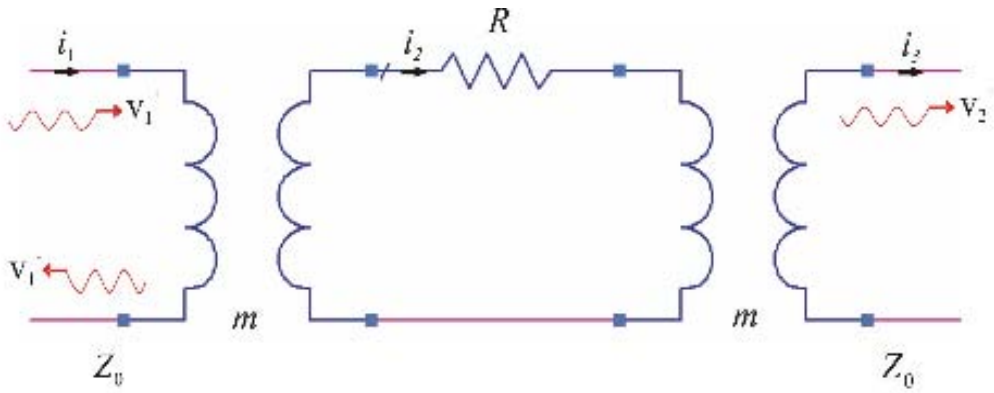

Figure 3.9. Two-Port resonator equivalent circuit at resonance.

The input voltage v_1^+ is supplied by a VNA through one of its ports, setting up current i_1 in the input circuit made up of the input coupling cable connected to the VNA. Current i_2 is induced in the resonator loop, which in turn induces current i_3 in the output circuit that goes back to the other port of VNA through the output coupling cable. Depending on the strength of the input and output couplings to the resonator, part of the input voltage is transmitted as v_2^+ to the output circuit whereas the residual (i.e. v_1^-) is reflected back into the input circuit. The detailed analysis of resonator equivalent circuit at resonance is presented in Appendix A, which provides the following expression for S_{21}:

$$S_{21} = \frac{-2g}{1+2g}, \tag{38}$$

where g is the coupling coefficient (i.e. same for input and output coupling because of symmetric coupling) defined as

$$g = \frac{\omega^2 m^2}{RZ_0}. \tag{39}$$

However, at a point slightly off the resonance the resonator impedance would not be purely resistive. To examine this, let $\omega = \omega_0 + \Delta\omega$, where $\Delta\omega$ is very small. Z_r can now be derived for this off resonance situation, starting from (37) as below:

$$Z_r = R + j\omega L\left(1 - \frac{1}{\omega^2 LC}\right) \tag{40}$$

$$= R + j\omega L\left(\frac{\omega^2 - \omega_0{}^2}{\omega^2}\right), \tag{41}$$

since $\omega_0{}^2 = \frac{1}{LC}$. Now $\omega^2 - \omega_0{}^2 = (\omega - \omega_0)(\omega + \omega_0) = \Delta\omega(2\omega - \Delta\omega) \simeq 2\omega\Delta\omega$ for small ω [1]. Therefore,

$$Z_r \cong R + j2L\Delta\omega$$

$$\cong R + j2L\omega_0 x, \tag{42}$$

where $x = \frac{\Delta\omega}{\omega_0} = \frac{\omega - \omega_0}{\omega_0}$. Given that the unloaded quality factor of the series *RLC* circuit is $Q_{\mathrm{U}} = \frac{\omega_0 L}{R}$ [1], (42) can be rewritten as

$$Z_r \cong R\left(1 + 2jQ_{\mathrm{U}}x\right). \tag{43}$$

It follows that the forward transmission coefficient at a point slightly off the resonance would be

$$S_{21} = \frac{-2g}{1 + 2g + 2jQ_{\mathrm{U}}x}. \tag{44}$$

The power transmission coefficient is thereby,

$$\left|S_{21}\right|^2 = \frac{4g^2}{(1+2g)^2 + 4Q_{\mathrm{U}}{}^2x^2},$$

$$= \frac{\frac{4g^2}{(1+2g)^2}}{1 + \frac{4Q_{\mathrm{U}}{}^2}{(1+2g)^2}x^2}. \tag{45}$$

In (45), the $\frac{Q_u{}^2}{(1+2g)^2}$ term in the denominator is equal to $Q_L{}^2$ implying that

$$Q_{\mathrm{L}} = \frac{Q_{\mathrm{U}}}{1+2g}. \tag{46}$$

Since (45) describes a Lorentzian curve, a curve fitting routine can be used to extract the microwave parameters of interest from the $\left|S_{21}\right|^2$ data gathered from a VNA. This has mostly been done in MathCAD thorough least squares regression method (e.g. [9]), and has proved to provide a very good fit. However, in this project an automated data acquisition system was developed using IGOR Pro software, which was chosen because of its powerful built-in curve fitting routines. A typical curve-fitted Lorentzian plot in IGOR Pro is illustrated in Figure 3.10.

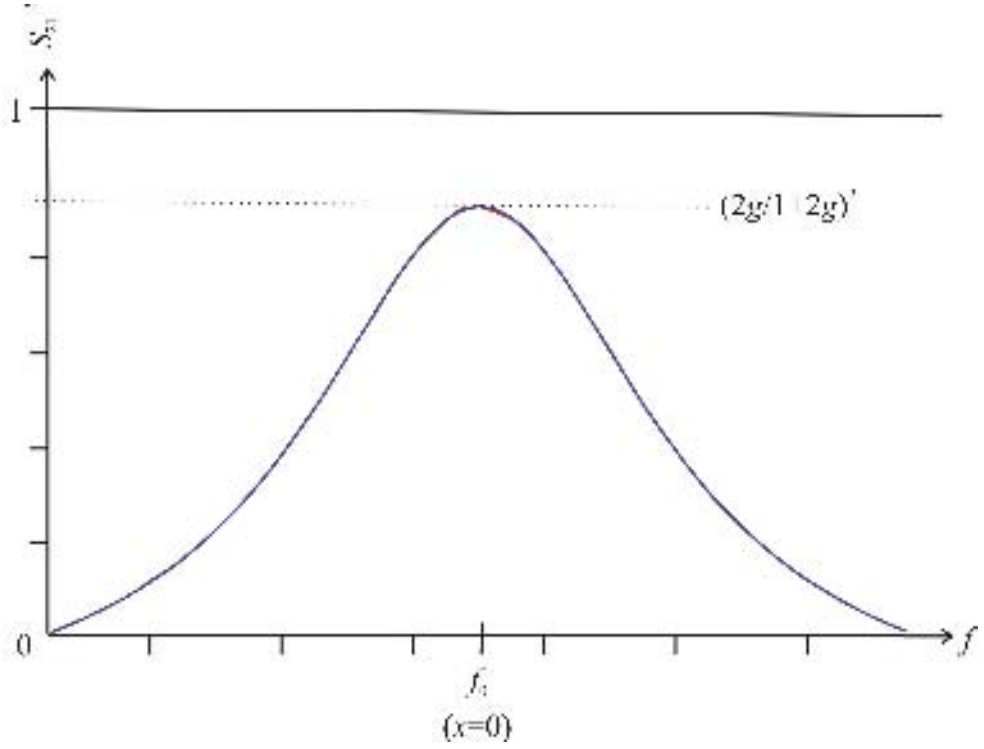

Figure 3.10. $|S_{21}|^2$ data acquired from 8753E VNA is curve-fitted to Lorentzian in IGOR Pro. The goodness of fit is apparent in that original curve (red) is almost completely hidden by the fitted curve (blue).

In Figure 3.10, at f_0, where $x=0$, $|S_{21}|^2=\left(\frac{2g}{1+2g}\right)^2$. Let this maximum value of $|S_{21}|^2$ be called as P_0, then (45) can be rewritten as

$$|S_{21}|^2=\frac{P_0}{1+4Q_{\mathrm{L}}{}^2\left(\frac{f-f_0}{f_0}\right)^2}, \tag{47}$$

where x has been replaced by $\frac{\Delta f}{f_0}=\frac{f-f_0}{f_0}$. For determination of f_{B}, consider now Figure 3.11.

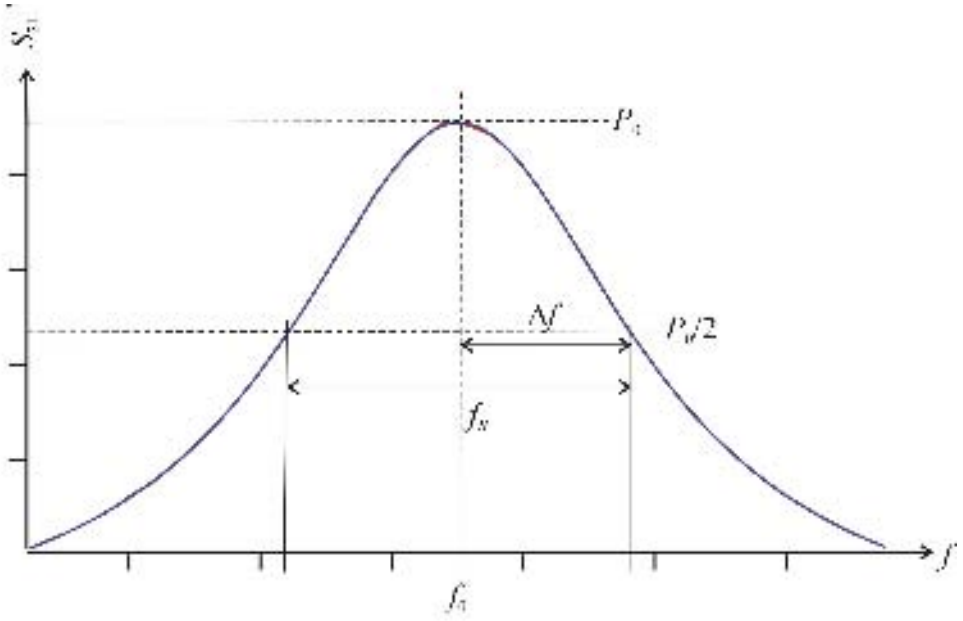

Figure 3.11. Determination of f_{B} from the power transmission coefficient.

Because f_{B} is the half-power bandwidth, it equals the span of the $|S_{21}|^2$ curve between those points where $|S_{21}|^2 = \frac{P_0}{2}$, as shown in Figure 3.11. Therefore, (47) becomes

$$\frac{P_0}{2} = \frac{P_0}{1 + 4Q_{\mathrm{L}}{}^2 \left(\frac{\Delta f}{f_0} \right)^2} \tag{48}$$

$$\Rightarrow 1 = 4Q_{\mathrm{L}}{}^2 \left(\frac{\Delta f}{f_0} \right)^2, \tag{49}$$

which results in the following expression for Δf :

$$\Delta f = \pm \frac{f_0}{2Q_{\mathrm{L}}}. \tag{50}$$

Consequently,

$$f_{\mathrm{B,L}} = 2\Delta f = \frac{f_0}{Q_{\mathrm{L}}}, \tag{51}$$

where $f_{B,L}$ signifies the loaded bandwidth related to Q_L. By analogy, the relationship between f_B and Q_U is

$$f_B = \frac{f_0}{Q_U}. \tag{52}$$

From (46) and (52),

$$f_{B,L} = \frac{f_0}{Q_L} = \frac{f_0(1+2g)}{Q_U}$$

$$= f_B(1+2g). \tag{53}$$

Hence, the bandwidth of a loaded resonator is higher by $(1+2g)$ times as compared to the unloaded case; this fact is quite intuitive given that Q_L is smaller than Q_U by the same factor. Nonetheless, evaluation of Q_U requires not only the measured Q_L but also the value of coupling coefficient *g*, which is not directly quantifiable. A practicable alternative method of estimating Q_U, that makes use of the *IL*, is described below:

3.4.5 **Evaluation of Q_U by IL**

The *IL* can be set to a desired value by adjusting the input and output coupling strength to the resonator. Let $|S_{21}|_0$ be the magnitude of the voltage transmission coefficient at the resonance; then

$$|S_{21}|_0 = \frac{2g}{1+2g} = 1 - \frac{1}{1+2g} \tag{54}$$

$$\Rightarrow \frac{1}{1+2g} = 1 - |S_{21}|_0. \tag{55}$$

It follows from the relationship between Q_L and Q_U that

$$Q_U = \frac{Q_L}{(1-|S_{21}|_0)} \tag{56}$$

and

$$f_B = f_{B,L}(1-|S_{21}|_0). \tag{57}$$

If transmitted power ratio in dB is represented by P, then

$$P = 20\log S_{21} \Rightarrow S_{21} = 10^{P/20}$$

and the definition of IL results in

$$\left|S_{21}\right|_0 = 10^{IL/20}. \tag{58}$$

From (56) and (58),

$$Q_{\mathrm{U}} = \frac{Q_{\mathrm{L}}}{\left(1-10^{IL/20}\right)}. \tag{59}$$

As an example, for IL= -20 dB, $Q_{\mathrm{U}} = \frac{Q_{\mathrm{L}}}{0.9}$ and for IL= -40 dB, $Q_{\mathrm{U}} = \frac{Q_{\mathrm{L}}}{0.99}$, meaning that the measured Q_{L} values of a resonator would not be far off from its Q_{U} if the input and output coupling strengths are such that they result in IL values below -20 dB [2].

References

[1] D. M. Pozar, *Microwave Engineering*, Third Edition, John Wiley & Sons, N.Y., 2005, ISBN 0-471-44878-8.

[2] A. Porch, *Private Communications*, 2008.

[3] S. Ramo, J. R. Whinnery, and T. V. Duzer, *Fields and Waves in Communication Electronics*, Third Edition, John Wiley & Sons, N.Y., 1994, ISBN 978-81-265-1525-7.

[4] S. Y. Liao, *Microwave Devices and Circuits*, Third Edition, Prentice-Hall International, 1990, ISBN 0-13-584681-1.

[5] R. A. Chipman, *Theory and Problems of Transmission Lines*, Schaum's Outline Series, McGraw-Hill, N.Y., 1968.

[6] E. da Silva, *High Frequency and Microwave Engineering*, Butterworth Heinemann, Oxford, 2001, ISBN 0-7506-5046-X.

[7] M. E. V. Valkenburg, *Network Analysis*, Third Edition, Prentice-Hall, N.J., 1974, ISBN 0-13-611095-9.

[8] P. J. Petersan and S. M. Anlage, "Measurement of Resonant Frequency and Quality Factor of Microwave Resonators: Comparison of Methods", *Journal of Applied Physics*, Vol. 84, pp. 3392-3402, September 1998.

[9] S. Robson, "Sapphire Dielectric Resonators for the Determination of Conductivity of Small Copper Spheres and Graphite Powder", *M.Eng. Project Report*, Cardiff School of Engineering, Cardiff University, May 2006.

CHAPTER 4

DESCRIPTION OF RESONATORS

4.1 Introduction

The various microwave resonator devices used in this project will now be described, starting from the hairpin resonator, which was introduced in chapter 3. It will be followed by detailed descriptions of the split ring and sapphire dielectric resonators. The design and construction of all resonators will be covered, as well as derivation of expressions for their resonant frequency and unloaded quality factor. First of all, however, some essential background knowledge related to the aforementioned resonators is discussed in the following paragraphs.

4.1.1 Amplitude Attenuation Constant

So far in this thesis, signal propagation along lossless (or nearly lossless) TLs has been considered. However, in practice all TLs will have losses arising due to resistance R of the conductors and conductance G of the dielectric [1]. The unit cell of a lossy TL is shown in Figure 4.1.

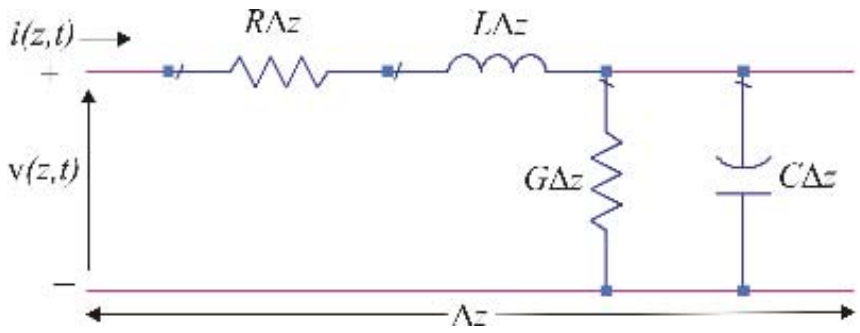

Figure 4.1. Unit cell of a lossy TL; R, resistance per unit length; L, inductance per unit length; G, conductance per unit length; C, capacitance per unit length [1,2].

The wave equation for voltage v along the lossy TL is [1,2]

$$\frac{\partial^2 \mathrm{v}}{\partial z^2} = \left(R + jwL\right)\left(G + jwC\right) \equiv \gamma^2 \mathrm{v}\,, \tag{1}$$

where $$\gamma = \sqrt{(R + j\omega L)(G + j\omega C)} \equiv \alpha + j\beta \quad (2)$$

is the complex propagation constant that is a function of frequency. It replaces the wavenumber β of the lossless line described earlier. The forward propagating solution to (1) can be found as

$$v(z,t) = V_0^+ e^{-\alpha z} e^{j(\omega t - \beta z)}, \quad (3)$$

in which the term $e^{j(\omega t - \beta z)}$ is the standard phasor associated with a travelling wave. The additional term $e^{-\alpha z}$ leads to an exponential decay of the travelling wave amplitude and hence $\alpha = \mathrm{Re}(\gamma)$ is known as the amplitude attenuation constant. For lossless TLs α has to be zero so that $\gamma = j\beta$; however, for lossy lines α must be related in some way to the TL losses represented by *R* and *G*. For the realistic case of lines with small losses

$$\alpha = \mathrm{Re}(\gamma) = \frac{R}{2Z_0} + \frac{GZ_0}{2} \equiv \alpha_c + \alpha_d, \quad (4)$$

where $\alpha_c = R/2Z_0$ is the attenuation constant due to conductor loss and $\alpha_d = GZ_0/2$ is the attenuation constant due to dielectric loss [1].

4.1.2 **Dielectric Loss and Loss Tangent**

Dielectric loss arises because of a finite dielectric conductivity, or a finite phase angle between the dielectric polarisation and the electric field producing it [1]. Thus, for all real world dielectric materials the relative permittivity is considered to be complex i.e.

$$\varepsilon_r = \varepsilon_1 - j\varepsilon_2 \equiv \varepsilon_1(1 - j\tan\delta). \quad (5)$$

The real part of ε_r (i.e. ε_1) is a measure of the electrical energy stored in the dielectric while the imaginary part ε_2 quantifies the loss or power dissipated in the medium as heat due to damping of the vibrating dipole moments [2]. The quantity $\tan\delta$ is called the loss tangent, defined as $\tan\delta \equiv \varepsilon_2/\varepsilon_1$. For dielectrics at room temperature and around 1 GHz frequency, $\tan\delta$ varies between approximately 10^{-5} for certain crystalline materials like sapphire, to about 1 for polar liquids like water, to above 1000 for conducting polymers [1]. Free-space or air, having a real $\varepsilon_r = 1$, is lossless (i.e. $\tan\delta = 0$). The connection between the dielectric

attenuation constant α_d and $\tan\delta$ will now be established. From (4), $\alpha_d = GZ_0/2$, where $Z_0 = \sqrt{L/C}$ and $G = \omega C \tan\delta$ [1]. Therefore,

$$\alpha_d = \frac{1}{2}\sqrt{\frac{L}{C}}\omega C \tan\delta = \frac{1}{2}\omega\sqrt{LC}\tan\delta . \tag{6}$$

However, $\omega\sqrt{LC} = \beta$ is the TL phase constant, so finally

$$\alpha_d = \frac{\beta}{2}\tan\delta \equiv \frac{\pi}{\lambda}\tan\delta , \tag{7}$$

where use has been made of the equality $\beta = 2\pi/\lambda$, developed earlier in chapter 3.

4.1.3 **Skin Depth and Surface Resistance**

The skin depth or characteristic depth of penetration, δ, of a conductor is the depth at which the current density reduces in magnitude to $1/e \approx 37\%$ of its surface value [1,2]. It is mathematically defined as

$$\delta = \sqrt{\frac{2}{\omega\mu\sigma}} = \sqrt{\frac{2\rho}{\omega\mu}} , \tag{8}$$

where $\mu = \mu_0\mu_r$ is the permeability of the material in H/m, σ is the conductivity in S/m and ρ is the resistivity in Ωm. The skin depth is, therefore, a function of three variables; resistivity (or conductivity), permeability, and frequency of operation. Since for most metals $\mu_r \approx 1$ [1,2], (8) can be rewritten as

$$\delta = \sqrt{\frac{2\rho}{\omega\mu_0}} . \tag{9}$$

At microwave frequencies, the skin depth is extremely small (i.e. $\approx$ 1 μm) for good conductors. Hence, a very thin coating of a good conductor such as gold or silver is required for low-loss microwave components [2]. A related parameter of interest to δ is the surface resistance, R_s, of a conductor, which for a cylindrical wire can be described as follows: At microwave frequencies (i.e. where wire radius >> δ), correct results are attained by presuming that all current flows uniformly in a surface film of thickness δ [1]. The microwave resistance of the wire having radius, a (m) and area, A (m^2) will then be

$$R = \frac{\rho l}{A} \approx \frac{\rho l}{2\pi a \delta} \approx \frac{\rho}{2\pi a \delta} \text{ per unit length } (l = 1 \text{ m}). \quad (10)$$

In (10), the quantity $R_s = \rho/\delta$ is known as the surface resistance of the conductor (S.I. unit Ω), in terms of which $R = R_s/2\pi a$ i.e. $R \propto R_s$. Thus, the surface resistance is inversely proportional to the skin depth and directly proportional to the operating frequency. As an example for copper at room temperature; at 1 MHz, R_s = 0.28 mΩ and at 10 GHz, R_s = 28 mΩ. Consequently, the microwave conduction losses for a material can be much higher than those at low frequencies [1].

4.2 **Hairpin Resonator**

The hairpin resonator is a variant of the wide microstrip line, therefore supporting TEM travelling waves along its length. It is made out of a copper strip (for maximising the *Q* due to the high conductivity) bent at one end to form the short-circuited termination while the other end is left open, hence forming the two-plated hairpin structure.

4.2.1 **Resonant Frequency**

Resonance occurs when the length, *l*, of the hairpin equals integer multiples of a quarter wavelength, with fundamental resonance mode occurring at $l = \lambda/4$ and the corresponding resonant frequency given as [1]

$$f_0 = \frac{c}{4l} \approx \frac{75}{l(\text{mm})} \text{GHz}. \quad (11)$$

Since the hairpin structure is based on a TL, the formula for its resonant frequency only depends on *l*. A schematic diagram of hairpin resonator is shown in Figure 4.2.

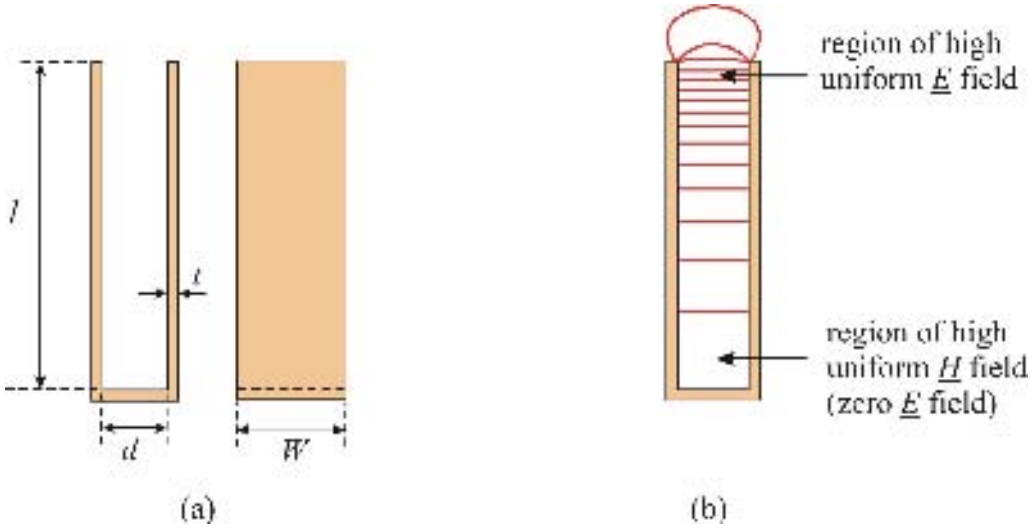

Figure 4.2. (a) Schematic diagram of hairpin resonator; *W*, plate width; *L*, plate length; *d*, plate separation; *t*, plate thickness. (b) Electric field (*E*) along the length of a resonant hairpin.

The *E* distribution along the hairpin length is illustrated in Figure 42.2(a). At resonance, *E* will be largest at the open circuit and zero at the short circuit. On the other hand, magnetic field (*H*) will be largest at the short circuit and zero at the open end [3]. There is a fringing *E* at the open end, implying that the effective resonator length l_{eff} will be larger than the geometrical length *l*. When $d << l$, to quite a good approximation $l_{eff} = l + d/2$, so that the resonant frequency given by (11) will be slightly reduced [1].

4.2.2 **Resonator Construction**

The hairpin used in this project is made from a 1 mm thick copper sheet with l = 25 mm and d = 5 mm, which gives $l_{eff} = 27.5$ mm and corrected $f_0 \approx 2.7$ GHz [4,5]. This value is extremely close to the experimental results for the empty hairpin. The whole structure is enclosed in a copper radiation shield that is machined from two pieces: one serving as a cylindrical housing around the hairpin and the other a base, to which the housing is press fitted. The shield is essential to ensure a high *Q*, as without it the resonator loses its stored energy to the surroundings through emission of electromagnetic radiation. The hairpin is secured via a steel nut and screw to the base of shield, and is excited magnetically by a pair of loop-terminated RG402 coaxial cables [3,4]. The loops are made as near identical to ensure symmetrical input/output coupling to the microwave magnetic field (so that the prior

microwave analysis remains valid) and the cables are soft-soldered into the copper shield. The complete resonator package along with the *E* and *H* field lines is illustrated in Figure 4.3.

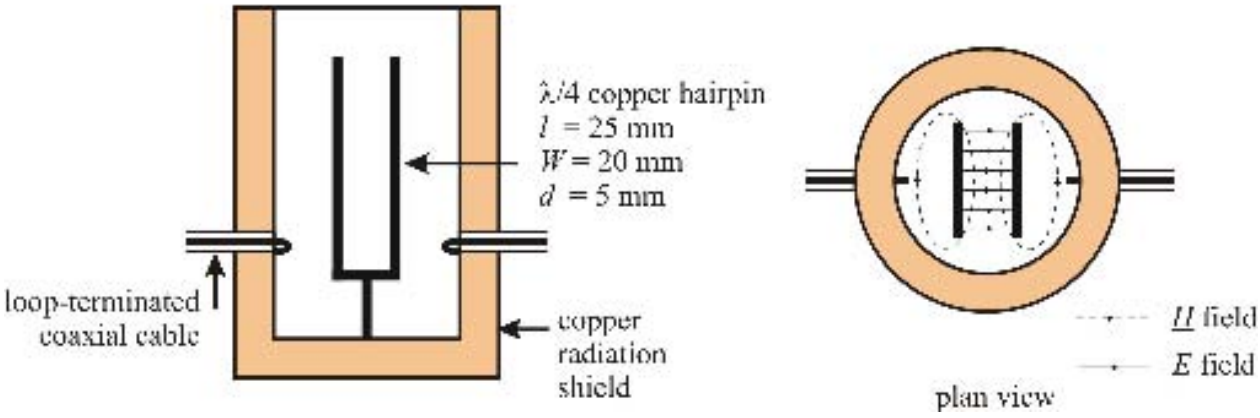

Figure 4.3. Schematic diagram of complete hairpin resonator package; *E* and *H* fields are shown in the plan view.

4.2.3 **Unloaded Quality Factor**

The starting point for deriving the unloaded quality factor of the hairpin resonator is Q_U of a TL resonator, which is [1,2]

$$Q_{\mathrm{U}} = \frac{\beta}{2\alpha}. \tag{12}$$

Since the hairpin structure is based on the short-circuited $\lambda/4$ line that has $\beta = n\pi/2l$, then for the fundamental resonance mode (i.e. $n = 1$) (12) becomes

$$Q_{\mathrm{U}} = \frac{\pi}{4\alpha l}. \tag{13}$$

Generally, for TL resonators Q_{U} is made up of two components i.e. $Q_{\mathrm{U}}^{-1} = Q_{\mathrm{c}}^{-1} + Q_{\mathrm{d}}^{-1}$ where Q_{c} is known as the conductor quality factor and Q_{d} is known as the dielectric quality factor. For the case of short-circuited $\lambda/4$ TL resonating in fundamental mode [1],

$$Q_{\mathrm{c}} \equiv n\pi / 4\alpha_{\mathrm{c}} l \tag{14}$$

and

$$Q_{\mathrm{d}} \equiv n\pi / 4\alpha_{\mathrm{d}} l = \left(\tan\delta\right)^{-1}. \tag{15}$$

Since the spacing between the two plates of the hairpin structure is filled with air, $\tan\delta=\alpha_d=0$ and Q_d is infinitely large, implying

$$Q_U = Q_c \equiv \frac{\pi}{4\alpha_c l}. \tag{16}$$

Now from (4), $\alpha_c = R/2Z_0$ where

$$Z_0 = \sqrt{\frac{L}{C}} \tag{17}$$

is the characteristic impedance. Substituting $L \approx \mu_0 d/W$ and $C \approx \varepsilon_0 W/d$ [1,2] in (17) gives

$$Z_0 \approx \sqrt{\frac{\mu_0}{\varepsilon_0}}\left(\frac{d}{W}\right) = \eta_0\left(\frac{d}{W}\right), \tag{18}$$

where $\sqrt{\mu_0/\varepsilon_0} = \eta_0 \approx 377\Omega$ is the impedance of free-space [1,2]. Consider next the hairpin resistance: at room temperature and the frequency of operation (i.e. 2.7 GHz) the skin depth for copper $\left(\rho = 2\times10^{-8}\ \Omega\text{m}\right)$ is $\delta = \sqrt{2\rho/\omega\mu_0} \approx 1.37\ \mu\text{m}$, which is much smaller than the 1 mm thickness of hairpin. So, the hairpin plates can be modelled as two parallel sheets of current, each having thickness δ. Current flows in opposite directions on the inner surfaces of both plates, as illustrated in Figure 4.4 [1].

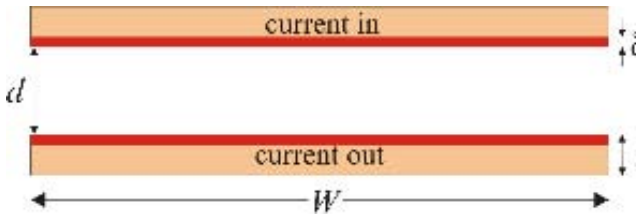

Figure 4.4. Hairpin model for calculation of resistance - surface layer of thickness δ is shown in red.

The hairpin resistance will then be

$$R = \frac{\rho l}{W\delta} + \frac{\rho l}{W\delta} = \frac{2R_s}{W} \text{ per unit length}, \tag{19}$$

where the area of each hairpin plate is $A = W\delta$. Using (18) and (19), the amplitude attenuation constant becomes

$$\alpha_c = \frac{\frac{2R_s}{W}}{\frac{2\eta_0 d}{W}} = \frac{R_s}{\eta_0 d}, \tag{20}$$

which upon substitution in (16) yields

$$Q_U = \frac{\pi\eta_0 d}{4lR_s}. \tag{21}$$

However, from (11) $f_0 = c/4l \Rightarrow 4l = c/f_0$. Substituting this in (21) gives

$$Q_U = \frac{\pi f_0 \eta_0 d}{cR_s}. \tag{22}$$

Since $c = 1/\sqrt{\varepsilon_0\mu_0}$ and $\eta_0 = \sqrt{\mu_0/\varepsilon_0}$, $\eta_0/c = \sqrt{\varepsilon_0\mu_0}\sqrt{\mu_0/\varepsilon_0} = \mu_0$ and thus,

$$Q_U = \frac{\pi f_0 \mu_0 d}{R_s}. \tag{23}$$

For the hairpin used in this project, $R_s = \rho/\delta = 2\times10^{-8}/1.37\times10^{-6} \approx 15\ \text{m}\Omega$ and so,

$$Q_U = \frac{\pi \times 2.7\times10^{9} \times 4\pi\times10^{-7} \times 5\times10^{-3}}{15\times10^{-3}} \approx 3550.$$

The *IL* of empty hairpin resonator was set to approximately -18 dB, which gives a theoretical Q_L value of $Q_L = Q_U\left(1-10^{IL/20}\right) \approx 3100$. The measured Q_L value for the empty hairpin was close to 2000 [4]. The reasons for this difference lie in the poor electrical quality of the mechanical copper surfaces, and neglecting the straight portion of the hairpin surface at the short-circuit end.

4.3 **Split Ring Resonator**

Unlike the distributed-element hairpin resonator, the split ring is a lumped-element device. In its simplest form, which was used in this project, it consists of an inductor made out of a cylindrical loop of a metal with a longitudinal gap acting as the capacitor [6]. In other configurations, it can have multiple gaps and is also known by various other names, such as the loop-gap resonator called so by Froncisz and Hyde [7]. A conducting shield is required around the resonator to prevent radiation of the fields, thereby maintaining high *Q* values at microwave frequencies. The shield radius should be smaller than the cut-off wavelength for

the lowest excited propagation mode in cylindrical waveguide and its length should be much larger than the resonator length [6,7]. This type of resonator has many useful applications where a medium-range *Q* is adequate and a miniature size is vital [8]. The resonant frequency of the split ring is determined primarily by the area of the axial hole (setting its lumped inductance) and gap width (setting its lumped capacitance). The electric fields are supported by the parallel surfaces of the gap and the magnetic fields surround the loop. Thus, the conduction current flows circumferentially on the loop and shield surfaces, converting into displacement current across the gap [8,9]. The current and field distributions in the resonator along with its critical dimensions are illustrated in Figure 4.5.

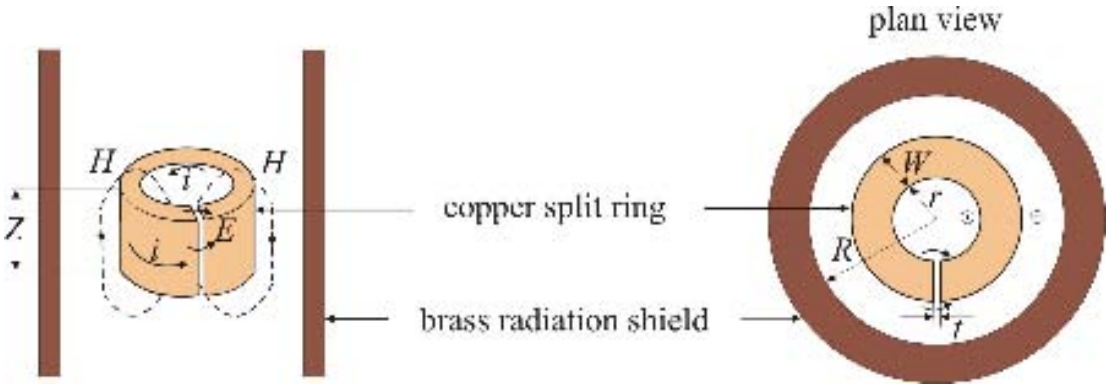

Figure 4.5. Current direction and electromagnetic field arrangement in the split ring. The critical resonator dimensions are *Z*, resonator length; *r*, resonator inner radius; *R*, shield radius; *t*, gap separation; *W*, gap thickness.

The *H* field intensity in the central and annular regions can be regarded as uniform for small gap distances. The magnetic fields that are located within the resonator length are named main magnetic fields while the curved magnetic field lines, which are located outside of the resonator length and connect the field lines of the central and annular regions, are called fringing magnetic fields [9]. Similarly, electric fields within physical the gap width are termed main electric fields whereas those outside the gap are named fringing electric fields, as shown in the plan view of Figure 4.5.

4.3.1 **Resonator Construction**

The split ring used in this project was made up of a copper ring having a length, thickness and inner radius each of 3 mm [10]. The gap was machined mechanically to a width (i.e. gap

separation) of 400 μm, yielding a resonant frequency of ≈ 3.6 GHz [5]. A brass cylindrical shield of 12 mm radius, coaxial with the resonator, was used to prevent radiation of the fields and a nylon screw along with a brass locking nut supported the split ring within the shield. The resonator was excited magnetically by a pair of identical loop-terminated, semi-rigid coaxial cables, as depicted in Figure 4.6.

Figure 4.6. Schematic diagram of the 3.4 GHz split ring resonator package.

4.3.2 **Resonant Frequency**

Attempts to develop a field analysis and derive an equation for the resonant frequency of the split ring resonator were made in [6] and [7]. In the simple analysis by Hardy and Whitehead [6] the electric and magnetic fringing fields are not considered but shield effects are catered for. The equation derived by them provides only a rough estimation of the resonant frequency in comparison to actual results. Froncisz and Hyde [7] added an experimental correction factor for the fringing gap capacitance, thereby coming up with better accuracy although they did not still cater for the fringing magnetic fields. In both the aforementioned calculation methods the length of split ring was approximated as infinite. Mehdizadeh *et al.* [8,9] have developed the following expression for the resonant frequency of the split ring taking into account both electric and magnetic fringing fields and the limited length of the resonator:

$$f_0 = \frac{c}{2\pi r}\sqrt{\frac{t}{\pi W}}\sqrt{1+\frac{r^2}{R^2-(r+W)^2}}\sqrt{\frac{1+\dfrac{\Delta Z}{Z}}{1+\dfrac{\Delta W}{W}}} \tag{24}$$

Here, the parameter ΔZ is the equivalent length extension due to the magnetic fringing fields at the two ends of the resonator and ΔW is the equivalent extension of the gap width due to the electric fringing fields. Curve fitting methods were used by Mehdizadeh *et al.* [8] for 30 split ring resonators varying in frequency between $1-10$ GHz and the following empirical expressions for ΔZ and ΔW were determined:

$$\Delta Z \approx 0.18R, \quad \Delta W \approx 3.0t\,. \tag{25}$$

The calculated value of f_0 for the split ring used in this project, attained using (24) and (25) is 3.78 GHz, which is slightly higher than the measured value (≈ 3.6 GHz).

4.3.3 **Unloaded Quality Factor**

Using the infinite length approximation, Hardy and Whitehead [6] derived an expression for the quality factor of a split ring resonator considering ohmic losses on the cylindrical walls of the resonator and the shield. Mehdizadeh *et al.* [8,9] were able to forego the infinite length approximation, coming up with the following equation:

$$Q_s = \frac{r}{\delta}\frac{(1+p)\left(1+\dfrac{\Delta Z}{Z}\right)}{1+\left(1+\dfrac{W}{r}+\dfrac{R}{r}+\dfrac{R^2}{3.8Zr}\right)p^2}, \tag{26}$$

where $p = \dfrac{r^2}{R^2-(r+W)^2}$ and Q_s is the quality factor considering only ohmic losses on resonator and shield walls. The derivation for Q_s does not account for the conductor losses in the gap (capacitor losses), considering which the expression for gap quality factor is obtained as [7,9]

$$Q_c = \frac{1.7\times10^5 t}{f_0^{3/2}\varepsilon_0 W^2\left(1+\dfrac{\Delta W}{W}\right)}. \tag{27}$$

Therefore, the overall unloaded quality factor is

$$\frac{1}{Q_U} = \frac{1}{Q_s} + \frac{1}{Q_c}. \tag{28}$$

For the split ring resonator used in this project, $Q_s \approx 4500$ and $Q_c \approx 2623$, resulting in $Q_U \approx 1657$. The *IL* of the empty resonator was set to approximately -22 dB, which gives $Q_L = Q_U\left(1-10^{IL/20}\right) \approx 1525$. The measured Q_L for the empty resonator was approximately 1400. Again, the difference between experiment and theory here lies in the degraded electrical quality of the machined copper surfaces.

4.4 **Sapphire Dielectric Resonator**

Similar to resonant segments of TEM TLs, sections of suitably terminated hollow metallic or dielectric rod waveguides constitute resonant circuits [1,2,11-13]. Such resonators present the benefits of possessing higher Q_U and the ability to withstand much larger power levels as compared to planar TL resonators. However, since waveguides cannot support TEM waves, such waveguide cavity resonators have either transverse electric (TE) or transverse magnetic (TM) resonant modes (or, indeed, hybrid HEM modes). TE modes have no electric field component in the direction of propagation (i.e. *z* axis) while TM modes have no magnetic field component along the *z* axis. As in TL resonators, the condition for resonance is satisfied when the length *l* of resonator equals an integer number *p* of half-wavelengths along the length *z* i.e. $\beta = 2\pi/\lambda = p\pi/l$. Since dielectric resonators (DRs) rather than metallic cavities were used in this project, the focus from this point onwards will solely be on this type of resonators.

4.4.1 **General Description of DRs**

The existence of DRs has been known for about seventy years now. In 1939, Richtmyer [14] showed that a dielectric material in free-space will exhibit radiation damping; yet if its dielectric constant is much greater than unity, the relative damping is sufficiently small to permit the dielectric to resonate. The high dielectric constant, ε_1, of the material ensures that the electric and magnetic fields of a given resonant mode are confined close to the resonator [2,11,15,16] . The fields attenuate to negligible values at a distance small compared to the free-space wavelength. Thus, the radiation loss is extremely small and Q_U is limited

primarily due to the losses inside the dielectric body. If all electric field energy of the resonant mode is stored inside the resonator, and there are no losses due to external fields, $Q_U = 1/\tan\delta$. However, for finite values of ε_1, external loss always occurs due to dissipation in a surrounding metal shield, thereby reducing Q_U. For ε_1 of around 100 or larger, the external loss is negligibly small and $Q_U \approx 1/\tan\delta$ is a good approximation [15].

4.4.2 **Advantages and Applications of DRs**

Dielectric resonators have the advantages of considerably smaller size, weight, and cost compared to empty metallic cavities having the same resonant frequency, provided ε_1 is considerably larger than unity [2,11,15,17]. The reason behind this is as follows: the dimensions of ordinary air-filled waveguide cavities for a particular resonant mode are of the order of λ (i.e. wavelength in air). On the other hand the dimensions of a dielectric resonator are on the order of the wavelength in the dielectric material, denoted by λ_d. As $\lambda_d = \lambda/\sqrt{\varepsilon_1}$, the resonator dimensions will be much smaller in comparison with λ, if ε_1 is big [11,15]. This condition is fulfilled by using dielectric materials with ε_1 ranging between about 10 and 100 for fabricating the resonators. Owing to their small sizes, dielectric resonators can be very easily incorporated into microwave integrated circuits and coupled to planar TLs [2]. They are increasingly being used to replace waveguide filters in demanding applications like satellite communications, where microstrip and stripline resonators cannot be used due to their intrinsically high losses [11].

4.4.3 **Shielding of DRs**

Unlike metallic cavities, there is some fringing or leakage of fields from the sides and ends of a DR, which can be overcome by placing it within a metallic shield, usually made if copper, aluminium or brass [1,2,11,15,18]. The shield may take the form of a box or a cylinder, depending upon the shape of the host resonator. Its size should be about twice the largest dimension of the DR so that current induced on the metallic surface by the resonator external field will not gravely degrade the overall unloaded Q [15]. While use of the shield does reduce the overall Q_U of DR, which is limited by conductor losses in the shield as well as by the loss tangent of the dielectric material, it actually helps in increasing the Q_L [18]. In

practice, shielding of DRs provides for loaded *Q*s of tens of thousands (about 30,000 being the value for the copper shielded sapphire DR used in this research).

4.4.4 **DR Shapes and Materials**

Three common shapes for a DR are rectangular, cylindrical disk (i.e. length < diameter) and cylindrical rod (i.e. length > diameter) [15]. In addition, other shapes like tubular, spherical, and parallelepiped can also be found [11]. The most practical shape although, is the cylindrical disk that has been widely reported in literature (see, for instance references [2,11,12,17]). The optimum ratio of length/diameter for a cylindrical resonator is about 0.4 because of good separation of modes near to the $TE_{01\delta}$ mode [1,15]. Historically, materials with $\varepsilon_1 \geq 100$ have been used for DRs with rutile (a crystalline mineral composed of titanium dioxide or titania) and strontium titanate ($SrTiO_3$) being the most popular [13,15,16,19]. At room temperature, the dielectric constant for rutile is 85 whereas for $SrTiO_3$, it is above 250. Materials with even higher dielectric constants, such as barium titanate ($BaTiO_3$, $\varepsilon_1 = 1200$) have been reported by Cohn [15]. Although the electric and magnetic fields are confined mostly within the DR using such materials, a major drawback is the variation of ε_1 with temperature in the aforementioned materials, together with large loss tangents. For instance, in rutile the relative change of ε_1 is approximately 1000 ppm/°C (1000 parts per million per degree Celsius). Since $f_0 \propto 1/\sqrt{\varepsilon_1}$, the corresponding change in frequency is 500 ppm/°C. The materials $SrTiO_3$ and $BaTiO_3$ with larger ε_1 have even greater temperature sensitivities. This is in stark contrast to a brass waveguide cavity that has an expansion coefficient and temperature sensitivity of 20 ppm/°C [15]. Thus, dielectric materials having good temperature stability together with low dielectric loss were developed since the 1970s, as reported by Kajfez and Guillon [11], and Pospieszalski [17]. Sapphire is one such material, which though having a comparatively lower dielectric constant ($\varepsilon_1 = 9.4$) [1,2] presents considerably improved temperature coefficient of permittivity (i.e. of the order of 40-70 ppm/°C) [20]. Sapphire is the monocrystalline form of the mineral corundum, which is an aluminium oxide (Al_2O_3). Single crystal sapphire has probably become the most popular material for use in DRs as it has the highly desirable feature of lowest known loss tangent

($\approx 10^{-5}$ at room temperature) at about 5 GHz [1]*. Sapphire dielectric resonators (SDRs) have been widely used in surface resistance measurements of superconducting materials [21-23]. Another area, where SDRs have found extensive application, is low-noise, high spectral purity microwave signal generation in X-band [24-26]. In this project, a disk shaped SDR has been used for compositional analysis of solvents flowing in a microcapillary.

4.4.5 **Resonant Modes and Frequencies of DRs**

Various conventions have been used to describe the resonant modes in DRs, the most common being TE, or H modes, and TM, or E modes. Whereas authors have mainly resorted to the TE/TM notation, differences still exist in their usage of the subscripts to describe field variations. Some have used two integer subscripts (i.e. m and n) [16,24,25,30], whilst a majority have employed three; the third subscript being the non-integer p [2,11,13,15,17,19,21,23,26,31-33]. The TE/TM notation along with three subscripts will be used in this thesis. The subscripts m, n, and p in mode designations TE_{mnp} and TM_{mnp} characterise half-period field variations in the azimuthal (or circumferential), radial and axial directions, respectively [2,11,15,33]†. Frequently, the index p is replaced by $l+\delta$, where l=0,1,2,… and $0 < \delta < 1$. This notation means that there are l and a fraction half-period variations in the resonator along the z-axis [11,15]. The most commonly used resonant mode in the popular cylindrical DRs is the $TE_{01\delta}$ (i.e. l =0) [2,11,15,17]. All of the surface resistance measurement methods mentioned in the previous paragraph have employed this mode. The electric field lines of the $TE_{01\delta}$ mode in an isolated DR (i.e. without a shielding enclosure) are simple circles concentric with the cylinder axis as shown in Figure 4.7a, while the magnetic field intensity is solenoidal in nature and sketched in Figure 4.7b.

---

* The polycrystalline version of sapphire is a ceramic material known as alumina that has a comparatively higher loss tangent of approximately 10^{-4} at 5 GHz.

† In addition to TE and TM modes, hybrid modes designated as HEM modes also exist in cavity resonators. For all $m > 0$, the modes are HEM, having both TE and TM parts. They will not be discussed further in this thesis; however, a detailed description regarding HEM modes can be found in [11].

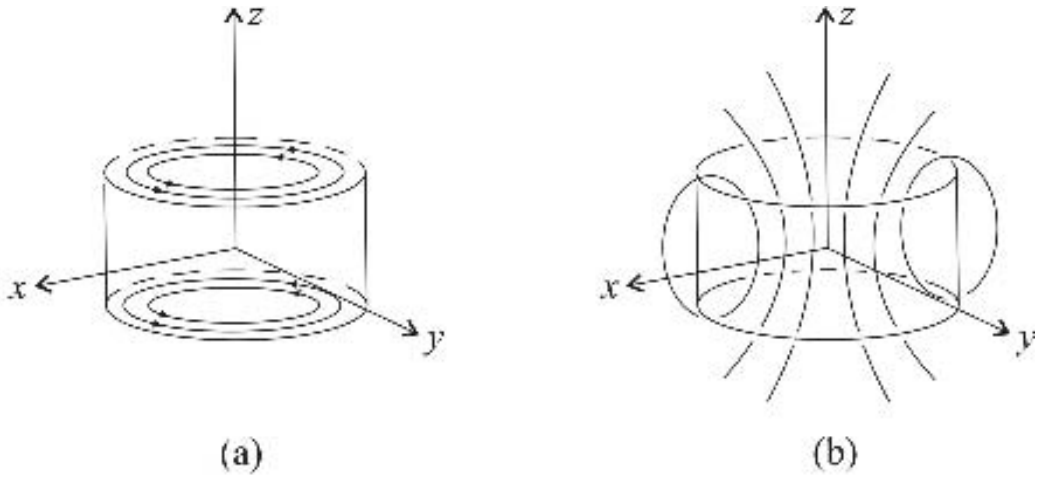

Figure 4.7. (a) Electric field, and (b) magnetic field lines of the $TE_{01\delta}$ resonant mode in an isolated cylindrical DR.

For a dielectric material with ε_1 around 40 and operating in the $TE_{01\delta}$ mode, over 95% of the stored electric energy and roughly 60% of the stored magnetic energy are located within the material. The remainder of energy is distributed around the DR in air, decaying exponentially with distance away from the surface of resonator. Although the geometrical structure of DRs is very simple, it is much more complicated to obtain an exact solution of Maxwell's equations for them as compared with hollow metal cavities. This problem holds true for an isolated DR and even more so for a shielded one; hence, the exact resonant frequency of a particular resonant mode can only be calculated by rather intricate numerical procedures [11]. As regards the $TE_{01\delta}$ mode, numerous attempts have been made to accurately compute its resonant frequency, resulting in errors of about 3.5 to 10 percent [13,15,17,27-29]. While all these methods are quite complex, Kajfez and Guillon [11] have provided the following simple formula for an approximate estimation of the resonant frequency of the isolated $TE_{01\delta}$ mode DR:

$$f_0\,(\mathrm{GHz}) = \frac{34}{a\sqrt{\varepsilon_1}}\left[\frac{a}{l} + 3.45\right]. \tag{29}$$

Here *a* and *l* are the radius and length, respectively, of the DR expressed in mm. This formula is accurate to about 2% in the range

$$0.5 < \frac{a}{l} < 2 \text{ and } 30 < \varepsilon_1 < 50\,.$$

(29) will be used to estimate the resonant frequency of the SDR used in this project, which operates in $TE_{01\delta}$ mode. The result will be fed as a starting point for Superfish software, as described later, to arrive at an accurate f_0 value.

4.4.6 **Unloaded Quality Factor**

The unloaded Q of a shielded DR is given by the fundamental relation

$$Q_{\mathrm{U}} = \frac{\omega_0 \langle U \rangle}{\langle P \rangle}, \tag{30}$$

where $\langle U \rangle$ is the time-averaged stored energy and $\langle P \rangle = \langle P_{\mathrm{c}} \rangle + \langle P_{\mathrm{d}} \rangle + \langle P_{\mathrm{r}} \rangle$ is the time averaged-power dissipated [1,11]. $\langle P_{\mathrm{c}} \rangle$ is the conductor power loss, $\langle P_{\mathrm{d}} \rangle$ is the power loss in dielectric and $\langle P_{\mathrm{r}} \rangle$ is the power loss due to radiation of fields. For a DR placed in a closed cavity with highly conductive walls, radiation is effectively non-existent, hence $\langle P_{\mathrm{r}} \rangle$=0. Thus $\langle P \rangle = \langle P_{\mathrm{c}} \rangle + \langle P_{\mathrm{d}} \rangle$ and

$$\frac{1}{Q_{\mathrm{U}}} = \frac{\langle P_{\mathrm{c}} \rangle}{\omega_0 \langle U \rangle} + \frac{\langle P_{\mathrm{d}} \rangle}{\omega_0 \langle U \rangle} = \frac{1}{Q_{\mathrm{c}}} + \frac{1}{Q_{\mathrm{d}}}, \tag{31}$$

where Q_{c} and Q_{d} are the conductor quality factor and dielectric quality factor, respectively. Taking Q_{c} first, the power loss due to conductor (of surface resistance R_{s}) is calculated as

$$\langle P_{\mathrm{c}} \rangle = \frac{1}{2} R_{\mathrm{s}} \int_S H_{\mathrm{s}}^2 dS, \tag{32}$$

where S is the surface area of cavity. In practice, the calculation of power dissipated by cavity walls should take into account the cavity walls as well as the end (top and bottom) flat surfaces. The total energy stored $\langle U \rangle$ is the sum of electric and magnetic energies, which are equal at resonance, so

$$\langle U \rangle = 2 \langle U_{\mathrm{m}} \rangle = \frac{1}{2} \int_V \mu_0 H^2 dV, \tag{33}$$

where V is the cavity volume. Thus, the conductor Q will be

$$Q_c = \frac{\omega_0 \mu_0}{R_s} \left(\frac{\int_V H^2 dV}{\int_S H_s^2 dS} \right). \tag{34}$$

The bracket term of (34) is called as resonator constant, Γ, which has dimensions of metres [1]. Hence, in addition to Γ, Q_c is determined by the resonant frequency of DR and surface resistance of the cavity material. Now, consider the dielectric quality factor, for which the power loss is given by

$$\langle P_d \rangle = \frac{1}{2} \omega_0 \varepsilon_0 \varepsilon_2 \int_{in} E^2 dV , \tag{35}$$

where the index *in* symbolizes power dissipated inside the dielectric making up the resonator. The total energy stored is combination of energy stored inside the dielectric and that in the air region around it, i.e.

$$\langle U \rangle = 2 \langle U_e \rangle = \frac{1}{2} \int_{in} \varepsilon_0 \varepsilon_1 E^2 dV + \frac{1}{2} \int_{out} \varepsilon_0 E^2 dV . \tag{36}$$

Here, the air region (ε_1=1) between the shielding cavity and the dielectric is represented by index *out*. From (35) and (36), the dielectric quality factor is

$$Q_d = \frac{\omega_0 \langle U \rangle}{\langle P_d \rangle} = \frac{\omega_0 \frac{1}{2} \int_{in} \varepsilon_0 \varepsilon_1 E^2 dV + \frac{1}{2} \int_{out} \varepsilon_0 E^2 dV}{\frac{1}{2} \omega_0 \varepsilon_0 \varepsilon_2 \int_{in} E^2 dV},$$

which on simplification becomes

$$Q_d = \frac{\varepsilon_1 \int_{in} E^2 dV + \int_{out} E^2 dV}{\varepsilon_2 \int_{in} E^2 dV}. \tag{37}$$

Dividing the numerator and denominator of the RHS of (37) yields

$$Q_d = \frac{1 + \left(\frac{\int_{out} E^2 dV}{\varepsilon_1 \int_{in} E^2 dV} \right)}{\tan \delta}. \tag{38}$$

The bracket term in the numerator of (38) is termed as W i.e.

$$W \equiv \frac{\text{electrcal energy outside dielectric}}{\text{electrcal energy inside dielectric}}.$$

For most practical DRs with $\varepsilon_1 >> 1$, W << 1, therefore

$$Q_d = \frac{1+W}{\tan\delta} \approx \frac{1}{\tan\delta}. \tag{39}$$

The dielectric quality factor can thus be very large, for example, $Q_d \approx \frac{1}{10^{-5}} = 100,000$ for a SDR. However, the overall unloaded Q calculated using (31) is reduced because of the contribution of Q_c, which is usually smaller than Q_d for SDRs [1]. The conductor, dielectric and overall quality factors of the SDR used in this research were calculated with the aid of Superfish and MathCAD software, as will shortly be elaborated.

4.5 **Description of SDR Used**

4.5.1 **Construction**

The cylindrical SDR employed in this project was a composite device made from two disks (hereafter called pucks) of single crystal sapphire, used in $TE_{01\delta}$ resonant mode. Sapphire being an anisotropic material, its dielectric constant depends upon the direction of electric field, with ε_1=9.4 for $\underline{E}$ along its basal *ab* plane and ε_1=11.0 along its *c* axis [1]. In order to attain symmetrically well confined modes, normally a cylindrical sapphire crystal is machined with the *c* axis aligned with the cylindrical *z* axis, as shown in Figure 4.8 [31]. Such crystals are normally called as *c* axis oriented [23,33], which applies to the pucks constituting the SDRs studied here.

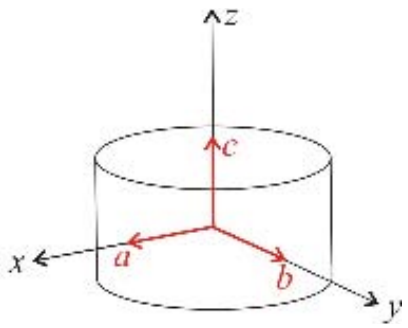

Figure 4.8. *c* axis oriented sapphire disc.

The pucks were procured from Pi-Kem Ltd. (Yew Tree House, Tilley, Wem, Shropshire, SY4 5HE, UK), each of which had a diameter of 20 mm and was 5 mm long; hence, the resonator total length was 10 mm. To avoid radiation losses, the resonator was enclosed in a two-part cylindrical shield made of copper, which was held together with two screws. The shield internal diameter and length were kept at 50 mm and 23.2 mm respectively. The pucks had integral 5 mm diameter sapphire posts in their centres, which went into holes in polytetrafluoroethylene (PTFE) supports built into the copper shield, thereby enabling the resonator to be held tightly inside it. This configuration is formally known as a split post dielectric resonator, or SPDR [1]. A gap of 1.2 mm was provided between the two pucks allowing for samples to be placed through slits in shield of the same height. Magnetic loop coupling to the outside world was enabled by means of two semi-rigid coaxial cables (RG 405U), soldered to the top of the shield. A schematic diagram of the resonator package used in this research, along with its microwave electromagnetic fields is shown in Figure 4.9.

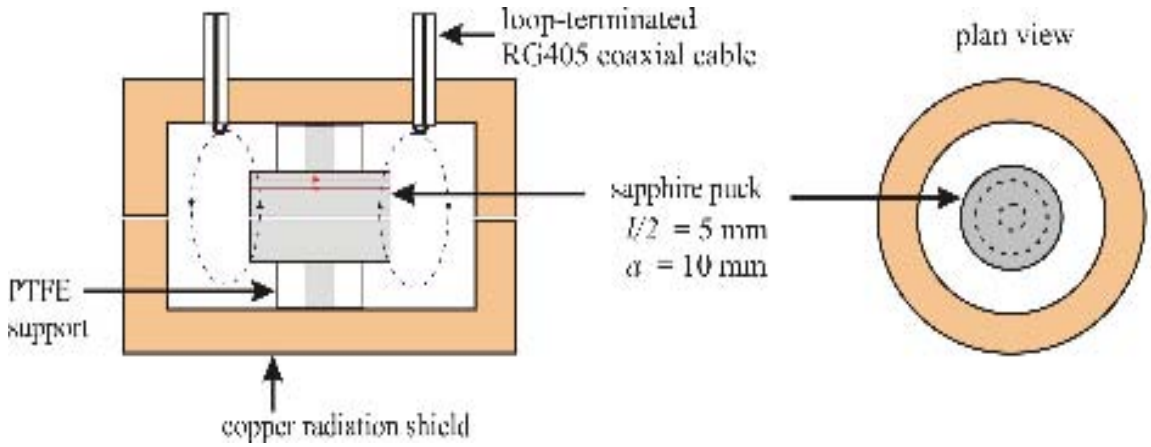

Figure 4.9. Schematic diagram of SDR and its microwave field profile. The $TE_{01\delta}$ mode $\underline{E}$ field is illustrated by solid red lines while $\underline{H}$ field is shown by dotted blue ellipses.

The approximate resonant frequency of the SDR under consideration was calculated using (29), which comes around 5 GHz. This value of f_0 was used as a starting point for working out the exact resonant frequency with the aid of Superfish, as detailed in the following section.

4.5.2 **Superfish Analysis of SDR**

Superfish is a freely available finite element method software package employed for computing resonant frequencies and radio-frequency (RF) EM fields in either two-dimensional Cartesian coordinates or axially symmetric cylindrical coordinates [34,35]. The original Superfish codes were written by Ronald Holsinger in collaboration with Klaus Halbach [36], who developed the theory, in the 1970s. The package was produced by Los Alamos National Laboratory (LANL), which is operated by the University of California for the U.S. Department of Energy. For several years, the Los Alamos Accelerator Code Group (LAACG) maintained a standard version of Superfish for Cray, UNIX, and VAX machines. A PC version was created in 1985 when Lloyd M. Young adapted an older Cray version to run on IBM-PC compatible computers. A major revision (Version 5) commenced in 1992 and the codes have been under nearly continuous development since that year. The latest version is Superfish 7.18 that was published on 2nd February 2007 and can be downloaded free of cost from the website of LANL (http://laacg1.lanl.gov/laacg/services/download_sf.phtml), as was done for use in this project. The first stage of solving an RF cavity problem in Superfish is to describe the cavity layout in a manner which can be utilized as input for solution of the Helmholtz equation. Regions containing different materials, such as air, sapphire and PTFE in the SDR being analysed, must be identified and the material properties (i.e. ε and μ) stated [35]. The Superfish codes run in the following order:

- Automesh
- Fish, CFish
- WSFplot
- SF7

Automesh, the Superfish Mesh Generator, is the first code for Superfish problems. Its input is a user-written text file, containing the regions and material properties mentioned above. Automesh sets up the mesh data, and then generates and optimizes the triangular mesh for all the RF field solvers including Fish, CFish and the tuning programs. Fish solves problems with real fields while CFish is a version of Fish that uses complex variables for the fields, permittivity and permeability. They must be run after Automesh to determine the resonant frequencies in RF cavities [34]. The Superfish code and postprocessors were written chiefly for problems with cylindrical symmetry, thereby implying that only one half of the problem geometry needs to be specified in the input file. In cylindrical coordinates, Fish and CFish

find solutions for the TM modes; however, Superfish can also solve for TE modes if the user merely interchanges the roles of $\underline{E}$ and $\underline{H}$ and applies the appropriate boundary conditions. This entails swapping the material properties ε and μ in the text input file for Automesh. Moreover, as Superfish problems use the horizontal (i.e. x) axis for the axis of symmetry, x and y coordinate axes for the problem cavity have to be exchanged as well. Since the axially symmetric SDR was employed in $TE_{01\delta}$ mode, cylindrical coordinate system was used for its Superfish simulation and the text file (see Appendix B) was written accordingly. Also because only real variables for permittivity and permeability were used, Fish was run following which, WSFplot was executed to plot the electric field pattern for the $TE_{01\delta}$ resonant mode of SDR, as illustrated in Figure 4.10.

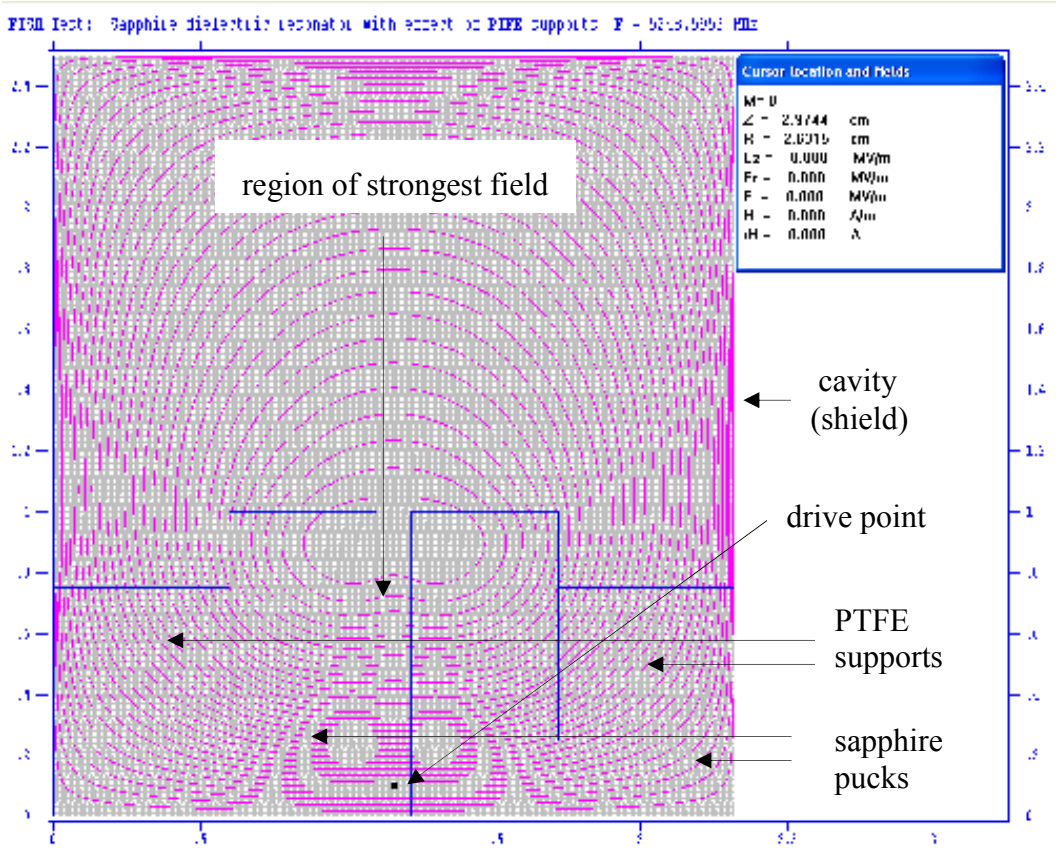

Figure 4.10. The $TE_{01\delta}$ electric field pattern in SDR as simulated in Superfish. The strongest field is in the region between radii of 7 mm and 8 mm on the sapphire rings.

The contours shown in Figure 4.10 are those of constant $r.\underline{H}$. As expected the field is much more concentrated within the sapphire pucks ac compared to the air region around them. The

value of f_0 obtained from Superfish simulation was 5.25 GHz, which is very nearly the same as that measured using a VNA.

4.5.3 **Calculation of Unloaded *Q* Using Mathcad**

The output results from Fish are read by postprocessor SF7, which allows the interpolation of fields at various points. For the TE mode problem geometries, SF7 calculates the field components at a large number of user defined points, which are then numerically integrated to compute quantities such as energy stored in the cavity and conductor losses on the wall of shield. SF7 writes file OUTSF7.TXT that contains a table of fields at the requested coordinates *r* and *z* (or *x* and *y*) coordinates[‡]. For RF problems in cylindrical coordinates the code reports E_z, E_r, E and H_ϕ, which have to be converted to their complementary quantities (i.e. H_z, H_r, H and E_ϕ) as the SF7 solution consists of the magnetic field. In this project, results from OUTSF7.TXT file were input into a MathCAD code (see Appendix C) that worked out the conductor, dielectric and overall unloaded quality factors of the SDR after requisite conversion of field parameters. The calculated Q_U value by Mathcad is around 34,400, which after figuring in the SDR *IL* of -22.5 dB, reduces to approximately 31,800 for the Q_L. The actual measured Q was about 28,500 i.e. a difference of roughly 12.5% from the theoretically predicted result. The reason behind this is that the calculated Q value assumes $\tan\delta \approx 10^{-5}$. A slight enhancement of this loss value and the surface resistance of the copper provide exact match with the experimental value of Q. The $\underline{E}$ and $\underline{H}$ field contours for SDR, as plotted by Mathcad, are shown in Figures 4.11 and 4.12, respectively.

[‡] In Superfish, the cylindrical coordinates are designated as *z*, *r*, and ϕ as against the normal convention of *z*, ρ, and ϕ adapted by most standard texts.

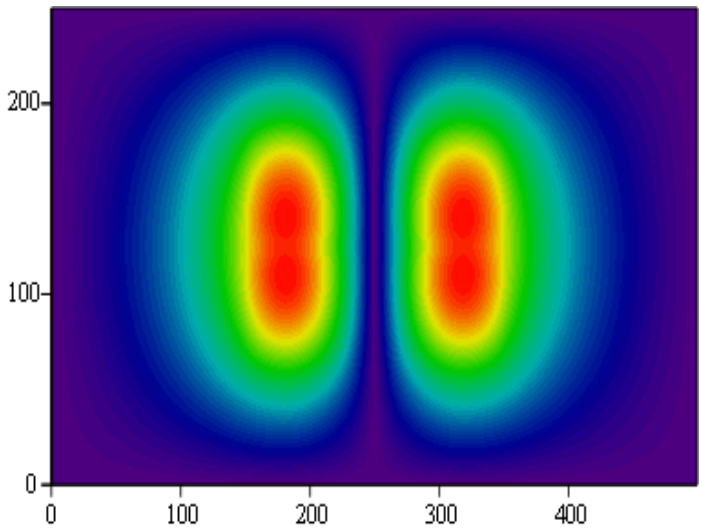

Figure 4.11. *E* field contours in SDR worked out by Mathcad, plotted against the cavity diameter expressed in terms of the number of points, N = 250. There are 500 points along the *x* axis as N corresponds to the cavity radius (see Appendix C).

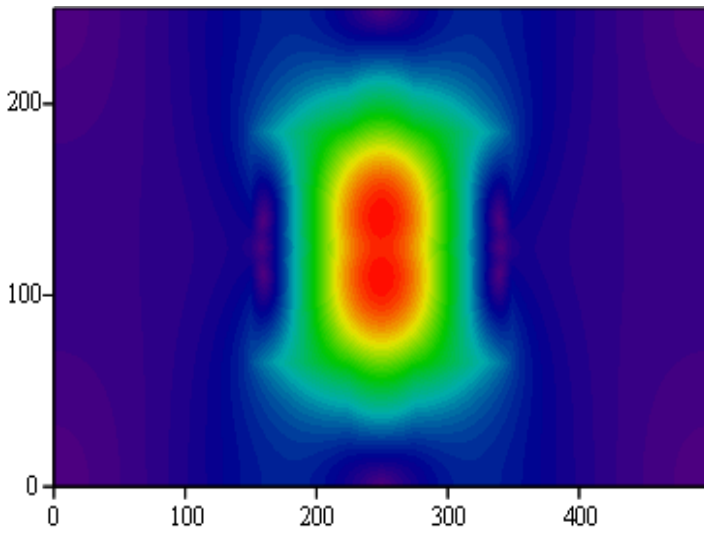

Figure 4.12. *H* field contours in SDR worked out by Mathcad, plotted against the cavity diameter expressed in terms of the number of points.

References

[1] A. Porch, *Private Communications*, 2008.

[2] D. M. Pozar, *Microwave Engineering*, Third Edition, John Wiley & Sons, N.Y., 2005, ISBN 0-471-44878-8.

[3] P. A. Anderson, A. R. Armstrong, A. Porch, P. P. Edwards and L. J. Woodall, "Structure and Electronic Properties of Potassium-Loaded Zeolite L", *Journal of Physical Chemistry B*, Vol. 101, No. 48, pp. 9892-9900, 1997.

[4] R. Göritz, A. Masood, O. Castell, D. A. Barrow, C. Allender and A. Porch "Microwave Compositional Analysis of Solvent Matrices in Microcapillary Manifold Systems", *The Proceedings of MicroTAS 2007 Conference*, Paris, pp.1689-1691, October 2007.

[5] R. Göritz, "Evaluation of the Dielectric Properties and the Mixing Ratio of Aqueous Liquids using Microwave Resonators and a Coaxial Probe", *Final Year Project Report*, Elektrotechnik, Diplom, Cardiff University, Cardiff School of Engineering, 10 May 2006.

[6] W. N. Hardy and L. A. Whitehead, "Split-ring Resonator for use in Magnetic Resonance from 200-2000 MHz", *Review of Scientific Instruments*, Vol. 52, No. 2, pp. 213-216, February 1981.

[7] W. Froncisz and James S. Hyde, "The Loop-Gap Resonator: A New Microwave Lumped Circuit ESR Sample Structure", *Journal of Magnetic Resonance*, Vol. 47, pp. 515-521, 1982.

[8] M. Mehdizadeh, T. K. Ishii, J. S. Hyde and W. Froncisz, "Loop-Gap Resonator: A Lumped Mode Microwave Resonant Structure", *IEEE Transactions on Microwave Theory and Techniques*, Vol. MTT-31, No. 12, pp. 1059-1064, December 1983.

[9] M. Mehdizadeh and T. K. Ishii, "Electromagnetic Field Analysis and Calculation of the Resonance Characteristics of the Loop-Gap Resonator", *IEEE Transactions on Microwave Theory and Techniques*, Vol. MTT-37, No. 7, pp. 1113-1118, July 1989.

[10] A. Masood, O. Castell, D. A. Barrow, C. Allender and A. Porch, "Split Ring Resonator Technique for Compositional Analysis of Solvents in Microcapillary Systems", *The Proceedings of MicroTAS 2008 Conference*, San Diego, pp.1636-1638, October 2008.

[11] D. Kajfez and P. Guillon (Editors), *Dielectric Resonators*, Second Edition, Noble Publishing Corporation, Atlanta, 1998, ISBN 1-884932-05-3.

[12] S. Ramo, J. R. Whinnery, and T. V. Duzer, *Fields and Waves in Communication Electronics*, Third Edition, John Wiley & Sons, N.Y., 1994, ISBN 978-81-265-1525-7.

[13] A. Okaya and L.F. Barash, "The Dielectric Microwave Resonator", *Proceedings of the Institute of Radio Engineers*, Vol. 50, pp. 2081-2092, October 1962.

[14] R. D. Richtmyer, "Dielectric Resonator", *Journal of Applied Physics*, Vol. 10, p. 391, June 1939.

[15] S. B. Cohn, "Microwave Bandpass Filters Containing High-Q Dielectric Resonators", *IEEE Transactions on Microwave Theory and Techniques*, Vol. MTT-16, No. 4, pp. 218-227, April 1968.

[16] W. H. Harrison, “A Miniature High-Q Bandpass Filter Employing Dielectric Resonators”, *IEEE Transactions on Microwave Theory and Techniques*, Vol. MTT-16, No. 4, pp. 210-218, April 1968.

[17] M. W. Pospieszalski, “Cylindrical Dielectric Resonators and Their Applications in TEM Line Microwave Circuits”, *IEEE Transactions on Microwave Theory and Techniques*, Vol. MTT-27, No. 3, pp. 233-238, March 1979.

[18] R.G. Carter, *Electromagnetic Waves - Microwave Components and Devices*, Chapman and Hall, London, 1990, ISBN 0-442-31183-4.

[19] J. C. Sethares and S.J. Naumann, “Design of Microwave Dielectric Resonators”, *IEEE Transactions on Microwave Theory and Techniques*, Vol. MTT-14, No. 1, pp. 2-7, January 1966.

[20] M.E. Tobar, J.G. Hartnett, D. Cros, P. Blondy, J. Krupka, E.N. Ivanov and P. Guillon, “Design of High-Q Frequency-temperature Compensated Dielectric Resonators”, *Electronics Letters*, Vol. 35, No. 4, pp. 303-305, February 1999.

[21] J. J. Wingfield, J. R. Powell, C. E. Gough and A. Porch, “Sensitive Measurement of the Surface Impedance of Superconducting Single Crystals using a Sapphire Dielectric Resonator”, *IEEE Transactions on Applied Superconductivity*, Vol. 7, No. 2, pp. 2009-2012, June 1997.

[22] J. Krupka, M. Klinger, M. Kuhn, A. Baranyak, M. Stiller and J. Hinken, “Surface Resistance Measurements of HTS Films by Means of Sapphire Dielectric Resonators”, *IEEE Transactions on Applied Superconductivity*, Vol. 3, No. 3, pp. 3043-3048, September 1993.

[23] J. Krupka, K. Derzakowski, A. Abramowicz, J. Baker-Jarvis, R. Ono and R. Geyer, “Surface Impedance of Thin High Temperature Superconducting Films with a Sapphire Dielectric Resonator”, *The Proceedings of 14th International Conference on Microwaves, Radar and Wireless Communications*, Vol. 2, pp. 391-393, May 2002.

[24] M. M. Driscoll, J. T. Haynes, R. A. Jelen, R. W. Weinert, J. R. Gavaler, J. Talvacchio, G. R. Wagner, K. A. Zaki and X. Liang, “Cooled, Ultrahigh Q, Sapphire Dielectric Resonators for Low-Noise, Microwave Signal Generation”, *IEEE Transactions on Ultrasonics, Ferroelectrics, and Frequency Control*, Vol. 39, No. 3, pp. 405-411, May 1992.

[25] K. A. Zaki and X. Liang, “Higher Order Modes, High Q Dielectric Resonators for Oscillator Applications”, *Proceedings of the 1992 IEEE Frequency Control Symposium*, pp. 163-166, May 1992.

[26] V. Giordano , R. Barhaila, D. Cros, G. Duchiron, “High - Q Si02 Whispering Gallery Mode Resonator”, *Proceedings of the 1999 Joint Meeting of the European Frequency and Time Forum and the IEEE International Frequency Control Symposium*, Vol. 2, pp. 593-596, April 1999.

[27] S. Fiedziuszko and A. Jeleński, “Comments on ‘The Dielectric Microwave Resonator’”, *Proceedings of the* IEEE, Vol. 58, pp. 992–993, June 1970.

[28] S.Fiedziuszko and A. Jeleński, “The Influence of Conducting Walls on Resonant Frequencies of the Dielectric Microwave Resonator”, *IEEE Transactions on Microwave Theory and Techniques*, Vol. MTT-19, p. 778, September 1971.

[29] H. Y. Yee, "Natural Resonant Frequencies of Microwave Dielectric Resonators", *IEEE Transactions on Microwave Theory and Techniques*, Vol. MTT-13, p. 256, March 1965.

[30] J. Liang, C. Wag, Q. Sun, K. A. Zaki and R. W. Weinert, "Supporting Structures Effects on High Q Dielectric Resonators for Oscillator Applications", *Proceedings of the 1994 IEEE International Frequency Control Symposium*, pp. 478-481, June 1994.

[31] M. E. Tobar, J. Krupka, E. N. Ivanov and R. A. Woode, "Dielectric Frequency Temperature Compensation of High Quality Sapphire Dielectric Resonators", *Proceedings of the 1996 IEEE International Frequency Control Symposium*, pp. 799-806, June 1996.

[32] B. Riddle, J. Baker-Jarvis and J. Krupka, "Complex Permittivity Measurements of Common Plastics over Variable Temperatures", *IEEE Transactions on Microwave Theory and Techniques*, Vol. 51, No. 3, pp. 727-733, March 2003.

[33] A. N. Luiten, A. G. Mann and D. G. Blair, "Ultrahigh Q-Factor Cryogenic Sapphire Resonator", *Electronics Letters*, Vol. 29, No. 10, pp. 879-881, May 1993.

[34] M. T. Menzcl and H. K. Stokes, "User's Guide for the Poisson/Superfish Group of Codes", *Accelerator Theory and Simulation Group, AT-6, Los Alamos National Laboratory*, January 1987.

[35] Reference Manual for the Poisson/Superfish Group of Codes, *Los Alamos Accelerator Code Group, MS H829, Los Alamos National Laboratory*, January 1987.

[36] K. Halbach and R. F. Holsinger, "SUPERFISH - A Computer Program for Evaluation of RF Cavities with Cylindrical Symmetry", *Particle Accelerators*, Vol. 7, pp. 213-222, 1976.

CHAPTER 5

COMPOSITIONAL ANALYSIS OF SOLVENTS IN MICROCAPILLARY SYSTEMS

5.1 Introduction

The theories of dielectric polarisation and resonator perturbation were covered in chapter 2 while the three types of microwave resonators employed in this project were described in detail in chapter 4. These concepts were then applied to microcapillary contained dielectric samples placed perpendicular to high microwave electric fields and the expected variations of the resonant frequency and quality factor were plotted. An essential part of this research was to corroborate the validity of the theoretical predictions by experimental methods. In this regard, in-situ compositional analysis of solvent matrices in microcapillary manifold systems was carried out in each of the three resonators. The microcapillaries were placed in region of high electric field in the resonators and Agilent (HP) 8753E VNA (hereafter called VNA) was employed to measure power transmission coefficient $|S_{21}|^2$ in the frequency domain. The VNA was interfaced through an IEEE-488 bus – also known as General Purpose Interface Bus (GPIB) – to a computer running IGOR Pro software i.e. a scientific data analysis and programming software tool made by Wavemetrics Inc., Oregon, USA. The in-built Lorentzian curve fitting of IGOR Pro was used to extract the microwave parameters of interest (i.e. Q_L, f_0 and f_B) from the VNA data. For this purpose, the IGOR Pro code written by Dr. Jonathan Lees (Research Associate, Cardiff School of Engineering) and Christopher Roff (Ph.D. Student, Cardiff School of Engineering) for use with Agilent (HP) 8510C VNA was suitably modified (see Appendix D).

Before start of actual experiments, a trial was conducted on the empty hairpin resonator to determine the measurement accuracy of IGOR Pro code. It transpired that the most accurate results were obtained when firstly, the frequency span (i.e. the difference between start and stop frequency) on the VNA was set to twice the resonator bandwidth and secondly, the $|S_{21}|^2$ plot was symmetrical with respect to f_0. The number of sweep points was also varied between 51 and 1601 to establish the effect on measured Q_L, f_0 and f_B, which revealed negligible difference over the whole range. Consequently, 51 sweep points (unless

otherwise stated) were used for making the analysis fast (≈ 0.1 s). The initial evaluation system for compositional analysis experiments was made of acetonitrile and toluene, selected due to the large difference in their molecular electric dipole moments [1]. The results obtained from this first system provided the motivation to evaluate mixtures made of acetonitrile and water, which are much more closely matched in terms of their electric dipole moments. Three sets of experiments were performed for both solution systems on each resonator and five measurements per solution were taken in each set, to bear out the repeatability of results.

5.2 The Acetonitrile:toluene Solution System

Acetonitrile (also known as Methyl cyanide or MeCN) is a polar solvent whereas toluene is non-polar at microwave frequencies. The results of compositional analysis of this solution system using the hairpin resonator were originally reported in the MicroTAS 2007 conference [1]. Only four solutions were investigated therein (i.e. 100% acetonitrile, 75:25, 50:50, 25:75 and 100% toluene) and their complex relative permittivity was first measured in the range 2.5 – 3 GHz using a coaxial reflectance probe. The data at 2.68 GHz, appropriate for the hairpin measurements, are shown in Figure 5.1.

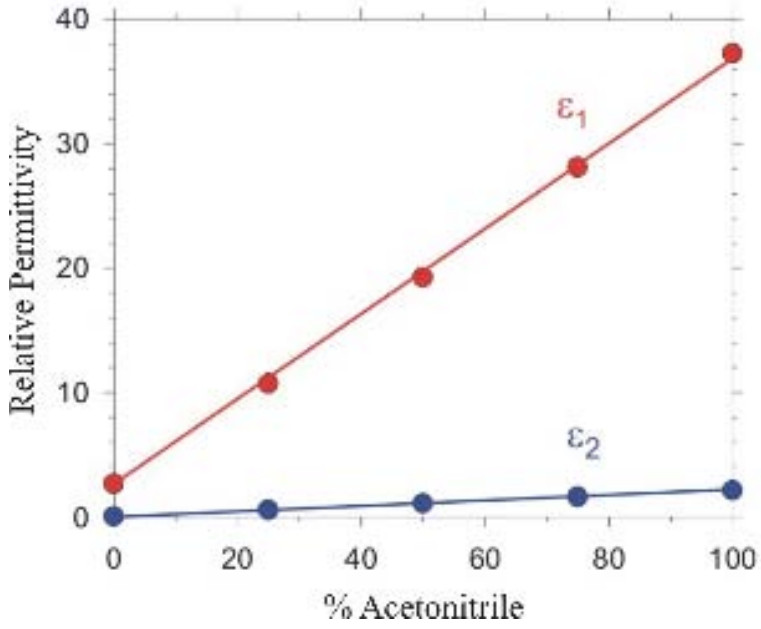

Figure 5.1. The polarisation ε_1 and loss ε_2 terms at 2.68 GHz of the relative permittivity of an acetonitrile:toluene mixture. Solid lines are the predictions of a simple linear mixing rule.

The results of the coaxial probe experiment provide the mixture dielectric constant and loss at the two extremes (i.e. $\varepsilon_1 \approx 37, \varepsilon_2 \approx 2$ for 100% acetonitrile and $\varepsilon_1 \approx 2.5, \varepsilon_2 = 0$ for 100% toluene). It is also evident from Figure 5.1 that the measured complex permittivity closely follows a simple linear mixing rule of the form $\varepsilon = (1-\beta)\varepsilon_A + \beta\varepsilon_B$, where $\varepsilon_A = \varepsilon_{A1}$ is the permittivity for the lossless solvent phase (i.e. toluene) and $\varepsilon_B = \varepsilon_{B1} - j\varepsilon_{B2}$ for the lossy phase (i.e. acetonitrile) [2]. In order to have a more complete analysis for this thesis, seventeen compositions of the acetonitrile:toluene system – ranging from 0% to 100% acetonitrile– were prepared [2,3]. However, since the mixing rule presented above was found to be very precise, the results of Figure 5.1 were considered sufficient for use with the seventeen-component solution system. For making up the solutions, HPLC* grade acetonitrile (99.99% pure, Fisher Scientific UK Ltd., Leicestershire) and toluene (99.8% pure**,** Acros Organics, New Jersey, USA) were mixed in requisite proportions using three Gilson Pipetman® (Gilson Inc., Wisconsin, USA) adjustable pipettes of different maximum capacities i.e. 5 ml, 1 ml and 200 µl. The main physical properties and specifications of acetonitrile and toluene are listed in Appendix E. The solutions were prepared in 50 ml quantity each and stored in 125 ml airtight jars (Fisher Scientific) to ensure long-term contamination free storage. The volumes of MeCN and toluene needed to make the solutions were worked out beforehand in MS Excel (see Appendix F). For conduct of experiments, a KD Scientific dual syringe pump (KD Scientific Inc., Massachusetts, USA) was used to drive BD Discardit™ II 10 ml disposable syringes (procured from Fisher Scientific) that were connected via luer adapter, fingertight fitting and/or appropriate sleeve to the fluid-carrying microcapillaries. The flow rate on pump was set to 1 ml/min; however, it had been established through prior trials that changes in flow rate did not effect the measurements.

5.2.1 **Hairpin Experiments**

The hairpin resonator was the starting point for compositional analysis experiments in this project. The solutions were made to flow in a microcapillary made of polyetheretherketone (PEEK) that is a semi crystalline thermoplastic. PEEK was chosen because of its flexibility, excellent mechanical and chemical resistance properties and ease of availability [2,3]. All

* HPLC stands for high performance liquid chromatography and these are high purity solvents.

PEEK microcapillaries used in this research were manufactured by Upchurch Scientific and acquired from its UK distributor, Kinesis based in Cambridgeshire**.** About a 20 cm long segment of the 1 mm ID and 1.58 mm OD capillary was cut using PEEK Tubing Cutter (Sigma-Aldrich Corp.). It passed through the open-end of the hairpin, where the microwave electric field is largest and approximately uniform in magnitude and perpendicular to the microcapillary axis (see Figure 5.2). Since the electric field decays very rapidly with distance outside of the hairpin plates, the measurement provided the average dielectric properties of the liquid contained in the 20 mm long section of capillary between the plates, corresponding to an active liquid volume of approximately 15 μl [1]. The microcapillary was connected to the syringe via a luer lock adapter and a fingertight fitting.

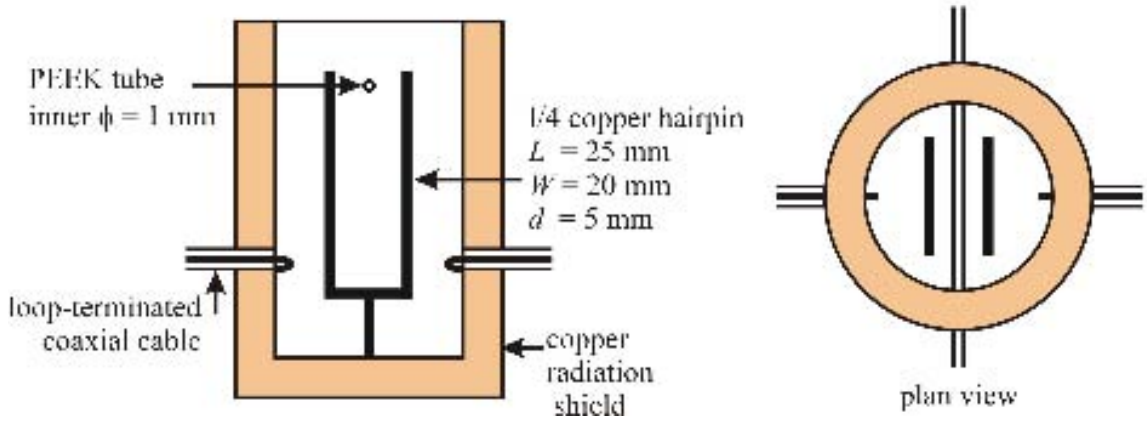

Figure 5.2. A schematic diagram of the hairpin resonator with fluid sample carrying PEEK microcapillary positioned at the region of maximum $\underline{E}$ field at the open end of resonator.

The mean results for the three sets of experiments are as shown in Table 5.1.

Solution		Mean Results (29 Aug 08)			Mean Results (12 Sep 08)			Mean Results (21 Sep 2008)		
% Toluene	% MeCN	f_0 (GHz)	f_B (MHz)	Q_L	f_0 (GHz)	f_B (MHz)	Q_L	f_0 (GHz)	f_B (MHz)	Q_L
100	0	2.671	1.669	1600	2.671	1.665	1604	2.668	1.651	1617
99.9	0.1	2.671	1.686	1585	2.671	1.672	1598	2.668	1.667	1601
99	1	2.670	1.803	1481	2.670	1.794	1488	2.667	1.791	1489
97.5	2.5	2.669	1.934	1380	2.669	1.905	1401	2.667	1.903	1401
95	5	2.666	2.138	1247	2.667	2.113	1262	2.664	2.114	1260
90	10	2.664	2.315	1151	2.663	2.352	1132	2.662	2.263	1176
82.5	17.5	2.661	2.389	1114	2.661	2.409	1104	2.659	2.349	1132
75	25	2.658	2.354	1129	2.658	2.390	1112	2.657	2.375	1119
50	50	2.656	2.056	1292	2.653	2.185	1214	2.651	2.143	1237
25	75	2.654	1.891	1403	2.652	2.031	1305	2.651	1.906	1391
17.5	82.5	2.654	1.844	1440	2.650	2.023	1310	2.649	1.944	1363
10	90	2.654	1.839	1443	2.652	1.896	1399	2.650	1.867	1419
5	95	2.650	1.998	1327	2.652	1.890	1403	2.647	1.931	1371
2.5	97.5	2.653	1.819	1459	2.650	1.951	1358	2.650	1.812	1462
1	99	2.652	1.842	1440	2.650	1.979	1339	2.649	1.833	1445
0.1	99.9	2.653	1.863	1424	2.651	1.856	1428	2.651	1.799	1473
0	100	2.651	1.867	1419	2.652	1.845	1438	2.650	1.803	1470
Sensitivity (MHz/μl)		1.33			1.27			1.20		
Empty Capillary		2.681	1.567	1711	2.680	1.585	1691	2.677	1.559	1717

Table 5.1. Measured Q_L, f_0 and f_B for the acetonitrile:toluene solution system in the hairpin resonator along with the measurement sensitivity obtained.

The sensitivity of frequency measurement over the complete range of solutions, calculated using the relation, $f_{0(max)} - f_{0(min)}/V_l$, where V_l is the active liquid volume is also tabulated in units of MHz/μl. It would serve as a ready reference for comparing the results attained with different resonator systems. The variation of resonant frequency, loaded quality factor and bandwidth against the solution composition is plotted in Figures 5.3 through 5.5.

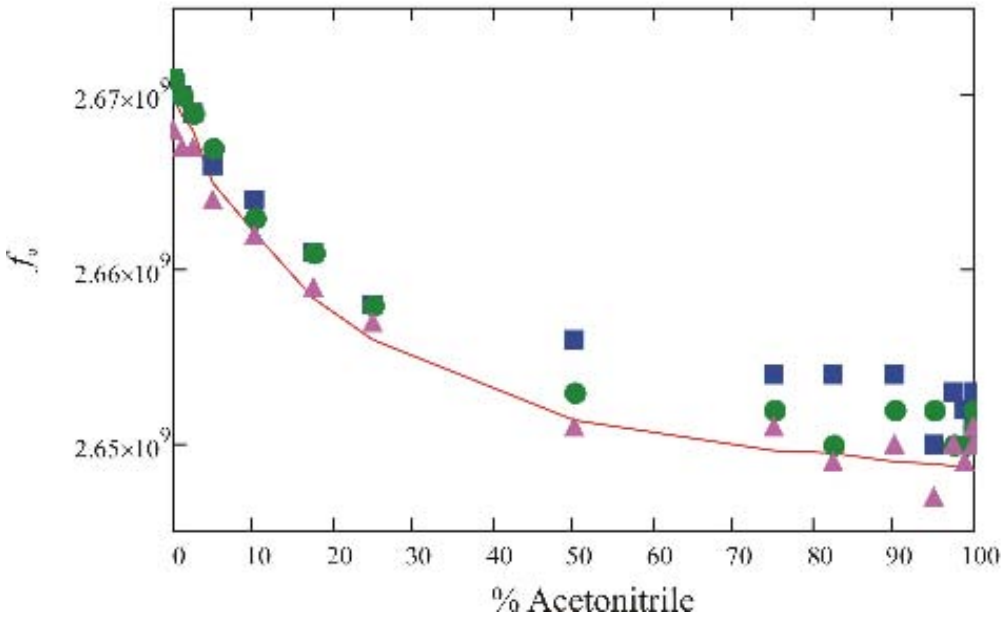

Figure 5.3. The resonant frequency as a function of solution composition for the acetonitrile:toluene system in hairpin resonator. The three sets of experiments are shown by the markers while the red line is the theoretical prediction from resonator perturbation analysis plotted using Mathcad.

.

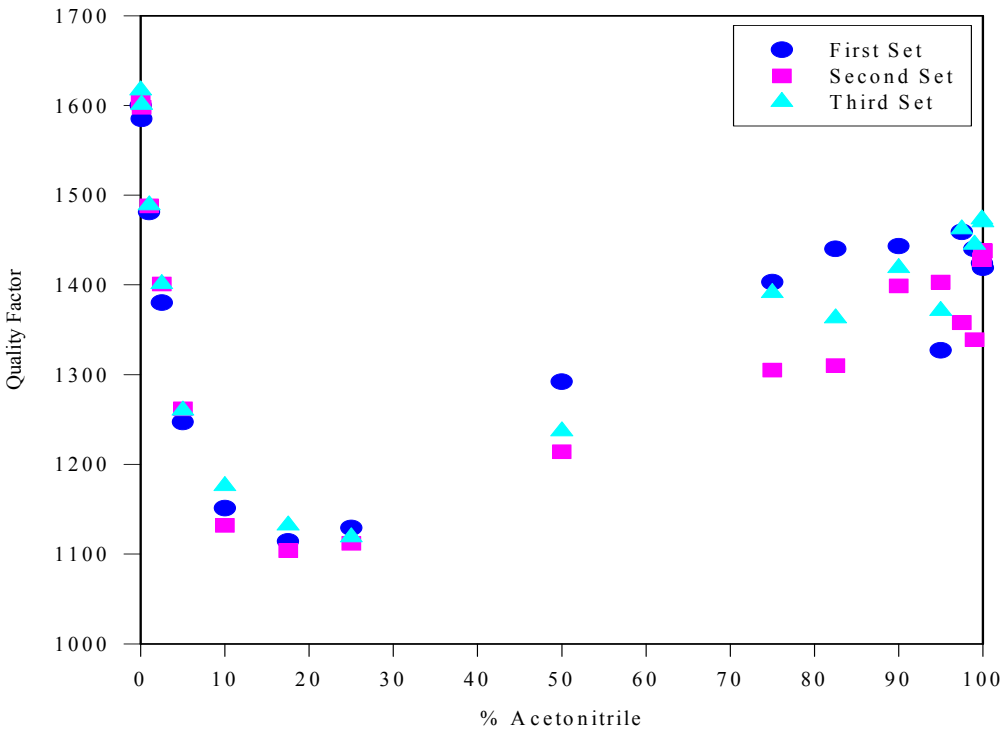

Figure 5.4. The loaded quality factor as a function of solution composition for the acetonitrile:toluene system in hairpin resonator.

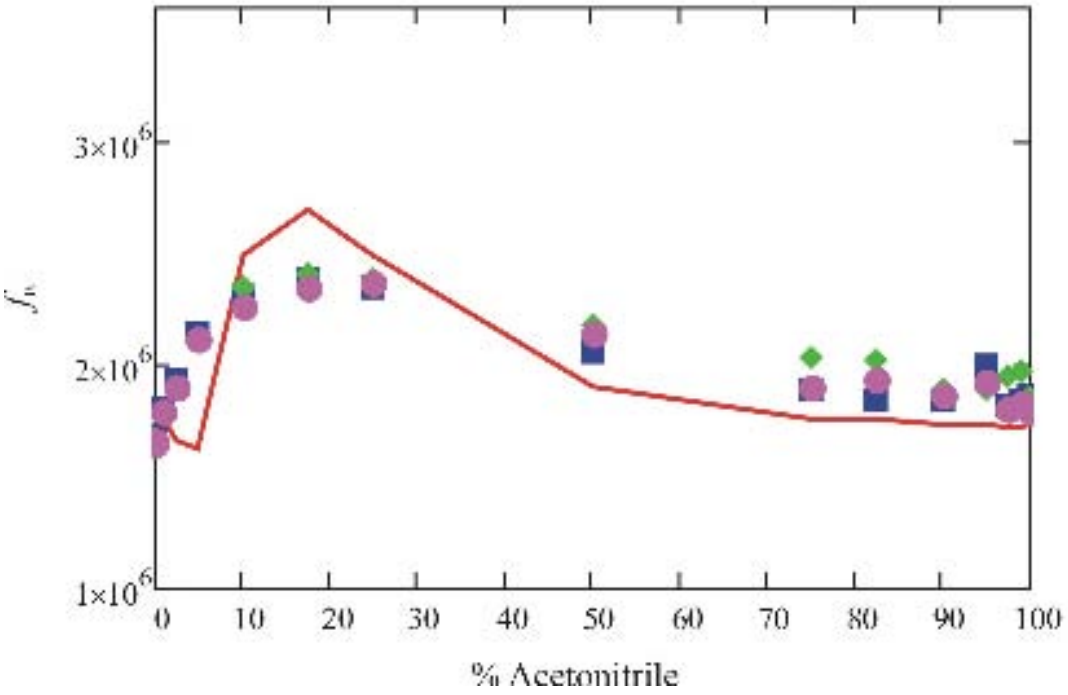

Figure 5.5. The bandwidth as a function of solution composition for the acetonitrile:toluene system in hairpin resonator. The red line is the theoretical prediction from resonator perturbation analysis.

The resonant frequency decreased monotonically as the polar nature of the solvent mix increases, which is in agreement with the theoretical prediction of resonator perturbation theory as shown by the red line in Figure 5.3. The loaded quality factor was minimized (i.e. bandwidth maximized) for small proportions of acetonitrile (≈17%), as observable in Figures 5.4 and 5.5. This rather unusual result was predicated by theory in chapter 2 (see Figure 2.7) and is again shown by the red line of Figure 5.5. It physical interpretation is the competition between the increased dielectric loss and the reduced internal electric field (by depolarization) within the solvent mixture as the proportion of acetonitrile was increased. The theoretical fits of Figure 5.3 and 5.5 were done in Mathcad using equations (9), (12) and (22) of chapter 2. The sensitivity of frequency measurement was about 1.30 MHz/μl, which is fairly high because of the small effective volume (V_{eff} ≈ 1 ml) of the hairpin i.e. half the total hairpin volume due to the non-uniform distribution of electric field across its length (see equation (9), chapter 2 and Figure 4.2) [1,2]. Nonetheless, measurement sensitivity for this solution system could be increased substantially by using the split ring resonator, which has a much smaller V_{eff}.

5.2.2 **Split Ring Experiments**

Ten mixtures of acetonitrile in toluene were measured for the data presented at the MicroTAS 2008 conference, again using a coaxial reflectance probe to establish the variation of complex permittivity with composition. The results relevant to the split ring resonator (i.e. at 3.4 GHz) are presented in Figure 5.6 and it is again obvious that they follow the predictions of a simple linear mixing rule stated in paragraph 5.2.

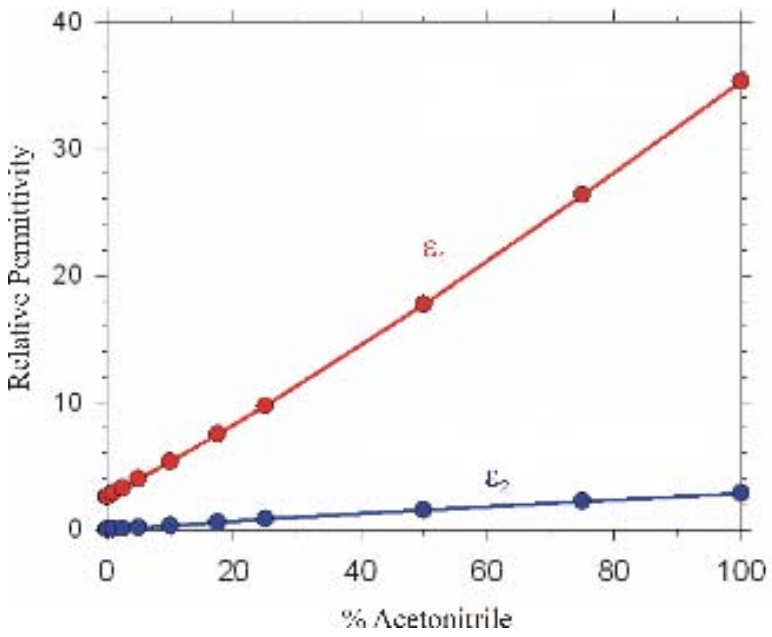

Figure 5.6. The polarisation ε_1 and loss ε_2 terms at 3.4 GHz of the complex permittivity of 10 acetonitrile:toluene solutions. Solid lines are the predictions of a simple linear mixing rule.

For compositional analysis experiments, the only change in the measurement setup from hairpin resonator was that smaller PEEK microcapillary of 360 μm OD and 150 μm ID was used, necessitated by the 400 μm gap width. As illustrated in Figure 5.7, the 30 cm long microcapillary passed through holes drilled in the top and bottom lids of the brass shield and the resonator gap, where the microwave electric field is uniform and perpendicular to its axis. The microcapillary was connected to the syringe via a luer lock adapter, a PEEK sleeve and a fingertight fitting. The aforementioned dimensions of the microcapillary imply an active liquid volume of approximately 50 nl [4].

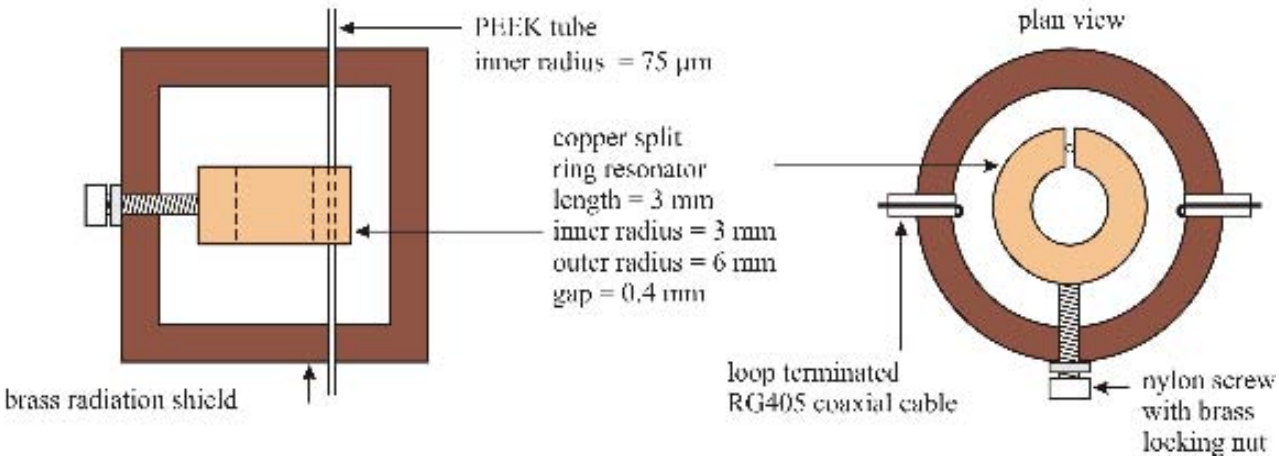

Figure 5.7. Schematic diagram of the split ring hairpin resonator package used for compositional analysis of acetonitrile:toluene solution system.

Given that the split ring gap was machined mechanically, it was not uniform across the resonator thickness of 3 mm implying potential inaccuracies in measured results, caused by placement of the capillary at different lateral positions in the gap. An initial experiment was thus conducted with a view to determining the differences in Q_L, f_0 and f_B values obtained from lateral insertion of the tubing through five different gap positions. The outcome of this experiment pointed out negligible dependence of microwave parameters of interest on the lateral positioning of the tubing in the resonator gap. However, care was taken to place the capillary in the middle of the gap in all solution measurements to avoid fringing electric fields. Moreover, it had been observed during the hairpin experiments (as well as earlier) that the results were strongly temperature dependent. The VNA was situated in a non temperature-controlled environment and on very warm days, its behaviour was found to be totally unpredictable resulting in non-reproducible measurements. Foregoing in view, the temperature during the conduct of all remaining compositional analysis experiments was monitored using a Kane-May KM340 digital thermometer (Comark Co., Hertfordshire, UK). The summarised results for the acetonitrile:toluene solutions on the split ring resonator are given in Table 5.2.

Solution		Mean Results (10 Nov 08)			Mean Results (17 Nov 08)			Mean Results (20 Nov 2008)		
% Toluene	% MeCN	f_0 (GHz)	f_B (MHz)	Q_L	f_0 (GHz)	f_B (MHz)	Q_L	f_0 (GHz)	f_B (MHz)	Q_L
100	0	3.448	4.031	855	3.437	4.241	810	3.438	4.269	805
99.9	0.1	3.448	4.053	851	3.437	4.301	799	3.438	4.340	792
99	1	3.445	4.487	768	3.434	4.762	721	3.435	4.803	715
97.5	2.5	3.443	4.874	706	3.432	5.153	666	3.433	5.152	666
95	5	3.437	5.753	597	3.426	6.117	560	3.426	6.102	562
90	10	3.430	6.589	521	3.419	6.941	493	3.419	6.929	494
82.5	17.5	3.420	7.217	474	3.408	7.711	442	3.408	7.695	443
75	25	3.413	7.170	476	3.400	7.757	438	3.400	7.763	438
50	50	3.401	6.383	533	3.388	6.872	493	3.387	6.923	489
25	75	3.395	5.589	607	3.380	6.134	551	3.389	5.992	566
17.5	82.5	3.395	5.438	624	3.384	5.802	583	3.388	5.827	581
10	90	3.393	5.313	639	3.383	5.685	595	3.387	5.559	609
5	95	3.393	5.229	649	3.384	5.522	613	3.386	5.504	615
2.5	97.5	3.394	5.145	660	3.385	5.474	618	3.386	5.417	625
1	99	3.392	5.149	659	3.386	5.401	627	3.386	5.361	632
0.1	99.9	3.391	5.094	666	3.385	5.281	641	3.386	5.322	636
0	100	3.391	5.031	674	3.380	5.390	627	3.386	5.330	635
Sensitivity (MHz/μl)		1140			1140			1040		
Empty Capillary		3.466	3.579	969	3.461	3.708	933	3.463	3.709	934
Temperature		19 - 21 °C			20 - 21 °C			21 - 22 °C		

Table 5.2. Q_L, f_0 and f_B results for the acetonitrile:toluene solution system in the split ring resonator along with the measurement sensitivity obtained and temperature variation during the experiments.

The variation of resonant frequency, loaded quality factor and bandwidth against the solution composition is plotted in Figures 5.8 through 5.10.

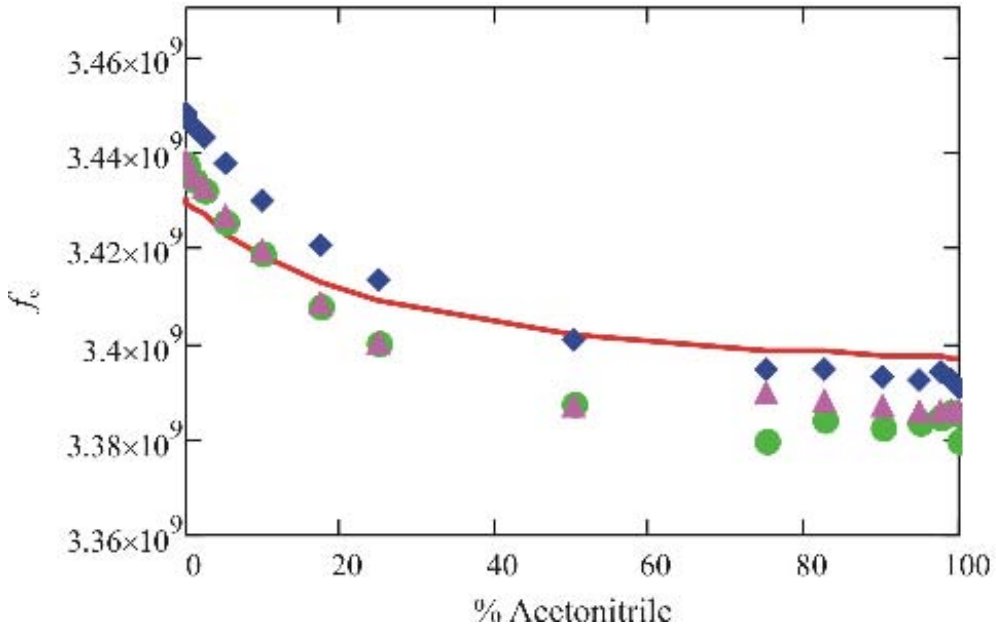

Figure 5.8. The resonant frequency as a function of solution composition for the acetonitrile:toluene system in split ring resonator. The red line is the theoretical prediction from resonator perturbation analysis.

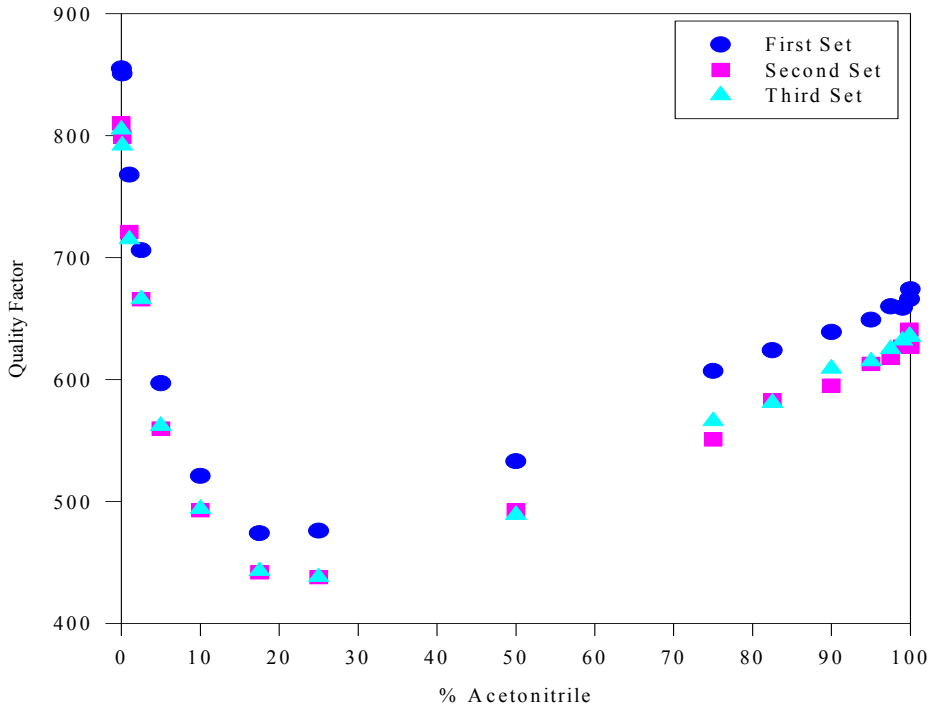

Figure 5.9. The quality factor as a function of solution composition for the acetonitrile:toluene system in split ring resonator. The red line is the theoretical prediction from resonator perturbation analysis.

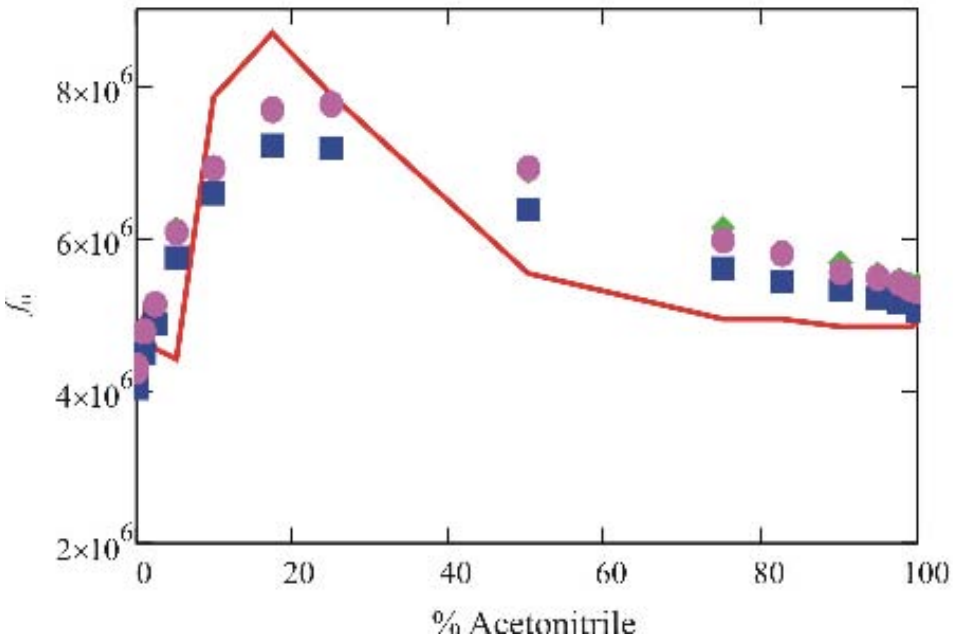

Figure 5.10. The bandwidth as a function of solution composition for the acetonitrile:toluene system in split ring resonator. The red line is the theoretical prediction from resonator perturbation analysis.

The results for the split ring follow the same trend as for those obtained with the hairpin as a consequence of the electric field being perpendicular to the microcapillary. However, the measurement sensitivity of about 1140 MHz/μl is almost 1000 times greater in this case owing to the very small $V_{eff} \approx 3.6$ μl for the split ring resonator[†]. Another notable difference is that the repeatability of measurements is much better here, especially for higher proportions of acetonitrile. The slight variations in results can be attributed to temperature variations over the course of experiments, as inferred from the empty capillary data. The predictions of resonator perturbation theory are in conformity with the measured results, as observable from the red lines of Figures 5.8 and 5.10. The moderate disparity in theory and experiments for both split ring and hairpin resonators is probably due to the reason that complex permittivity data for ten solution compositions was used instead of the actual seventeen measured.

[†] The effective volume for the split ring resonator is the same as the total gap volume because of the uniform microwave electric field across the gap.

5.2.3 **SDR Experiments**

It is evident from the hairpin and split ring resonators' results discussed so far that their perpendicular microwave electric field causes depolarisation of the fluid sample, thus reducing the internal electric field within it. However, the $TE_{01\delta}$ resonant mode operating SDR has electric field purely parallel with respect to its axis and a circular channel can be machined into one or both of the pucks. The electric field is parallel everywhere to this channel and thus the induced electric dipole moment will be maximised for this field orientation, since no depolarisation occurs. From Superfish simulation of the SDR, the electric field was found to be strongest in the region between radii of 7 mm and 8 mm on the sapphire rings (see Figure 4.10), which is where the circular duct should be situated. Nevertheless, before machining the channel an initial test was carried out to confirm this theoretical prediction using the acetonitrile:toluene solution system as follows.

5.2.3.1 **PEEK Microcapillary Measurements**

A section of the PEEK microcapillary used for experimentation on the split ring resonator was placed in the form of a circular loop within the region of maximum electric field on the bottom sapphire puck in the SDR. In order to ensure that it stays at the correct position throughout the conduct of experiment, the microcapillary was secured to the puck outside the maximum field region with a piece of adhesive tape. One set of measurements was performed as before and the obtained results indicated that there was no sample depolarisation, since Q_L decreased monotonically with increasing percentage of acetonitrile in the solution mix. The resonant frequency was also consistently reduced with increased proportion of acetonitrile. Although this proof of principle experiment validated the theoretical prediction of resonator perturbation theory yet the rather crude setup employed therein was likely to be prone to errors and a more rigorous apparatus was needed to reach an unambiguous conclusion. An apparent course of action would have been milling a circular duct in the region of maximum electric field on the pucks. Fluid samples flowing through the duct could then be characterised; however, this approach was discarded so as to preserve the resonator in its originality for use in research elsewhere. It was instead decided to machine the duct in the region of high electric field on a disc of an appropriate material using the 'Xtreme' laser facility available in Cardiff School of Engineering. A fluid carrying microcapillary could than

be placed inside the duct before inserting the sample in the resonator gap for compositional analysis [2,3].

5.2.3.2 **Selection of Material**

Direct testing was conducted to select the most suitable material i.e. the disc was placed inside the resonator gap and Q_L was measured. The materials tested are as depicted in Table 5.3; the Q_L value for the empty resonator here was approximately 28,500.

Material	Q_L
Glass (Microscope slides)	250
Silicon	359
Pyrex	622
Sapphire[‡]	29,000
PEEK	5,600
PTFE	12,200
Alumina	18,900
Fused Silica	9,480
Teflon® AF	26,500

Table 5.3. Q_L values for various material samples placed in SDR gap

Quite obviously, sapphire emerges as the obvious candidate for use as the base material for machining of the micro channel while Teflon® AF is a close second. However, Teflon® AF was preferred because of the following two reasons [2,3,5]:

- Sapphire is a very hard and brittle material and so quite difficult to laser machine. The minimum dimensions of the duct for this particular application would have to about 400 μm × 400 μm[§] so as to accommodate the smallest available PEEK microcapillary of 360 μm OD. Trying to ablate a sapphire disk for attaining the aforementioned size of duct had the potential to break it during the laser ablation process. On the other hand Teflon® AF is an amorphous fluoropolymer having considerable strength,

[‡] Sapphire gives a larger Q since $\langle U \rangle$ is greater in presence of the sapphire sample, and $Q \propto \langle U \rangle$.

[§] It is much easier to laser machine a channel of square cross section as compared to a circular one [4].

thereby offering it comparative advantage for the laser machining of channel. Additionally, Teflon® AF has the lowest dielectric constant (≈ 1.9) of any known fluoropolymer and low loss tangent (≈ 10^{-4}) [6].

- In place of PEEK, a compatible Teflon® AF microcapillary could be used for compositional analysis experiments.

5.2.3.3 **Teflon® AF Measurements**

In view of the above, it was decided to go ahead with laser machining of the requisite channel on Teflon® AF. Two discs of 30 mm diameter and 1.32 mm thickness each were on hand in the Applied Microfluidics Laboratory of Cardiff School of Engineering. As regards availability of appropriate microcapillary, DuPont – the manufacturer of Teflon® AF resin – holds patents and requires research license for purchase of its articles from authorized suppliers. Accordingly, two research licenses were obtained from DuPont and 2 metres length of the thinnest available Teflon® AF tubing (0.5 mm OD and 0.25 mm ID) was acquired from Biogeneral Inc., California, USA. A duct of dimensions slightly bigger than 500 μm × 500 μm was then laser machined on one of the Teflon® AF discs within the maximum electric field region by Neil Sykes (manager and senior process engineer for the laser facility). A photograph of the machined disc is shown in Figure 5.11.

Figure 5.11. Laser machined channel in the region of high electric field on Teflon® AF disc.

The second Teflon® AF was to act as a top cover for the machined disc, in order to ensure that the microcapillary stays inside the channel. The introduction of both discs in the SDR

gap required its height to be increased, which was correspondingly made 2.8 mm by inserting 1.6 mm thick copper shims between the two halves of the copper shield. This caused a small reduction in empty resonator quality factor, to about 27,500, nonetheless permitting placement of the discs between the pucks with which a Q of around 22,000 was measured. Subsequently Teflon® AF microcapillary was put snugly inside the duct on the machined disc that was covered with the other disc. Both discs were then placed in position in the reconfigured SDR (i.e. with increased gap) and the acetonitrile:toluene solution system was measured, with results as expressed in Table 5.4. The microcapillary was connected to the syringe via a luer lock adapter, a sleeve made out of bigger silicone tubing and a fingertight fitting.

Solution		**Mean Results (2 Dec 08)**			**Mean Results (4 Dec 08)**			**Mean Results (5 Dec 08)**		
% Toluene	**% MeCN**	f_0 **(GHz)**	f_B **(MHz)**	Q_L	f_0 **(GHz)**	f_B **(MHz)**	Q_L	f_0 **(GHz)**	f_B **(MHz)**	Q_L
100	0	5.2705	0.2895	18207	5.2705	0.2988	17639	5.2701	0.3088	17065
99.9	0.1	5.2705	0.2933	17970	5.2705	0.3021	17444	5.2700	0.3123	16876
99	1	5.2704	0.3058	17233	5.2705	0.3161	16676	5.2700	0.3273	16104
97.5	2.5	5.2703	0.3361	15679	5.2704	0.3286	16038	5.2700	0.3389	15552
95	5	5.2702	0.3743	14082	5.2703	0.3683	14308	5.2698	0.3773	13968
90	10	5.2700	0.4216	12500	5.2701	0.4151	12695	5.2697	0.4214	12505
82.5	17.5	5.2697	0.5410	9740	5.2698	0.5311	9922	5.2693	0.5295	9951
75	25	5.2693	0.6677	7892	5.2694	0.6610	7972	5.2688	0.6537	8061
50	50	5.2679	1.0228	5150	5.2680	1.0149	5191	5.2675	0.9919	5311
25	75	5.2664	1.3247	3976	5.2665	1.3210	3987	5.2660	1.2869	4092
17.5	82.5	5.2660	1.4025	3755	5.2661	1.3896	3790	5.2656	1.3553	3886
10	90	5.2655	1.4546	3620	5.2657	1.4406	3655	5.2652	1.4021	3755
5	95	5.2652	1.4985	3514	5.2654	1.4683	3586	5.2649	1.4379	3662
2.5	97.5	5.2652	1.4834	3549	5.2653	1.4802	3558	5.2648	1.4484	3635
1	99	5.2652	1.5056	3497	5.2652	1.4912	3531	5.2648	1.4394	3658
0.1	99.9	5.2652	1.4933	3526	5.2652	1.4822	3552	5.2647	1.4559	3616
0	100	5.2652	1.4724	3576	5.2653	1.4741	3572	5.2648	1.4494	3632
Sensitivity (MHz/μl)		2.16			2.16			2.16		
Empty Capillary		5.2711	0.2382	22133	5.2712	0.2378	22170	5.2706	0.2395	22002
Temperature		20 °C			20 °C			21 - 22 °C		

Table 5.4. Q_L, f_0 and f_B results for the acetonitrile:toluene solution system in the SDR along with the measurement sensitivity obtained and temperature variation during the experiments.

The coaxial probe results of Figure 5.6 were deemed fit for use with the SDR experiments as the complex permittivity of acetonitrile does not change much between 3 and 6 GHz and that of toluene is virtually constant, it being non-polar [7,8]. The variation of SDR resonant frequency, loaded quality factor and bandwidth against the solution composition is plotted in Figures 5.12 through 5.14.

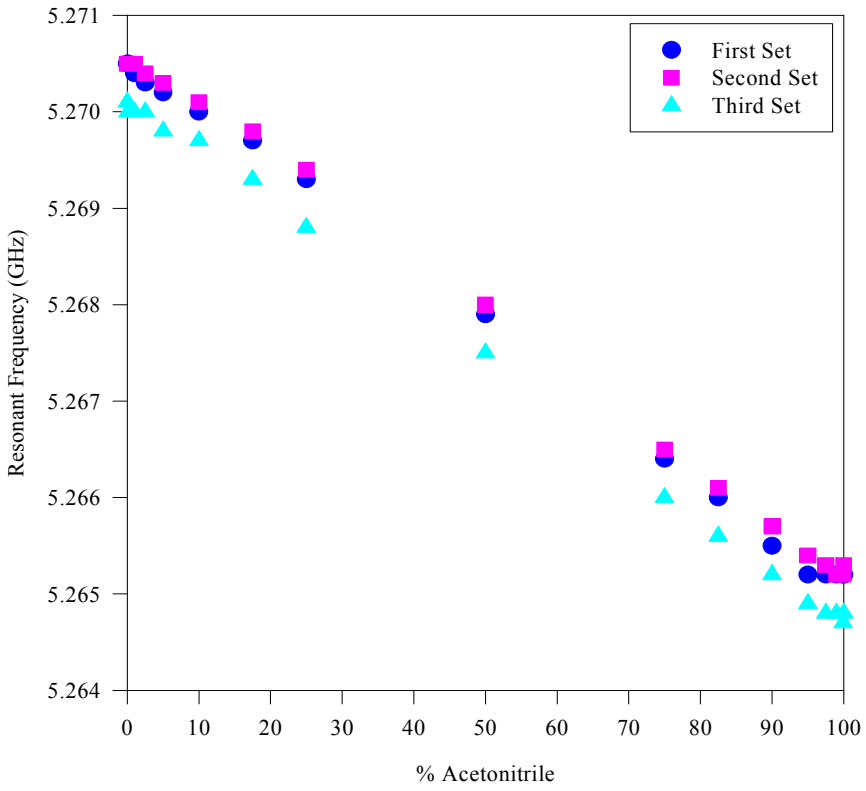

Figure 5.12. The resonant frequency as a function of solution composition for the acetonitrile:toluene system in SDR.

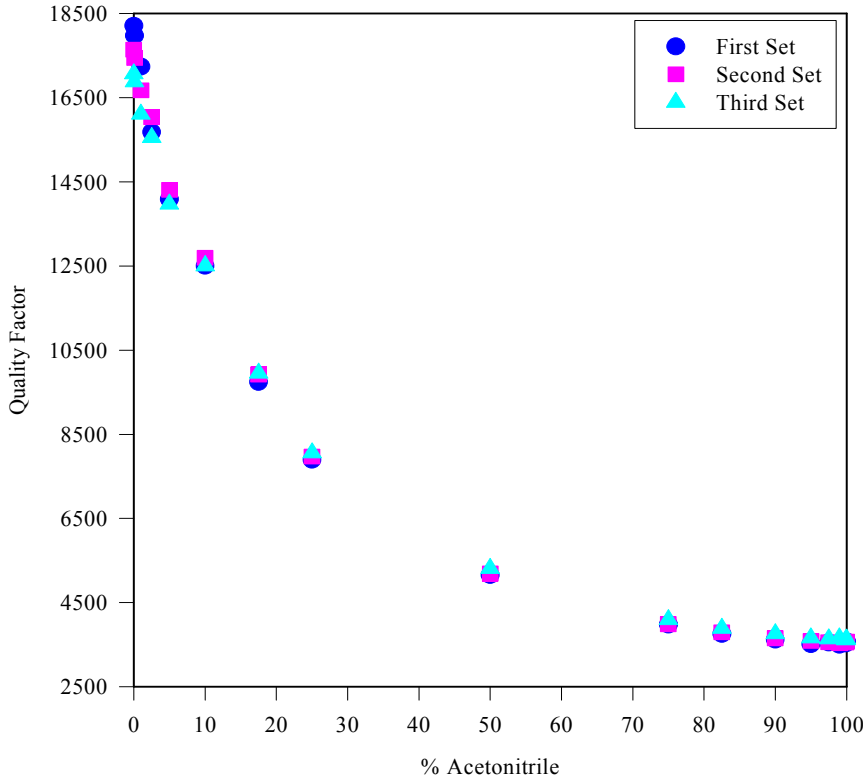

Figure 5.13. The loaded Q as a function of solution composition for the acetonitrile:toluene system in SDR.

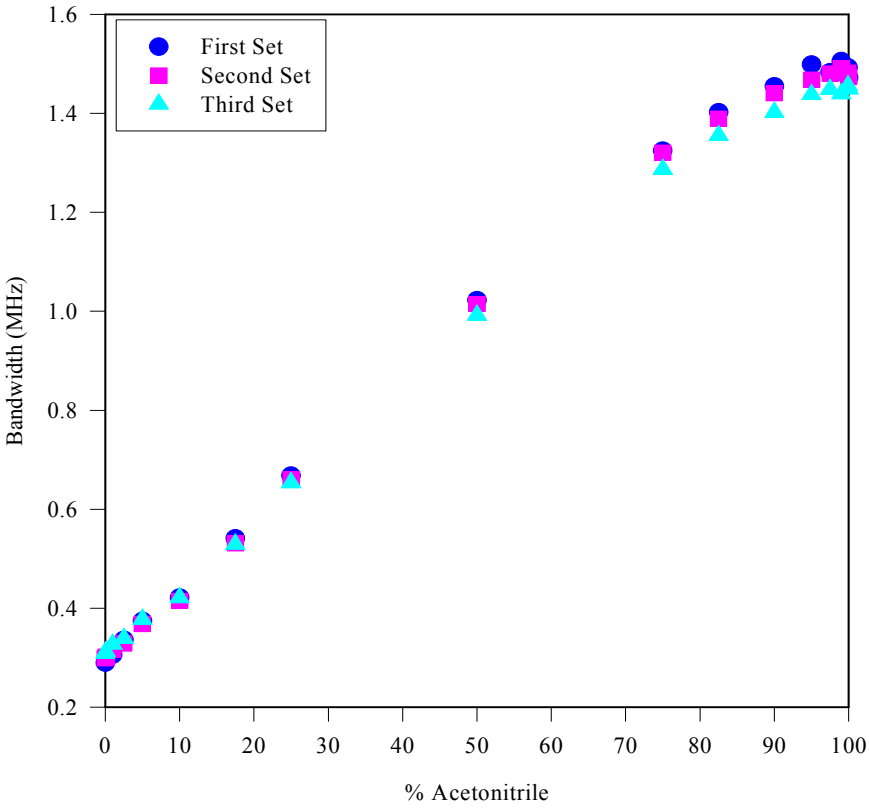

Figure 5.14. The bandwidth as a function of solution composition for the acetonitrile:toluene system in SDR.

5.2.3.4 **Analysis of Results**

The acetonitrile:toluene solution system experiments conducted in the SDR bring forth the following points:

- The results depict excellent repeatability over the three measurement sets.
- Q_L decreases monotonically (Figure 5.13) as the percentage of acetonitrile in the solution mix increases. This result is expected as acetonitrile has higher dielectric loss as compared to toluene and there is no reduction in the electric field inside the solution samples (there being no depolarisation due to the electric field parallel to the microcapillary). In this regards, the SDR is superior to the hairpin and split ring resonators, both of which exhibited reduction in internal electric field due to perpendicular direction of field relative to the microcapillary.
- The resonant frequency plotted in Figure 5.12 also constantly decreases as the polar nature of the solution increases (i.e. %age of acetonitrile becomes larger), which is again in line with resonator perturbation theory prediction. The sensitivity of measurement has been worked out for 2.31 µl active liquid volume in SDR (see Appendix K), which is about 2.16 MHz/µl. It is understandably much lower than that provided by the split ring as the effective volume for SDR is considerably higher. A Superfish simulation (see section 4.4.2) had pointed out the non-uniform distribution of microwave electric field over the surface of sapphire pucks, so the effective volume for SDR is approximately one third of the total resonator volume [2], which is about $V_{eff} = \frac{1}{3}\left(\pi a^2 l\right) = \frac{1}{3}\left(\pi\right) \approx 1$ ml i.e. about 300 times more than that of the split ring. Nonetheless, the SDR provides about twice as much sensitivity as the hairpin even though their effective volumes are approximately the same.

5.3 The Acetonitrile:water Solution System

The results obtained from the initial evaluation system show that highly sensitive compositional analysis of solvents in microcapillaries is achievable from the resonators in question, particularly the split ring. Hence, it was decided to analyse liquid mixtures whose components are more closely matched in terms of their molecular electric dipole moments. A popular solution system in this regard is acetonitrile:water (see e.g. [9]) because of room

temperature miscibility of the two solvents. This solvent mix is used commonly in applications related to the biosciences field [2]. The variation of the static dielectric constant of acetonitrile:water mixtures was measured by Gagliardi *et al*. [9] and fitted to an empirical equation as a simultaneous function of temperature and acetonitrile composition, as shown in Figure 5.15. Their results can extrapolated for use here as the complex permittivity of both water and acetonitrile does not vary much over the range 0 – 6 GHz [7,10].

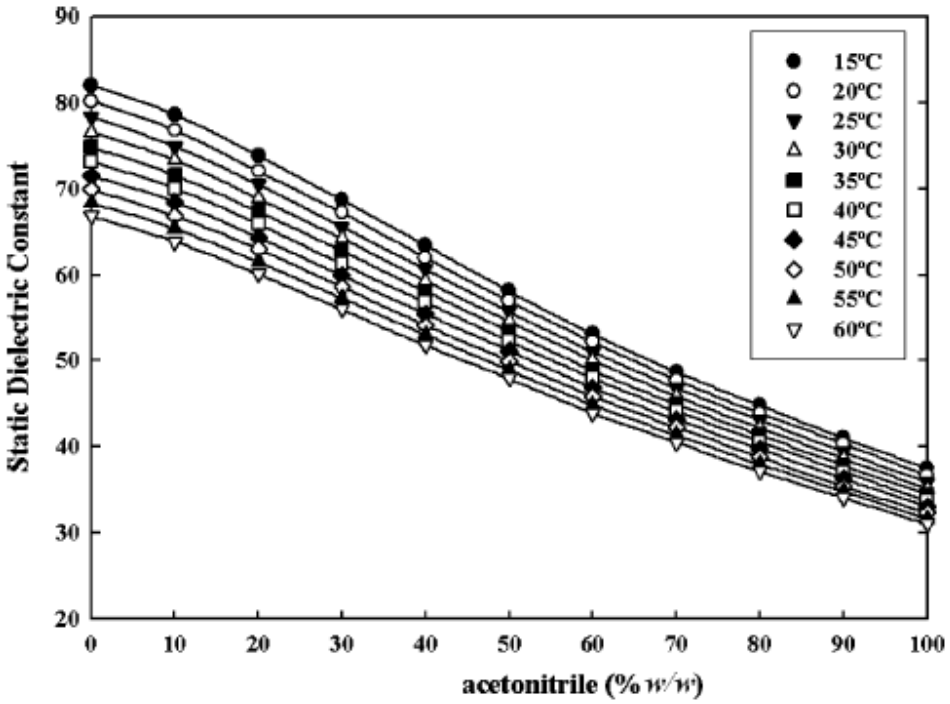

Figure 5.15. The static dielectric constants of acetonitrile:toluene mixtures at various temperatures, against acetonitrile composition in weight percent. Symbols represent experimental values and lines to predictions from an empirical equation used to fit the dielectric constant values (Reproduced from [9]).

For the sake of pedagogical completeness, it was decided to measure the solutions in all three resonator systems. Instead of making up the solutions manually, a Thermo Finnigan Surveyor® LC Pump** (Thermo Finnigan LC and LC/MS Product Group, California, USA) was used to mix the requisite volumes of HPLC grade acetonitrile (Fisher Scientific) and water (Acros Organics). The availability of Surveyor® pump in Applied Microfluidics

** The Surveyor® LC Pump is a member of the Surveyor® family of liquid chromatography (LC) instruments. It is a dual-piston, quaternary, low-pressure mixing pump with a built in vacuum degasser and pulse dampener [11].

Laboratory, which was not known at the commencement of acetonitrile:toluene experiments, proved very handy as it saved the large amount of time needed to prepare the seventeen solutions [12]. To start with, the flow rate was set to 1 ml/min and the microcapillaries were connected to the pump through the same connections as stated in the respective resonator sections on acetonitrile:toluene measurements. A photograph of the Surveyor® pump is shown in Figure 5.16.

Figure 5.16. The Surveyor® LC pump is at the bottom of stack; the solvent containing vessels are on top.

5.3.1 **Hairpin Experiments**

As before, the hairpin resonator was first in line for compositional analysis experiments on the acetonitrile:water solution system. It was found at the very beginning that the plot of $|S_{21}|^2$ data acquired in IGOR pro was very noisy (see Figure 5.17) and so did not provide the desired curve fitting accuracy. Consequently, the number of sweep points was increased from 51 points to 1601 i.e. the maximum capability of the VNA. Another modification made was reducing the flow rate to 0.75 ml/min for solutions having > 50% proportion of water. This was necessitated by the LC pump giving error message at 1 ml/min flow rate for solutions made of 75% water and above, probably due to the high viscosity of water (i.e. 1 cP at 20 °C) that made the pump pressure exceed its safe limit. Table 5.5 provides the mean results obtained for the three sets of measurements while the plots for f_0, Q_L and f_B are shown in Figures 5.18 to 5.20.

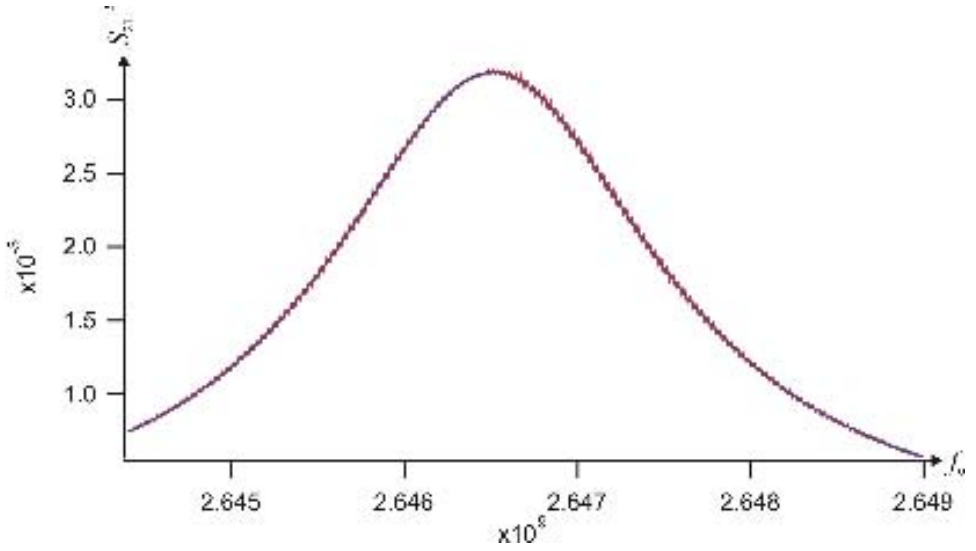

Figure 5.17. $|S_{21}|^2$ data acquired from 8753E VNA for one of the solution samples of the acetonitrile:water system measured in hairpin resonator, is curve-fitted to Lorentzian in IGOR Pro. 1601 sweep points provided the desired goodness of fit as apparent from comparison of original curve (red) to fitted curve (blue).

Solution		**Mean Results (12 Jan 09)**			**Mean Results (13 Jan 09)**			**Mean Results (14 Jan 09)**		
% Water	**% MeCN**	f_0 **(GHz)**	f_B **(MHz)**	Q_L	f_0 **(GHz)**	f_B **(MHz)**	Q_L	f_0 **(GHz)**	f_B **(MHz)**	Q_L
100	0	2.6452	2.560	1033	2.6459	2.393	1106	2.6465	2.338	1132
99.9	0.1	2.6452	2.553	1036	2.6459	2.381	1111	2.6465	2.334	1134
99	1	2.6452	2.559	1034	2.6459	2.385	1109	2.6465	2.331	1135
97.5	2.5	2.6452	2.570	1029	2.6459	2.398	1103	2.6467	2.318	1142
95	5	2.6453	2.596	1019	2.6459	2.425	1091	2.6467	2.326	1138
90	10	2.6453	2.635	1004	2.6460	2.455	1078	2.6468	2.359	1122
82.5	17.5	2.6455	2.667	992	2.6461	2.492	1062	2.6469	2.393	1106
75	25	2.6456	2.669	991	2.6462	2.499	1059	2.6470	2.394	1106
50	50	2.6463	2.529	1046	2.6468	2.404	1101	2.6475	2.310	1146
25	75	2.6471	2.268	1167	2.6481	2.130	1244	2.6481	2.131	1242
17.5	82.5	2.6474	2.162	1225	2.6484	2.056	1288	2.6483	2.056	1288
10	90	2.6477	2.045	1294	2.6486	1.966	1347	2.6486	1.961	1350
5	95	2.6479	1.968	1345	2.6488	1.905	1390	2.6488	1.891	1401
2.5	97.5	2.6480	1.937	1367	2.6489	1.879	1409	2.6489	1.867	1419
1	99	2.6480	1.920	1379	2.6489	1.868	1418	2.6490	1.853	1430
0.1	99.9	2.6481	1.912	1385	2.6489	1.860	1424	2.6490	1.845	1436
0	100	2.6481	1.898	1395	2.6490	1.846	1435	2.6491	1.833	1445
Sensitivity (MHz/μl)		0.19			0.20			0.17		
Temperature		20 °C			21 - 22 °C			21 °C		

Table 5.5. Q_L, f_0 and f_B results for the acetonitrile:water solution system in the hairpin resonator.

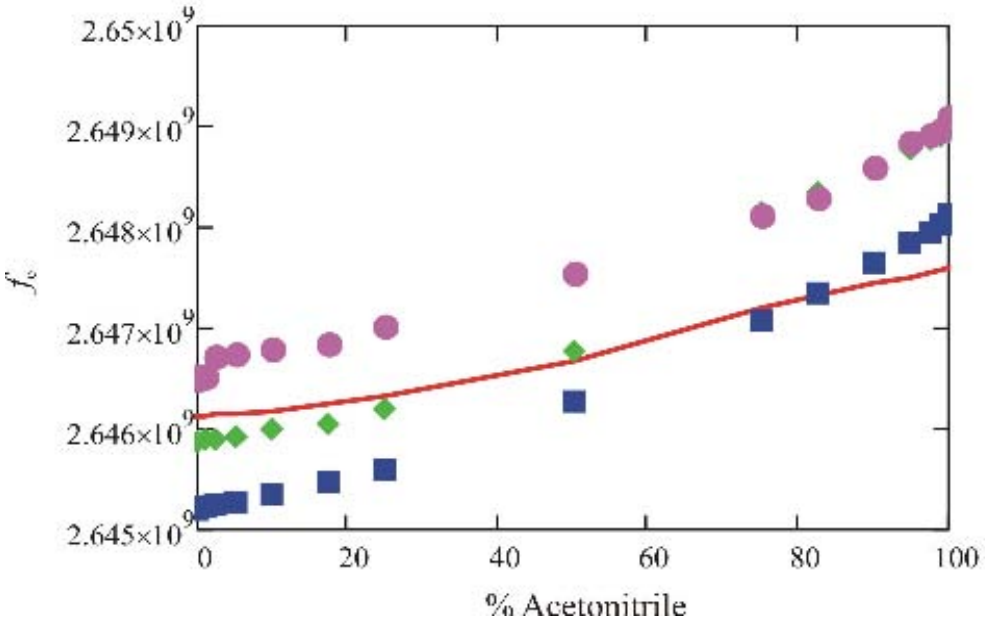

Figure 5.18. The resonant frequency as a function of solution composition for the acetonitrile:water system in hairpin resonator. The red line is the theoretical prediction from resonator perturbation analysis.

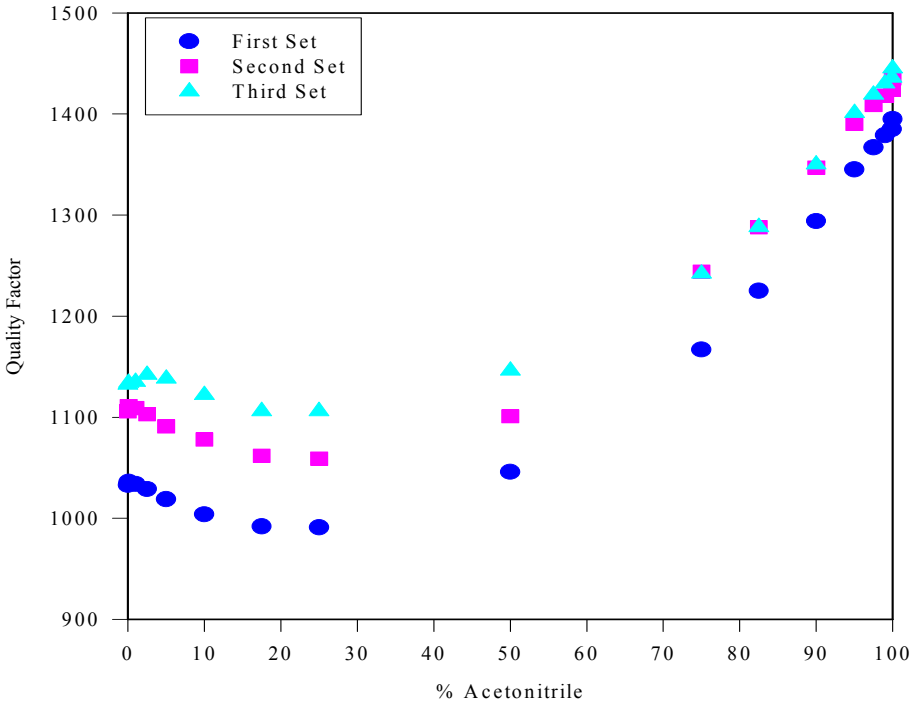

Figure 5.19. The loaded quality factor as a function of solution composition for the acetonitrile:water system in hairpin resonator. The red line is the theoretical prediction from resonator perturbation analysis.

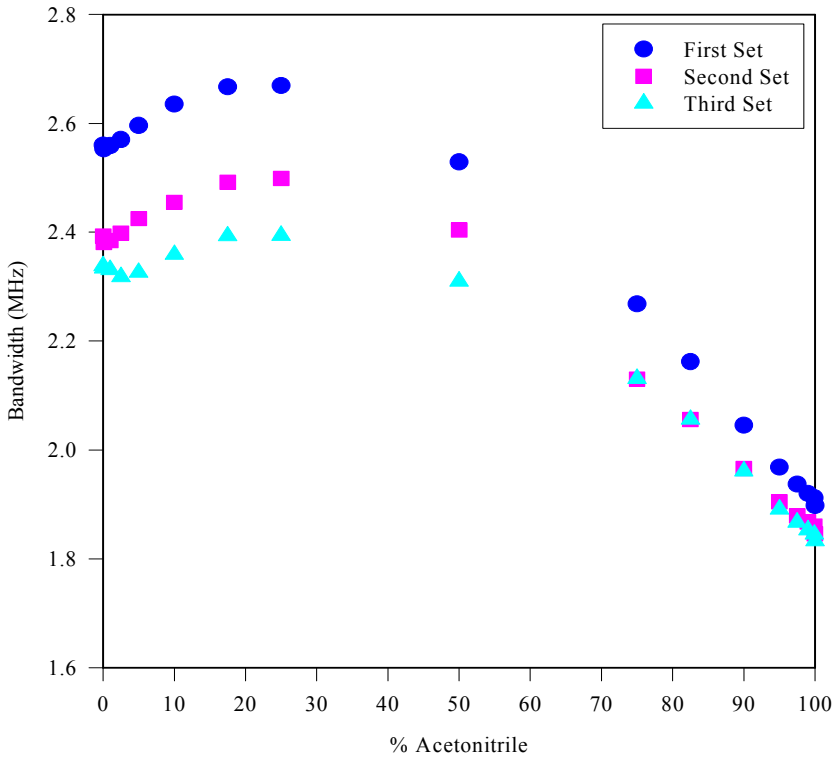

Figure 5.20. The bandwidth as a function of solution composition for the acetonitrile:water system in hairpin resonator.

There is somewhat large variation in the hairpin results for small percentages of acetnoitrile, while the data converges nicely for large proportions of it. The reason behind this is not apparent; however, quite predictably, the resonant frequency (Figure 5.18) once more decreases monotonically as the polar nature (i.e. proportion of water) of the solvent mix increases. The theoretical fit for the resonant frequency from resonator perturbation analysis is closely correlated to the experimental results but that for the bandwidth was found to show a very large difference (in Mathcad) and is therefore not shown. The most likely reason behind this is that the ε_2 data used for theoretical fit was extrapolated for the seventeen solutions from the extreme values for water and acetonitrile due to non availability of measured data. The sensitivity of frequency measurement is only about 0.20 MHz/µl because of smaller mismatch between the molecular electric dipole moments of water and acetonitrile.

5.3.2 **Split Ring Experiments**

The split ring experiments were conducted with the sweep reverted to 51 points on the IGOR code as it provided sufficiently good curve fitting results. The mean results are depicted in Table 5.6 whilst variations of f_0, Q_L and f_B are shown in Figures 5.21 through 5.23.

Solution		**Mean Results (7 Jan 09)**			**Mean Results (8 Jan 09)**			**Mean Results (9 Jan 09)**		
% Water	**% MeCN**	f_0 **(GHz)**	f_B **(MHz)**	Q_L	f_0 **(GHz)**	f_B **(MHz)**	Q_L	f_0 **(GHz)**	f_B **(MHz)**	Q_L
100	0	3.366	6.323	532	3.366	6.305	534	3.369	6.301	535
99.9	0.1	3.366	6.337	531	3.366	6.295	535	3.369	6.304	534
99	1	3.366	6.340	531	3.366	6.295	535	3.369	6.319	533
97.5	2.5	3.366	6.397	526	3.366	6.353	530	3.369	6.341	531
95	5	3.366	6.464	521	3.366	6.425	524	3.369	6.446	523
90	10	3.366	6.580	512	3.366	6.527	516	3.369	6.484	520
82.5	17.5	3.366	6.696	503	3.367	6.631	508	3.369	6.579	512
75	25	3.367	6.799	495	3.367	6.714	502	3.370	6.650	507
50	50	3.368	6.854	491	3.368	6.786	496	3.371	6.705	503
25	75	3.370	6.341	532	3.370	6.465	521	3.372	6.417	526
17.5	82.5	3.371	6.123	551	3.371	6.256	539	3.373	6.201	544
10	90	3.372	5.855	576	3.372	5.976	564	3.374	5.936	568
5	95	3.373	5.645	597	3.372	5.780	583	3.374	5.724	589
2.5	97.5	3.373	5.549	608	3.373	5.655	596	3.375	5.628	600
1	99	3.373	5.491	614	3.373	5.585	604	3.375	5.547	608
0.1	99.9	3.373	5.445	620	3.373	5.545	608	3.375	5.521	611
0	100	3.374	5.395	625	3.373	5.491	614	3.376	5.457	619
Sensitivity (MHz/µl)		160			140			140		
Temperature		21 - 22 °C			21 - 22 °C			21 - 22 °C		

Table 5.6. Q_L, f_0 and f_B results for the acetonitrile:water solution system in the split ring resonator.

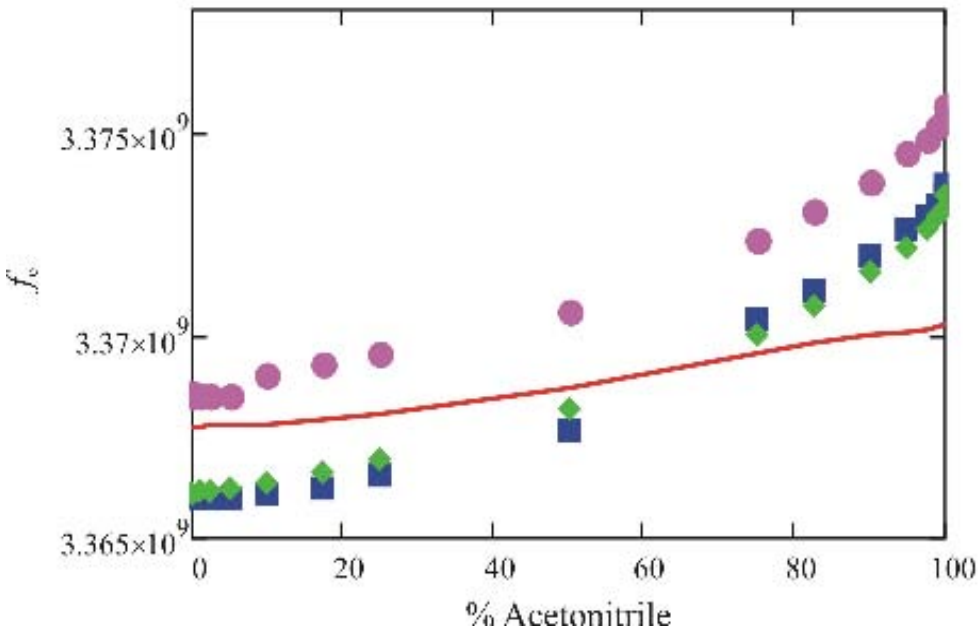

Figure 5.21. The resonant frequency as a function of solution composition for the acetonitrile:water system in split ring resonator. The red line is the theoretical prediction from resonator perturbation analysis.

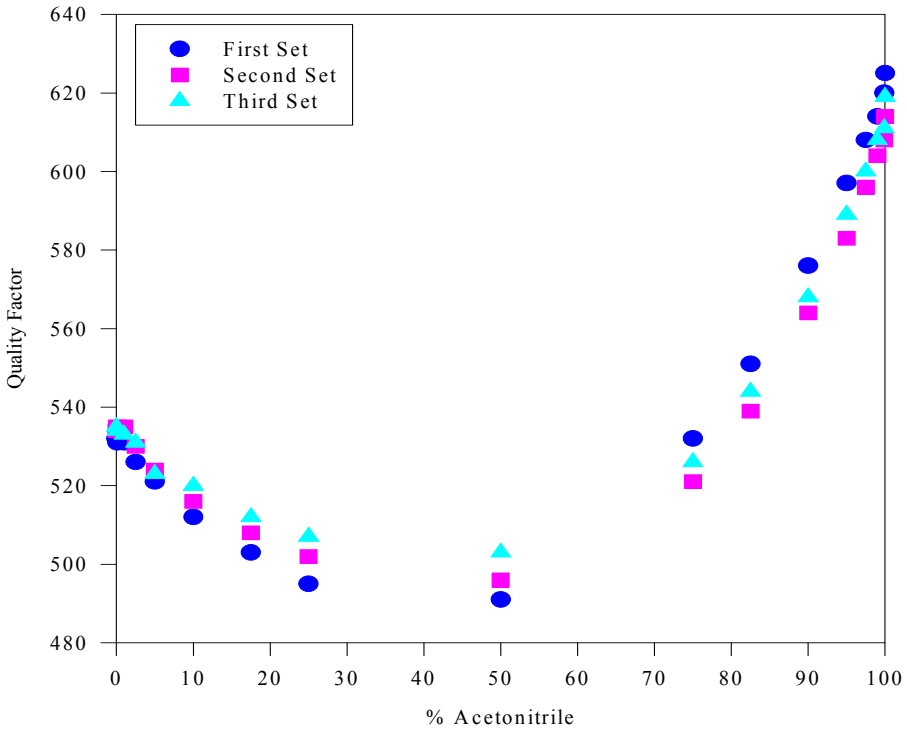

Figure 5.22. The quality factor as a function of solution composition for the acetonitrile:water system in split ring resonator.

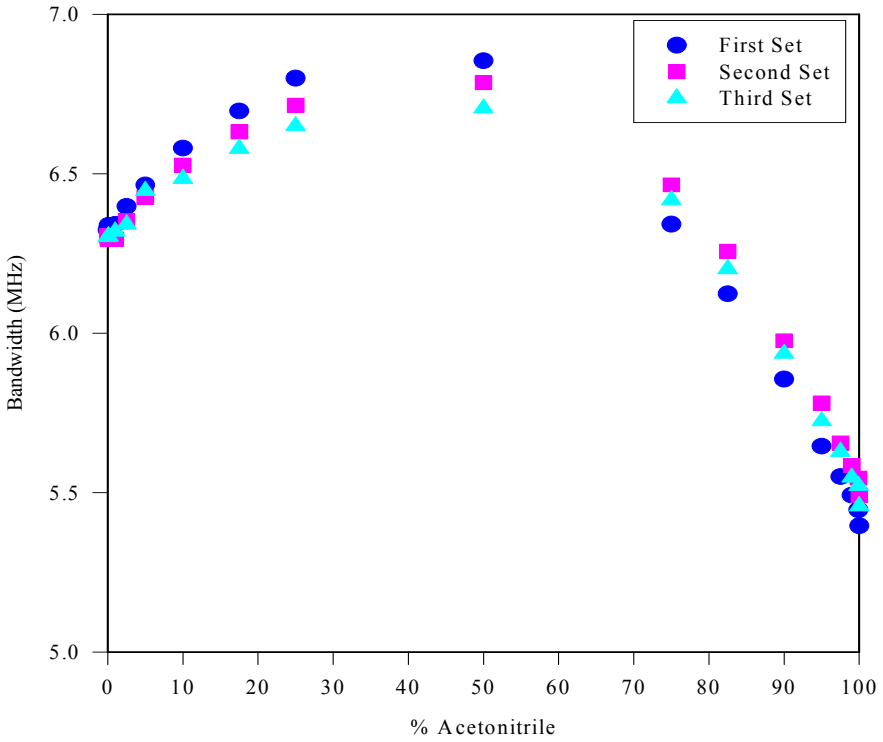

Figure 5.23. The bandwidth as a function of solution composition for the acetonitrile:water system in split ring resonator.

The split ring results follow exactly the same trend as obtained earlier for the hairpin albeit with a considerable improvement in sensitivity of frequency measurement as well as reproducibility of results, especially for solutions with high proportions of water. Again, the resonator perturbation analysis fit for f_0 is in agreement with the experimental results but that for the bandwidth was found to show a very large divergence, because of non availability of reliable loss factor data.

5.3.3 **SDR Experiments**

For the conduct of acetonitrile:water solution system on the SDR, the sweep had to be reset to 1601 points as the $|S_{21}|^2$ plots were very noisy probably because of the low Q values, as illustrated in Figure 5.24.

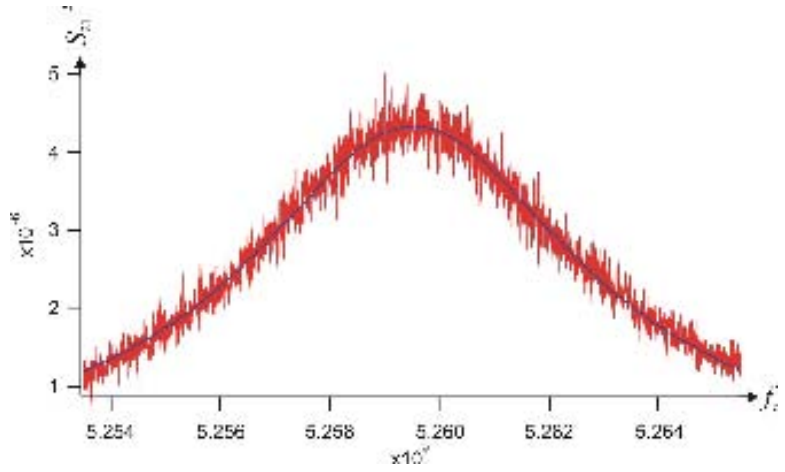

Figure 5.24. The very noisy $|S_{21}|^2$ data for the acetonitrile:water system as measured in SDR, is nicely curve-fitted to Lorentzian in IGOR Pro using 1601 sweep points.

The summarized results for the three data sets are shown in Table 5.7 whilst variations of f_0, Q_L and f_B are plotted in Figures 5.25 through 5.27.

Solution		**Mean Results (29 Dec 08)**			**Mean Results (31 Dec 08)**			**Mean Results (5 Jan 09)**		
% Water	**% MeCN**	f_0 **(GHz)**	f_B **(MHz)**	Q_L	f_0 **(GHz)**	f_B **(MHz)**	Q_L	f_0 **(GHz)**	f_B **(MHz)**	Q_L
100	0	5.2604	7.8533	670	5.2601	7.4898	702	5.2596	7.4662	705
99.9	0.1	5.2606	7.8243	672	5.2601	7.3951	711	5.2596	7.3911	712
99	1	5.2606	7.9250	664	5.2603	7.4921	702	5.2596	7.4967	702
97.5	2.5	5.2602	7.8163	673	5.2604	7.4869	703	5.2596	7.5222	699
95	5	5.2608	7.6995	683	5.2604	7.5087	701	5.2598	7.6862	684
90	10	5.2608	7.6601	687	5.2612	7.1026	741	5.2601	7.5529	697
82.5	17.5	5.2615	7.1958	731	5.2609	7.2714	724	5.2603	7.5370	698
75	25	5.2619	7.2477	726	5.2614	6.9681	755	5.2608	7.1071	740
50	50	5.2629	5.6652	929	5.2629	5.2498	1003	5.2624	5.4498	966
25	75	5.2651	3.2134	1639	5.2644	3.3167	1587	5.2643	3.4142	1542
17.5	82.5	5.2654	2.6545	1984	5.2649	2.7711	1900	5.2648	2.8016	1879
10	90	5.2658	2.0995	2508	5.2654	2.1776	2418	5.2652	2.2125	2380
5	95	5.2661	1.8163	2899	5.2658	1.8396	2863	5.2656	1.8686	2818
2.5	97.5	5.2663	1.6655	3162	5.2660	1.6547	3183	5.2658	1.7249	3053
1	99	5.2664	1.5761	3342	5.2662	1.5871	3318	5.2659	1.6555	3181
0.1	99.9	5.2666	1.5394	3421	5.2663	1.5251	3453	5.2660	1.6116	3268
0	100	5.2667	1.5275	3448	5.2664	1.5191	3467	5.2662	1.5359	3429
Sensitivity (MHz/µl)		2.60			2.60			3.03		
Temperature		18 - 19 °C			19 °C			19 °C		

Table 5.7. Q_L, f_0 and f_B results for the acetonitrile:water solution system in the SDR.

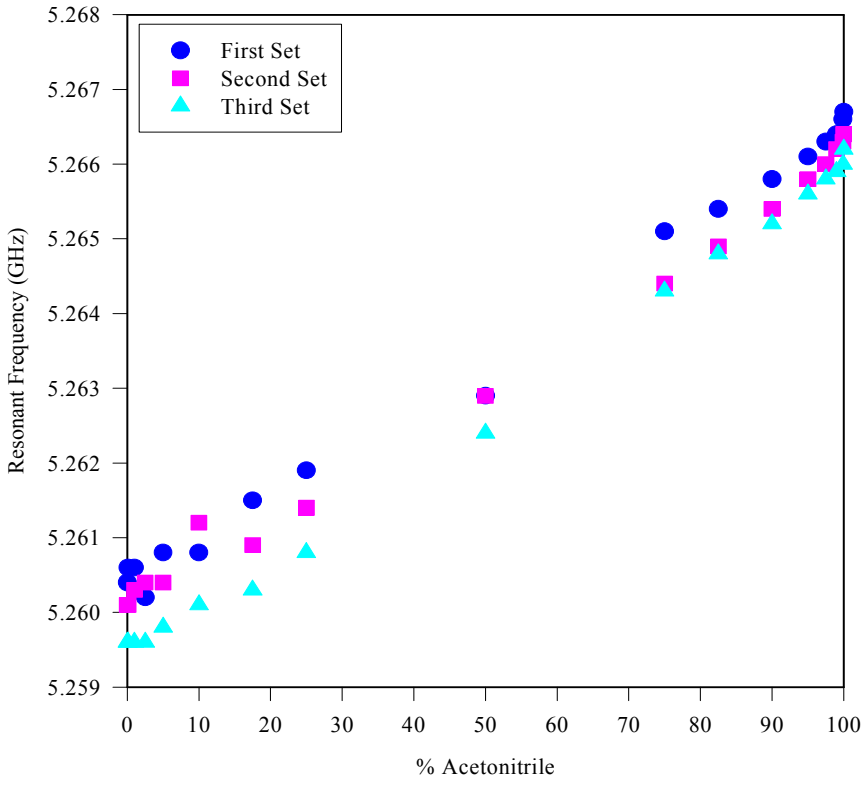

Figure 5.25. The resonant frequency as a function of solution composition for the acetonitrile:water system in SDR.

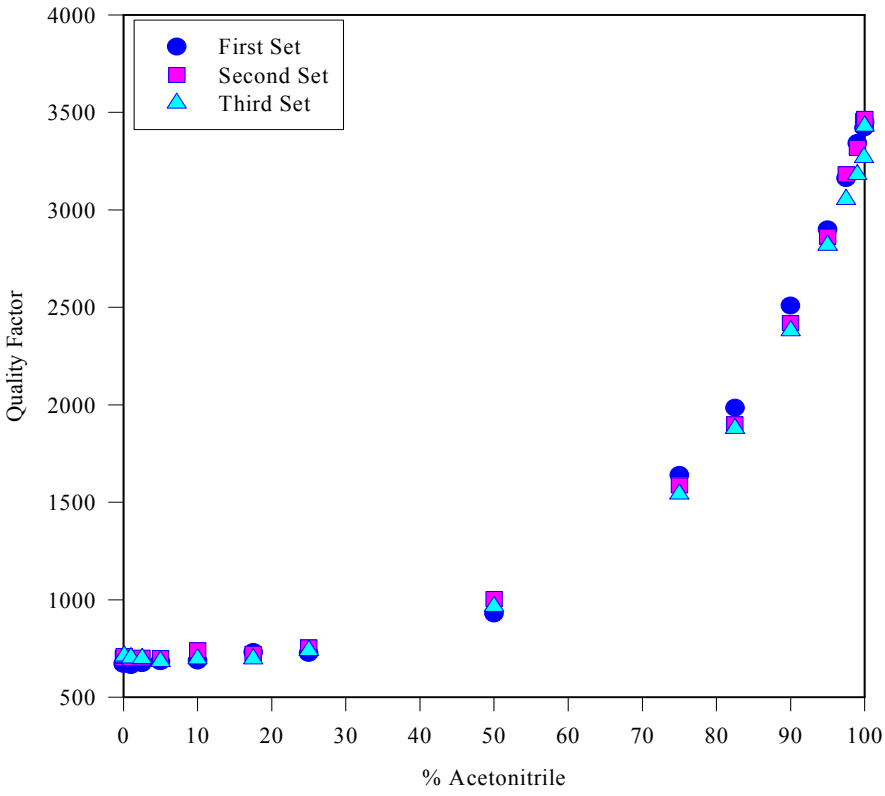

Figure 5.26. The loaded quality factor as a function of solution composition for the acetonitrile:water system in SDR.

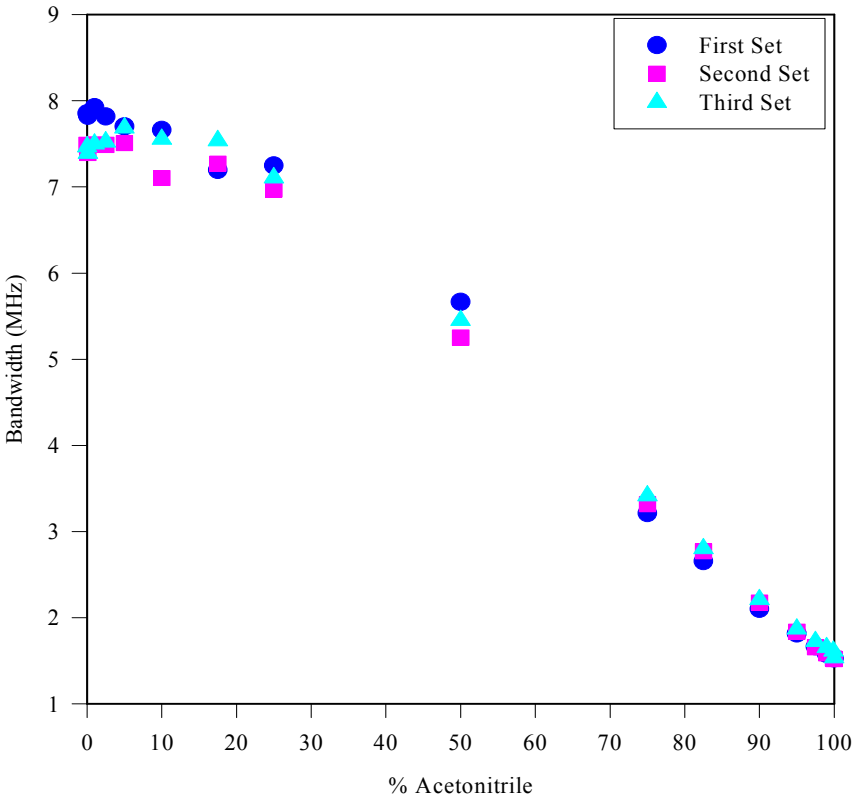

Figure 5.27. The bandwidth as a function of solution composition for the acetonitrile:water system in SDR.

The results of acetonitrile:water system in SDR indicate no depolarisation effects, as predicted by the resonator perturbation theory. The repeatability of measurements is extremely good and frequency sensitivity is about 2.6 MHz/µl over the whole range of solutions.

5.4 Summary of Results

The averaged measured frequency sensitivity for the three sets of compositional analysis experiments carried out in each of the above mentioned resonator systems is summarised in Table 5.8.

	Resonator		
	Hairpin	**Split Ring**	**SDR**
Sensitivity for MeCN:toluene (MHz/μl)	1.27	1106.67	2.16
Sensitivity for MeCN:water (MHz/μl)	0.19	146.67	2.74

Table 5.8. Summarised results for sensitivity of frequency measurement for both solution systems evaluated.

For both the split ring and hairpin resonators, the decrease in measured sensitivity from MeCN:toluene to MeCN:water mixtures is by factor of approximately seven. This fits quite nicely with the respective mismatches in the molecular electric dipole moments of the two systems' components. However, there is a slight improvement in sensitivity for the MeCN:water system measured in SDR, which is expected since $\Delta f_0 \propto (\varepsilon_1 - 1)$ there. All in all, the split ring provides the maximum sensitivity of measurement out of the three resonators used so far though it suffers from reduction in internal electric field caused by depolarisation, which is not the case in SDR. Further enhancement in sensitivity can be accomplished by reducing the effective volume of SDR i.e. by building a miniaturised version of it, as described in the next chapter.

References

[1] R. Göritz, A. Masood, O. Castell, D. A. Barrow, C. Allender and A. Porch, "Microwave Compositional Analysis of Solvent Matrices in Microcapillary Manifold Systems", *The Proceedings of MicroTAS 2007 Conference*, Paris, pp.1689-1691, October 2007.

[2] A. Porch, *Private Communications*, 2007-8.

[3] D. A. Barrow, *Private Communications*, 2007-8.

[4] A. Masood, O. Castell, D. A. Barrow, C. Allender and A. Porch, "Split Ring Resonator Technique for Compositional Analysis of Solvents in Microcapillary Systems", *The Proceedings of MicroTAS 2008 Conference*, San Diego, pp.1636-1638, October 2008.

[5] N. Sykes, *Private Communications*, 2007.

[6] http://www2.dupont.com/Teflon_Industrial/en_US/assets/downloads/h44587.pdf (accessed 6th June 2009).

[7] J. Barthel, K. Bachhuber, R. Buchner, J. B. Gill and M. Kleebauer, "Dielectric Spectra of Some Common Solvents in the Microwave Region. Dipolar Aprotic Solvents and Amides", *Chemical Physics Letters*, Vol. 167, No. 1,2, pp. 62-66, March 1990.

[8] A. P. Gregory and R. N. Clarke, "A Review of RF and Microwave Techniques for Dielectric Measurements on Polar Liquids", *IEEE Transactions on Dielectrics and Electrical Insulation*, Vol. 13, No. 4, pp. 727-743, August 2006.

[9] L. G. Gagliardi, C. B. Castells, C. Ràfols, M. Rosés and E. Bosch, "Static Dielectric Constants of Acetonitrile/Water Mixtures at Different Temperatures and Debye–Hückel A and a_0B Parameters for Activity Coefficients", *Journal of Chemical and Engineering Data*, Vol. 52, Issue 3, pp. 1103-1107, May 2007.

[10] K. S. Kunz and R. J. Luebbers, "*The Finite Difference Time Domain Method for Electromagnetics*", CRC Press, 1993, ISBN 0849386578.

[11] Surveyor® LC Pump Hardware Manual (Revision B), *Thermo Finnigan LC and LC/MS Product Group,* San Jose, California, USA, November 2002.

[12] O. Castell, *Private Communications*, 2008-9.

CHAPTER 6

THE MINIATURISED SAPPHIRE DIELECTRIC RESONATOR

6.1 Introduction

In Chapter 5, experiments for compositional analysis of acetonitrile:toluene and acetonitrile:water solution systems using the hairpin resonator, split ring resonator and SDR were described. The outcomes of these measurements clearly indicate the superiority of SDR over the hairpin and split ring resonators in terms of no reduction in internal electric field (by depolarisation), due to the field being parallel to the microcapillary containing the solution samples. However, the measurement sensitivity attained with SDR is much smaller as compared to the split ring resonator because of the substantially larger effective volume (≈ 1 ml) of the former. This in turn necessitates the need for building a miniaturised resonator that would maximise the respective strengths of the split ring and the SDR, as elaborated in this chapter.

6.2 Miniaturisation of SDR

The practical implementation of a miniaturised SDR for highly sensitive compositional analysis of very small fluid volumes, involved the following main steps:

- Resonator design
- Design of metallic shield
- Superfish simulation and Q_U calculation
- Resonator fabrication and testing
- Design of microfluidic channel
- Implementation of microfluidic channel
- Bonding of sapphire rings
- Bonding of microcapillary segments and device functional test

Each of these steps is now elaborated in the following sub sections.

6.2.1 **Resonator Design**

Since the SDR is a distributed structure (i.e. its resonant frequency is inversely proportional to the physical dimensions of the resonator) there is limited scope for miniaturisation without the resonant frequency becoming unfeasibly large. The first and foremost requirement, therefore, was to ensure that the resonant frequency of the miniaturised resonator stays within the measurement capabilities of available equipment. The Agilent (HP) 8753E VNA can be used for frequencies up to 6 GHz only; however, the newly procured Agilent N5242A PNA-X Network Analyser at Cardiff School of Engineering is capable of *S* parameter measurements up to 26.6 GHz. The miniaturised resonator was envisaged to have an unperturbed resonant frequency of approximately 25 GHz. This, to a first approximation, meant decreasing the dimensions of the bigger resonator by a factor of 5 i.e. for the miniaturised version, the sapphire disks would have radius, *a*, and total length, *l*, each of 2 mm. The reduced dimensions of the miniaturised resonator would present $V_{eff} = (1/3)V = (1/3)\pi a^2 l \approx 0.008$ ml, thereby improving the measurement sensitivity by a factor of 125.

The resonator would still be a composite device made of two sapphire discs; nonetheless, without any intermediate gap as instead of using a microcapillary, it was decided [1,2] to incorporate a microchannel in one of the discs, to carry fluid samples undergoing compositional analysis. In addition to eliminating the need for the middle gap, this arrangement would also circumvent the requirement of having integral sapphire posts in the discs, which were used in the bigger SDR to hold the pucks inside the copper shield. Alternatively, sapphire discs with central holes of about 1 mm diameter (i.e. rings) would be used for fabricating the miniaturised resonator. A rod of a suitable dielectric material would be passed through the two rings making up the composite resonator, so as to hold the resonator tightly in the cylindrical copper shield. The next important consideration was the availability of sapphire rings of appropriate size, for which Pi-Kem Ltd. was accordingly approached. The nearest size offered was outer diameter = 4.5 mm, inner diameter = 1 mm and length = 1 mm, which being quite close to the dimensions of original design, was accepted and four rings were purchased. These rings would slightly increase V_{eff} of the miniaturised resonator (i.e. from 0.008 ml to around 0.01 ml), still providing enhancement in the measurement sensitivity by a factor of almost 100 as compared to the bigger SDR. The

approximate resonant frequency of the isolated resonator for the intended $TE_{01\delta}$ mode of operation was calculated to be 22.5 GHz, using (29) from chapter 4.

6.2.2 **Design of Metallic Shield**

In accordance with the shape of sapphire rings, the shielding enclosure was a copper cylinder. The designed size of shield was about twice the dimensions of the resonator so as to minimize the degradation of the unloaded Q [3]. The sapphire rings were to be tightly held in the middle of the shield by a PTFE rod of suitable dimensions passing through the central holes such that its upper end would be aligned with the top surface of the upper ring. PTFE was chosen because of its desirable properties as a microwave substrate [2] and previous successful use in the SDR. The shield would be made of two parts - held together by four M3 screws - a base holding the PTFE rod/sapphire rings and a lid covering the base. The lower part of PTFE rod would pass enough into the shield base so as to provide firm support to the rings. Two holes drilled into the walls of the shield base would allow for coupling cables to magnetically excite the resonator. The shield design, attached as Appendix G, was drawn in CorelDRAW.

6.2.3 **Superfish Simulation and *Q* Calculation**

Superfish was used to simulate resonator operation in $TE_{01\delta}$ mode, the input text file for which is attached as Appendix H. The resulting electric field pattern, generated by WSFplot, is shown in Figure 6.1.

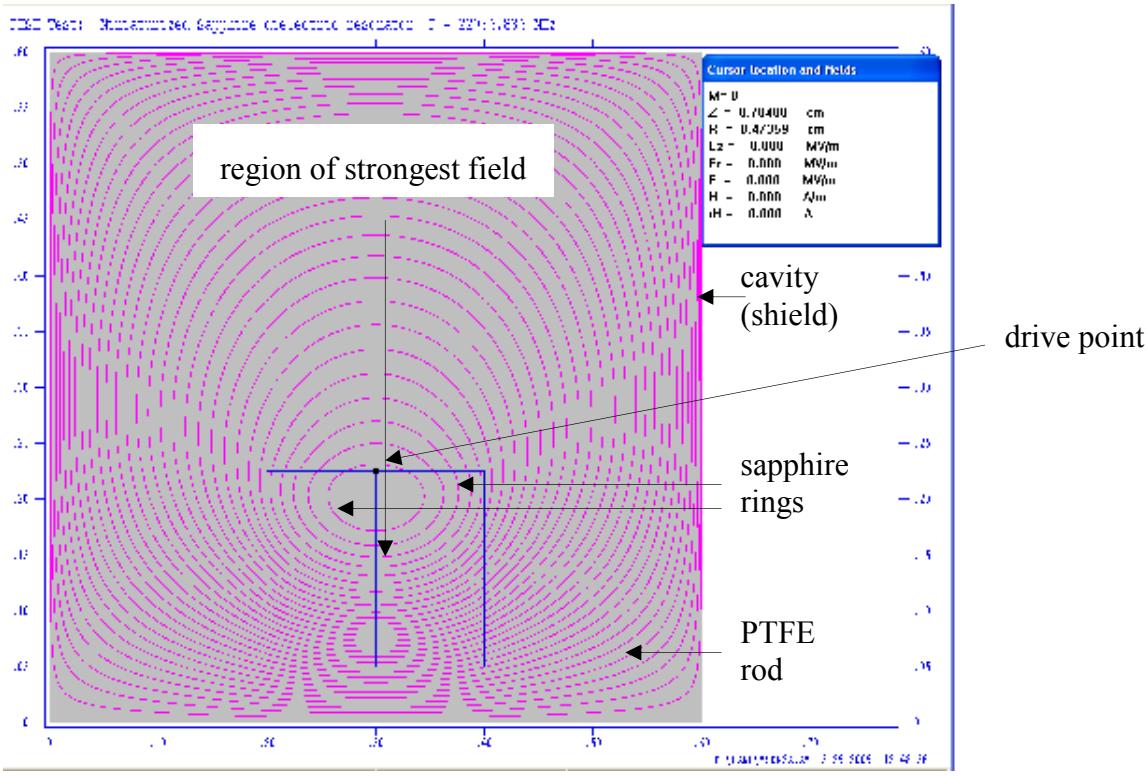

Figure 6.1. Superfish simulated $TE_{01\delta}$ electric field pattern in miniaturised SDR

The value of f_0 determined by Superfish for the shielded resonator was 22.76 GHz, which is very close to the estimate made for the isolated device. The electric field was found to be strongest in the region between radii of 1.4 mm and 1.7 mm on the sapphire rings, as illustrated in Figure 6.2.

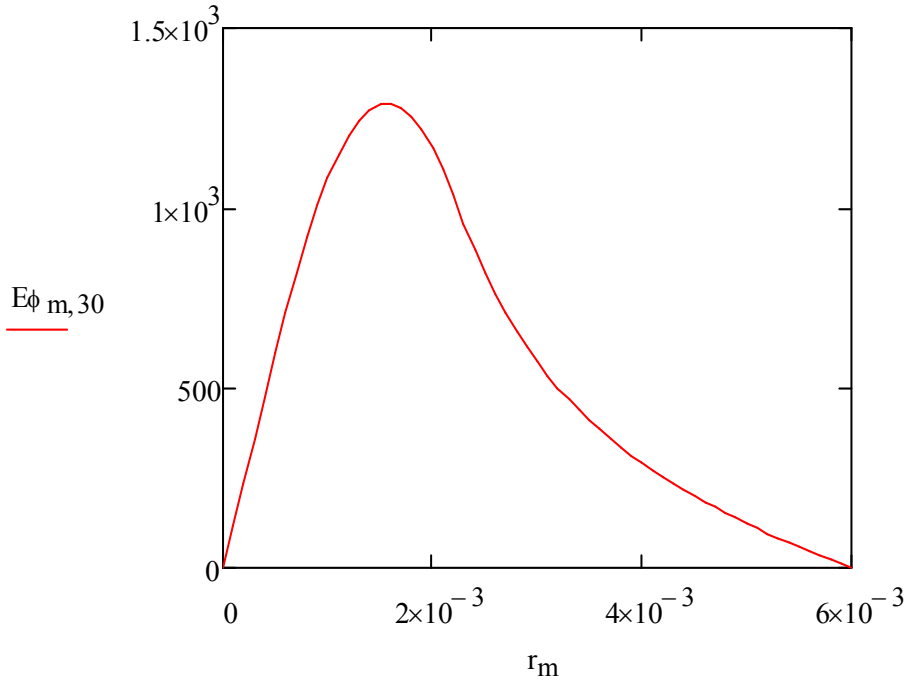

Figure 6.2. The *E* field in miniaturised SDR at the centre of the axis plotted against axial radius (in m). The field is maximum in the region between a = 1.4 mm and 1.7 mm, as indicated by the curve peak. The index 30 in the vertical axis caption indicates that the *E* field is plotted for the middle surface of the two sapphire rings (i.e. the x location of drive point in Figure 6.1.)

The unloaded Q of the device was determined by providing the output of SF7 to an appropriate Mathcad code (see Appendix J), which came out to be around 21,000. It is pertinent to mention here that the values of loss tangent for sapphire and PTFE used for Q_U calculation were 2.5×10^{-5} and 7×10^{-4}, respectively because of the much higher f_0 of the miniaturised SDR. The electric and magnetic field contour plots for the device are as shown in Figures 6.3 and 6.4, respectively. The verification of the designed parameters of the miniaturised SDR paved the way for its physical realization and testing.

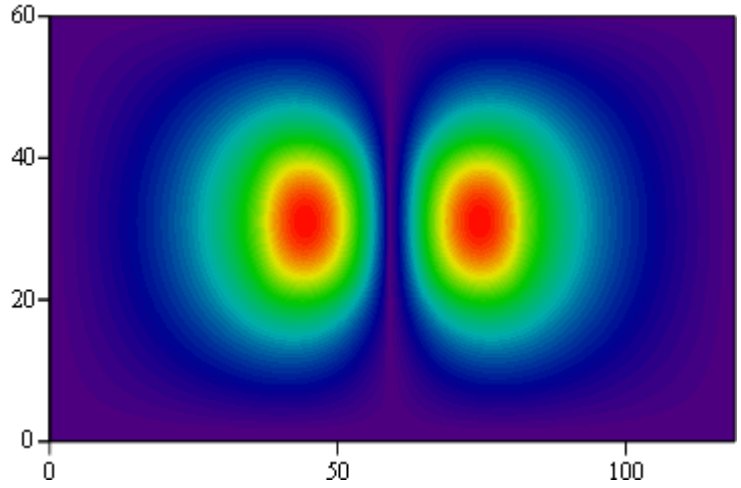

E

Figure 6.3. *E* field contours in miniaturised SDR as plotted in Mathcad against the cavity diameter expressed in terms of the number of points, N = 60. There are 120 points along the *x* axis as N corresponds to the cavity radius (see Appendix J).

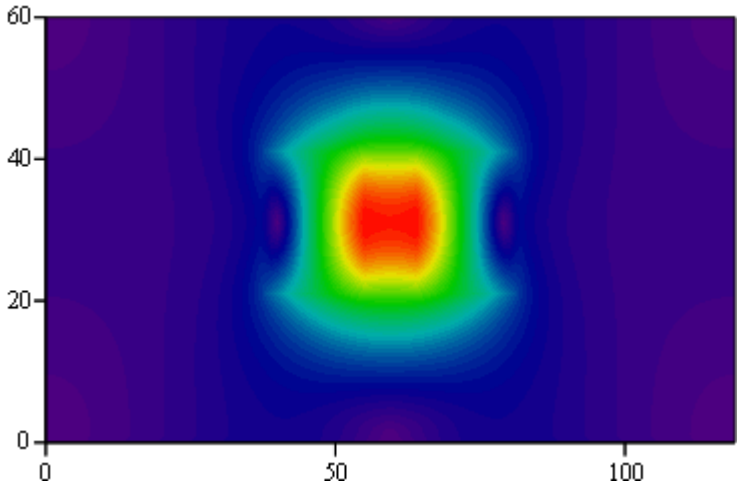

H

Figure 6.4. *H* field contours in miniaturised SDR as plotted in Mathcad against the cavity diameter expressed in terms of the number of points.

6.2.4 **Resonator Fabrication and Testing**

Based on the design described above, the shield was fabricated in the mechanical workshop of Cardiff School of Engineering, following which the sapphire rings were placed in position on the PTFE rod inside it. Magnetic loop coupling to the resonator was provided by means of

two semi-rigid coaxial cables (RG 405U). However, before the resonator was put to test, detailed inspection of the shield revealed that the dimensions of the lid were not according to the design. Instead of the planned 1 mm height for the lid (see Appendix G), the fabricated shield cover had 2 mm deep segment protruding into the base, thereby reducing the cavity height by 1 mm. This inaccuracy in shield fabrication had the potential of giving rise to unwanted waveguide modes, which was confirmed by measurement of the device voltage transmission coefficient S_{21}. With the lid in fabricated position, the S_{21} plot was extremely cluttered with modes and maximum value of Q_{L} obtained (by varying the coupling strength) was approximately 11,000, far off from the simulated result. The lid was then placed upside down (i.e. with the raised surface facing upwards) as depicted in Figures 6.5 and 6.6, following which the resonator was again tested. This modification worked out as the device Q_{L} was measured to be around 18,600 at an *IL* of roughly -28 dB, a disparity of less than 8% from the simulated outcome obtained from Mathcad. The measured resonant frequency was 22.11 GHz, again very close to the Superfish simulation result.

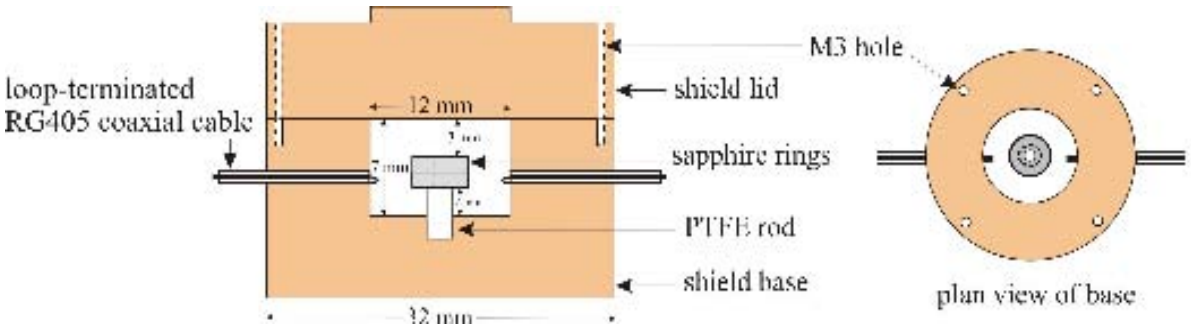

Figure 6.5. Schematic diagram of the miniaturised SDR with the lid in upside down position.

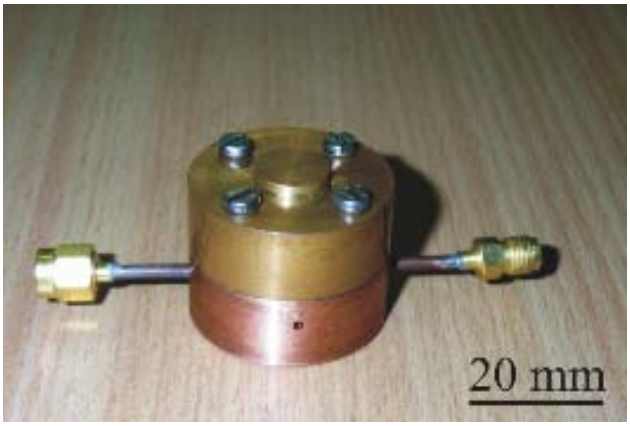

Figure 6.6. Photograph of the miniaturised SDR with the lid in upside down position.

6.2.5 **Design of Microfluidic Channel**

Superfish simulation had shown that a 300 μm wide circular channel (i.e. between a = 1.4 mm and 1.7 mm) could be machined in the resonator, entirely within the maximum E field that is also parallel everywhere to the channel. Therefore, the condition for maximisation of fluid sample's induced electric dipole moment p would be satisfied, as no depolarisation occurs (see chapter 2). The reduction in effective volume of the miniaturised SDR by factor of 100 as compared to its bigger counterpart implies increase in the measurement sensitivity by the same figure, if the volume of fluid sample is unchanged. However, the enhancement in sensitivity offered by the miniaturised device could be better utilized for compositional analysis of fluid samples of substantially smaller volumes. For instance, the same absolute measurement sensitivity could be achieved as from the bigger SDR, for fluid volumes shrunk by a ratio of 100 from 2.31 μl. Had this been the aim, the microchannel dimensions would have to be around 50 μm × 50 μm, as worked out in Appendix K. To ablate a channel of such dimensions on sapphire is actually comparatively easier using the 'Xtreme' laser facility than a bigger one [4]. Nonetheless, the problem of formation and deposition of surface debris would be much more pronounced for a smaller channel [1,5-10]. The debris is formed during the laser machining process and although there are measures for its elimination – discussed in the next paragraph – yet a channel of small dimensions is quite likely to be clogged by it. Therefore, a compromise was reached in going for channel dimensions of 100 μm × 100 μm [1,2,4], which would improve the absolute measurement sensitivity by a factor of approximately 4 (see Appendix K). The microchannel was to be laser machined on the bottom sapphire ring by Neil Sykes. That the fluid samples flow within the microchannel, and hence in the region of maximum E field, would be ensured by adequately bonding the two sapphire rings. Connections for fluid inlet and outlet at opposite ends would be made via microcapillary segments embedded into straight ducts leading to the main circular channel. The smallest commercially available 100 μm ID microcapillary (made of fused silica) has OD of 164 μm, based on which the dimensions of inlet/outlet channels were kept as 175 μm × 175 μm, as shown in Figure 6.7.

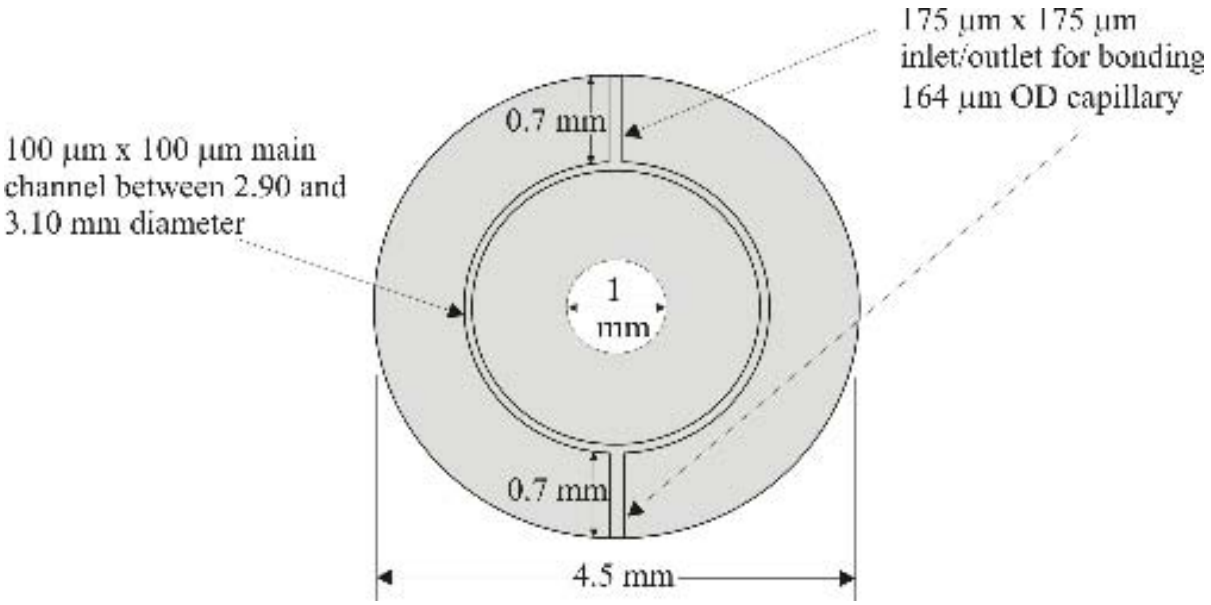

Figure 6.7. Design of microchannel on sapphire ring of miniaturised resonator.

6.2.6 **Implementation of Microfluidic Channel**

Laser ablation is a clean, safe, fast and convenient process for the machining of microchannels, particularly in comparison to other technologies such as chemical etching, deposition processes and lithography [5,6]. For the application in question of microchannel machining on the miniaturised SDR, it was the best option because of the ability of the on hand Ti:Sa femtosecond laser to ablate a hard material like sapphire [4]. However, it presented a formidable challenge in having to deal with formation and deposition of surface debris, which results because of the production of small, volatile fragments during the interaction of laser radiation energy with the sample [5,6]. It is easy to appreciate that a 100 μm × 100 μm channel would be badly clogged by the debris, thereby rendering fluid flow through it impossible. As such, a method for effective removal of surface debris during laser ablation had to be devised. A detailed survey of relevant literature led to a number of potential solutions for this difficulty. Shin *et al.* [5,6] have made use of an erasable ink pasted on the material (i.e. polymer in their research) being laser ablated. The surface debris ejected from the polymer was combined with the ink layer and finally both of them were removed using adhesive tape or alcohol solvent. Results achieved by them suggest that this technique is straightforward, inexpensive and most of all very effective in debris elimination. Another popular debris removal method is underwater laser processing, widely used for laser processing of silicon [7-9]. The fundamental principle behind this technique is in making use

of water convection and bubble motion for the removal of debris redeposition. The results obtained from underwater laser micromachining experiments make it a much better option than normal processing in the presence of air alone. However, it is somewhat complicated as compared to the erasable ink method of Shin *et al.* A third technique, again used for laser microfabrication of silicon, is processing under low air pressure conditions. It has been demonstrated by Mizeikis *et al.* [10] to be essentially debris-free process, thus making it extremely suitable for cutting and scribing of silicon wafers as well as for hole drilling. However, the main limitation of this method is the requirement of an airtight chamber coupled to a rotary pump that maintains air pressure at about 5 Torr.

Having reviewed and discussed all three aforementioned techniques, the approach of Shin *et al*. was chosen for microchannel fabrication on sapphire, primarily because of its simplicity and efficiency [1,4]. The erasable ink used by them comprises an organic solvent (ethanol, isopropanol), a carbon black, a dispersing agent (polyvinylbutyral) and a release agent (n-Butyl stearate). This ink composition is based on a patent of Sakura Colour Products and is the same as used for whiteboard markers [5]. Since Sakura brand markers were not commercially available in the UK, an alternative make (namely Paper Mate) was acquired from WHSmith and trial machining of microchannel using Ti:Sa femtosecond laser ($\lambda = 795$ nm, pulse energy = 1 mJ) was carried out on sapphire disc. The layer of whiteboard marker ink applied before laser ablation was stripped off using 3M Scotch Magic^{TM} Tape, subsequent to which the machined sample was ultrasonically cleaned in an alcohol bath. Inspection of the cleaned sample under electron microscope revealed debris free channels. Following this successful experiment, the same practice was used for laser machining of the microchannel on one of the sapphire rings and dimensions of the main and inlet/outlet ducts were measured using electron microscope. Images of the machined sapphire ring, taken by a Nikon Measuring Microscope MM-800 (Nikon Corp., Tokyo, Japan) are as shown in Figure 6.8. The approximate microchannel dimensions measured from these images, and verified via a Veeco NT 3300 Optical Interferometer (Veeco Instruments Inc.**,** New York, USA), are as follows:

- Main channel - width $\approx$ 100 μm, depth $\approx$ 60 μm
- Inlet channel - width $\approx$ 190 μm, depth $\approx$ 350 μm
- Outlet channel - width $\approx$ 190 μm, depth $\approx$ 340 μm

These dimensions would result in an active fluid volume of about 56 nl that is expected to provide approximately 2.5 times increase in obtained absolute measurement sensitivity from the miniaturised SDR over the bigger resonator (see Appendix K).

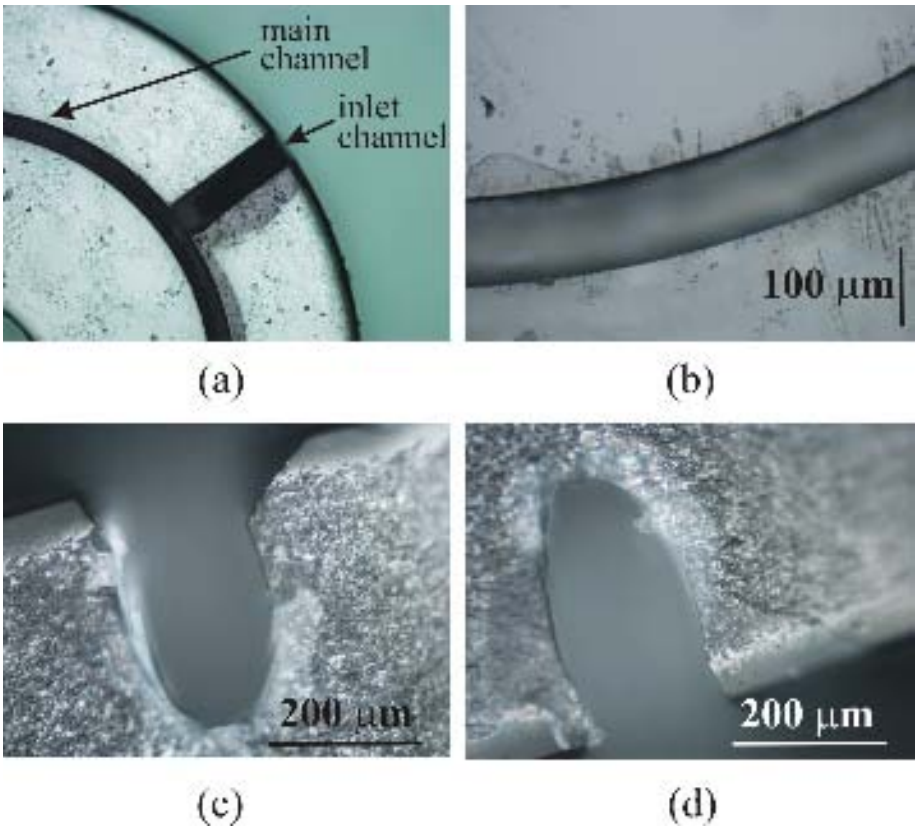

Figure 6.8. Pictures of machined sapphire ring taken with a Nikon Measuring Microscope MM-800. In (a) the main channel and one of the inlet/outlet channels are indicated, (b) shows the main microfluidic channel whereas in (c) and (d), the edge profile of inlet and outlet channels is illustrated.

The difficulties involved in accurate laser micromachining of sapphire are evident from the dimensions mentioned above as well as Figure 5.8, which point out that instead of the intended square, rounded cross sections were achieved for all channels. Nonetheless, the inlet/outlet channels were big enough to accommodate the microcapillary segments and the dimensions of main channel were also deemed large enough [1] to embark on bonding of the rings.

6.2.7 **Bonding of Sapphire Rings**

Since the fluids being analysed would be flowing through the machined microchannel, bonding of rings was one of the most critical stages in the realization of a miniaturised SDR. The following considerations were critical for the bonding process [1]:

- It must not clog the channel i.e. ideally no intermediate layer should form between the rings after bonding,
- The bonding temperature must not be too high to deform the rings i.e. they must remain fairly flat after bonding and the microchannels do not buckle,
- Bonding must be strong enough to ensure that no leakage of fluid occurs.
- The bond should be long lasting and immune to the chemical effects of the fluids being characterized.
- Last but not the least, the bonding should be reversible, i.e. it could be undone to separate the sapphire rings in case it clogs the microchannel.

6.2.7.1 **Bonding by Applied Microengineering Ltd.**

As no bonding facility that fulfils the above mentioned requirements is at hand in Cardiff School of Engineering, Applied Microengineering Ltd. (AML) – an Oxfordshire, UK based company specializing in provision of bonding services – was contacted to undertake this work [1]. AML has a dedicated facility called as BONDCENTRE, where commercial wafer bonding service for many novel materials including sapphire is available [11]. Two sapphire wafers of 0.43 mm thickness and 25 mm diameter, having one surface fine ground and other polished, were sent to AML for an evaluation trial. The samples were plasma surface treated and bonded, followed by a low temperature anneal process [12]. Although they were found suitable for bonding yet the result was about 60% to 70% bond area in the centre of the wafers, with non bonded regions at the edges as observable in Figure 6.9.

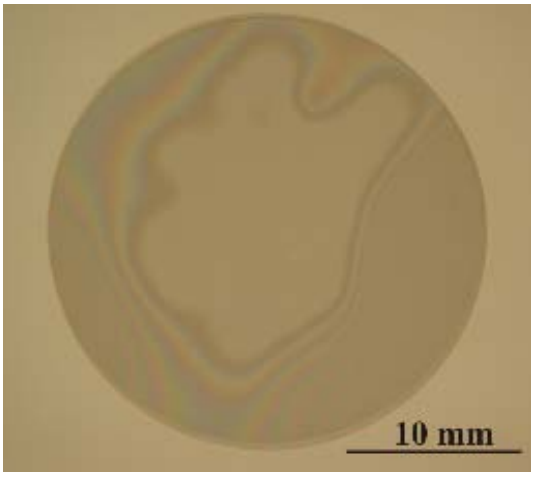

Figure 6.9. Photograph of the AML bonded sapphire wafers showing bonded area in the centre with non bonded edges. Interference fringes denoted a physical nanoscale gap between the wafers.

The non bonded areas were probably caused by non-flat material, or particle contamination which was not removed by AML's cleaning process, thereby implying the need for some more surface metrology before future bonding work. On the other hand, the bonding strength was quite high, which could be further enhanced by increasing the anneal temperature because of the very high melting point of sapphire (≈ 2000 °C) [12]. From the point of view of suitability of AML's bonding service for the miniaturised SDR, the biggest plus was that it did not form any intermediate layer between the wafers, thus circumventing the possibility of channel blockage. As this bonding trial was conducted before the rings for miniaturised SDR were procured, based on its outcomes, Pi-Kem Ltd. was asked to supply rings having both surfaces optically polished. That was expected to ensure surface flatness, thus facilitating achievement of 100% bonding by AML. However, surface analysis of the laser ablated ring using optical interferometer divulged formation of a region with a raised surface of height ≈ 500 nm along the edges of the main channel, as illustrated in Figure 6.10.

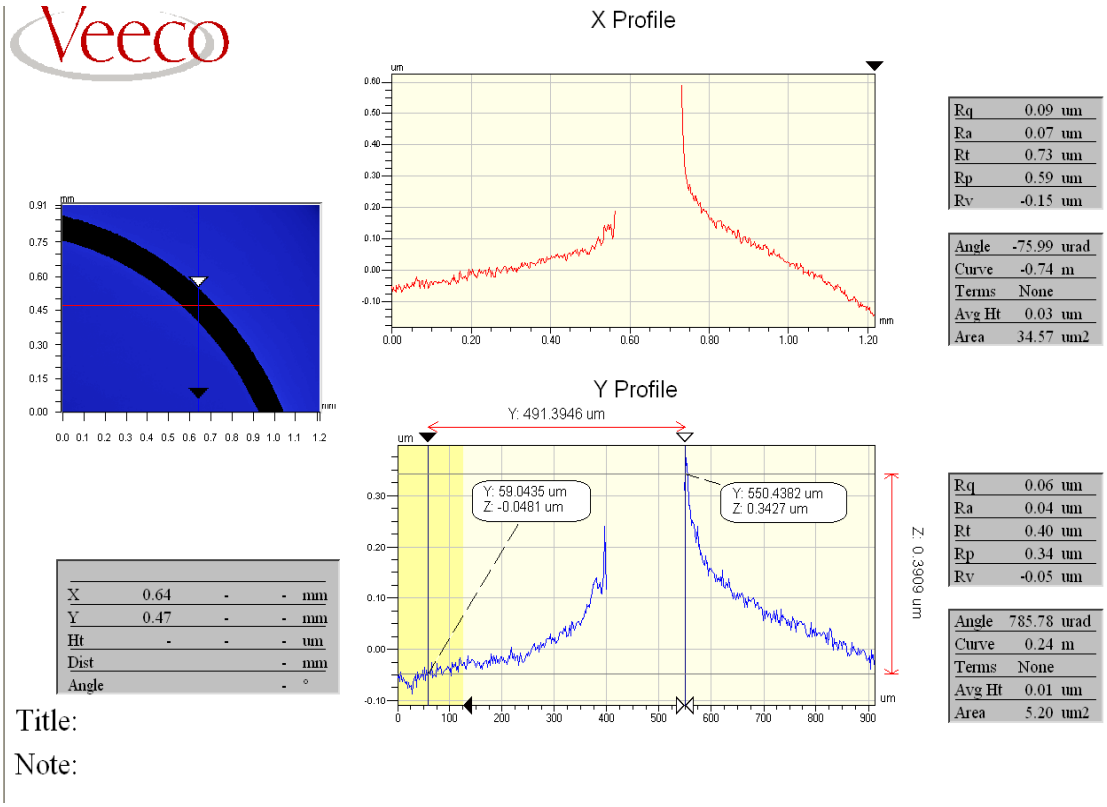

Figure 6.10. The raised areas, approximately 500 nm high alongside main microchannel edges can be seen in X and Y profile images obtained from Veeco NT 3300 Optical Interferometer.

This discovery meant that the surface flatness requirement had been compromised during the laser machining process and AML could not possibly bond the rings [1]. Nonetheless, the interferometer image was emailed to AML to formally seek its verdict; the reply being that the bond was not expected to be successful as typically a 1 μm diameter raised area could create a void of 1 cm in the bond. Given that the sapphire rings were of smaller diameter than 1 cm, there would be no bonding at all. The only remedy to this problem would be re-polishing the machined sapphire ring to make its surface flat again. Non availability of such facility at AML effectively ended all prospects of using its bonding services for the miniaturised SDR [12].

6.2.7.2 **Paraffin Wax Bonding**

As per original plan B, the feasibility of paraffin wax was assessed for bonding of sapphire rings [1,2]. Paraffin wax is most commonly used in the solid form as the burning fuel in household candles and is, therefore, available aplenty. A test bonding using paraffin wax was

carried out as follows: wax removed from a white candle was melted in a small beaker by heating up to about 100 °C on a hot plate. Liquid wax thus obtained was applied by a cotton bud on the polished surface of a sapphire disc having 25 mm diameter and 430 μm thickness, also placed on the hot plate. A microscope slide was used to wipe away excess wax so as to achieve a thin, uniform layer. Another sapphire disc of same size was placed over the waxed one, such that their polished surfaces were mating and well aligned. A metal weight (≈ 50 g) was placed on top of both disks to facilitate the bonding process and the hot plate turned off to allow the wax to cool down. The discs were checked after about one hour and found to have bonded quite well. However, another fundamental issue yet to be resolved was the behaviour of wax in the presence of organic solvents like toluene and acetonitrile, which were to be used for compositional analysis experiments. Hence, a further experiment was carried out by placing the bonded sapphire discs in a vessel containing toluene. Another set of sapphire discs was bonded using the approach described above and put in a bottle of acetonitrile. The discs were left overnight, completely immersed in the solvents so as to precisely ascertain the effect of solvents on wax. Upon examination next morning, it was found that wax had completely dissolved in toluene, causing separation of discs while those immersed in acetonitrile were unaffected. However, the results of the immersion experiment warranted discarding this bonding method.

6.2.7.3 **Bonding by Ultraviolet Curable Adhesive**

Another option for bonding the sapphire rings was to use ultraviolet (UV) curable adhesives that use UV light or other radiation sources to initiate curing, so allowing a permanent bond without heating. A suitable UV curable adhesive for bonding hard materials like sapphire is ELC-4481, manufactured by Electro-Lite Corporation, USA (see Appendix L for manufacturer's technical data sheet). It was acquired from Global Optics (UK) Ltd. and tested to establish its viability by bonding together the polished surfaces of two 25 mm diameter and 430 μm thickness sapphire disks. After application of a thin layer of ELC-4481 on one disk, the other was aligned with it and the sample was placed under light from UVGL-58 handheld UV lamp (Ultra-Violet Products Ltd, Cambridge, UK) for two hours. A 50 g weight was kept on top of both discs for the initial ten minutes to aid bonding, which was found to be fairly strong. At the same time, it was realized that the bonding provided by ELC-4481 was irreversible thus making it unsuitable for use with the sapphire rings in miniaturised

SDR. Global Optics (UK) Ltd. (as well as a few other pertinent suppliers) was contacted to determine the availability of reversible UV curable adhesive, which led to this approach also being abandoned.

6.2.7.4 **Bonding by Teflon® AF 1600**

As per the original plan for bonding of rings, AML was on top of the list whereas paraffin wax and UV curable adhesive were the back-ups. Having been unable to use any of these methodologies, a literature search was under taken to explore alternative bonding techniques. The most notable among them, a paper by Kopperschmidt *et al.* [13], describes back-to-back bonding of sapphire wafers in a microcleanroom setup. Although claiming success in their direct wafer bonding (DWB) method, the authors did not elaborate the exact procedure used for achieving the bond. Accordingly, the corresponding author was approached through email to enquire about the bonding details but there was no response. Subsequent to that, other relevant literature was consulted to find out more information about DWB. It was established from the paper by Haisma *et al*. [14] that adequate polishing of surfaces is needed to achieve a finish suitable for direct bonding. For the case of hard materials like sapphire, the desired surface finish is obtained by a method termed as enhanced tribochemical polishing. This method involves the use of a polishing slurry of colloidal suspension of SiO_2 nanoparticles in an alkaline aqueous solution, a polishing pad of pearlitic iron and a polishing pressure of about 100 kPa. Whereas Haisma *et al*. have stated commercial availability of the required polishing slurry, no mention is made as to where the pearlitic iron pad can be procured from. However, an attempt was made to ascertain its availability form Buehler, which is the world's premier manufacturer of scientific equipment and supplies for use in materials analysis.

Based on the prohibitive cost associated with employing Buehler's suggested solution, it was ultimately decided to make use of a bonding method that could be implemented with equipment and stores at hand in Cardiff School of Engineering. To this end, Teflon® AF 1600 solution (made from Teflon® AF 1600 resin) was used for bonding the sapphire rings [1]. Teflon® AF is a family of amorphous fluoropolymers, manufactured by DuPont, which holds patents for the end uses of its resin. They are distinct from other fluoropolymers in that they can be dissolved in certain perfluorinated solvents to produce highly uniform thin films and coatings via spin, spray and dip coating methods. Teflon® AF

coating has high resistance to chemical attack and a low loss tangent, thereby making it appropriate for bonding the sapphire rings in miniaturised SDR [15]. There are two available grades of Teflon® AF resin: 1600 and 2400, differing in their T_g i.e. glass transition temperature*. Surplus Teflon® AF 1600 resin was readily available from an earlier project, which was used to make about 10 ml volume of 50 mg/ml solution in Galden HT135 (i.e. a perfluorinated solvent procured from Fluorochem Ltd., Derbyshire, UK) as follows: Teflon® AF 1600 granules were added to Galden HT135 and the solution vessel was clamped to Thermolyne Maxi-Mix III™ Type 65800 vortex mixer (shaker) at a speed of around 1000, left overnight to ensure a homogeneous mix.

Having made the solution, it was decided to use a spin coating method to apply a uniform thin film to the surface of plain ring [16]. In spin coating, an excess amount of a solution is placed on the substrate, which is then rotated at high speed in order to spread the fluid by centrifugal force. The preference for spin coating over other parallel techniques was dictated by previous experience in its use and availability of the spinner in Cardiff School of Engineering [1]. However, before venturing onto the actual coating of the ring, it was critical to determine the optimum thickness of the coated film (i.e. not causing channel blockage once the rings are bonded), which came about 1 μm (see Appendix K). The next step was to establish a procedure for coating the film of requisite thickness on the sapphire ring. As a start, a sapphire disk of 25 mm diameter and 430 μm thickness was ultrasonically cleaned in an alcohol bath before spin coating using a Precima model PRS 14E spinner (Cammax Precima, Colchester, UK). The spin time was set to 5 sec and spin speed to approximately 1000 rpm, with vacuum turned on during the coating process to make certain that the sample doesn't fly off. A droplet of the prepared Teflon® AF 1600 solution was applied with a glass pipette onto the sapphire disc surface, after which the spinner was turned on twice, 1 sec apart. The coated film was given about 5 minutes to dry and ten spin coatings were carried out in the aforementioned way. The coated sample was observed under optical interferometer to ascertain the film thickness, which revealed that the film had not adhered particularly well to the sapphire surface.

* When an amorphous polymer is heated, the temperature at which it changes from a glass (i.e. hard, rigid and brittle) to the rubbery (i.e. soft and flexible) form is called T_g. Teflon® AF 1600 has a T_g of 160 °C while Teflon® AF 2400 has T_g = 240 °C.

Consequently, it was decided to deposit an adhesion-promoting layer of 1H,1H,2H-perfluorodecyltriethoxysilane (PFDT) (Lancaster Co., Morecambe, UK) on the sapphire disc prior to spin coating [1,17]. A 5% solution of PFDT in Fluka Fluorinert® FC-77 (Sigma-Aldrich Corp.) was prepared. The sapphire disc was ultrasonically cleaned in a Galden HT135 bath to dissolve the coated Teflon® AF layer, before being immersed in the PFDT solution for about 10 minutes. It was then oven baked at 110 °C for 15 minutes and cooled down to room temperature, following which the spin coating procedure was carried out. Analysis by optical interferometer showed that although the thickness of coated Teflon® AF 1600 film was higher than before, it still did not still satisfactorily stick to sapphire. Thus, an alternative way of improving Teflon® AF adhesion was devised in the form of cleaning in Piranha solution. Piranha solution, also known as piranha etch, is a mixture of sulphuric acid (H_2SO_4) and hydrogen peroxide (H_2O_2), used to clean organic residues off substrates [18]. The protocol for preparation and use of piranha etch is described in Appendix M, based on which the sapphire sample was cleaned with H_2SO_4 (Fisher Scientific) and H_2O_2 (Acros Organics) [19]. After that, it was again PFDT dipped and baked before being spin coated with ten layers of Teflon® AF 1600 solution that resulted in about 4 μm film thickness, as measured using optical interferometer. Based on this trial, the requisite film thickness of ≈ 1 μm could be obtained by reducing the number of coatings from ten to three. This assumption was confirmed by spinning three Teflon® AF coatings on a sapphire sample; the resulting film thickness was approximately 1.2 μm, as depicted in Figure 6.11.

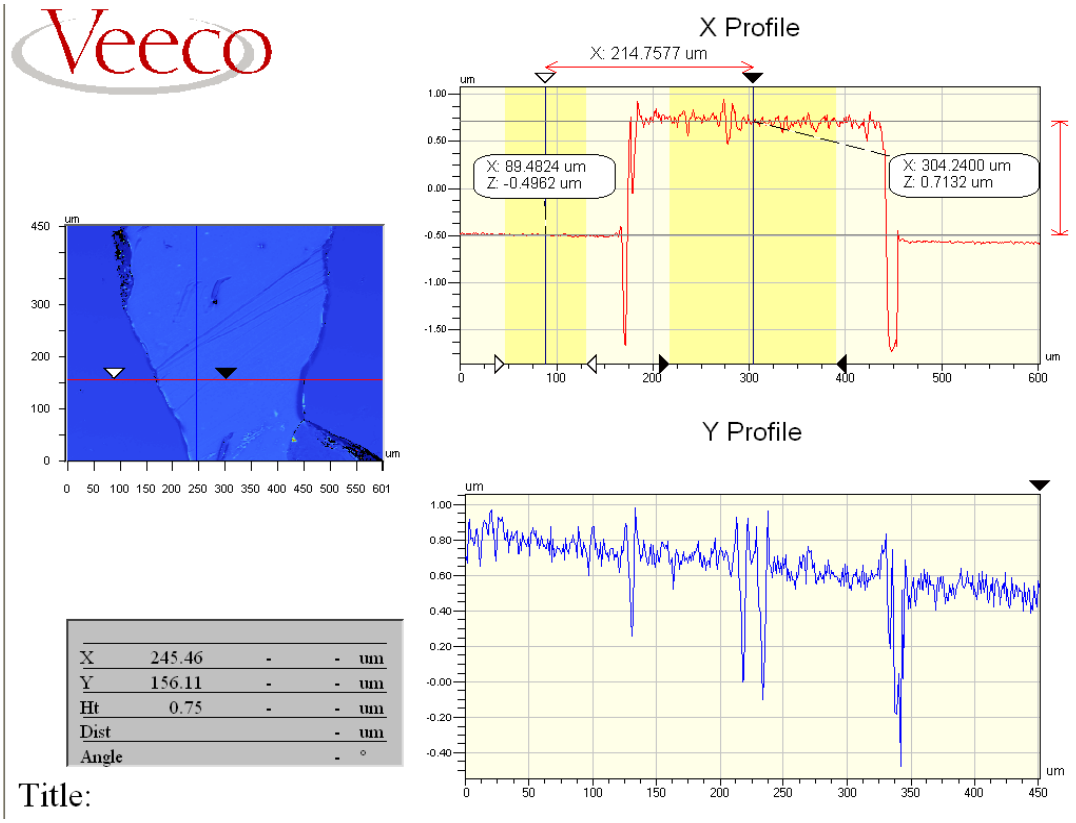

Figure 6.11. Veeco NT 3300 Optical Interferometer image showing the ≈ 1.2 μm thick Teflon® AF 1600 film on a sapphire sample, as can be viewed in the X profile.

Consequently, both the machined and plain ring were piranha etched and deposited with PFDT layer before the plain ring was spin coated three times with Teflon® AF 1600 solution. The thickness of coated film was measured to be about 1 μm, by means of optical interferometer. The next step was to bond the two rings together, for which they were placed in position inside the copper shield (see Figure 5.5) in order that the machined ring was on bottom with its microchannel surface facing up, mating with the coated surface of plain ring. A PTFE disc of 3 mm height and 5 mm diameter, fabricated in the school mechanical workshop, was placed on top of the rings and the two halves of shield were assembled together by tightening the M3 screws. The top surface of the PTFE disc was pressed by the shield lid so as pressurise the rings to facilitate the bonding process. The whole assembly was placed in Memmert oven (Memmert GmbH + Co., Germany), set to a temperature of 180 °C so that the film could melt and bond the rings. A Kane-May KM340 digital thermometer was used to monitor the temperature inside the oven, which was kept on for two hours. After allowing to cool down overnight, the assembly was removed from the oven and inspected to find that the rings had not bonded together. The most probable cause behind that was the

thick metallic walls of shield had acted as a buffer, i.e. not allowing the oven heat to be transferred to the Teflon® AF 1600 film on the sapphire ring resulting in it not melting. It was also realised that the temperature shown by the thermometer was that of the inside of oven but not exactly of the sapphire rings, where it was not possible to accurately measure the temperature using this layout. Based on these observations, this approach was disposed of and it was decided to attempt bonding the rings using a hot plate [1]. The plain ring was placed on the surface of IKA® RCT basic hot plate (IKA®Werke, GmbH & Co., Germany) and the machined ring placed on it with the microchannel facing downwards. This arrangement was adapted with a view to further minimize the possibility of channel blockage, as otherwise the melting Teflon® film could flow into the microchannel by gravity. A small brass rod of diameter slightly less than 1 mm and 1.7 mm height (made by the school mechanical workshop) was inserted in the central hole of rings to ensure their alignment during the bonding process. The hot plate was set to its maximum temperature of 300 °C and an analogue (dial) thermometer was used to monitor its surface temperature. A metal rod supported on a stand was used to apply weight on the rings, to aid the bonding as illustrated in Figure 6.12.

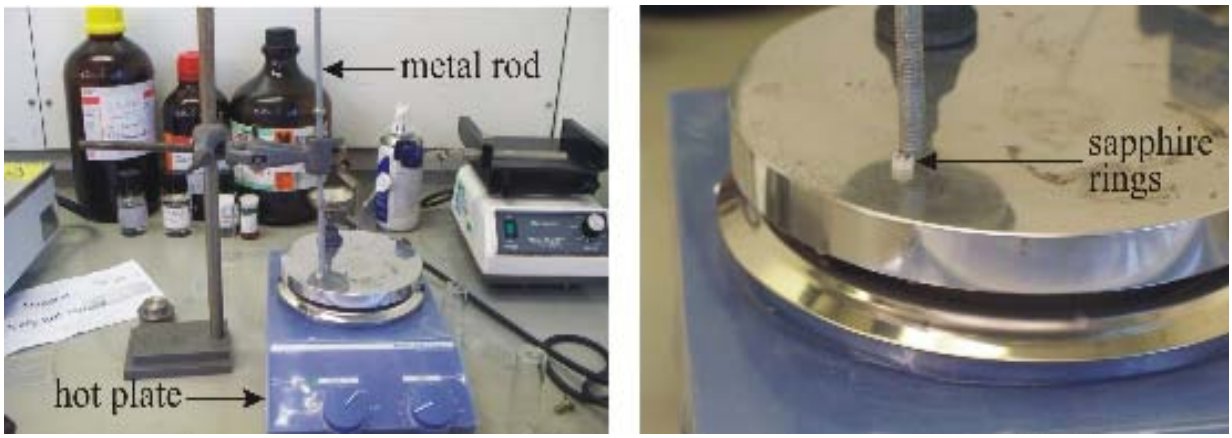

Figure 6.12. Photographs showing the setup used for bonding of the sapphire rings of miniaturised SDR.

The hot plate was kept turned on at 300 °C for roughly an hour, after which the metal rod was removed from top of the rings and they were let to cool down for about 30 minutes. The rings were found to have bonded quite well; nonetheless, the brass rod had got stuck in the middle hole. A syringe needle was used to drive the rod out through a 2.2 mm diameter hole in a 4 mm thick brass plate, on which with the rings were placed.

6.2.8 **Bonding of Microcapillary Segments and Device Functional Test**

As mentioned before in this chapter, fluid undergoing compositional analysis would flow in and out of the circular microchannel at opposite ends through microcapillary segments embedded into the inlet/outlet microchannels. The required microcapillary of 100 ± 4 μm ID and 164 ± 6 μm OD (Polymicro Technologies, Arizona, USA) was acquired from Composite Metal Services (CMS) Ltd., Shipley, UK. It is made of flexible fused silica with a standard polyimide coating. In order to connect the inlet microcapillary segment to standard, luer-tipped syringes (or HPLC pump) that have earlier been used for compositional analysis experiments in this research, the under mentioned Upcurch Scientific parts were purchased from Presearch Ltd., Hampshire, UK:

- P-659 – Adapter female luer to female 10-32 coned PEEK (for fitting on the end of the syringe).
- F-130X – Long one-piece fingertight 10-32 fitting (for connection to the P-659).
- F-238X – Tubing sleeve Teflon® FEP 180 μm ID, 1.58 mm OD and 40 mm length (for enclosing the syringe-leading portion of the inlet fused silica microcapillary segment).

Moreover, the microcapillary segments for fluid inlet and outlet had to go through the shield walls for which appropriate holes needed to be made. Because of the flexibility and tiny OD of the microcapillary involved, a PEEK tubing of 175 μm ID and 1.58 mm OD was used as sleeve for it [1]. This purpose could have been served by the F-238X sleeve, but the PEEK capillary was preferred as it could be cut in pieces of any desired length. Accordingly, two holes of approximately 1.6 mm diameter were drilled by school mechanical workshop such that they were vertically aligned with the microchannel (i.e. top surface of the machined ring). They were kept perpendicular to the already bored holes for the coupling cables, as demonstrated in Figure 6.13.

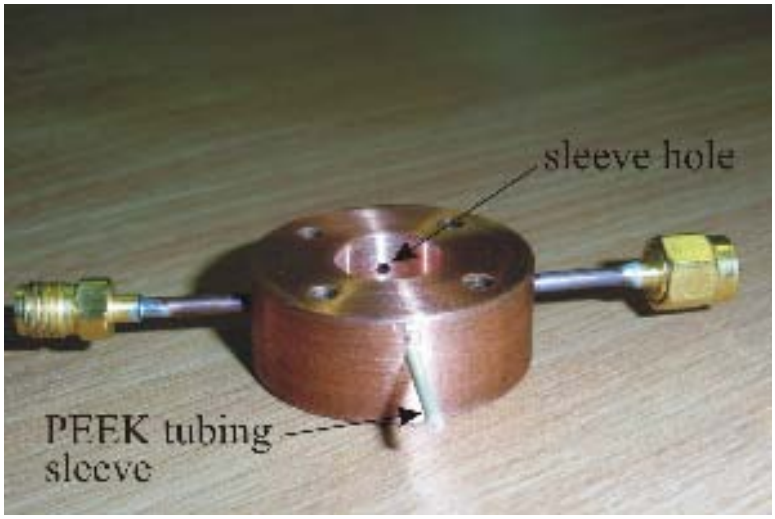

Figure 6.13. Photograph showing the PEEK tubing sleeve/hole for accommodating the inlet/outlet microcapillary segments.

Having accomplished the requisite configuration, a functional check of the miniaturised SDR based microfluidic device was carried out by injecting a test fluid made of a green pigment added into chloroform (Sigma-Aldrich Corp.), for ease of optical visibility in the small microchannel. A KD Scientific dual syringe pump was used to drive a BD Discardit™ II 10 ml syringe, with the flow rate set at 0.01 ml/min. The resonator was placed for close observation under a Nikon SMZ800 electron microscope. The fused silica microcapillary was cut into a segment of about 25 mm length using a specialist ceramic cleaver (Polymicro Technologies) while its sleeve was made using PEEK Tubing Cutter (Sigma-Aldrich Corp.). Initially, only one microcapillary segment was used for the fluid inlet to the main channel, which resulted in fluid leakage at the interface between the fused silica microcapillary and the machined ring (i.e. where the inlet segment entered the microchannel). Having failed in this first attempt, the outlet microcapillary segment was also attached to the main channel and its other end was connected to a N75 KN18 vacuum pump (KNF Neuberger, GmbH, Germany) through appropriate fingertight fitting and tubing. The idea behind this improvisation was that the vacuum pump would assist fluid flow by sucking it at the outlet. However, it failed to work, leading to the notion that the main channel had been clogged during bonding. It was therefore decided to bond the rings again using a lesser quantity of Teflon® AF 1600 coating as the actual dimensions of the circular microchannel might be smaller than those measured [1]. Additionally, since the microchannel was not uniform throughout it could have been blocked at a narrower and/or shallow point(s). Based on these suppositions, it was decided to reduce the number of spin coatings from three to one.

The rings were separated by heating on the hot plate at 300 °C for about 45 minutes, ultrasonically cleaned in Galden HT135 bath and piranha etched followed by bonding using the setup of Figure 5.11. Nonetheless, the outcome again was leakage of test fluid from the inlet. The failure in achieving fluid flow through the microchannel even after bonding the rings with one Teflon® AF coating led to the awareness that the inlet microcapillary segments was not sealed at its point of contact with the machined ring [1]. As the fluid would face a large resistance in flowing through the minute microchannel, it was imperative to seal the inlet without which the leakage was inevitable. Dow Corning® 730 Fluorosilicone sealant along with Dow Corning® 1200 OS Primer was procured for the purpose from Dow Corning Corp., Michigan, USA. This particular sealant was chosen because of its good resistance to solvents, room temperature cure, ease of application and good adhesion to many materials, aided by use of primer (see Appendix N for detailed product information). As regards application of the sealant to the requisite location, it was first tried by filling it in a syringe but was too flexible to be injected in this way. A syringe needle was then considered for applying the sealant but none thin enough could be found. Eventually, a narrow glass capillary of approximately 1 mm OD and 15 cm length was made into a very sharp-tipped needle using a 'Puller for Glass Micro-electrodes' (Scientific and Research Instruments (SRI), UK), which was available in the Applied Micofluidics Laboratory. This device was found suitable for the application in question and was used to seal the inlet microcapillary segment under observation of the electron microscope.

The inlet channel was treated using 1200 OS Primer prior to application of the sealant. The results of this effort were encouraging in the sense that the test fluid managed to flow halfway through the main microchannel before leaking from the inlet. Based upon advice of Oliver Castell, who is the microfluidics application designer within the engineering school, more quantity of sealant was applied in the next attempt as well as sealing the outlet microcapillary segment (see Figure 6.14). Moreover, Araldite® Rapid epoxy adhesive (Bostik Ltd., Leicester, UK) was used to seal all the inter connections between the F-238X sleeve and the copper shield in order to prevent the inlet microcapillary segment from being twisted (and thus damaged) during connection/disconnection to the syringe pump.

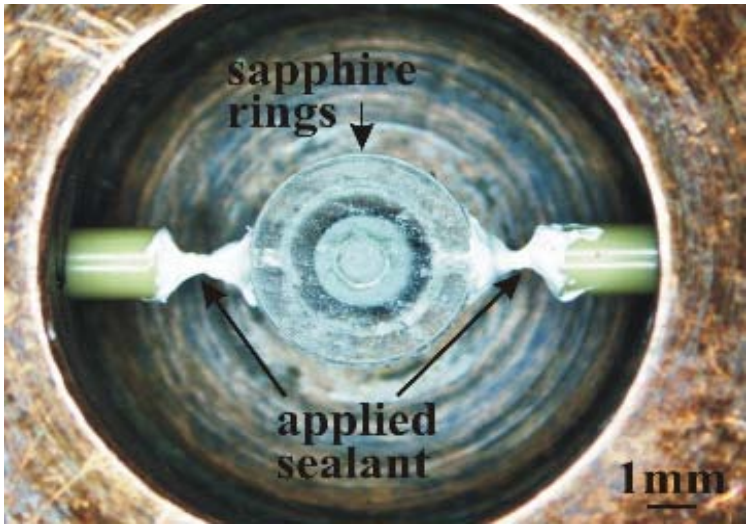

Figure 6.14. Photograph of the applied DOW CORNING® 730 Fluorosilicone sealant on the inlet/outlet microcapillary segments of the miniaturised SDR based microfluidic device (taken with a Nikon SMZ800 electron microscope).

The device was subsequently tested using firstly a BD Discardit™ II syringe, which caused the fluid to flow back into the syringe rather than going forward, and then a 10 ml SGE luer lock glass syringe (SGE Analytical Science Pty Ltd., Australia) that made the syringe pump stall. Apparently the pressure required for injection of the fluid through the minuscule microcapillary and channel was too high to be achieved using the syringe pump, thus resulting in fluid flow-back/stalled pump as sealing had impeded fluid leakage [20]. Consequently the HPLC pump was tried to inject fluid because of its capability to withstand higher pressure, and flow was achieved up to half the length of the microchannel, after which leakage again occurred, although from within the main channel rather than the inlet. It was later established by carefully examination of the operating software of HPLC pump that even though the flow rate on it was set to constant value of 0.01 ml/min, periodic bursts were generated by the pump, observable in the form of large pressure fluctuations. This phenomenon had gone unnoticed during the acetonitrile:water solution system experiments conducted formerly using the HPLC pump since the pressure variations did not affect the microcapillaries used there. However, for the case of the miniaturised SDR they led to the main channel being ruptured. The option of using the HPLC pump was thus discarded and it was decided to revert to the syringe pump, with the following adjustments [1,20]:

- In place of a long (≈ 25 mm) segment of the fused silica microcapillary, a PEEK tubing of 1 mm ID and 1.58 mm OD would be used for the most part between the syringe and the copper shield. The fluid inlet to the microchannel would still be

through a fused silica microcapillary segment, but interfaced to the bigger PEEK tube shortly after emerging from the shield. This modification was expected to considerably reduce the pressure requirement on the syringe pump.

- The test fluid of chloroform would be substituted by one having a lesser viscosity to ease flow. In this connection, acetone (viscosity = 0.36 cP against 0.57 cP for chloroform) would be used [21].

The rings were once more separated, cleaned and bonded with one spin-coated layer of Teflon® AF 1600 solution. The 1 mm ID PEEK tubing was connected to the SGE glass syringe via P-659 luer lock adapter and F-130X fingertight fitting; the need for F-238X tubing sleeve was circumvented in this setup. The far end of the PEEK capillary was connected through another fingertight fitting and union to the inlet fused silica microcapillary segment, sleeved in the 175 μm ID PEEK tube (see Figure 6.16). A trial for injecting acetone (Sigma –Aldrich) with a red dye (Sudan Red 7B, Sigma –Aldrich)† into the microchannel was carried out at flow rate of 0.01 ml/min. It was observed after around ten minutes that acetone had started leaking from the inlet and the applied sealant covering was being dissolved by it. This latest failure directed to abandonment of further attempts using Dow Corning® 730 Fluorosilicone sealant. The only way out was probably in using an epoxy adhesive, which will have much better chemical immunity as compared to silicone sealants. This option, though considered at the time of selecting the sealant, was not pursued because of its perceived irreversibility (i.e. permanence of application), not to mention the high loss tangent of most epoxy resins [2]. However, it was found that fully cured epoxy adhesive can be removed after ultrasonic treatment in a bath of 1-methyl-2-pyrrolidinone (NMP) for about one hour [20]. To confirm the validity of this information, a thick layer of Araldite® Rapid epoxy adhesive was applied to a scrap piece of sapphire. After the epoxy had fully set, the sample was ultrasonically treated in NMP (on hand in Applied Microfluidics Laboratory) bath for one hour that made the applied layer soft and swollen up. It was then easily removed from the sample in full with the aid of a spatula. This experiment cleared the way for employment of an epoxy adhesive for the required sealing job; however, the selection of an appropriate adhesive still remained.

† The green pigment used earlier with chloroform was found to be insoluble in acetone, thus necessitating this change.

Several manufacturers/suppliers of epoxy adhesives, namely Huntsman Advanced Materials, Switzerland, Loctite UK Ltd., Hertfordshire, Bostik Ltd., Leicester, UK and RS Components Ltd., Northamptonshire, UK, were contacted to establish the best solution for application under consideration. However, none was able to give a definite answer, with most asking instead to go for a trial and error approach. Based on this response plus the ready availability of Araldite® Precision and Araldite® Rapid epoxies (see Appendix O for product information) in the Applied Microfluidics Laboratory, a small trial was conducted to ascertain their feasibility for sealant use as follows: Two pieces of scrap sapphire were ultrasonically cleaned in an alcohol bath, following which the epoxies were separately applied to them using syringe needles. Having found the adhesion to be adequate after curing, two further samples were prepared and placed overnight in vessels containing toluene and acetonitrile to establish the chemical immunity of the epoxies. It transpired that Araldite® Rapid had become quite soft in toluene whereas the other three samples were unaffected. Therefore, Araldite® Precision epoxy was applied with the sharp glass needles for sealing the inlet/outlet microcapillary segments, as depicted in Figure 6.15.

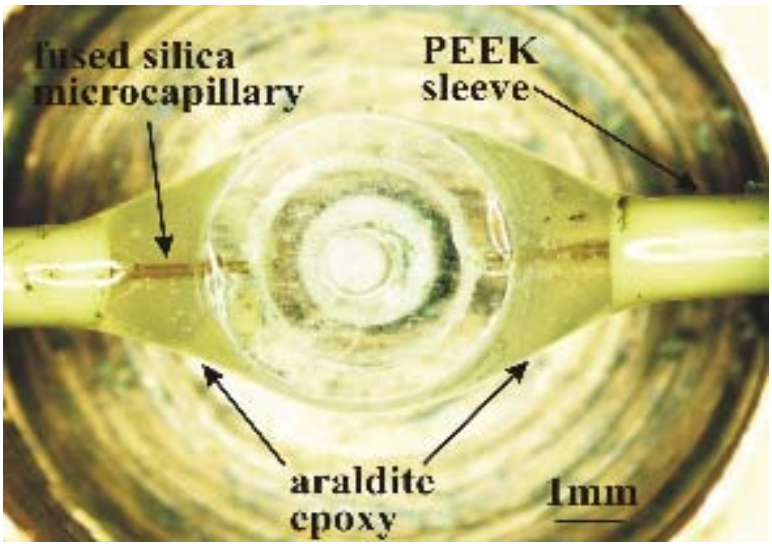

Figure 6.15. Photograph of the applied Araldite® Precision epoxy adhesive to seal inlet/outlet microcapillary segments of the miniaturised SDR based microfluidic device (taken with a Nikon SMZ800 electron microscope).

Next, the setup of Figure 6.16 was used to inject red acetone into the microchannel at 0.01 ml/min flow rate and a successful outcome was finally achieved.

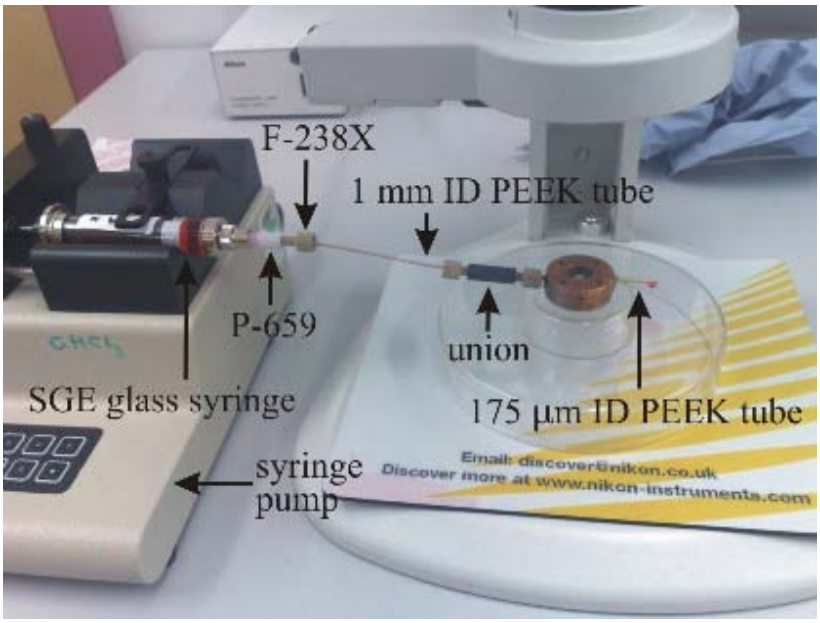

Figure 6.16. Photograph of the setup using which fluid flow through the miniaturised SDR based microfluidic device was achieved (note the emerging droplet on the right hand capillary).

In order to ascertain the reliability of the miniaturised SDR based microfluidic device against sustained injection of fluid, it was tested with acetone for one hour at the aforementioned flow rate. After successfully going through this assessment it was subject to a further 30 minutes trial with the flow rate doubled (i.e. 0.02 ml/min), which was also successful smoothly. The increase in flow rate was important with regards to conduct of compositional analysis experiments as it would help in speeding them up. Furthermore, since SGE glass syringes were not on hand in sufficient quantity, BD Discardit^{TM} II syringes were tested by injecting acetone and worked sufficiently well for about half an hour.

6.3 Compositional Analysis Experiments with Miniaturised SDR

After functional testing of the miniaturised SDR based microfluidic device, the stage was set for carrying out compositional analysis experiments on it to practically confirm the expected enhancement in measurement sensitivity. Both solution systems characterised previously in this research (i.e. acetonitrile:toluene and acetonitrile:water) were experimented employing Agilent N5242A PNA-X Network Analyser (hereafter called PNA). The integrated PC of PNA was used to run IGOR Pro software for fitting the measured $|S_{21}|^2$ data to a Lorentzian

lineshape in order to determine the Q_L, f_0 and f_B. The IGOR Pro code was developed by Simon Woodington (PhD student in the Centre for High Frequency Engineering, Cardiff School of Engineering) as the newly acquired PNA was mostly under his use and available for the compositional study experiments for only a limited time, mostly on weekends. Before undertaking the compositional analysis experiments, the Q_L of empty device was measured to be around 1000 because having gone through the bonding procedures. Based on this rather low starting number, the sweep on the IGOR Pro code was set to 1601 points and ten measurements per set were taken for each solution composition. 10 ml BD Discardit™ II syringes were used for fluid injection in conjunction with a KD Scientific dual syringe pump, the flow rate being set to 0.02 ml/min. Based on past experience with other resonator systems, the ambient temperature was monitored with a Kane-May KM340 digital thermometer during the course of all experiments. The resonator device was placed on a stand of adjustable height to align the fluid inlet microcapillary with the syringe, as illustrated in Figure 6.17.

Figure 6.17. Photograph showing layout for conducting compositional analysis experiments in the miniaturised SDR based microfluidic device. The resonator is positioned on stand next to the syringe pump and the PNA is on the far right.

6.3.1 **Acetonitrile:toluene Experiments**

The seventeen solutions prepared and stored in airtight jars at the beginning of compositional analysis using the hairpin resonator, as described in section 5.2, were available in sufficient quantity. Two sets of measurements were carried out instead of three – each consuming more than a day's time – because of the large length of time involved in gathering the data for the 17 solutions. The average Q_L, f_0 and f_B results of the ten measurements are as shown in Table 6.1, as are the ambient temperature and sensitivity of measurement (worked out for 56 nl fluid volume) in units of MHz/µl.

Solution		**Mean Results (25 Feb 09)**			**Mean Results (27 Feb 09)**		
% Toluene	**% MeCN**	f_0 **(GHz)**	f_B **(MHz)**	Q_L	f_0 **(GHz)**	f_B **(MHz)**	Q_L
100	0	21.7230	23.1048	940	21.7211	23.3711	929
99.9	0.1	21.7226	23.4096	928	21.7211	23.6289	919
99	1	21.7211	24.3024	894	21.7209	24.3549	892
97.5	2.5	21.7188	25.9270	838	21.7188	25.8477	840
95	5	21.7137	29.8637	727	21.7159	28.7674	755
90	10	21.7095	33.9232	640	21.7138	30.7529	706
82.5	17.5	21.6999	41.9635	517	21.7073	36.9109	588
75	25	21.6936	48.3166	449	21.6966	46.4245	467
50	50	21.6718	56.0534	387	21.6770	55.0459	394
25	75	21.6534	66.3936	326	21.6600	61.7507	351
17.5	82.5	21.6465	71.9773	301	21.6552	66.7387	325
10	90	21.6377	77.5974	279	21.6524	63.1456	343
5	95	21.6306	82.0981	263	21.6458	72.7514	299
2.5	97.5	21.6424	76.2876	284	21.6425	76.6754	282
1	99	21.6419	74.6585	290	21.6459	73.4236	295
0.1	99.9	21.6349	76.5362	283	21.6476	70.8358	306
0	100	21.6335	78.0313	277	21.6467	72.3433	300
Sensitivity (MHz/µl)		1590			1321		
Temperature		20 - 23 °C			19 - 22 °C		

Table 6.1. Measured Q_L, f_0 and f_B for the acetonitrile:toluene solution system.

The variation of resonant frequency, loaded quality factor and bandwidth against the solution composition is plotted in Figures 6.18 to 6.20.

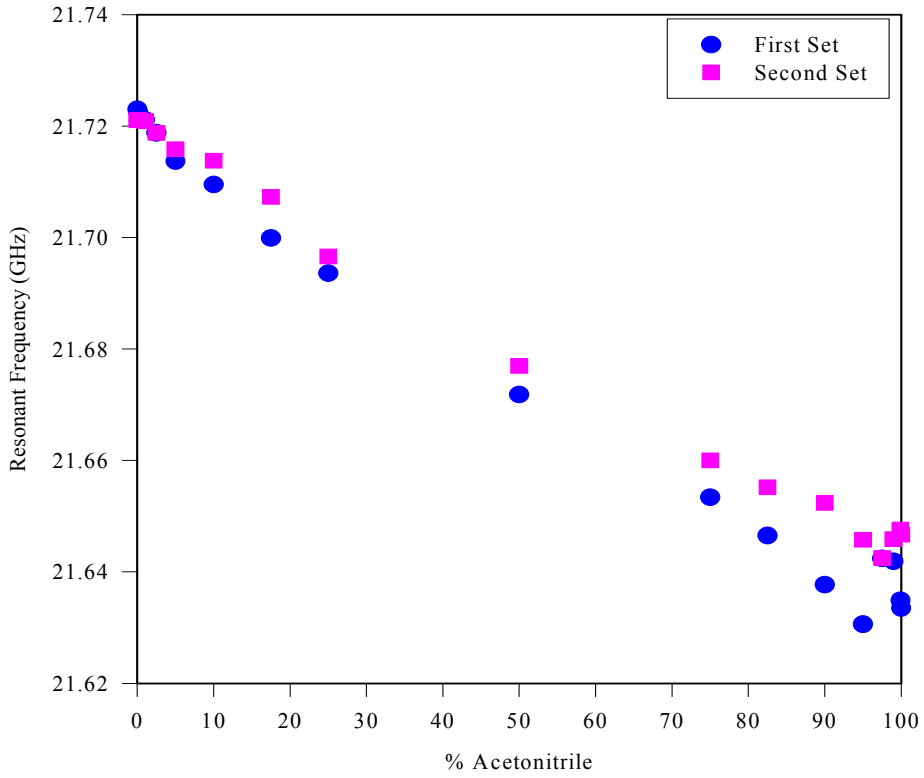

Figure 6.18. The resonant frequency as a function of solution composition for the acetonitrile:toluene system in miniaturised SDR.

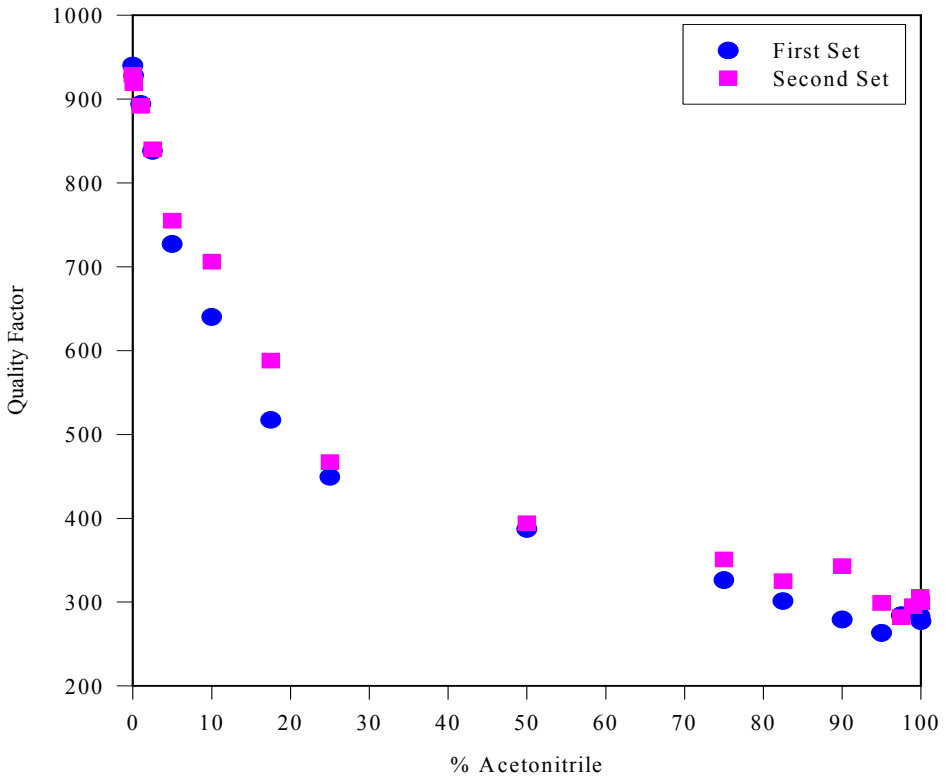

Figure 6.19. The loaded quality factor as a function of solution composition for the acetonitrile:toluene system in miniaturised SDR.

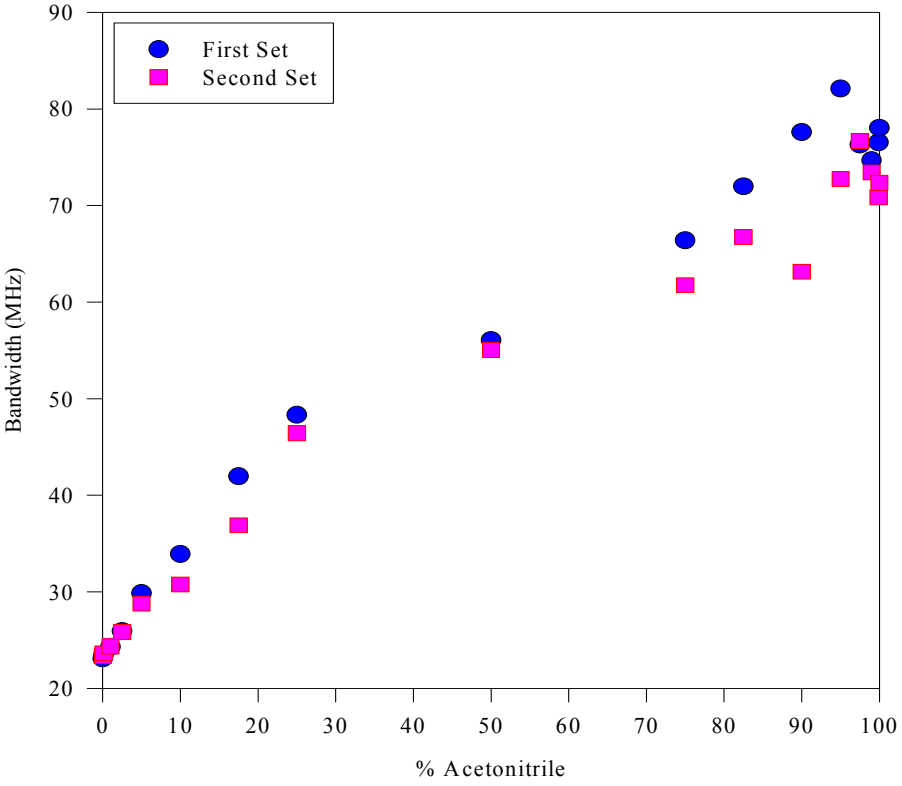

Figure 6.20. The bandwidth as a function of solution composition for the acetonitrile:toluene system in miniaturised SDR .

6.3.2 **Acetonitrile:water Experiments**

Previous experiments for this solution system were conducted using the HPLC pump, which mixes the required composition of solvents internally. Therefore, no solutions were available and had to be prepared for use with the miniaturised SDR. HPLC Grade acetonitrile (Fisher Scientific) and deionised water (Acros Organics) were used to make 15 ml quantity of each of the 17 solutions, employing the 5 ml, 1 ml and 200 µl Gilson Pipetman® adjustable pipettes following the same modus operandi as described for preparation of the acetonitrile:toluene solutions. The solutions were stored in 125 ml airtight jars (Fisher Scientific) and two sets of experiments were conducted using the same setup as shown in Figure 6.17. The mean Q_L, f_0 and f_B results are depicted in Table 6.2.

Solution		Results (1 Mar 09)			Results (15 Mar 09)		
% MeCN	% Water	f_0 (GHz)	f_B (MHz)	Q_L	f_0 (GHz)	f_B (MHz)	Q_L
100	0	21.6460	66.9990	323	21.6203	77.6566	278
99.9	0.1	21.6420	72.0190	308	21.6200	81.2780	266
99	1	21.6390	73.8070	293	21.6216	82.6112	262
97.5	2.5	21.6380	73.3170	290	21.6184	83.6156	259
95	5	21.6360	75.3690	287	21.6160	83.1380	260
90	10	21.6380	82.5190	262	21.6160	89.6920	241
82.5	17.5	21.6360	88.1920	245	21.6130	102.4300	211
75	25	21.6300	100.1600	216	21.6100	113.7360	190
50	50	21.6190	128.5200	168	21.6060	130.9450	165
25	75	21.6140	139.3200	155	21.6000	144.9660	149
17.5	82.5	21.6130	142.5500	152	21.6030	148.9860	145
10	90	21.6130	141.6400	153	21.5980	151.0340	143
5	95	21.6100	143.1000	151	21.5970	154.2640	140
2.5	97.5	21.6100	143.0100	151	21.5970	155.3741	139
1	99	21.6100	144.3200	150	21.5960	156.4928	138
0.1	99.9	21.6060	143.6100	150	21.5890	158.7426	136
0	100	21.6050	143.6400	150	21.5870	162.3080	133
Sensitivity (MHz/μl)		732			589		
Temperature:		19 - 21 °C			22 °C		

Table 6.2. Measured Q_L, f_0 and f_B for the acetonitrile:water solution system along with the temperature and measurement sensitivity obtained.

The variation of resonant frequency, loaded quality factor and bandwidth against the solution composition is plotted in Figures 6.21 to 6.23.

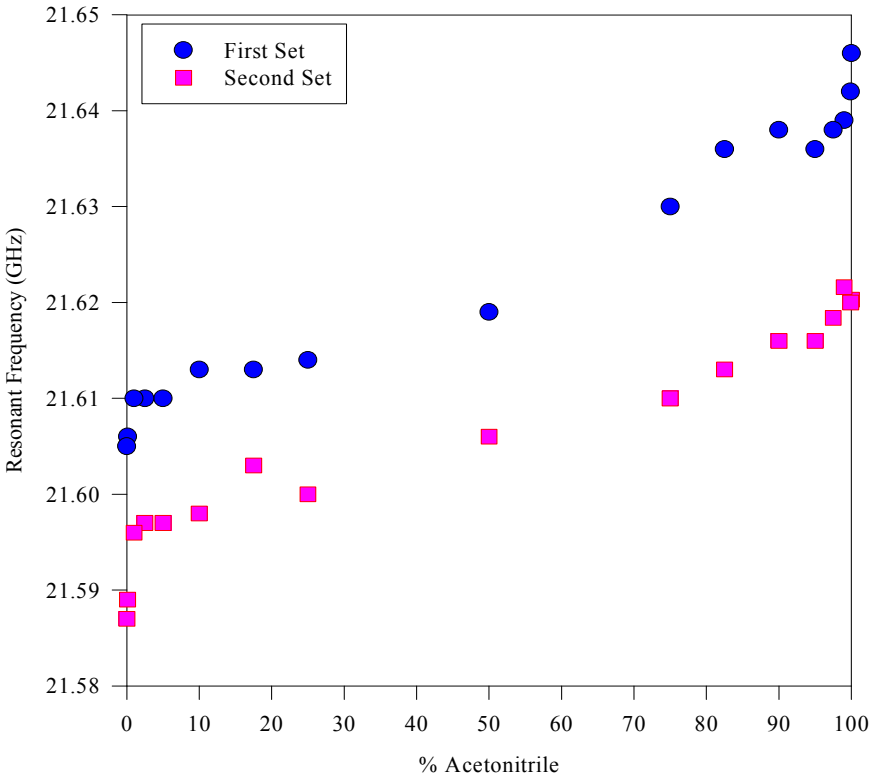

Figure 6.21. The resonant frequency as a function of solution composition for the acetonitrile:water system in miniaturised SDR.

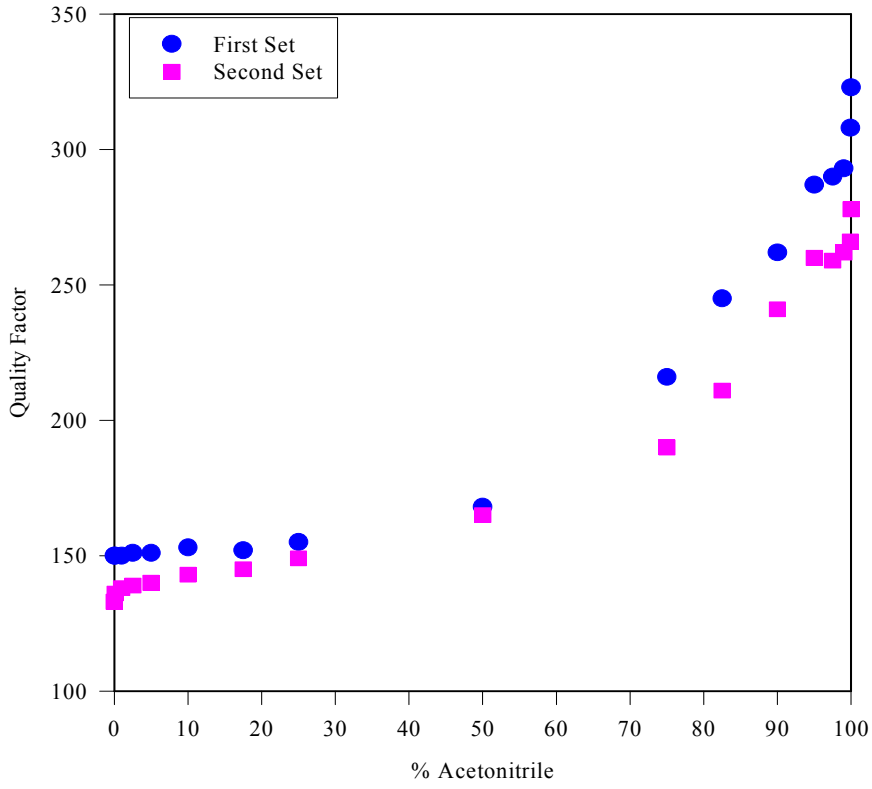

Figure 6.22. The loaded quality factor as a function of solution composition for the acetonitrile:water system in miniaturised SDR.

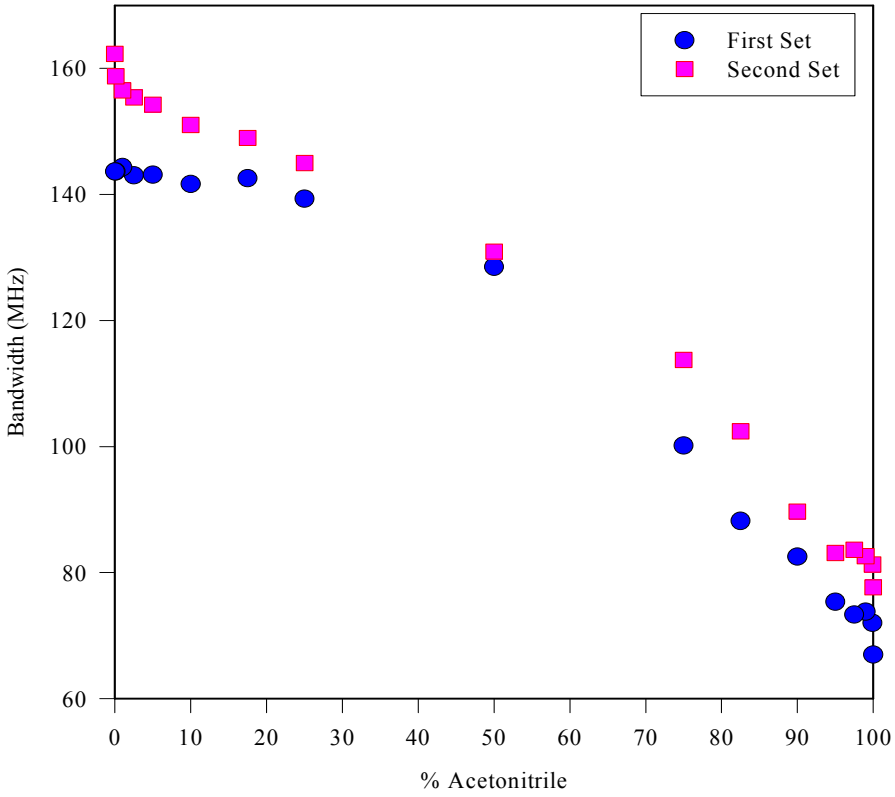

Figure 6.23. The bandwidth as a function of solution composition for the acetonitrile:water system in miniaturised SDR.

6.3.3 **Analysis of Experimental Results**

The mean of measured frequency sensitivity for the two sets of compositional analysis experiments carried out in the miniaturised resonator is compared with that of SDR in Table 6.3.

	Resonator	
	Miniaturised SDR	**SDR**
Sensitivity for MeCN:toluene (MHz/µl)	1455	2.16
Sensitivity for MeCN:water (MHz/µl)	661	2.74

Table 6.3. Summarised results for sensitivity of frequency measurement for both solution systems evaluated in miniaturised SDR.

The results obtained with the miniaturised dielectric resonator bring forth the following notable points:

- The measurements are repeatable (i.e. they follow the same trend for the two sets), thereby meaning that the experimental setup was robust. The slight difference in results can be attributed to temperature variations as the experiments were not conducted in a constant temperature environment. Due to the large length of time involved in completion of a measurement set, the temperature varied by up to 4 °C as indicated in Tables 6.1 and 6.2. Since the complex permittivity of polar liquids (i.e. water and acetonitrile) is strongly temperature dependent as against the non-polar toluene [22-24], the temperature deviations have a considerable bearing on the accuracy of measured results.
- For most part, the resonant frequency decreases monotonically as the polar nature of the solution increases (Figures 6.18 and 6.21), which is expected because of the electric field being parallel to the micro fluidic channel. The measurement sensitivity over the full range of solutions is a great deal more here, i.e. 1455 MHz/µl for the acetonitrile:toluene system and 661 MHz/µl for the acetonitrile:water system. This corresponds to a 700 fold increase in sensitivity over the bigger SDR for the former whereas about 250 folds for the latter, both of which are much greater than the expected 100 are times enhancement. The apparent reason behind this discrepancy is imprecise (i.e. less than actual) measurement of the microchannel dimensions, especially width. The comparatively larger enhancement in measurement sensitivity for the acetonitrile:toluene system can be attributed to the fact the complex permittivity of water exhibits stronger frequency dependence than acetonitrile. The dielectric constant (ε_1) of water reduces from about 75 at 5 GHz (i.e. the resonant frequency for bigger SDR) to approximately 39 at 22 GHz [2,22,25], while the corresponding drop for acetonitrile is from 37 to 28 [24,26][‡]. The dielectric properties of toluene do not display any frequency dependence as its ε_1 stays largely constant at 2.5 over the frequency range under consideration [27]. Hence, the better match in molecular electric dipole moments (i.e. $\propto \varepsilon_1$) of the acetonitrile:water becomes even closer at higher frequencies, thus resulting in relatively smaller enhancement in measurement sensitivity.

[‡] Ideally the variation of complex permittivity over the full range of both solutions should be measured by say, coaxial probe. However, this could not be done due to extremely limited availability of the PNA.

- Q_L decreases consistently (Figures 6.19 and 6.22) as the percentage of acetonitrile in acetonitrile:toluene system and water in acetonitrile:water mixtures increases. This result is expected from the resonator perturbation analysis presented in chapter 2 because of the substantially higher loss ($\varepsilon_2 \approx 37$ for water and ≈ 12 for acetonitrile at 22 GHz) of the polar solvents than non-polar toluene [25,26].

References

[1] D. A. Barrow, *Private Communications*, 2007-9.

[2] A. Porch, *Private Communications*, 2007-8.

[3] S. B. Cohn, "Microwave Bandpass Filters Containing High-Q Dielectric Resonators", *IEEE Transactions on Microwave Theory and Techniques*, Vol. MTT-16, No. 4, pp. 218-227, April 1968.

[4] N. Sykes, *Private Communications*, 2007-8.

[5] D. S. Shin, J. H. Lee and J. Suh, "Microfabrication of Polymers Using KrF Excimer Laser Beam", *Key Engineering Materials*, Vols. 326-328, pp. 115-118, 2006.

[6] D. S. Shin, J. H. Lee, J. Suh and T. H. Kim, "Elimination of Surface Debris Generated by KrF Excimer Laser Ablation of Polyimide", *Materials Science and Engineering A*, Vol. 416, pp. 205-210, 2006.

[7] K. L. Choo, Y. Ogawa, G. Kanbargi, V. Otra, L.M. Raff and R. Komanduri, "Micromachining of Silicon by Short-pulse Laser Ablation in Air and Under Water", *Materials Science and Engineering A*, Vol. 372, pp. 145-162, 2004.

[8] G. Daminelli, J. Kruger and W. Kautek, "Femtosecond Laser Interaction with Silicon under Water Confinement", *Thin Solid Films*, Vol. 467, pp. 334-341, 2004.

[9] A. Kruusing, "Underwater and Water-assisted Laser Processing: Part 1—General Features, Steam Cleaning and Shock Processing", *Optics and Lasers in Engineering*, Vol. 41, pp. 307-327, 2004.

[10] V. Mizeikis, S. Juodkazis, J. Ye, A. Rode, S. Matsuo and H. Misawa, "Silicon Surface Processing Techniques for Micro-systems Fabrication", *Thin Solid Films*, Vols. 438-439, pp. 445-451, 2003.

[11] http://www.aml.co.uk/bondcentre.htm (accessed 4th June 2009).

[12] N. Aitken (AML), *Private Communications*, 2007-8.

[13] P. Kopperschmidt, G. Kästner, D. Hesse, U. M. Gösele and M. Lorenz, "Back-to-back Substrate Wafer Bonding: A New Approach to the Fabrication of Double-side Coated Wafers", *Applied Physics A*, Vol. 64, pp. 211-212, 1997.

[14] J. Haisma, G. A. C. M. Spierings. T. M. Michielsen and C. L. Adema, "Surface Preparation and Phenomenological Aspects of Direct Bonding", *Philips Journal of Research*, Vol. 49, No. l/2, pp. 23-46, 1995.

[15] http://www2.dupont.com/Teflon_Industrial/en_US/assets/downloads/h44587.pdf (accessed 6th June 2009).

[16] M. N. Rahaman, *Ceramic Processing and Sintering*, Second Edition, CRC Press, 2003, ISBN 0-8247-0988-8.

[17] R. Sharma, V. E. Hamilton-winbush and T. L. Penner, "Method for Cleaning an Ink Jet Print Head", *United States Patent 6193352*, 27 February 2001.

[18] Wikipedia contributors, "Piranha solution", *Wikipedia, The Free Encyclopedia,* http://en.wikipedia.org/w/index.php?title=Piranha_solution&oldid=287429724 (accessed 8th June 2009).

[19] W. Kern (Editor), "*Handbook of Semiconductor Wafer Cleaning Technology: Science, Technology, and Applications*", Noyes Publishers, N.J., 1993, ISBN 0-8155-1331-3.

[20] O. Castell, *Private Communications*, 2008-9.

[21] http://macro.lsu.edu/howto/solvents/viscosity.htm (accessed 10th June 2009).

[22] A. P. Gregory and R. N. Clarke, "A Review of RF and Microwave Techniques for Dielectric Measurements on Polar Liquids", *IEEE Transactions on Dielectrics and Electrical Insulation*, Vol. 13, No. 4, pp. 727-743, August 2006.

[23] J. Lou, A. K. Paravastu, P. E. Laibinis and T. A. Hatton, "Effect of Temperature on the Dielectric Relaxation in Solvent Mixtures at Microwave Frequencies", *Journal of Physical Chemistry A*, Vol. 101, Issue 51, pp. 9892-9899, December 1997.

[24] Krishnaji and A. Mansingh, "Dielectric Relaxation in Alkylcyanides", *Journal of Chemical Physics*, Vol. 41, No. 3, pp. 827-831, August 1964.

[25] K. S. Kunz and R. J. Luebbers, "*The Finite Difference Time Domain Method for Electromagnetics*", CRC Press, 1993, ISBN 0849386578.

[26] J. Barthel, K. Bachhuber, R. Buchner, J. B. Gill and M. Kleebauer, "Dielectric Spectra of Some Common Solvents in the Microwave Region. Dipolar Aprotic Solvents and Amides", *Chemical Physics Letters*, Vol. 167, No. 1,2, pp. 62-66, March 1990.

[27] J. Lou, T. A. Hatton and P. E. Laibinis, "Effective Dielectric Properties of Solvent Mixtures at Microwave Frequencies", *Journal of Physical Chemistry A*, Vol. 101, Issue 29, pp. 5262-5268, July 1997.

CHAPTER 7

CONCLUSIONS AND RECOMMENDATIONS

7.1 Conclusions

a. Microwave resonators of both lumped and distributed element type have been used for analysing acetonitrile:toluene and acetonitrile:water mixtures in microcapillary manifold systems. The experimental results are shown to be highly reproducible and follow the predictions of resonator perturbation theory. There are numerous benefits of this resonant microwave technique over other methods. Firstly, it is extremely sensitive and has been demonstrated to accurately analyse liquid volumes as small as 50 nl. The sensitivity of measurement in the worst case (i.e. hairpin resonator) is 190 KHz/μl that is still much better than resonator techniques where the field energy is distributed over a larger volume (e.g. [1]). Secondly, it is fast with data accumulation on a timescale of approximately 0.1 s, thereby enabling compositional analysis in situations where fluid flow and/or chemical reaction are occurring. Thirdly, it is non-destructive and applicable to arbitrarily-shaped sample volumes.

b. The biggest contribution of this work has been the development of a miniaturised SDR based device for compositional analysis of liquid mixtures. It turned out to be enormously challenging – especially due to little support available from current literature on the subject – taking around a year's time for completion. Nonetheless, the reward was in the form of astonishing sensitivity of frequency measurement (≈ 1 GHz/μl) for the acetonitrile:toluene solution system.

c. The proportion of acetonitrile in toluene has been measured to an accuracy of < 0.1% by all resonators employed in this project. Keeping in view the sensitivity provided by the split ring and miniaturised SDR, it is expected that they can detect even smaller amounts of acetonitrile. This could be confirmed by measuring solutions of 0.05% - 0.1% acetonitrile in toluene in both the aforementioned resonators. Similar accuracies of measurement are observed

for detection of water in acetonitrile in all the resonators used. Other solution systems could be tested in future to further validate the findings of this research.

7.2 Recommendations

a. The real ε_1 and imaginary ε_2 parts of the complex relative permittivity of the component liquids for acetonitrile:toluene mixtures were measured with a coaxial probe, which sufficed for hairpin, split ring and SDR experiments. However, the permittivity measurement at 22 GHz frequency i.e. for use with miniaturised SDR could not be done due to non-availability of the PNA. Likewise, the acetonitrile:water solutions could also not be measured for any of the resonators and instead static permittivity data from relevant literature (i.e. [2]) was used. Since the complex permittivity of polar liquids is strongly frequency dependent, it should ideally have been measured at 22 GHz for both solution systems used in order to establish its variation with solution composition. This could be carried out in future work on the subject.

b. The measurements in this project were carried out in non-constant temperature environment, which was found to affect the accuracy of results provided by the network analysers used. Although a record of variations in ambient temperature over the course of experiments was maintained, its influence on obtained results was not determined because the recorded temperature did not represent that of fluid sample. It is thus recommended for future projects that such experiments are conducted with an arrangement to monitor the sample temperature as closely as possible (e.g. using a thermocouple) so as to establish temperature effects on measured results.

c. The resonators used in this research are equally suitable for effective volumetric heating of the liquid samples, which was not considered as this is beyond the scope of this project. However, this aspect could be explored in future work for achievement of microwave assisted chemical synthesis in microfluidic reactors. In this connection, the miniaturised SDR based microfluidic device can provide heating at an extremely minute scale.

d. The high sensitivity of resonators under consideration to small concentrations of a polar solvent within a non-polar host might have interesting applications for the detection of water contamination in solvents. In this connection, the problem of water contamination in oil in transformer coils is worth mentioning, which could be tackled by making suitable modifications in the geometry of the split ring resonator.

e. The resonators employed in this research have considerable potential for use in pharmaceutical applications, such as monitoring phase separation of a multiphase-flow regime utilised for continuous molecular enrichment [3]. This was carried out with the aid of a hairpin resonator and could be further pursued for related work.

f. Transmission mode measurements with microwave resonators have the potential to provide real-time diagnosis of chemical reaction completion. This has already been evaluated (in association with Cardiff School of Chemistry) for an ester formation from a carboxylic acid (benzoic acid) and an alcohol (*n*-butanol). Water is liberated during the formation of the ester (*n*-butyl benzoate) and the amount of water in the reaction mixture has been monitored by the split-ring resonator. This simple ester formation has demonstrated that even small amounts of water (≈ 3%) can be reliably detected using this methodology and the presence of other molecules such as the alcohol and the ester do not interfere with the measurement. The possibilities of such real-time reaction monitoring with microwave resonators could be further investigated, particularly in the backdrop of the fast-expanding inter disciplinary research activities.

References

[1] K. Saeed, A. C. Guyette, I. C. Hunter and R. D. Pollard, "Microstrip Resonator Technique for Measuring Dielectric Permittivity of Liquid Solvents and for Solution Sensing", *IEEE/MTT-S International Microwave Symposium 2007*, pp. 1185-1188, June 2007.

[2] L. G. Gagliardi, C. B. Castells, C. Ràfols, M. Rosés and E. Bosch, "Static Dielectric Constants of Acetonitrile/Water Mixtures at Different Temperatures and Debye–Hückel A and a_0B Parameters for Activity Coefficients", *Journal of Chemical and Engineering Data*, Vol. 52, Issue 3, pp. 1103-1107, May 2007.

[3] O. Castell, A. Masood, R. Göritz, D. A. Barrow, C. Allender and A. Porch, "Microwave Technique for Monitoring Separation of a Multiphase-Flow Regime Utilised for Continuous Molecular Enrichment", *The Proceedings of MicroTAS 2008 Conference*, San Diego, pp.137-139, October 2008.

APPENDIX A: Two-Port Resonator Analysis with Symmetrical Coupling

Before proceeding with the analysis, it should be noted that the polarity of voltage induced through transformer action depends on the direction of current and whether it is flowing in the primary or secondary coil, as shown in Figure A.1 [2].

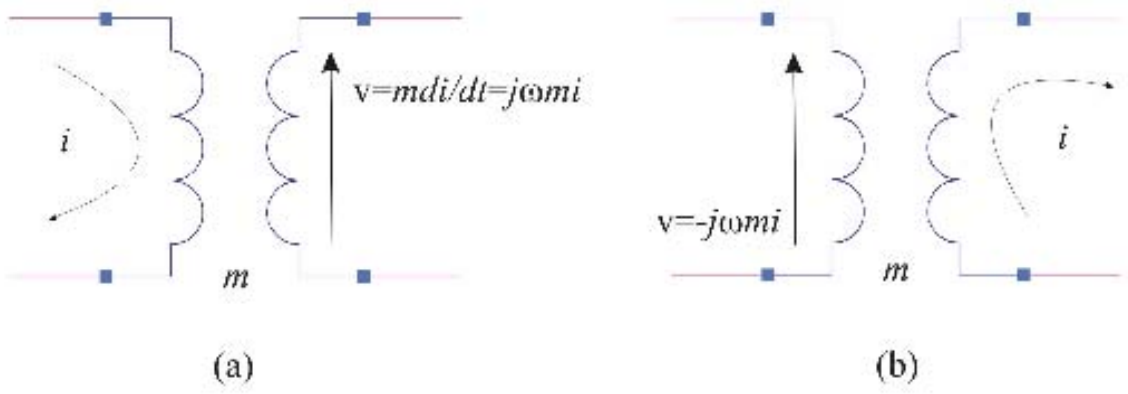

Figure A.1 Polarity of voltage induced in the secondary coil is positive when current is flowing in clockwise direction in the primary, as shown in (a) whereas the same current flowing in the same direction in the secondary coil induces a voltage of equal magnitude but opposite polarity in the primary, as illustrated in (b)

It follows from above that the equivalent circuit of a resonator at resonance, with induced voltage polarities, would be as depicted in Figure A.2.

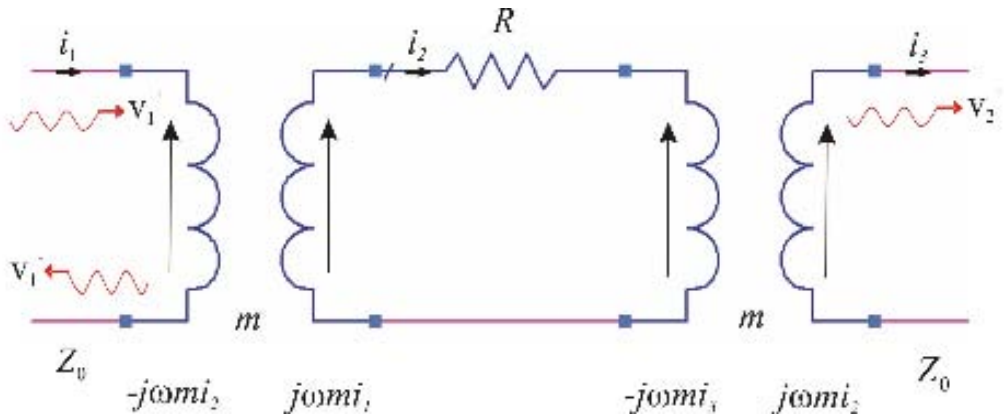

Figure A.2 Two-Port resonator equivalent circuit at resonance. Note the polarities of voltages induced in the input, resonator, and output circuit

Now, the voltage/current equations for the three circuits of Figure A.2 can be written as below [1,2]:

Input Circuit:

$$v_1^+ + v_1^- = -j\omega m i_2 , \tag{A.1}$$

$$v_1^+ - v_1^- = i_1 Z_0 . \tag{A.2}$$

Output Circuit:

$$v_2^+ = j\omega m i_2 = -(v_1^+ + v_1^-) , \tag{A.3}$$

$$i_3 = \frac{v_1^+}{Z_0} = \frac{-(v_1^+ + v_1^-)}{Z_0} . \tag{A.4}$$

Resonator Circuit:

$$j\omega m i_1 + j\omega m i_2 = i_2 R . \tag{A.5}$$

Since $i_1 = \frac{v_1^+ - v_1^-}{Z_0}$ (from (A.2)) and $i_2 = \frac{-(v_1^+ + v_1^-)}{j\omega m}$ (from (A.3)), (A.5) can be rewritten as

$$\frac{j\omega m}{Z_0}(v_1^+ - v_1^-) - \frac{j\omega m}{Z_0}(v_1^+ + v_1^-) = -\frac{R}{j\omega m}(v_1^+ + v_1^-) . \tag{A.6}$$

$$\therefore 2v_1^- = \frac{-RZ_0}{\omega^2 m^2}(v_1^+ + v_1^-) = -\frac{1}{g}(v_1^+ + v_1^-) , \tag{A.7}$$

where g is the coupling coefficient defined as $g = \frac{\omega^2 m^2}{RZ_0}$.

Now, (A.7) and definition of S_{11} (i.e. $S_{11} = \frac{v_1^-}{v_1^+}$) give

$$S_{11} = -\frac{1}{1+2g} . \tag{A.8}$$

Further on, from (A.3) S_{21} can be written as

$$S_{21} = -(1 + S_{11}) , \tag{A.9}$$

which along with (A.8) yields

$$S_{21} = \frac{-2g}{1+2g}. \tag{A.10}$$

References

[1] A. Porch, *Private Communication*, 2008.

[2] D. M. Pozar, *Microwave Engineering*, Third Edition, John Wiley & Sons, N.Y., 2005, ISBN 0-471-44878-8.

APPENDIX B: Text Input File for Superfish Analysis of SDR

```
FISH Test:  Sapphire dielectric resonator
1 iteration, no resonance search
&reg kprob=1,icylin=1,dx=.01,dy=.01          ;kprob defines the problem (1: Superfish
                                              problem, 0: Poisson problem), icylin
                                              designates coordinate system (0:
                                              Rectangular, 1: Cylindrical), dx and dy
                                              specify the x and y mesh size,
                                              respectively, in the first region
nbsup=0, nbslo=0, nbsrt=0, nbslf=0,          ;Describe the boundary conditions on the
                                              edges of the problem geometry
XDRI=1.16,YDRI=0.10,maxcy=10,freq=5000 &     ;xdri and ydri state x and y location for
                                              drive point, maxcy sets maximum
                                              number of cycles to find resonance, freq
                                              provides approximate resonant frequency

&po x=0.0,y=0.0 &
&po x=0.0,y=2.5 &
&po x=2.32,y=2.5 &                           ;Assign the boundaries for cavity
&po x=2.32,y=0.0 &
&po x=0.0,y=0.0 &

&reg mat=2 &
&po x=0.0,y=0.0 &
&po x=0.0,y=0.25 &
&po x=0.6,y=0.25 &
&po x=0.6,y=1.0 &                            ;Assign the boundaries for top sapphire puck
&po x=1.1,y=1.0 &
&po x=1.1,y=0.0 &
&po x=0.0,y=0.0 &

&mt mtid=2
epsilon=1,                                   ;Assign ε and μ values for top sapphire puck
mu=9.4 &


&reg mat=3 &
&po x=1.22,y=0.0 &
&po x=1.22,y=1.0 &
&po x=1.72,y=1.0 &
&po x=1.72,y=0.25 &                          ;Assign the boundaries for bottom sapphire puck
&po x=2.32,y=0.25 &
&po x=2.32,y=0.0 &
&po x=1.22,y=0.0 &


&mt mtid=3
epsilon=1,                                   ;Assign ε and μ values for bottom sapphire puck
```

```
mu=9.4 &


&reg mat=4 &
&po x=0.0,y=0.25 &
&po x=0.0,y=0.75 &
&po x=0.6,y=0.75 &                    ;Assign the boundaries for top PTFE support
&po x=0.6,y=0.25 &
&po x=0.0,y=0.25 &

&mt mtid=4
epsilon=1,                            ;Assign ε and μ values for top PTFE support
mu=2.06 &


&reg mat=5 &
&po x=1.72,y=0.25 &
&po x=1.72,y=0.75 &
&po x=2.32,y=0.75 &                   ;Assign the boundaries for bottom PTFE support
&po x=2.32,y=0.25 &
&po x=1.72,y=0.25 &

&mt mtid=5
epsilon=1,                            ;Assign ε and μ values for bottom PTFE support
mu=2.06 &
```

APPENDIX C: Mathcad Code for Calculation of SDR Unloaded Q

$Rc := 2.5 \cdot 10^{-2}$ radius of cavity in m

$Lc := 2.32 \cdot 10^{-2}$ length of cavity in m

$N := 250$ number of points along the radial and longitudinal directions

$\Delta r := \frac{Rc}{N} \quad \Delta z := \frac{Lc}{N}$

$\mu 0 := 4 \cdot \pi \cdot 10^{-7} \quad \varepsilon 0 := 8.854 \cdot 10^{-12}$

A := READPRN("C:\LANL\outsf7.txt")

$f := A_{(N+1)^2, 0} \cdot 10^9$ resonant frequency (Hz), computed by SF $f = 5.2486 \times 10^9$

$\omega := 2 \cdot \pi \cdot f$

$\rho := 2 \cdot 10^{-8} \quad Rs := \sqrt{\pi \cdot \mu 0 \cdot f \cdot \rho}$ resistivity (Ωm) and surface resistance of cavity walls

$Rs = 0.02036$

$m := 0 .. N \qquad n := 0 .. N$

$E\phi_{m,n} := A_{n+m\cdot(N+1),5}$

$Hz_{m,n} := A_{n+m\cdot(N+1),2}$

$Hr_{m,n} := A_{n+m\cdot(N+1),3}$

$Htot_{m,n} := A_{n+m\cdot(N+1),4}$

$H_{m,n} := Htot_{N-m,n} \qquad r_m := m \cdot \Delta r$

$H_{m+N-1,n} := Htot_{m,n} \qquad z_n := n \cdot \Delta z$

$E_{m,n} := E\phi_{N-m,n}$

$E_{m+N-1,n} := E\phi_{m,n}$

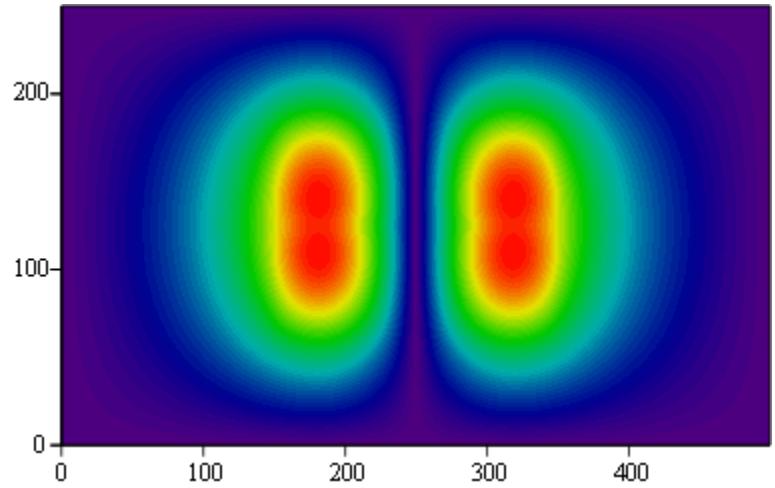

E

Magnitude of E (axis in centre)

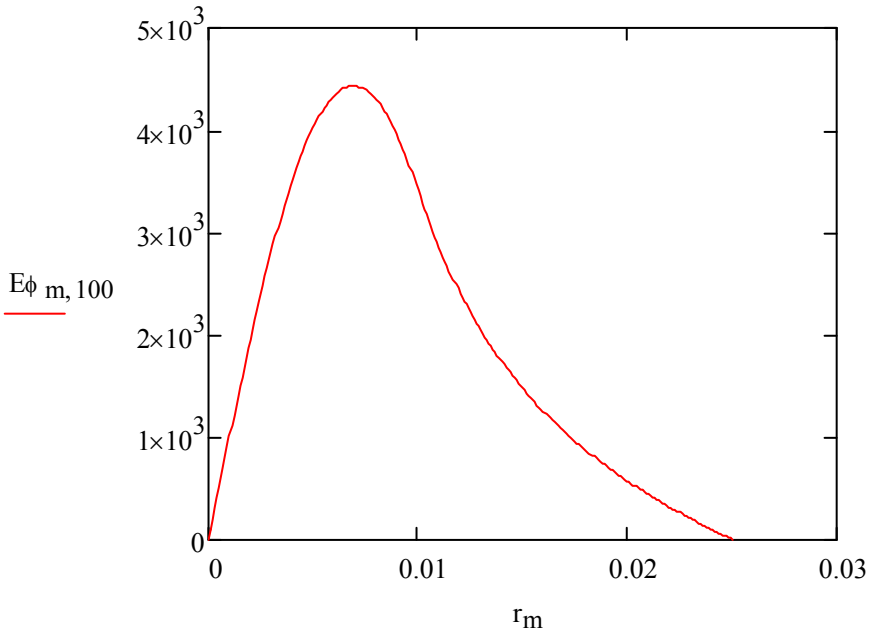

Radial uniformity of Eϕ

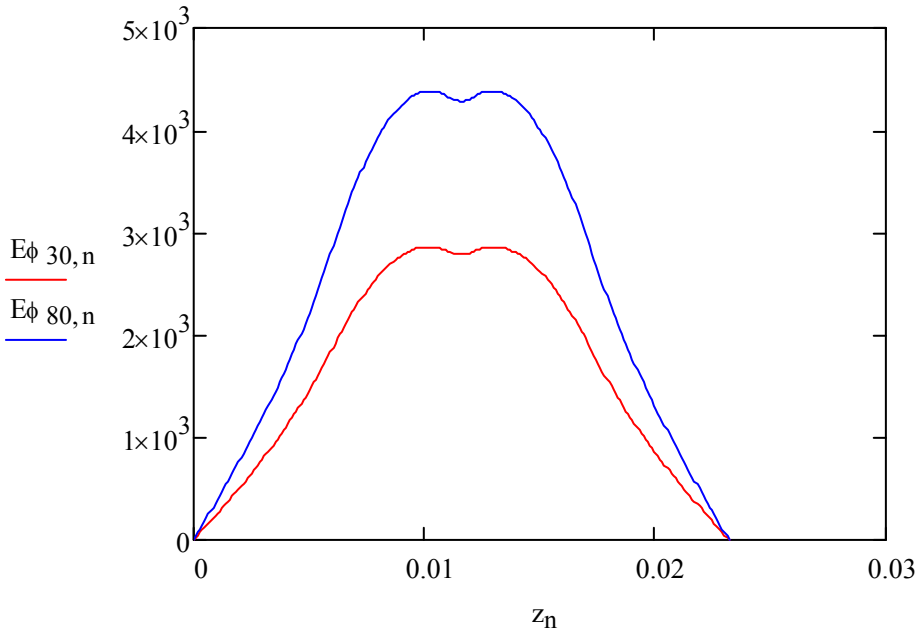

Longitudinal uniformity of Eϕ

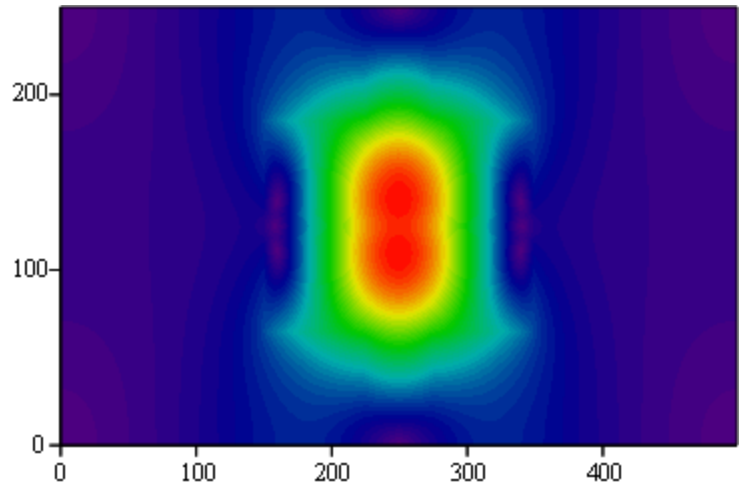

H

Magnitude of H (axis in centre)

Conductor Curved Wall Losses

$m := 0 .. (N - 1)$ $n := 0 .. (N - 1)$

$\Delta Sc := 2 \cdot \pi \cdot Rc \cdot \Delta z$

$Hav_n := \frac{1}{2} \cdot \left(Hz_{N,n} + Hz_{N,n+1} \right)$ $Pc := \sum_{n=0}^{231} \left[\left(Hav_n \right)^2 \cdot \Delta Sc \cdot Rs \right]$

Conductor End Wall Losses

$m := 0 .. (N - 1)$ $\Delta S_m := \pi \cdot \left[(m + 1)^2 - m^2 \right] \cdot \Delta r^2$

$n := 0 .. (N - 1)$

$Hav\_t_m := \frac{1}{2} \cdot \left(Hr_{m,N} + Hr_{m+1,N} \right)$ $Hav\_b_m := \frac{1}{2} \cdot \left(Hr_{m,0} + Hr_{m+1,0} \right)$

$Pt := \sum_{m=0}^{N-1} \left[\left(Hav\_t_m \right)^2 \cdot \Delta S_m \cdot Rs \right]$ $Pb := \sum_{m=0}^{N-1} \left[\left(Hav\_b_m \right)^2 \cdot \Delta S_m \cdot Rs \right]$

$Pc = 4.72631 \times 10^{-6}$ $Pt = 1.87411 \times 10^{-5}$ $Pb = 1.87417 \times 10^{-5}$

$Ptot := Pc + Pt + Pb$

$Ptot = 4.22091 \times 10^{-5}$

Stored Energy for Qc

$\Delta V_m := \Delta z \cdot \pi \cdot \left[(m + 1)^2 - m^2 \right] \cdot \Delta r^2$

$Hav_{m,n} := \frac{1}{4} \cdot \left(Htot_{m,n} + Htot_{m,n+1} + Htot_{m+1,n} + Htot_{m+1,n+1} \right)$

$UM := \frac{1}{2} \cdot \mu 0 \cdot \sum_{m=0}^{N-1} \left[\sum_{n=0}^{231} \left(Hav_{m,n} \right)^2 \cdot \Delta V_m \right]$

$UM \cdot 10^{12} = 37.64189$

$Utot := 2 \cdot UM$ Total energy stored in the volume of the cavity

$Utot = 7.52838 \times 10^{-11}$

$$Qc := \omega \cdot \frac{Utot}{Ptot}$$

$Qc = 5.8819 \times 10^{4}$ Q value of conductor

Stored Energy for Qd

$tan\delta := 1 \cdot 10^{-5}$ $\varepsilon r := 9.4$ loss tangent and dielectric constant of sapphire

$tan\delta 1 := .0002$ $\varepsilon r1 := 2.06$ loss tangent and dielectric constant of PTFE

$$Eav_{m,n} := \frac{1}{4} \cdot \left(E\phi_{m,n} + E\phi_{m,n+1} + E\phi_{m+1,n} + E\phi_{m+1,n+1} \right)$$

$$\Delta V_m := \Delta z \cdot \pi \cdot \left[(m+1)^2 - m^2 \right] \cdot \Delta r^2$$

$$UE1 := \sum_{m=75}^{249} \left[\sum_{n=0}^{59} \left(Eav_{m,n} \right)^2 \cdot \Delta V_m \right] \qquad UE1 = 3.58941$$

$$UE2 := \sum_{m=25}^{74} \left[\sum_{n=0}^{59} \left(Eav_{m,n} \right)^2 \cdot \Delta V_m \cdot \varepsilon r1 \right] \qquad UE2 = 2.91401$$

$$UE3 := \sum_{m=0}^{24} \left[\sum_{n=0}^{59} \left(Eav_{m,n} \right)^2 \cdot \Delta V_m \cdot \varepsilon r \right] \qquad UE3 = 0.34185$$

$$UE4 := \sum_{m=0}^{99} \left[\sum_{n=60}^{109} \left(Eav_{m,n} \right)^2 \cdot \Delta V_m \cdot \varepsilon r \right] \qquad UE4 = 162.41804$$

$$UE5 := \sum_{m=100}^{249} \left[\sum_{n=60}^{109} \left(Eav_{m,n} \right)^2 \cdot \Delta V_m \right] \qquad UE5 = 10.02697$$

$$UE6 := \sum_{m=0}^{249} \left[\sum_{n=110}^{121} \left(Eav_{m,n} \right)^2 \cdot \Delta V_m \right] \qquad UE6 = 8.72961$$

$$UEtot := 2 \cdot UE1 + 2 \cdot UE2 + 2 \cdot UE3 + 2UE4 + 2UE5 + UE6$$

$$UEtot = 367.31018$$

$$Ws := \frac{UEtot - 2 \cdot UE3 - 2UE4}{2 \cdot UE3 + 2UE4} \qquad Ws = 0.12838 \qquad \text{W for sapphire}$$

$$Qds := \frac{1 + Ws}{tan\delta} \qquad Qds = 1.12838 \times 10^5 \qquad \text{Qd of sapphire}$$

$$Wp := \frac{UEtot - 2 \cdot UE2}{2 \cdot UE2} \qquad Wp = 62.02495 \qquad \text{W for PTFE}$$

$$Qdp := \frac{1 + Wp}{tan\delta l} \qquad Qdp = 3.15125 \times 10^5 \qquad \text{Qd of PTFE}$$

$$Qd := \frac{Qdp \cdot Qds}{Qdp + Qds} \qquad Qd = 8.30868 \times 10^4 \qquad \text{Overall Qd}$$

$$Qu := \frac{Qd \cdot Qc}{Qd + Qc} \qquad Qu = 3.44389 \times 10^4 \qquad \textbf{Final unloaded Q}$$

$$IL := -22.5 \qquad \text{Resonator insertion loss}$$

$$QL := Qu \cdot \left(1 - 10^{\frac{IL}{20}} \right) \qquad QL = 3.18564 \times 10^4 \qquad \text{Calculated loaded Q}$$

$$Qmeas := 28300 \qquad \text{Measured Q} \qquad error := \frac{QL - Qmeas}{Qmeas}$$

$$error \cdot 100 = 12.5667 \qquad \%\text{age error between measured and loaded QL}$$

APPENDIX D: IGOR Pro Code Used for Acquiring $|S_{21}|^2$ Data from Agilent (HP) 8753E VNA and Curve Fitting to Lorentzian

```
#pragma rtGlobals=1          // Use modern global access method.
#pragma rtGlobals=1          // Use modern global access method.
#include  <SaveGraph>

//WAVEFORM SOFTWARE
//This file is for GPIB Control,

//          GPIB CONTROL specific procedures, functions, etc

Proc GPIB_Init()

        //Start of variable definitions
        // GPIB controlled instruments wave - used to set what is and is not used in
        //particular measurement setup, controlled through panel
make/o/n=(30) instr_used

        // Other Global definitions here

// Create global variables used for holding current values of tick boxes for instruments used
variable/G inst16  // 8753 at address 16

string/g Command // decide exactly which instruments require initialisation

dowindow select_instruments_used  // interrogate the window
        if(v_flag==0)
                execute "select_instruments_used()"  // if not open, then open window
        else
        dowindow/f select_instruments_used  // if already open, just switch to that window
        endif
        // update variables associated with checkbox values from instr_used array
        inst16=instr_used[16]

        // assign variables to checkboxes, select the panel, and grey out if instrument GPIB
        //address cannot be found
checkbox HP_8753 variable=inst16, win=select_instruments_used, disable=Inst_Register[16]


End

Function GPIB_Output(Instrument,command)        //Writes Data to the GPIB Bus
variable Instrument
string command
variable/G Instrument_G=Instrument
string/G command_G=command
Silent 1;PauseUpdate
```

```
	Execute "GPIB device, Instrument_G"
	Execute "GPIBWrite/F=\"%s\" Command_G"
	//Kills external variables once complete
	killvariables/z Instrument_G
	killstrings/z command_G
End

Macro SetupGPIB()  //Used To initialise All 'required' Instruments on the GPIB Bus

	Silent 1

	string/G gpibBoardName="gpib0"     // sets the interface board name
	Variable/G gpibBoardNum=0                    // sets the interface number
	Variable/G gGPIBBoardRef, gGPIBDeviceRef          // Values set by SetupGPIB.
	Variable/G HP_8753
	Variable Board_num, count, temp = 0

	// find the GPIB interface board ud
	NI488 ibfind gpibBoardName, gGPIBBoardRef

	//Initalise and set GPIB interface board as 'controler in charge'
	NI488 ibsic gpibBoardNum
	NI488 SendIFC 0
	// Find out what instruments are there
	Make/O gAddressList = {16, -1}       // -1 is NOADDR - marks end of list.
	Make/O/N=30 gResultList; gResultList=-1   // make and initialise the result list wave
		Make/O/N=30 Inst_Register; Inst_Register=0  // make and initialise another
	//wave to hold the 'present' flag
	NI488 FindLstn gpibBoardNum, gAddressList, gResultList, 10       // may need to
	//increase '5' when adding more instruments
	Printf "Number of responses: %d\r", V_ibcnt

	// Can use the above 'Inst_Register' to generate register wave that is in turn used to
	//grey out in instrument,
	// disabling if not available for use
	do
		FindValue/V=(count) gResultList
		temp=V_value
		if (temp == -1)
			Inst_Register[count]=2
		else
		Inst_Register[count]=0          // use 2 as this greys out checkbox, and array can
//be used directly with 'disable' switch. 0 will cause the item to be activated
		endif
		count+=1
	while (count<=30)

// use NI488 'ibdev' command to assign identifiers to instruments. Timeout values are set to
//13=10 seconds for all instruments.
```

```
	if (inst_register[16]==0)		// nb . using gpib address as index to array
		NI488 ibdev gpibBoardNum, 16, 0, 13, 1, 0, HP_8753		// assign a
ud for the AWG at address 25
		NI488 ibclr HP_8753
	endif


end

// dedicated Checkproc function for selecting instruments to be used
Function CheckProc_instr(ctrlName,checked) : CheckBoxControl
	String ctrlName
	Variable checked

	wave instr_used
	strswitch (ctrlName)
		case "HP_8753":
			if (checked==1)
				instr_used[16]=1
			else
				instr_used[16]=0
			endif
		break

	endswitch
End


//	End of GPIB CONTROL specific procedures, functions, etc


//		Windows and panels specific to GPIB

Window select_instruments_used() : Panel
	PauseUpdate; Silent 1		// building window...
	NewPanel /W=(857.25,50,1188.75,269)
	ShowTools
	SetDrawLayer UserBack
	SetDrawEnv fsize= 14,fstyle= 1,textrgb= (0,12800,52224)
	DrawText 15,26,"Select the Instruments to be initialised"
	CheckBox HP8753,pos={15,32},size={78,14},proc=CheckProc_instr,title="[16]
HP8753"
	CheckBox HP8753,variable= inst16
	Button init,pos={9,134},size={86,26},proc=Simple_Buttons,title="Initialise"
	Button general_init,pos={105,134},size={57,26},proc=Simple_Button
	CheckBox HP_8753,pos={172,134},size={40,14},variable= inst16
EndMacro

//	Windows and panels specific to GPIB
```

```
proc Simple_Buttons(ctrlName) : ButtonControl
	String ctrlName
		GPIB_Init()
		SetupGPIB()
		GPIB_Output(HP_8753,"rst")
End

Function/s GPIB_Read(Instrument)			//Writes Data to the GPIB Bus
	variable Instrument
	string ReadString
	variable/G Instrument_G=Instrument
	string/G ReadString_G
	Silent 1;PauseUpdate
	Execute "GPIB device, Instrument_G"
	Execute "GPIBRead/N=10000/T=\"\\n\" ReadString_G"
	//Kills external variables once complete
	ReadString=ReadString_G
	Killstrings/z ReadString_G
	killvariables/z Instrument_G
	return ReadString
End

Function/s GPIB_Read_Data(Instrument)		//reads one piece of data up to a comma
	variable Instrument
	string ReadString
	variable/G Instrument_G=Instrument
	string/G ReadString_G

	Silent 1;PauseUpdate
	Execute "GPIB device, Instrument_G"
	Execute "GPIBRead/T=\",\\n\" ReadString_G"

	ReadString=ReadString_G
	Killstrings/z ReadString_G
	killvariables/z Instrument_G
	return ReadString
End

proc sparameter_measurement()
	variable freq_no_steps= 51
	variable freq_start= 3.349
	variable freq_stop= 3.379
	variable BW, Q
do

Command="DEBUON;"
GPIB_Output(HP_8753, Command)
```

```
make/o/t/n=(freq_no_steps) s21_textwave     // Make text wave with "freq_no_steps" points
to store s21 results in

Command="STAR "+num2str(freq_start)+" GHz;"  // Stimulus - start frequency = global
                                             //variable freq_start in GHz
GPIB_Output(HP_8753, Command)

Command="STOP "+num2str(freq_stop)+" GHz;"   // Stimulus - stop frequency =  global
                                             //variable freq_stop in GHz
GPIB_Output(HP_8753, Command)

Command="POIN "+num2str(freq_no_steps)+" ;"   // Stimulus - number of frequency steps
                                              // = global variable freq_no_steps
GPIB_Output(HP_8753, Command)

Command="CONT;" // Returns to Continuous sweep
GPIB_Output(HP_8753, Command)


// MEASURE S21
Command="S21;"
GPIB_Output(HP_8753, Command)

Command="SMIC;"+"AUTO;" //Select format and response
GPIB_Output(HP_8753, Command)

Command="LINM;"+"AUTO;" //Select format and response
GPIB_Output(HP_8753, Command)

Command="FORM4; SING; OUTPDATA;" // Stops sweep, freezing display, outputs
corrected data in form 5, // OR use SING for single sweep??
GPIB_Output(HP_8753, Command)

s21_textwave=GPIB_Read(HP_8753)          // Copy result from buffer into a textwave

Command="CONT;" // Returns to Continuous sweep
GPIB_Output(HP_8753, Command)


// Calls function to convert captured S-parameter textwaves into S-parameter Complex wave
Sparam_parse()


make/o/n=(numpnts(s21_complex)) s21_mag=magsqr(s21_complex); setscale/I
x,(freq_start*1e9),(1e9*freq_stop), s21_mag

        Display s21_mag
        CurveFit lor s21_mag /D
        ModifyGraph rgb(fit_s21_mag)=(0,0,65280)
```

```
        BW =2*sqrt(K3)
        Q = K2/BW
        Print “fo=”, K2, “Hz”
        Print “BW=”BW, “Hz”
        Print “Q=”, Q
        I+=1
While(i<5)
End

Function Sparam_parse()
        NVAR freq_no_steps

// This function reads in the textwave containing S-parameter data from the 8753 saved as
//strings. It separates the real and imaginary parts into two new strings. These strings are
//converted to numeric values before being inserted into a complex wave for each S-
//parameter

wave/T s21_textwave // bring the textwave saved from the 8753 into the function


make/o/c/n=(freq_no_steps) S21_complex=nan       // numeric wave that will contain the
//complex value of S21

// create strings to hold the separated parts of each S-parameter strings received from the
//8753
string S21_real="chris's initial state", S21_imag="chris's initial state"

// create variables for a counter as well as the real and imaginary parts of the S-parameters in
//numeric form
variable chris_count=0
variable  S21_real_numeric, S21_imag_numeric

// create temporary strings to hold one point of the S-parameter text waves at a time
        string S21_textwave_temp="chris's initial state"

        do


// S21 Process
S21_textwave_temp=S21_textwave[chris_count]     // temporary string tostore one line of the
                                                //S21 text wave at a time
S21_real=StringFromList(0, S21_textwave_temp, ",")       // separate real part of S21
S21_imag=StringFromList(1, S21_textwave_temp, ",")       // separate imag part of //S21

sscanf S21_real, "%f", S21_real_numeric             //convert real part of S21 into a numeric
                                                    //value
sscanf S21_imag, “%f”, S21_imag_numeric             // convert imaginary part of S21 into a
                                                    //numeric value
```

```
S21_complex[chris_count]=cmplx(S21_real_numeric, S21_imag_numeric) //combine
//numeric values of S21 into a complex wave


chris_count+=1                    // increment counter

while (chris_count<(freq_no_steps+1))

end
```

APPENDIX E: Properties and Specifications of HPLC Grade Acetonitrile and Toluene Used for Preparation of Solutions

Acetonitrile

- Purity: 99.99% min; Water: 0.036% max
- Alternative names: Methyl cyanide, Cyanomethane, Ethanenitrile
- Molecular formula: CH_3CN
- Molecular weight: 41.05
- Melting point: −45 °C
- Boiling point: 82 °C
- Solubility in water: Miscible
- Solubility: Organic solvents
- Appearance: Clear, colourless
- Density at 25 °C: 0.78 g/mL
- Refractive index at 20 °C: 1.344
- Dielectric constant at 25°C: 37.5
- Viscosity: 0.38 cP at 20°C

Toluene

- Purity: 99.8% min; Water: 0.03% max
- Alternative names: Phenylmethane, Toluol, Methylbenzene
- Molecular formula: C_7H_8 ($C_6H_5CH_3$)
- Molecular weight: 92.14
- Melting point: −93 °C
- Boiling point: 110.6 °C
- Solubility in water: 0.47 g/l (20–25°C)
- Appearance: Colourless liquid
- Density at 20 °C: 0.865 g/mL
- Refractive index at 20 °C: 1.4969
- Dielectric constant at 25°C: 2.379
- Viscosity: 0.59 cP at 20°C

References

- https://extranet.fisher.co.uk/insight2_uk/mainSearch.do (accessed 17th June 2009).
- Wikipedia contributors, "Acetonitrile," *Wikipedia, The Free Encyclopedia,* http://en.wikipedia.org/w/index.php?title=Acetonitrile&oldid=295945684 (accessed 17th June 2009).
- http://www.piercenet.com/products/browse.cfm?fldID=5B48BF7B-C962-EC8-80E9-81166AE122B1 (accessed 17th June 2009).
- Wikipedia contributors, "Toluene (data page)," *Wikipedia, The Free Encyclopedia,*http://en.wikipedia.org/w/index.php?title=Toluene_(data_page)&oldid=270478097 (accessed 17th June 2009).
- Wikipedia contributors, "Toluene," *Wikipedia, The Free Encyclopedia,* http://en.wikipedia.org/w/index.php?title=Toluene&oldid=296701470 (accessed 17th June 2009).
- https://extranet.fisher.co.uk/webfiles/uk/web-docs/606_CH.pdf (accessed 17th June 2009).
- Wikipedia contributors, "Acetonitrile (data page)," *Wikipedia, The Free Encyclopedia,*http://en.wikipedia.org/w/index.php?title=Acetonitrile_(data_page)&oldid=287238384 (accessed 17th June 2009).

APPENDIX F: Volumes of Toluene and Acetonitrile (MeCN) Required for Preparation of 50 ml Solutions

Solution		Volume (ml)		Total Volume (ml)	No. of Toluene Pipettes			No. of MeCN Pipettes		
% Toluene	% MeCN	Toluene	MeCN		5 ml	1 ml	200 µl	5 ml	1 ml	200 µl
100	0	50	0	50	10 full	0	0	0	0	0
99.9	0.1	49.95	0.05	50	9 full	4 full	4 full, 1 x 150 µl	0	0	1 x 50 µl
99	1	49.5	0.5	50	9 full	4 full	2 full, 1 x 100 µl	0	0	2 full, 1 x 100 µl
97.5	2.5	48.75	1.25	50	9 full	3 full	3 full, 1 x 150 µl	0	1 full	1 full, 1 x 50 µl
95	5	47.5	2.5	50	9 full	2 full	2 full, 1 x 100 µl	0	2 full	2 full, 1 x 100 µl
90	10	45	5	50	9 full	0	0	1 full	0	0
82.5	17.5	41.25	8.75	50	8 full	1 full	1 full, 1 x 50 µl	1 full	3 full	3 full, 1 x 150 µl
75	25	37.5	12.5	50	7 full	2 full	2 full, 1 x 100 µl	2 full	2 full	2 full, 1 x 100 µl
50	50	25	25	50	5 full	0	0	5 full	0	0
25	75	12.5	37.5	50	2 full	2 full	2 full, 1 x 100 µl	7 full	2 full	2 full, 1 x 100 µl
17.5	82.5	8.75	41.25	50	1 full	3 full	3 full, 1 x 150 µl	8 full	1 full	1 full, 1 x 50 µl
10	90	5	45	50	1 full	0	0	9 full	0	0
5	95	2.5	47.5	50	0	2 full	2 full, 1 x 100 µl	9 full	2 full	2 full, 1 x 100 µl
2.5	97.5	1.25	48.75	50	0	1 full	1 full, 1 x 50 µl	9 full	3 full	3 full, 1 x 150 µl
1	99	0.5	49.5	50	0	0	2 full, 1 x 100 µl	9 full	4 full	2 full, 1 x 100 µl
0.1	99.9	0.05	49.95	50	0	0	1 x 50 µl	9 full	4 full	4 full, 1 x 150 µl
0	100	0	50	50	0	0	0	10 full	0	0

APPENDIX G: CorelDRAW Design of Copper Radiation Shield for Miniaturised SDR

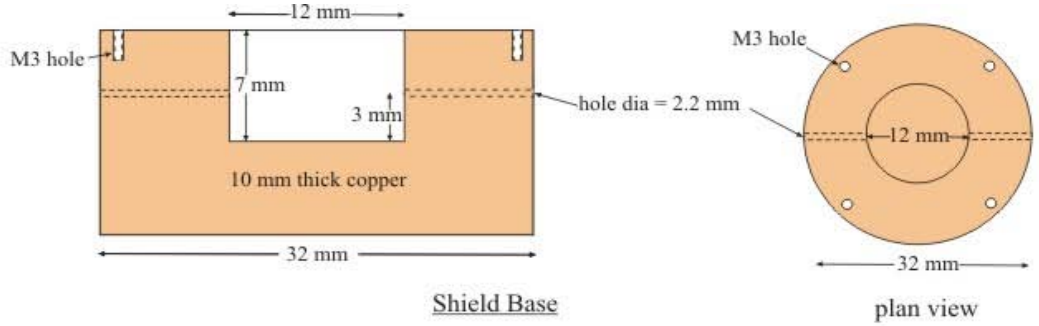

Shield Base

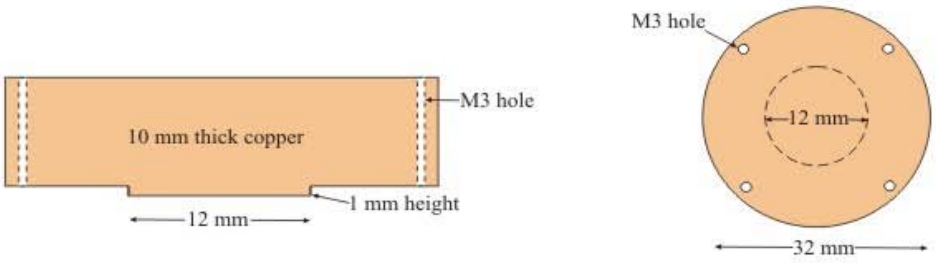

Shield Lid

PTFE Support

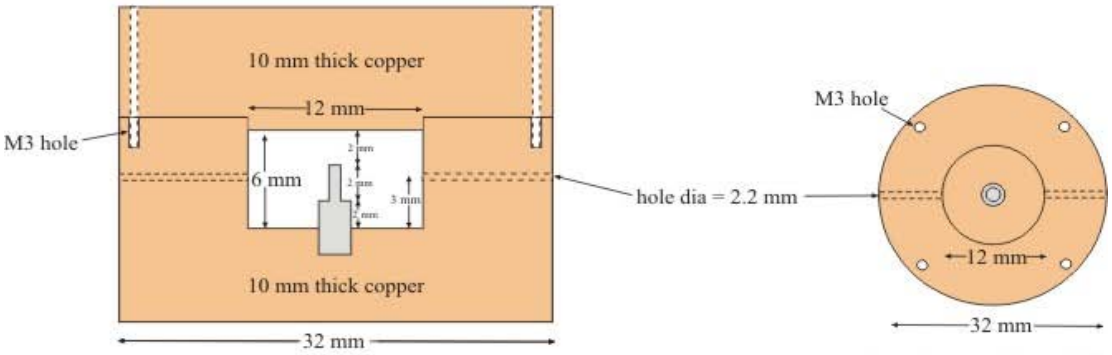

Assembled Shield

APPENDIX H: Text Input File for Superfish Analysis of Miniaturised SDR

```
FISH Test:  Miniaturized Sapphire dielectric resonator
1 iteration, no resonance search
&reg kprob=1,icylin=1,dx=.001,dy=.001,        ;kprob defines the problem (1: Superfish
                                               problem, 0: Poisson problem), icylin
                                               designates coordinate system (0:
                                               Rectangular, 1: Cylindrical), dx and dy
                                               specify the x and y mesh size,
                                               respectively, in the first region
nbsup=0, nbslo=0, nbsrt=0, nbslf=0,           ;Describe the boundary conditions on the
                                               edges of the problem geometry
XDRI=0.3,YDRI=0.225,maxcy=4,freq=22500 &      ;xdri and ydri state x and y location for
                                               drive point, maxcy sets maximum
                                               number of cycles to find resonance, freq
                                               provides approximate resonant frequency

&po x=0.0,y=0.0 &
&po x=0.0,y=0.6 &
&po x=0.6,y=0.6 &                             ;Assign the boundaries for cavity
&po x=0.6,y=0.0 &
&po x=0.0,y=0.0 &


&reg mat=2 &
&po x=0.2,y=0.05 &
&po x=0.2,y=0.225 &
&po x=0.3,y=0.225 &                           ;Assign the boundaries for top sapphire ring
&po x=0.3,y=0.05 &
&po x=0.2,y=0.05 &

&mt mtid=2
epsilon=1,                                    ;Assign ε and μ values for top sapphire ring
mu=9.4 &


&reg mat=3 &
&po x=0.3,y=0.05 &
&po x=0.3,y=0.225 &
&po x=0.4,y=0.225 &                           ;Assign the boundaries for bottom sapphire ring
&po x=0.4,y=0.05 &
&po x=0.3,y=0.05 &


&mt mtid=3
epsilon=1,                                    ;Assign ε and μ values for bottom sapphire ring
mu=9.4 &
```

```
&reg mat=4 &
&po x=0.2,y=0.0 &
&po x=0.2,y=0.05 &
&po x=0.4,y=0.05 &
&po x=0.4,y=0.1 &                    ; Assign the boundaries for PTFE rod
&po x=0.6,y=0.1 &
&po x=0.6,y=0.0 &
&po x=0.2,y=0.0 &


&mt mtid=4
epsilon=1,                           ;Assign ε and μ values for PTFE rod
mu=2.06 &
```

APPENDIX J: Mathcad Code for Calculation of Miniaturised SDR Q_U

$Rc := 0.6 \cdot 10^{-2}$ radius of cavity in m

$Lc := 0.6 \cdot 10^{-2}$ length of cavity in m

$N := 60$ number of points along the radial and longitudinal directions

$\Delta r := \frac{Rc}{N}$ $\Delta z := \frac{Lc}{N}$

$\mu 0 := 4 \cdot \pi \cdot 10^{-7}$ $\varepsilon 0 := 8.854 \cdot 10^{-12}$

$A := READPRN("C:\LANL\outsf7.txt")$

$f := A_{0,0} \cdot 10^{9}$ resonant frequency (Hz), computed by SF $f = 2.27568 \times 10^{10}$

$\omega := 2 \cdot \pi \cdot f$

$\rho := 2 \cdot 10^{-8}$ $Rs := \sqrt{\pi \cdot \mu 0 \cdot f \cdot \rho}$ resistivity (m) and surface resistance of cavity walls

$Rs = 0.04239$

$m := 0 .. N$ $n := 0 .. N$

$E\phi_{m,n} := A_{n+m\cdot(N+1),5}$

$Hz_{m,n} := A_{n+m\cdot(N+1),2}$

$Hr_{m,n} := A_{n+m\cdot(N+1),3}$

$Htot_{m,n} := A_{n+m\cdot(N+1),4}$

$H_{m,n} := Htot_{N-m,n}$ $r_m := m \cdot \Delta r$

$H_{m+N-1,n} := Htot_{m,n}$ $z_n := n \cdot \Delta z$

$E_{m,n} := E\phi_{N-m,n}$

$E_{m+N-1,n} := E\phi_{m,n}$

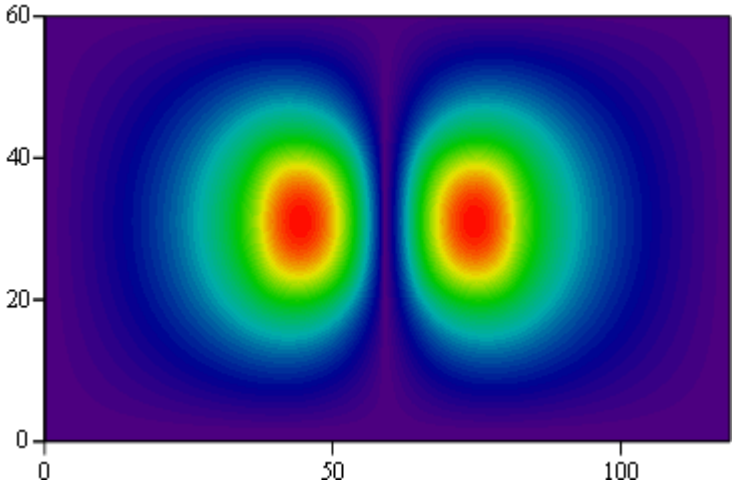

E

Magnitude of E (axis in centre)

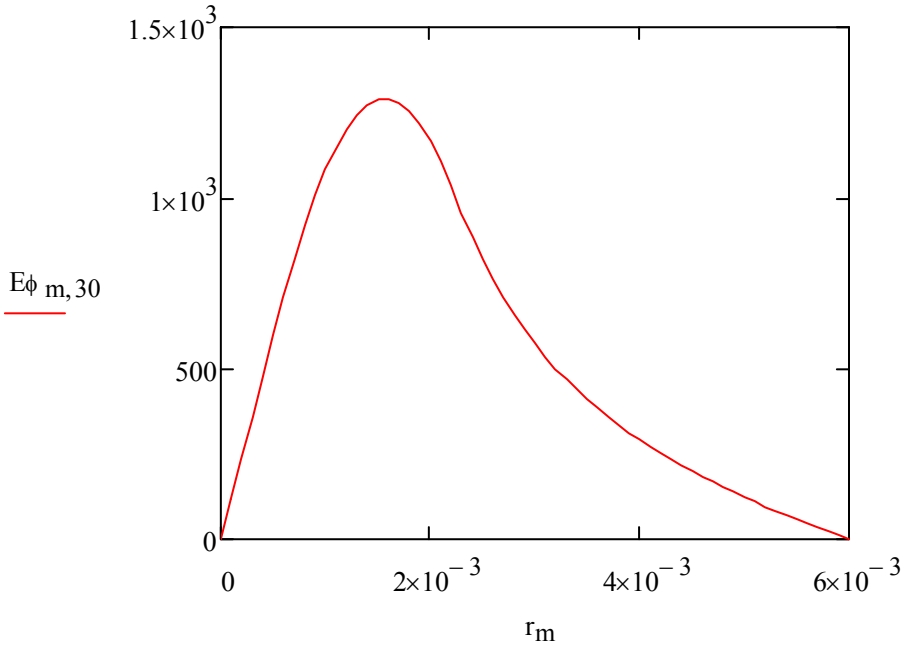

Radial uniformity of Eϕ

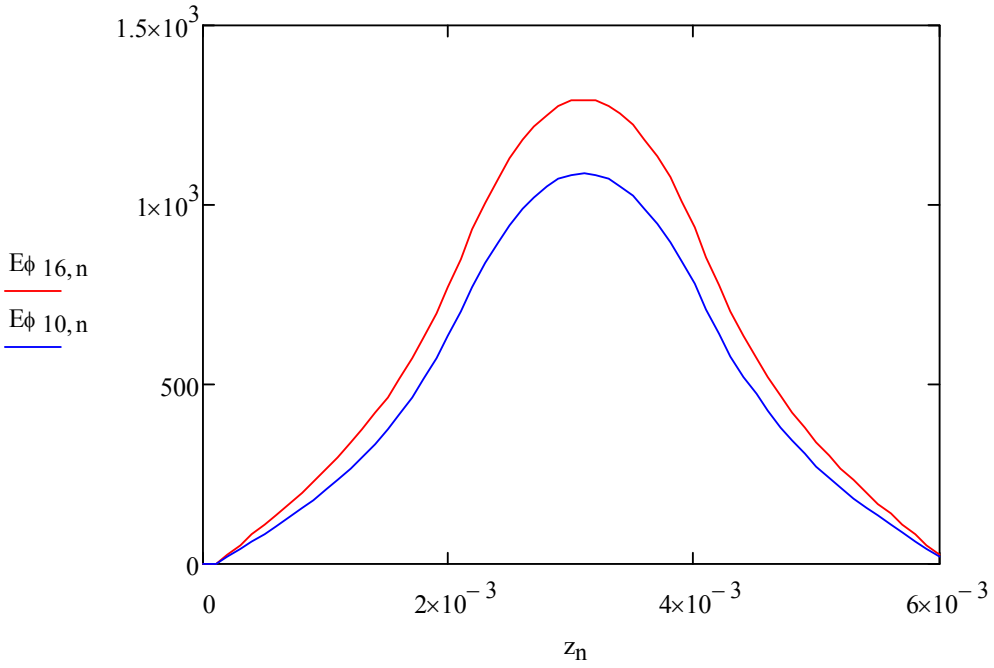

Longitudinal uniformity of Eϕ

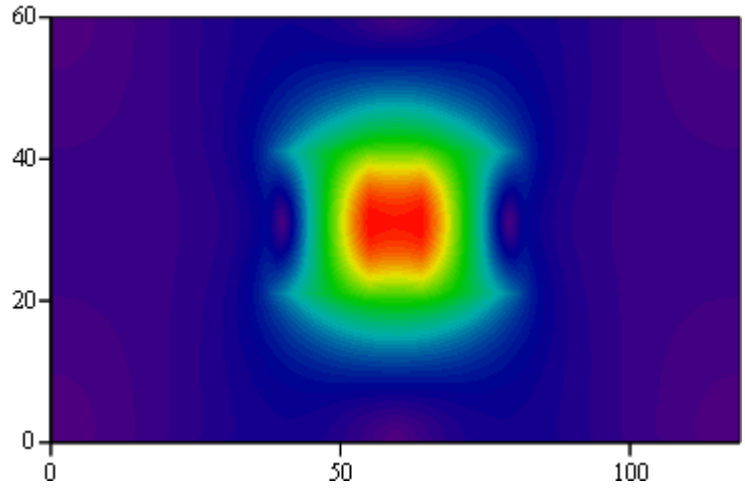

H

Magnitude of H (axis in centre)

Conductor Curved Wall Losses

$m := 0 .. (N - 1)$ $n := 0 .. (N - 1)$

$\Delta Sc := 2 \cdot \pi \cdot Rc \cdot \Delta z$

$Hav_n := \frac{1}{2} \cdot \left(Hz_{N,n} + Hz_{N,n+1} \right)$ $Pc := \sum_{n=0}^{N-1} \left[\left(Hav_n \right)^2 \cdot \Delta Sc \cdot Rs \right]$

Conductor End wall losses

$m := 0 .. (N - 1)$ $\Delta S_m := \pi \cdot \left[(m+1)^2 - m^2 \right] \cdot \Delta r^2$

$n := 0 .. (N - 1)$

$Hav\_t_m := \frac{1}{2} \cdot \left(Hr_{m,N} + Hr_{m+1,N} \right)$ $Hav\_b_m := \frac{1}{2} \cdot \left(Hr_{m,0} + Hr_{m+1,0} \right)$

$Pt := \sum_{m=0}^{59} \left[\left(Hav\_t_m \right)^2 \cdot \Delta S_m \cdot Rs \right]$ $Pb := \sum_{m=0}^{59} \left[\left(Hav\_b_m \right)^2 \cdot \Delta S_m \cdot Rs \right]$

$Pc = 3.65637 \times 10^{-8}$ $Pt = 7.43866 \times 10^{-8}$ $Pb = 7.74534 \times 10^{-8}$

$Ptot := Pc + Pt + Pb$

$Ptot = 1.88404 \times 10^{-7}$

$\Delta V_m := \Delta z \cdot \pi \cdot \left[(m+1)^2 - m^2 \right] \cdot \Delta r^2$

$Hav_{m,n} := \frac{1}{4} \cdot \left(Htot_{m,n} + Htot_{m,n+1} + Htot_{m+1,n} + Htot_{m+1,n+1} \right)$

$UM := \frac{1}{2} \cdot \mu 0 \cdot \sum_{m=0}^{59} \left[\sum_{n=0}^{N-1} \left(Hav_{m,n} \right)^2 \cdot \Delta V_m \right]$

$UM \cdot 10^{12} = 0.03101$

$Utot := 2 \cdot UM$ Total energy stored in the volume of the cavity

$Utot = 6.20111 \times 10^{-14}$

$Qc := \omega \cdot \frac{Utot}{Ptot}$ Q value of conductor

$Qc = 4.70622 \times 10^{4}$

$\varepsilon 1s := 9.4$ $tan\delta s := .000025$ loss tangent and dielectric constant of sapphire

$\varepsilon 1p := 2.06$ $tan\delta p := .0007$ loss tangent and dielectric constant of PTFE

$$Eav_{m,n} := \frac{1}{4} \cdot \left(E\phi_{m,n} + E\phi_{m,n+1} + E\phi_{m+1,n} + E\phi_{m+1,n+1} \right)$$

$$\Delta V_m := \Delta z \cdot \pi \cdot \left[(m+1)^2 - m^2 \right] \cdot \Delta r^2$$

$$UE1 := \sum_{m=0}^{N-1} \left[\sum_{n=0}^{20} \left(Eav_{m,n} \right)^2 \cdot \Delta V_m \right] \qquad UE1 = 9.4084 \times 10^{-3}$$

$$UE2 := \sum_{m=5}^{23} \left[\sum_{n=20}^{30} \left(Eav_{m,n} \right)^2 \cdot \Delta V_m \cdot \varepsilon rs \right] \qquad UE2 = 0.17619$$

$$UE3 := \sum_{m=23}^{N-1} \left[\sum_{n=20}^{30} \left(Eav_{m,n} \right)^2 \cdot \Delta V_m \right] \qquad UE3 = 0.0108$$

$$UE4 := \sum_{m=0}^{5} \left[\sum_{n=20}^{30} \left(Eav_{m,n} \right)^2 \cdot \Delta V_m \cdot \varepsilon rp \right] \qquad UE4 = 4.83911 \times 10^{-4}$$

$$UE5 := \sum_{m=0}^{10} \left[\sum_{n=40}^{N-1} \left(Eav_{m,n} \right)^2 \cdot \Delta V_m \cdot \varepsilon rp \right] \qquad UE5 = 1.44552 \times 10^{-3}$$

$$UE6 := \sum_{m=10}^{N-1} \left[\sum_{n=40}^{N-1} \left(Eav_{m,n} \right)^2 \cdot \Delta V_m \right] \qquad UE6 = 0.01081$$

$$UEtot := UE1 + 2\cdot UE2 + 2\cdot UE3 + 2UE4 + UE5 + UE6$$

$$UEtot = 0.39661$$

$$Ws := \frac{UEtot - 2UE2}{2\cdot UE2} \qquad Ws = 0.12553$$ W for sapphire

$$Wp := \frac{UEtot - 2UE4 - UE5}{2\cdot UE4 + UE5} \qquad Wp = 163.34244$$ W for PTFE

$$Qds := \frac{1 + Ws}{\tan\delta s} \qquad Qds = 4.50212 \times 10^4$$ Qd of sapphire

$$Qdp := \frac{1 + Wp}{\tan\delta p} \qquad Qdp = 2.34775 \times 10^5$$ Qd of PTFE

$$Qd := \frac{Qds\cdot Qdp}{Qds + Qdp} \qquad Qd = 3.7777 \times 10^4$$ Overall Qd

$$Qu := \frac{Qc\cdot Qd}{Qc + Qd}$$

$$Qu = 2.09557 \times 10^4$$ **Final unloaded Q**

APPENDIX K: Calculation of Main Microchannel Dimensions and Optimum Thickness of Coated Teflon® AF Film in Miniaturised SDR

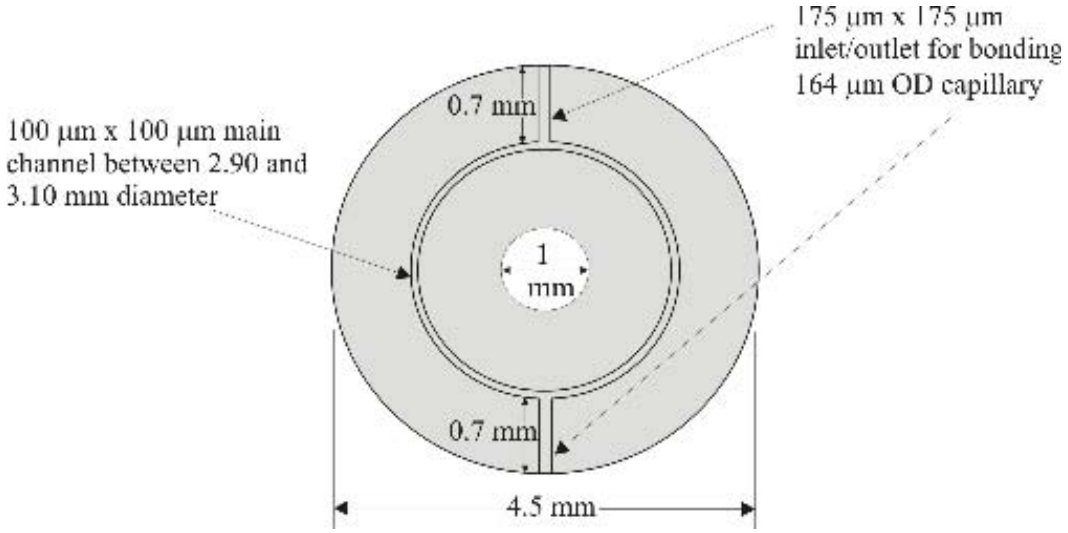

Figure K1. Designed microchannel on sapphire ring of miniaturised resonator

Designed channel width, $W = 100$ μm

Designed channel depth, $D = 100$ μm

Area of channel, $A = \pi (1.55 \times 10^{-3})^2 - \pi (1.45 \times 10^{-3})^2 = 0.94 \times 10^{-6}$ m^2

Volume of channel, $V = 0.94 \times 10^{-6} \times 100 \times 10^{-6} = 94 \times 10^{-12}$ m^3

The fluid volume in Teflon® AF microcapillary experiments conducted on the SDR can be calculated as follows:

Length of capillary = circumference of the channel outer circle = $2 \times \pi \times 7.5 \times 10^{-3} = 47 \times 10^{-3}$ m^3

$\Rightarrow$ Fluid volume $= 47 \times 10^{-3} \times \pi \times (0.125 \times 10^{-3})^2 = 2.31 \times 10^{-9}$ m^3

Since V_{eff} for miniaturised SDR is about 100 times smaller than for SDR, a fluid volume around 2.31×10^{-11} m^3 would provide the same measurement sensitivity there. This volume could be achieved by having channel dimensions of 50 μm × 50 μm, as worked out below:

$W = D = 50$ μm

$A = \pi (1.55 \times 10^{-3})^2 - \pi (1.5 \times 10^{-3})^2 = 0.48 \times 10^{-6}$ m^2

$V = 0.48 \times 10^{-6} \times 50 \times 10^{-6} = 2.4 \times 10^{-11}\ \text{m}^3$, which is very close to $2.31 \times 10^{-11}\ \text{m}^3$.

The designed microchannel would give improved measurement sensitivity by a factor of $\frac{100 \times 94 \times 10^{-12}\ \text{m}^3}{2.31 \times 10^{-9}\ \text{m}^3} \approx 4$ over SDR.

For the actual microchannel, the volume of fluid would be as follows:

$W \approx 100\ \mu\text{m}$

$D \approx 60\ \mu\text{m}$

$A = \pi (1.55 \times 10^{-3})^2 - \pi (1.45 \times 10^{-3})^2 = 0.94 \times 10^{-6}\ \text{m}^2$

$V = 0.94 \times 10^{-6} \times 60 \times 10^{-6} \approx 56 \times 10^{-12}\ \text{m}^3$

Thus, the enhancement in measurement sensitivity provided by the miniaturised SDR over its bigger counterpart would be $\frac{100 \times 56 \times 10^{-12}\ \text{m}^3}{2.31 \times 10^{-9}\ \text{m}^3} \approx 2.5$ times.

Calculation of Optimum Thickness of Coated Teflon® AF Film

The area of ring in miniaturised SDR can be worked out as under:

$$\text{Ring area} = \pi (\frac{4.5}{2} \times 10^{-3})^2 - \pi (\frac{1}{2} \times 10^{-3})^2$$

$$= \pi (5.06 \times 10^{-6}) - \pi (0.25 \times 10^{-6}) \approx 15 \times 10^{-6}\ \text{m}^2$$

The volume available in microchannel is $\approx 56 \times 10^{-12}\ \text{m}^3$. If the coated Teflon® AF film were to fill all of microchannel during the bonding process, its thickness, *t*, would have to be $t = \frac{56 \times 10^{-12}\ \text{m}^3}{15 \times 10^{-6}\ \text{m}^2} = 3.73 \times 10^{-6}\ \text{m}$. In the worst case, however, the channel must not be filled more than 25% by the coating so as to allow enough room for the solution samples to flow in it [1]. Therefore, the Teflon® AF film thickness must not exceed $\frac{3.73 \times 10^{-6} \times 25}{100} \approx 1\ \mu\text{m}$.

Reference

[1] D. A. Barrow, *Private Communication*, 2007-9.

APPENDIX L: Technical Data Sheet ELC-4481 UV Curable Epoxy Adhesive

Description

ELC 4481LV is a UV curing structural adhesive designed for joining fibre optics as well as the assembly of glass to glass, and glass to metal applications. Cure times are dependent on the intensity of the light source used and the nature of the components involved. Some possible uses include: unitizing fibre bundles, fibre optic splicing, transparent potting, and lens assembly.

Features

*Excellent Adhesion	*No Odour
*Good Water & Chemical Resistance	*Good Surface Cure

Typical Specifications

Refractive Index	1.48
Tensile shear	ASTM D -10027000 psi
Gap filling	+/-.250 in.
Thermal range	-45 to 300°F
Dielectric strength	700V/ml.
Elongation at 79°F	20%
Colour	Clear
Specific gravity	1.08
Flash point	over 200°F
Viscosity	5000 cps
Out gassing/degassing	Above 375°F
Hardness	85D

Cure Schedule

Cure speed is dependent upon the UV light source, thickness of material, distance from the light, and UV transmission of substrates through which the UV light must pass to reach the adhesive. Certain lighting conditions may cause ELC 4481LV to become a light yellow; the properties of the adhesive, however, are not affected.

Storage & Handling

Store out of sunlight and in original container. Maintain at 68°F +/-20°F for a maximum shelf life. Material removed from containers may be contaminated during use and should not be reused. Avoid exposing material to moisture.

Availability

ELC-4481LV is available in 10 ml syringes, 30ml syringes, and 1000ml Bottles. For custom size containers please contact the Sales Department.

Hygiene & Safety

Low potential for skin and eye irritation or sensitization. See OSHA Material Safety Data Sheet for more details on proper handling and precautions.

Reference

http://www.electro-lite.com/foundations/store/kb_results.asp?type=category (accessed 17th June 2009).

APPENDIX M: Protocol for Preparation and Use of Piranha Solution

Piranha refers to an acid-peroxide mixture that gains its name from its aggressive etching of organic contaminants. Needless to say, this stuff is dangerous so appropriate care should be exercised. Always wear full safety gear i.e. goggles, face shield, rubber gloves, apron etc. and work in a fume hood. Do not store the prepared solution in sealed container.

- A typical mixture is 3:1 concentrated sulphuric acid (H_2SO_4) to 30% hydrogen peroxide (H_2O_2) solution; other protocols may use mixtures varying from 2:1 to 7:1.
- Piranha solution may be prepared by **adding the peroxide to the acid in (**as opposed to the usual rule of adding acid to water).
- Maintain 3:1 ratio of H_2SO_4:H_2O_2 at 130 °C for 15 minutes. Since this is a highly exothermic reaction the temperature will heat up to about 100-110 °C on its own within minutes, then it will start to drop after 4 -5 minutes, so maintaining 130 °C can be tricky.
- The mixture may fizz out of your container, so assume your gloves/hands are covered with piranha solution regardless, and act accordingly.
- Rinse with deionised (DI) water for at least 1 minute. About 500 ml water should be enough for two sapphire discs of 25 mm diameter.
- Dry well to help ensure a clean surface. Dry the samples immediately after rinsing with dry nitrogen or through use of a drying cabinet.

References

- W. Kern (Editor), "*Handbook of Semiconductor Wafer Cleaning Technology: Science, Technology, and Applications*", Noyes Publishers, N.J., 1993, ISBN 0-8155-1331-3.
- Wikipedia contributors, "Piranha solution", *Wikipedia, The Free Encyclopedia,* http://en.wikipedia.org/w/index.php?title=Piranha_solution&oldid=287429724 (accessed 8th June 2009).

APPENDIX N: Product Information for Dow Corning® 730 Solvent Resistant Adhesive/Sealant

Features

- One-component fluorosilicone adhesive/sealant
- Cures at room temperature when exposed to moisture in the air
- Acetoxy (i.e. on exposure to atmospheric moisture; gives off a small amount of acetic acid) cure system
- Non-sag, paste consistency
- Easy to apply
- Cures to a tough, flexible rubber
- Good adhesion to many substrates
- Stable and flexible from -65 ºC (-85 ºF) to 200 ºC (392 ºF)
- Retains its properties under exposure to fuels, oils and solvents

Applications

- For bonding and sealing applications where resistance to the swelling effects of fuels, solvents and oils is required.
- For assembling and/or repairing of fuel systems and tanks of aircraft.
- Used for formed-in-place gaskets where irregular shapes and harsh conditions reject ordinary seals.
- For bonding or sealing of components exposed to moisture, vibration, shock, fuels, solvents and oils for long periods of time.

Typical Properties

Specification writers: These values are not intended for use in preparing specifications. Please contact your local Dow Corning sales representative prior to writing specifications on this product.

As Supplied

Colour .....White

CTM[1] 0097 Specific Gravity at 77 °F (25 °C) 1.40

CTM 0364 Extrusion Rate, 1/8-inch orifice at 90 psi, g/minute…….250

CTM 0098 Skin-Over Time, minutes.....10

CTM 0095 Tack-Free Time, minutes.....25

Physical Properties – As Cured 7 Days in Air at 77 °F (25 °C) and 50% RH

CTM 0099 Durometer Hardness, Shore A, points 40

CTM 0137A Tensile Strength, psi 300

CTM 0137A Elongation, percent..... 200

CTM 1112 Tear Strength, ppi 27

CTM 0293 Peel Strength, Aluminium Alloy Alclad 2024T3,with Dow Corning® 1200 RTV Prime Coat, ppi…… 15

Electrical Properties – As Cured 7 Days in Air at 77 °F (25 °C) and 50% RH

Arc Resistance, seconds.....124

CTM 0114 Dielectric Strength, volts/mil 331

CTM 1139 Dielectric Constant, 100 kHz 5.5

CTM 1139 Dissipation Factor, 100 kHz.....0.0043

CTM 0313 Volume Resistivity, ohm cm.....2.1×10^{13}

Repairability .....Excellent

[1]CTMs (Corporate Test Methods) correspond to standard American Society for Testing and Materials (ASTM) tests in most instances. Copies of CTMs are available upon request.

How to Use

Substrate preparation

All surfaces must be clean and dry. Degrease and wash off any contaminants that could impair adhesion. Suitable solvents include isopropyl alcohol, acetone or methyl ethyl ketone. Unprimed adhesion may be obtained on many substrates such as glass, metals and most common engineering plastics. Substrates to which good adhesion is normally not obtained include PTFE, polyethylene, polypropylene and related materials. For maximum adhesion, the use of DOW CORNING® 1200 OS Primer is recommended. After solvent cleaning, a thin coat of DOW CORNING 1200 OS Primer is applied by dipping, brushing or spraying. Allow primer to dry for 15 to 90 minutes at room temperature and a relative humidity of 50% or higher.

How to apply

Apply DOW CORNING 730 Solvent Resistant Adhesive/Sealant to one of the prepared surfaces, and then quickly cover with the other substrate to be bonded. On exposure to moisture, the freshly applied material will "skin-over" in about 5 minutes at room temperature and 50% relative humidity. Any tooling should be completed before this skin forms. The surface is easily tooled with a spatula. The adhesive/sealant will be tack-free in about 25 minutes.

Cure Time

After skin formation, cure continues inward from the surface. In 24 hours (at room temperature and 50% relative humidity) DOW CORNING 730 Solvent Resistant Adhesive/Sealant will cure to a depth of about 3mm. Very deep sections, especially when access to atmospheric moisture is restricted, will take longer to cure completely. Cure time is extended at lower humidity levels. Before handling and packaging bonded components, users are advised to wait a sufficiently long time to ensure that the integrity of the adhesive seal is not affected. This will depend on many factors and should be determined by the user for each specific application.

Compatibility

Dow Corning 730 Solvent Resistant Adhesive/Sealant releases a small amount of acetic acid during cure. This may cause corrosion on some metallic parts or substrates, especially in direct contact or when the cure is carried out in a totally enclosed configuration which would not allow cure by-products to escape.

Handling Precautions

Product safety information required for safe use is not included. Before handling, read product and safety data sheets and container labels for safe use, physical and health hazard information. The material safety data sheet is available on the Dow Corning website at www.dowcorning.com. You can also obtain a copy from your local Dow Corning sales representative or Distributor or by calling your local Dow Corning Global Connection.

Usable Life and Storage

When stored at or below 32ºC (90ºF) in the original unopened containers, Dow Corning 730 Solvent Resistant Adhesive/Sealant has a usable life of 18 months from the date of production. As Dow Corning 730 Solvent Resistant Adhesive/Sealant cures by reaction with moisture in air, keep the container tightly sealed when not in use. A plug of used material may form in the tip of a tube or cartridge during storage. This is easily removed and does not affect the remaining contents.

Packaging

This product is available in standard industrial container sizes. For details please refer to your Dow Corning sales office.

Limitations

This product is neither tested nor represented as suitable for medical, food contact or pharmaceutical uses.

Health and Environmental Information

To support Customers in their product safety needs, Dow Corning has an extensive Product Stewardship organization and a team of Product Safety and Regulatory Compliance (PS&RC) specialists available in each area. For further information, please see our website, www.dowcorning.com or consult your local Dow Corning representative.

LIMITED WARRANTY INFORMATION – PLEASE READ CAREFULLY

The information contained herein is offered in good faith and is believed to be accurate. However, because conditions and methods of use of our products are beyond our control, this information should not be used in substitution for customer's tests to ensure that Dow Corning's products are safe, effective, and fully satisfactory for the intended end use. Suggestions of use shall not be taken as inducements to infringe any patent. Dow Corning's sole warranty is that the product will meet the Dow Corning sales specifications in effect at the time of shipment. Your exclusive remedy for breach of such warranty is limited to refund of purchase price or replacement of any product shown to be other than as warranted.

DOW CORNING SPECIFICALLY DISCLAIMS ANY OTHER EXPRESS OR IMPLIED WARRANTY OF FITNESS FOR A PARTICULAR PURPOSE OR ERCHANTABILITY. DOW CORNING DISCLAIMS LIABILITY FOR ANY INCIDENTAL OR CONSEQUENTIAL DAMAGES.

Table I: Typical Fluid Resistance Values[1]
These values are not intended for use in preparing specifications.

Fluids	Volume Swell, %	Durometer Hardness, pts change
Methanol	0.7	-3
JP-5	3.8	-2
Diesel	2.6	-4
Isopropanol	0.7	-2
JP-8	4.0	-1
DOW CORNING® OS 20 Fluid	4.4	-3
Jet Reference Fuel[2]	16.9	-8

[1] Dow Corning 730 Solvent Resistant Sealant, cured 7 days before immersion; properties obtained after 7 days immersion at room temperature.
[2]Properties obtained after 7 days immersion at 80 ºC (176 ºF).

(Reproduced from http://www1.dowcorning.com/DataFiles/090007c8801abc0c.pdf and http://www1.dowcorning.com/DataFiles/090007c880001ff4.pdf)

APPENDIX O: Product Information for Araldite® Epoxies for Consumer Use

ARALDITE® EPOXIES FOR CONSUMER USE

DESCRIPTION:

ARALDITE® epoxies for Consumer use are solvent free, room temperature curing, high strength adhesives supplied in two part form. They are manufactured by CIBA Specialty Chemicals, world leaders in epoxy resin adhesives. Three products are specially made for DIY applications:

Precision - a tough adhesive with a long pot life for precision positioning

Rapid - a powerful adhesive with a fast setting time for rapid bonding

Instant Clear - a strong, ultra fast adhesive which is clear and colourless

MATERIALS BONDED/APPLICATIONS:

ARALDITE® epoxies for Consumer use will bond a variety of materials around the home including metal, wood, ceramics, masonry, glass, dry concrete, chipboard, leather, cardboard and most hard plastics, fabrics and rubbers.

IMPORTANT: **ARALDITE®** epoxies are not suitable for bonding rear-view mirrors to car windscreens. Do not use for items which may contain food or drink, as the joint however secure and clean it may appear, may entrap bacteria from the environment. Not intended for repairs on safety critical items e.g. rotating parts of hover mowers. Please note that some items are moulded from polymers such as polythene or polypropylene, for example, and are simply not designed for repair. Repair may not be viable or would need specialist chemical treatment to achieve a bond.

BONDING INSTRUCTIONS:

1. Make sure surfaces are dry, clean and free from dust, dirt and grease. For even better bonding slightly roughen surfaces with sandpaper.

2. Following the instructions on the back of the blister card, dispense equal volumes of resin and hardener onto a clean disposable surface. Stir well for 15 seconds with the plastic palette knife provided, ensuring a thorough mix. Reseal the syringe/tubes of resin and hardener as directed on the blister card as soon as possible.

3. Apply the mixed adhesive to both surfaces of the joint and assemble carefully. If using ARALDITE® Instant Clear the joint must be assembled immediately.

4. Keep the joint supported until set. A rubber band or sticky tape is ideal for ARALDITE® Precision and Rapid. ARALDITE® Instant Clear sets very rapidly so hold the joint together until bonded. An approximate guide to support and handling times at room temperature is given below.

Adhesive	Support Time at Room Temperature	Handling Time At Room Temperature
Precision	at least 6 hours (or 4 hours at 40°C)	at least 16 hours
Rapid:	about 10 minutes	about one hour
Instant Clear:	about 1½ minutes	about 10-15 minutes

The times given above are for guidance only and are dependant on temperature. Setting times may be shorter in hot weather and depend on the quantity mixed. In cold conditions the rate of curing of the mixed adhesive may be slowed down significantly and weak joints may result. For best results use between 20°C to 25°C.

5. For a perfect finish carefully remove any excess adhesive with a sharp knife before the adhesive has fully hardened.

CLEANING:

Uncured resin/hardener mixtures can be cleaned from tools using cellulose thinners or acetone. Solvents must always be handled with due care as they may be hazardous or flammable. Methoxypropanol is an alternative solvent which significantly reduces the flammability hazard. Please note that solvents may attack some rubbers, plastics, painted surfaces, fabrics, etc., Bear this in mind if intending to use solvent to remove excess adhesive, and carry out a preliminary test first.

Cured adhesive residues can usually be dissolved from tools by soaking in commercial paint stripper. Refer to the paint stripper manufacturer's instructions for use and safe handling.

The adhesive may be removed from the skin using a suitable proprietary hand cleaner. Contact with the skin should however be avoided. Do not use solvents in contact with the skin. Always open and use adhesive products over a protected surface, and avoid contact with clothing.

TYPICAL ADHESIVE CHARACTERISTICS:

	Resin	Hardener
Physical form:	Liquid	Liquid
Chemical type:	Epoxy resin	Dependent on product (Refer to pack or Material Safety Data sheet)
Solids content:	100%	100%

	Mixed
Colour:	Pale yellow except Instant Clear (colourless)
S.G:	1.1 - 1.2 according to grade

Setting Time*:	**Precision**	About 2 hours for 100 g
	Rapid	About 4 minutes for 5 g
	Instant Clear	About 90 seconds for 2 g

* Typical Pot life at 20-25°C. Pot life will vary according to ambient temperature, temperatures of resin and hardener, and quantity mixed.

TYPICAL PERFORMANCE CHARACTERISTICS:

Temperature resistance.	-50°C to + 65°C depending on conditions of use
Water resistance:	Good
Oil & Petrol resistance:	Good
Chemical resistance.	Good
Sandability.	Sandable when hardened (wear a dust mask when sanding)
Paintability:	Good

PACKAGING

Please refer to Customer Service Department for details of current pack sizes.

SUBSTANCE IDENTIFICATION NUMBER

UN No. 3082 (bisphenol A - epoxy resin).

HEALTH, SAFETY AND THE ENVIRONMENT

See the individual product Material Safety Data sheet.

STORAGE AND TRANSPORTATION

Store under dry conditions between 5 and 25°C.

SHELF LIFE

Maximum shelf life three years from the date of manufacture under the recommended storage conditions.

(Reproduced from Bostik Information Sheet Number B1329/2, issued September 1998)